REPORT ON RESEARCH ACTIVITIES FOR THE QUARTER JULY 1, 1991 THROUGH SEPTEMBER 30, 1991

Prepared for

Nuclear Regulatory Commission
Contract NRC-02-88-005

Prepared by

Center for Nuclear Waste Regulatory Analyses
San Antonio, Texas

November 1991

REPORT ON RESEARCH ACTIVITIES FOR THE QUARTER JULY 1 THROUGH SEPTEMBER 30, 1991

Prepared for

Nuclear Regulatory Commission
Contract NRC-02-88-005

Edited by

Wesley C. Patrick

Center for Nuclear Waste Regulatory Analyses
San Antonio, Texas

November 1991

TABLE OF CONTENTS

TABLE OF CONTENTS (Cont'd)

TABLE OF CONTENTS (Cont'd)

TABLE OF CONTENTS (Cont'd)

LIST OF FIGURES

LIST OF FIGURES (Cont'd)

LIST OF FIGURES (Cont'd)

LIST OF FIGURES (Cont'd)

LIST OF FIGURES (Cont'd)

LIST OF TABLES

LIST OF TABLES (Cont'd)

LIST OF TABLES (Cont'd)

ACKNOWLEDGMENTS

This report was prepared to document work performed by the Center for Nuclear Waste Regulatory Analyses (CNWRA) for the U. S. Nuclear Regulatory Commission under Contract No. NRC-02-88-005. The research activities reported here were performed on behalf of the NRC Office of Nuclear Regulatory Research, Division of Engineering. The report is an independent product of the CNWRA and does not necessarily reflect the views or regulatory position of the NRC.

Each chapter of this report acknowledges those investigators who, although not specifically involved in writing the report, made significant contributions to the research projects. In addition, the authors gratefully acknowledge the technical support and technical reviews conducted by other members of the CNWRA and Institute staffs. Appreciation is particularly due Bonnie Garcia, Cathy Garcia, and Mary Ann Gruhlke, who prepared input to the individual chapters of the report, and to Pamela Smith, who prepared the final text of this document. We also acknowledge the able assistance of Curtis Gray, who provided graphical assistance, and Dr. Shirley Heller, who provided a full range of expert editorial services in the preparation of the final document.

1 EXECUTIVE SUMMARY

1.1 INTRODUCTION

This is one in a series of research quarterly reports that document and make available to the technical community work undertaken by the Center for Nuclear Waste Regulatory Analyses (CNWRA) as part of its contract with the U.S. Nuclear Regulatory Commission (NRC). Reports are prepared each calendar quarter and published as CNWRA documents. The fourth such report each year constitutes the annual progress report and is published as a NUREG/CR.

Each of the research projects discussed here is conducted in accordance with approved Research Project Plans, which were developed in response to research needs identified by the NRC and the CNWRA. These Plans are the vehicle for establishing the objectives, technical approach, justification, and funding for each of the studies. They also describe the interrelationships among the various projects which provide a sound basis for integrating research results. Because the Plans address primarily planning and management matters, they are not discussed in this report (with the exception of stating project objectives).

Eight individual research projects are discussed herein. Because a few of the projects have only recently been initiated, they have relatively little work to report at this time. In such cases, this report provides basic information on the objectives of the new projects as well as early activities such as literature assessments. Other projects begun earlier have significant technical progress in laboratory, calculational, or field studies or in a combination of such investigations to report.

This document provides, first, an Executive Summary that covers in capsule form the progress of each research project over the past quarter. The Executive Summary is followed by Chapters 2 through 9 representing each of the eight currently active research projects, respectively. Project objectives and a report of research activities and results (as appropriate) to date are given in each chapter.

1.2 UNSATURATED MASS TRANSPORT (GEOCHEMISTRY)

A major geologic feature potentially affecting the suitability of Yucca Mountain, Nevada, as a repository site for high-level nuclear wastes (HLW) is the presence of laterally extensive zones of zeolitic tuff. Because of their sorptive properties, zeolites could provide important geologic barriers to migration of radionuclides from the repository to the accessible environment. An evaluation of the relative importance of zeolites as retardation agents requires a knowledge of their thermodynamic stabilities and ion exchange properties under geochemical conditions relevant to the Yucca Mountain system.

In the experimental task of the Geochemistry Research Project, experiments are ongoing to determine the rate of dissolution and the equilibrium solubility of the zeolite

mineral analcime. These experiments were initiated during the previous calendar quarter, and additional aqueous samples were taken during the current reporting period. The experimental data are given in subsection 2.1 of this report, and initial kinetic and thermodynamic interpretations of some of these data are discussed in subsection 2.2.

In addition, isotherm experiments were conducted at 25°C involving the zeolite mineral clinoptilolite and aqueous mixtures of NaCl/KCl and NaCl/$CaCl_2$ at total solution concentrations of 0.005, 0.05, and 0.50 N. These experiments were designed to check the reproducibility of previously derived isotherms and to evaluate the predictive ability of thermodynamic models at ionic strengths closer to those of Yucca Mountain groundwaters. A complete set of experimental results are given in subsection 2.1. The isotherm data demonstrate that the exchange reactions are binary in nature and that participation of H^+ or other cations initially present with Na^+ in the Na-clinoptilolite is negligible. The data also confirm the previously observed concentration-valency effect, which accounts for the strong dependence of isotherm shapes and selectivities on ionic strength in exchanges involving cations of different ionic charges.

In the modeling task of the Geochemistry Research Project, principles of thermodynamics, kinetics, and mass balance are applied to the interpretation of natural and experimental systems pertinent to the Yucca Mountain. One specific objective is the interpretation of data generated in the experimentation task of the project. Theoretical interpretation permits extraction of meaningful and useful parameters from the experimental data, assists design of future experiments, and provides a method to evaluate aspects of the models including theory and codes.

Kinetic and thermodynamic interpretations of experimental data for analcime dissolution in experiments ADCTIA, ADCTIIA, and ACDTIIIA indicate that equilibrium is approached in the experiments permitting extraction of a provisional equilibrium constant of $10^{-16.24}$. Dissolution is apparently stoichiometric with respect to Si and Al release, and congruent with absence of secondary phase growth. Provisional specific rates of reaction for analcime dissolution under conditions far from equilibrium have been extracted from the data.

1.3 THERMOHYDROLOGY

Technical issues and uncertainties in the understanding of thermally influenced, unsaturated flow behavior at the proposed Yucca Mountain HLW repository site indicate a need for research on thermohydrological phenomena, i.e., phenomena associated with heat and fluid flow, to provide information relevant to performance assessment and design criteria. The class of thermohydrological phenomena examined in this project includes phenomena driven by heat emanating from HLW emplaced in a geologic repository. Information derived principally from research is used to establish a knowledge base of thermohydrologic phenomena, which will be utilized to assess models of processes used in performance assessments.

A revised Project Plan for the Thermohydrology Research Project has been submitted to NRC/RES. The plan was modified for the purpose of redefining the project tasks so that the objectives of the project could be pursued in a more direct fashion. These modifications were written to reflect in the Project Plan the greater understanding of thermohydrologic phenomena that has been achieved through the course of the research project. Accordingly, selected portions of the revised plan have received greater attention than they had originally. These include the investigation of matrix/fracture hydraulic properties; a higher involvement in numerical simulations of two-phase flow phenomena; and execution of highly instrumented, two-dimensional experiments.

Task 1 of the Project Plan was previously completed. Task 2, Design and Execution of Separate Effect Experiments, was completed during this past reporting period. Task 3, Design and Execution of Thermohydrological Experiments in Unsaturated Media, has been started with the initiation of Test 7.

Results from Test 6, the last of the separate-effects experiments, have been investigated in greater detail. Vector plots of suction pressures and total pressure were prepared from moisture saturation measurements collected on days 25, 75 and 113 of Test 6. Moisture content values were calculated using the gamma-ray densitometer measurements.

Experiment Test 7 is a continuation of the series of two-dimensional experiments that was conducted as part of the scoping portion of the research project and as part of Task 2, Design and Execution of Preliminary Separate Effects Experiments. The objective of the experiment is to investigate thermohydrological phenomena using experiments that (1) exhibit these phenomena and (2) provide a means to observe and quantify the processes of interest. Experiments conducted in the course of this research project have been designed to incorporate features expected in a geologic, HLW disposal environment (e.g., a fractured, porous medium) at partially saturated, nonisothermal conditions.

1.4 SEISMIC ROCK MECHANICS

A state-of-the-art literature review revealed that the seismic effects calculations performed to date on underground structures have not been subjected to an adequate level of experimental and field investigations. The experimental support for most of the programs has focused on soils rather than on structurally complex rock formations. Computer programs are currently available to model dynamic events of underground structures in rock formations. However, these programs have not been validated with well-planned and rigorous experimental and field protocols. This Seismic Rock Mechanics Research Project is aimed at developing a better understanding of the key parameters affecting the repository under seismic loadings and consequently validation of computer programs for use in seismic assessment of underground structures in tuff media.

Most of the research activities were on hold during this period due to budget constraint. The only activity that was carried out for the Seismic Rock Mechanics Project

during this reporting period was data collection for the instrumented field studies at the Lucky Friday Mine. The displacement data around underground openings indicate that the long-term displacements at the LFM95-C1 site are relatively smaller compared to those at the LFM95-C2 site. This is because that the LFM95-C2 site is about 150 feet closer than the LFM95-C1 site to the orebody currently being mining. Both sites are located at about 5,210 feet below surface. The LFM95-C1 site is also relatively insensitive to seismic events induced by mining activities compared to the responses of the opening at the LFM95-C2 site because the seismic-event sources events are relatively closer to the LFM95-C2 site. Pore-water pressure monitoring to date shows that seismic activities in the Lucky Friday Mine did not cause any noticeable hydrologic water-pressure change. However, mining activity is still quite distant from the hydrologic monitoring site.

1.5 INTEGRATED WASTE PACKAGE EXPERIMENTS

The NRC regulation 10 CFR 60.113 requires waste packages to provide substantially complete containment of radionuclides for a minimum period of 300 to 1000 years. The NRC, in its role of licensor, must understand the important parameters that affect long-term performance of waste package components and the applicability and limitations of the test techniques used to obtain these parameters. The goal of the Integrated Waste Package Experiments (IWPE) project is to assist NRC in the licensing process and to provide information for timely prelicensing guidance to DOE. Because the current waste package concept relies on a thin-walled container, most of the attention in the IWPE project is focused on evaluation of degradation processes that affect the candidate container materials. The project consists of both confirmatory and exploratory activities and is divided into six tasks: Task 1: Corrosion, Task 2: Stress Corrosion Cracking, Task 3: Materials Stability, Task 4: Microbiologically Influenced Corrosion, Task 5: Other Degradation Modes, and Task 6: General Reporting. The accomplishments in Tasks 1 are reported here.

Experimental investigation of the localized corrosion of alloy CDA-715 (Cu-30% Ni alloy), using a screening-type electrochemical test, was completed in this quarter. A two-level, full-factorial test matrix was used that examined bicarbonate, chloride, sulfate, and temperature as independent variables. Unlike the case of Fe-Ni-Cr-Mo alloys such as alloy 825 and type 316L stainless steel previously reported, the electrochemical response of the copper-based alloy to varying environmental compositions was determined to be more complex. In environments containing bicarbonate concentration comparable to the nominal concentrations found in the J-13 water (85 ppm), uniform corrosion was the predominant mode of corrosion. Hysteresis in the potentiodynamic polarization curves, which has been used for the Fe-Ni-Cr-Mo alloys as a partial indicator of localized corrosion, was not indicative of localized corrosion. No localized corrosion was observed even when significant hysteresis was exhibited by the electrochemical polarization curves. Presence of high concentrations of chloride and sulfate did not cause pitting, but exacerbated the uniform corrosion.

The full-factorial experiments indicated a four-factor interaction between the environmental factors studied. Pitting was observed only in environments containing high bicarbonate concentrations (8500 ppm) at low temperatures (30°C). This pitting was exacerbated by the presence of high concentrations (1000 ppm) of chloride or sulfate. In a solution containing 8500 ppm bicarbonate, 1000 ppm chloride, and 1000 ppm sulfate, pitting was observed up to a temperature of 80°C but not at 95°C. The pits were always capped by green corrosion products.

1.6 STOCHASTIC ANALYSIS OF FLOW AND TRANSPORT

Quantitative characterization of large-scale flow and radionuclide transport through the heterogeneous unsaturated fractured rock of Yucca Mountain will be necessary to evaluate compliance with the siting criteria and performance objectives associated with the proposed Yucca Mountain HLW repository (10 CFR 60.122 and 60.113). Realistic modeling of the complex, heterogeneous flow and transport processes at Yucca Mountain will require incorporating the effects of relatively small-scale as well as large-scale space-time variability in modeling unsaturated flow and radionuclide transport. To ensure the quality of the predictions obtained from these highly complex models of flow and transport, the development of methods for assessing their consistency and validity is required.

The specific objectives of the project are to: perform a review of the literature and assess available models and data relevant to the subject site, select a global approach to model large-scale flow and transport in unsaturated fractured rock, develop submodels for incorporation into the global model, perform large-scale simulations, and participate in the validation of flow/transport models for the Yucca Mountain repository.

Work accomplished during this quarter is described in Chapter 6. The main focus is on the development of methods for assessing model complexity, for measuring model consistency, and for testing model validity in the case of modeling the flow of water in unsaturated porous media. Several aspects of unsaturated-flow model testing are addressed including numerical formulation; tests for internal consistency; intercomparison of models; in-situ experiments; performance measures; and the underlying concepts of probabilistic induction, and parameter estimation, that may be employed to select appropriate experimental tests and to evaluate the degree to which the model is validated or refuted. The primary conclusion of this work is that universal validation of models is not possible; suitable measures and tests can be defined for validating models for specific purposes.

1.7 GEOCHEMICAL ANALOGS

The Geochemical Natural Analog Research Project is designed to provide knowledge of the state of the art in natural analog studies applied to contaminant transport, to conduct investigations of a specific site or sites, and to permit evaluation of the use of analog data to support modeling appropriate for performance assessment of a Yucca Mountain repository. Task 1 of the project, "Literature Review," was completed with the submission of the report

entitled "Geochemical Natural Analog Literature Review" (Pearcy and Murphy, 1991a). The first activity within Task 2, "Identification of Site and Development of Workplan," has been completed with the submission of a workplan report for the Peña Blanca natural analog. The remainder of Task 2 will consist of field evaluation of the Akrotiri natural analog; this work is planned for 1992,, when the Akrotiri site will next be available for direct observation.

Objectives of Task 2 included selection of a site at which to conduct analog research likely to yield information relevant to processes and events controlling contaminant transport in the proposed HLW repository at Yucca Mountain, Nevada, and development of a workplan to obtain that information. These objectives were met through literature review (Pearcy and Murphy, 1991a) and the conduct of field and laboratory research (Pearcy and Murphy, 1991c). The Nopal I deposit in the Peña Blanca, Mexico, uranium district was selected for research.

The primary objective of Task 3 is to develop methodologies for data acquisition and to implement those methodologies for the Peña Blanca natural analog. This is the main data acquisition activity for the natural analog study and as such encompasses a wide variety of techniques such as sampling of water, rock, and gas; mapping of lithology, structure, mineralogy, and alteration; petrographic analysis of rocks; chemical analysis of water, rock, gases, and minerals; and isotopic analysis of waters, rocks, gases, and minerals. These data will provide the basis for development of conceptual and numerical models within Task 4.

During this quarter (optical petrography, scanning electron microscopy, electron-microprobe energy-dispersive and wave-length-dispersive analyses, and x-ray diffractometry) were conducted on samples from the Peña Blanca analog site to characterize the ore and host-rock mineralogy, chemical composition, and phase relations. The primary ore mineral assemblage of the Nopal I deposit has been tentatively established as uraninite+ kaolinite+pyrite. This assemblage has undergone oxidative alteration producing a suite of secondary uranyl silicate and uranyl oxy-hydroxide minerals. Areas of the deposit in which the primary mineralization is preserved are strongly silicified, suggesting that the reduced permeability of these silicified zones contributed to the preservation of the uraninite.

The altering fluids appear to have been restricted to migration along pre-existing veinlets in some areas, whereas in other areas the altering fluids appear to have migrated through the matrix of the host tuffs. Primary uranium mobility during the formation of the Nopal I deposit appears to have been essentially restricted to the breccia pipe. No mineralogic nor radiometric indication of uranium precipitation laterally beyond the margins of the brecciated zone is evident. Similarly, lateral migration out of the orebody during secondary oxidative alteration is nowhere indicated. Oxidation of the original uraninite appears to have occurred with only minor redistribution of the uranium within the orebody.

The alteration proceeded by pervasive replacement of the fine grained uraninite as the altering fluids moved through the mineralized veinlets (rather than the matrix) forming diffuse, arcuate oxidative reaction fronts. Most commonly, the primary mineral assemblage

(uraninite + pyrite + kaolinite) is replaced by a secondary suite of uranyl silicates and uranyl oxy-hydroxides dominated by soddyite ($(UO_2)_2SiO_4 \bullet 2H_2O$) near the uraninite and dominated by uranophane ($Ca(UO_2)_2Si_2O_7 \bullet 6H_2O$) further from the uraninite. Other secondary ore minerals have relatively minor occurrence; the composition of these less abundant phases is likely a function of local elemental activities and is not indicative of the broader state of the system during oxidative replacement of the original assemblage.

1.8 PERFORMANCE ASSESSMENT RESEARCH

Evaluation of Performance Assessment (PA) technology developed by Sandia National Laboratory (SNL) for the NRC is the objective of Task 3 of the PA Research Projects. The test cases applied for evaluation of SNL's dual porosity flow model DCM3D are described in this chapter.

The DCM3D code transferred to the CNWRA in 1991 was developed by SNL for application to saturated-unsaturated flow in fractured porous media. It is based on the dual porosity formulation which conceptualizes the fractured media as two overlapping continua. A set of two equations coupled through a fluid interchange term are solved to obtain the pressure field in the dual continuum.

Four test cases for DCM3D are described. The test cases range from comparison of DCM3D to quasi-analytic results to comparison with other codes under complex geometric conditions. In general, DCM3D results compare well with the quasi-analytic results and those from other codes. The dual-continuum concept cannot be fully tested however, because the fluid interchange term that couples the flow equations for the rock matrix and fractures is generally not known. It is recommended that the fracture-matrix flow interaction be studied experimentally to evaluate various conceptualizations including that of dual porosity.

1.9 SORPTION MODELING FOR HIGH-LEVEL WASTE PERFORMANCE ASSESSMENT

An evaluation of the effectiveness of geologic systems as barriers to radionuclide migration requires an understanding of the chemical and physical processes by which aqueous species are sorbed on geologic materials. These processes, which may include adsorption, ion exchange, or precipitation, are commonly represented collectively by empirical parameters, such as sorption coefficient (K_d) or retardation factor (R_f), in transport calculations supporting performance assessments (PA) of geologic repositories. The usefulness, however, of these empirical parameters in quantitatively describing aqueous-solute/rock interactions for calculations of radionuclide transport often used in PA is actively debated. Transport models using these parameters, particularly those that assume constant K_d's or R_f's, do not explicitly account for many important geochemical phenomena occurring during transport in natural systems. These phenomena include aqueous complexation, precipitation/dissolution reactions, competitive sorption, changes in groundwater chemistry, and variability in substrate

composition, temperature and pressure. Therefore, questions have been raised regarding the adequacy of transport calculations using K_d or R_f in PA.

The general objectives of this project are to (1) to obtain a mechanistic understanding of the important radionuclide sorption processes and physical and chemical parameters that affect sorption behavior in the Yucca Mountain, Nevada, environment; (2) investigate the applicability of coupled-hydrogeochemical models which use simple representations of sorption phenomena to Yucca Mountain PA; and (3) develop practical but scientifically defensible approaches to modeling sorption at Yucca Mountain, and the requisite databases to support such models.

During this quarter, a major milestone report entitled *Sorption Modeling for HLW Performance Assessment: A Literature Review* by David R. Turner was completed and submitted to NRC for review. Based on the literature review, a workplan is being developed for Task 2 of this project. This workplan will be submitted to NRC during the early part of next quarter. Additional literature review was also conducted this quarter with an emphasis on specific sorption models and or techniques for estimating the parameters required by these models. Results of this activity are discussed in Section 9.3.

Under Task 3, scoping experiments were initiated studying the kinetics of uranium sorption on the zeolite mineral clinoptilolite. The kinetic experiments were conducted under conditions in equilibrium with atmospheric $CO_2(g)$, and at initial pH values of 3.0 and 9.0 where the predominant uranium aqueous species (>90% ΣU) are UO_2^{2+} and $UO_2(CO_3)_3^{4-}$, respectively, based on calculations using MINTEQA2. At pH conditions where UO_2^{2+} is the predominant species, ion exchange as a sorption mechanism was hypothesized. The hypothesis was based on literature data and from consideration of the comparative size of the UO_2^{2+} ion and the clinoptilolite intracrystalline channels.

Preliminary results for experiments with initial pH=3.0 indicate that no significant sorption reaction occurred between the zeolite and the uranium species in solution. The pH of the aqueous solutions did increase, however, suggesting that ion exchange occurred between H^+ initially in solution and Na^+ initially in the zeolite. Control experiments designed to evaluate potential ion exchange between these cations showed that the molal decrease in H^+ concentration corresponded stoichiometrically with the increase in Na^+ concentration. These results suggest that the presence of competing cations reduces the importance of ion exchange as a mechanism for uranium sorption on zeolite minerals. Under acidic conditions, hydronium (H_3O^+) species competes effectively with UO_2^{2+} species in ion exchange reactions with clinoptilolite, most likely due to its comparatively smaller ionic size.

2 UNSATURATED MASS TRANSPORT (GEOCHEMISTRY)

by Roberto T. Pabalan and William M. Murphy

Investigators: William M. Murphy (CNWRA), Roberto T. Pabalan (CNWRA), James D. Prikryl (CNWRA), and Ronald H. Martin (CNWRA)

2.1 EXPERIMENTAL STUDIES by Roberto T. Pabalan

2.1.1 Technical Objectives

A major geologic feature potentially affecting the suitability of Yucca Mountain, Nevada, as a repository site for HLW is the presence of thick, laterally extensive zones of zeolitic tuff. Because of their sorptive properties, zeolites could provide important geologic barriers to migration of radionuclides from the repository to the accessible environment. An evaluation of the relative importance of zeolites as retardation agents requires a knowledge of their thermodynamic stabilities and ion exchange properties under geochemical conditions relevant to the Yucca Mountain system. These properties may vary with groundwater chemistry, zeolite composition, and temperature. In addition, uncertainties exist in determining groundwater chemistries in the vadose zone at Yucca Mountain. It may be possible to reduce these uncertainties by investigating groundwater/zeolite equilibria through ion-exchange and phase-equilibrium experiments, coupled with thermodynamic modeling.

To support the NRC's HLW program, the CNWRA is conducting experimental studies on the thermodynamic and ion-exchange properties of zeolites under Task 3 of the Geochemistry Research Project. The following sections describe the experiments that have been conducted and the results that have been obtained from these studies during the third quarter of 1991.

2.1.2 Analcime Dissolution Experiments

Analcime dissolution experiments were initiated during the second quarter of 1991. The objectives, procedures, and initial results for these experiments were presented previously in the CNWRA report of research activities for that period (Pabalan, 1991a). Additional aqueous samples were taken during the third quarter of 1991, and were analyzed for pH and for concentrations of SiO_2, Al, and Na. For convenience, the experimental parameters for the analcime dissolution experiments are given in Table 2-1, and a complete set of data are given in Tables 2-2 to 2-5.

Sufficient information is now available on the dissolution rate of analcime under the experimental conditions used in these studies. Interpretation of the kinetics of analcime dissolution based on data given in Tables 2-2 and 2-4 are discussed in subsection 2.2. There is some ambiguity on whether the experimental systems have achieved equilibrium conditions. The most recent data on the mixture ACDTIIA (analcime-clinoptilolite dissolution test IIA) indicate that the measured solubilities have reached an asymptotic value, which may correspond

Table 2-1. EXPERIMENTAL MATRIX FOR ANALCIME DISSOLUTION EXPERIMENTS

Experimental Condition	ACDTIA & ACDTIB	ACDTIIA & ACDTIIB	ACDTIIIA & ACDTIIIB
Grain size based on nominal sieve opening	75-63 μm 200-230 mesh	63-45 μm 230-325 mesh	45-32 μm 325-450 mesh
Average grain length based on SEM photo	150 μm	100 μm	90 μm
Solution (Initial volume = 1000 ml)	0.10 M NaCl 0.010M $NaHCO_3$	0.10 M NaCl 0.010M $NaHCO_3$	0.10 M NaCl 0.010M $NaHCO_3$
Mass analcime	3.75 g	2.50 g	2.25 g
Temperature	25.0±0.1°C	25.0±0.1°C	25.0±0.1°C
Specific surface area	1200 cm^2g^{-1} calculated	1800 cm^2g^{-1} BET measured	2000 cm^2g^{-1} calculated
Initial pH	8.99±0.02	8.99±0.02	8.99±0.02
Initial SA/SV	4.5 cm^{-1}	4.5 cm^{-1}	4.5 cm^{-1}

to the equilibrium solubility of analcime. However, the data on the mixtures ACDTIA and ACDTIIIA indicate that the solubilities are still increasing, which suggests that equilibrium has not been achieved. The amounts of solution remaining in the mixtures ACDTIA, ACDTIIA, and ACDTIIIA are only enough for one additional set of samples. This will be taken in about four weeks to provide additional data on the dissolution rate of analcime.

In order to better constrain the equilibrium solubility of analcime, additional experiments are being initiated. These will be strictly solubility experiments which will involve taking aqueous samples for analysis after equilibrium has been achieved. The solid-mass/solution-volume ratio will be optimized to result in faster reaction rates, based on kinetic information derived from the previous experiments.

In addition, reverse kinetic experiments will be initiated by adding to the ACDTIA, ACDTIIA, and ACDTIIIA systems a new batch of aqueous solutions, which contain silica concentrations much higher than the equilibrium value. Ideally, analysis of aqueous solutions which are taken as a function of time will yield information on the rate of precipitation

Table 2-2a. MEASURED SILICA CONCENTRATIONS* FROM ANALCIME DISSOLUTION EXPERIMENTS ACDTIA, IIA, AND IIIA

Time (hours)	ACDT Sample IA 3.75g analcime (moles SiO_2/kg H_2O)	ACDT Sample IIA 2.50g analcime (moles SiO_2/kg H_2O)	ACDT Sample IIIA 2.25g analcime (moles SiO_2/kg H_2O)
0	0.00E+00	0.00E+00	0.00E+00
48	2.28E-06	1.71E-06	1.94E-06
95	4.46E-06	2.89E-06	2.66E-06
168	5.36E-06	4.70E-06	5.12E-06
261	6.83E-06	5.08E-06	5.93E-06
358	7.59E-06	6.12E-06	6.50E-06
497	9.49E-06	7.16E-06	7.78E-06
594	9.87E-06	7.83E-06	8.11E-06
713	12.6E-06	8.54E-06	9.01E-06
834	11.1E-06	8.35E-06	9.20E-06
934	11.6E-06	9.25E-06	9.82E-06
1074	12.2E-06	10.0E-06	10.7E-06
1193	12.7E-06	10.4E-06	11.0E-06
1505	15.1E-06	10.4E-06	11.8E-06
1915	18.1E-06	10.3E-06	10.8E-06
2369	15.3E-06	13.1E-06	14.4E-06
2849	17.7E-06	16.1E-06	17.3E-06
3209-a	20.0E-06	15.7E-06	19.0E-06
3209-b	19.2E-06	15.5E-06	19.3E-06

* - Corrected for background concentrations

Table 2-2b. MEASURED ALUMINUM CONCENTRATIONS* FROM ANALCIME DISSOLUTION EXPERIMENTS ACDTIA, IIA, AND IIIA

Time (hours)	ACDT Sample IA 3.75g analcime (moles Al/kg H_2O)	ACDT Sample IIA 2.50g analcime (moles Al/kg H_2O)	ACDT Sample IIIA 2.25g analcime (moles Al/kg H_2O)
0	0.00E+00	0.00E+00	0.00E+00
48	1.71E-06	1.55E-06	1.34E-06
95	2.51E-06	1.83E-06	2.23E-06
168	3.85E-06	2.96E-06	3.07E-06
261	5.12E-06	3.74E-06	4.10E-06
358	5.14E-06	3.53E-06	4.17E-06
497	6.54E-06	5.65E-06	5.30E-06
594	6.85E-06	5.29E-06	5.77E-06
713	7.63E-06	5.83E-06	6.35E-06
834	6.35E-06	5.03E-06	5.48E-06
934	7.73E-06	6.18E-06	6.51E-06
1074	7.01E-06	3.69E-06	5.98E-06
1193	6.90E-06	6.12E-06	6.62E-06
1505	7.22E-06	4.60E-06	5.48E-06
1915	9.27E-06	7.51E-06	8.37E-06
2369	8.32E-06	7.16E-06	7.61E-06
2849	8.12E-06	8.54E-06	8.39E-06
3209-a	9.23E-06	8.49E-06	9.15E-06
3209-b	8.31E-06	8.53E-06	9.06E-06

* - Corrected for background concentrations

Table 2-3a. MEASURED SiO_2 CONCENTRATIONS* FROM ANALCIME DISSOLUTION EXPERIMENTS ACDTIB, IIB, AND IIIB

Time (hours)	ACDT Sample IB 3.75g analcime (moles SiO_2/kg H_2O)	ACDT Sample IIB 2.50g analcime (moles SiO_2/kg H_2O)	ACDT Sample IIIB 2.25g analcime (moles SiO_2/kg H_2O)
0	0.00E+00	0.00E+00	0.00E+00
168	4.41E-06	3.18E-06	4.32E-06
358	7.68E-06	5.60E-06	6.45E-06
664	9.06E-06	6.93E-06	7.59E-06
1001	10.4E-06	7.92E-06	8.82E-06
1505	11.2E-06	8.63E-06	10.7E-06

Table 2-3b. MEASURED Al CONCENTRATIONS* FROM ANALCIME DISSOLUTION EXPERIMENTS ACDTIB, IIB, AND IIIB

Time (hours)	ACDT Sample IB 3.75g analcime (moles Al/kg H_2O)	ACDT Sample IIB 2.50g analcime (moles Al/kg H_2O)	ACDT Sample IIIB 2.25g analcime (moles Al/kg H_2O)
0	0.00E+00	0.00E+00	0.00E+00
168	3.86E-06	2.49E-06	2.94E-06
358	4.86E-06	3.59E-06	4.03E-06
664	6.35E-06	4.85E-06	5.37E-06
1001	7.07E-06	5.29E-06	5.97E-06
1505	5.94E-06	4.65E-06	5.22E-06

* - Corrected for background concentrations

Table 2-4. pH, SODIUM CONCENTRATION, AND TOTAL WEIGHT OF SOLUTIONS FROM ANALCIME DISSOLUTION EXPERIMENTS ACDTIA, IIA, AND IIIA AS A FUNCTION OF TIME

Time (hours)	ACDT Sample IA 3.75g analcime			ACDT Sample IIA 2.50g analcime			ACDT Sample IIIA 2.25g analcime		
	Total soln weight (g)	Na^+ (ppm)	Soln pH	Total soln weight (g)	Na^+ (ppm)	Soln pH	Total soln weight (g)	Na^+ (ppm)	Soln pH
0	1094.4	2420	8.99	1094.5	2470	8.99	1092.8	2460	8.99
48	1043.4	2550	8.98	1043.7	2540	8.99	1039.5	2540	8.98
95	992.7	2620	9.00	992.9	2580	9.00	988.7	2530	8.99
168	941.8	2550	8.99	941.9	2560	8.95	937.9	2500	8.97
261	890.9	2520	8.99	890.9	2520	8.99	886.9	2500	8.97
358	839.8	2480	8.97	840.0	2490	8.99	835.9	2480	9.01
497	788.6	2570	8.98	788.9	2520	8.97	784.8	2500	8.98
594	737.7	2500	8.99	737.9	2510	8.99	733.7	2500	8.98
713	686.7	2490	9.00	686.5	2510	9.00	682.5	2510	8.99
834	635.3	2500	8.98	635.5	2490	8.97	631.3	2500	8.97
934	584.1	2620	8.98	584.3	2590	8.98	579.9	2540	8.98
1074	533.0	2560	9.00	532.7	2520	9.00	528.7	2530	9.00
1193	481.9	2550	9.00	481.4	2540	9.00	476.9	2530	9.00
1505	429.7	2520	9.01	429.0	2670	9.02	424.2	2600	9.01
1915	377.3	2540	9.00	376.4	2530	9.01	372.1	2570	9.01
2369	324.6	2590	9.00	323.2	2600	9.00	319.1	2590	9.00
2849	272.2	2530	9.02	269.5	2500	9.02	266.1	2500	9.02
3209-a	170.0	2620	8.99	166.6	2650	9.00	163.4	2600	9.00
3209-b	170.0	2590	9.00	166.6	2630	9.01	163.4	2650	9.00

Table 2-5. pH, SODIUM CONCENTRATION, AND TOTAL WEIGHT OF SOLUTIONS FROM ANALCIME DISSOLUTION EXPERIMENTS ACDTIB, IIB, AND IIIB AS A FUNCTION OF TIME

Time (hours)	ACDT Sample IB 3.75g analcime			ACDT Sample IIB 2.50g analcime			ACDT Sample IIIB 2.25g analcime		
	Total soln weight (g)	Na^+ (ppm)	Soln pH	Total soln weight (g)	Na^+ (ppm)	Soln pH	Total soln weight (g)	Na^+ (ppm)	Soln pH
0	1094.8	2470	8.98	1094.3	2470	8.98	1093.2	2480	8.99
168	1043.0	2540	8.96	1042.9	2540	8.96	1041.9	2510	8.95
358	991.4	2490	8.98	991.6	2460	8.97	990.4	2500	9.00
664	939.0	2520	9.01	940.0	2510	8.99	938.7	2510	8.99
1001	886.3	2560	9.00	887.9	2580	9.00	886.0	2600	9.00
1505	832.5	2550	9.01	835.1	2630	9.00	832.2	2600	9.01

of analcime and the rate of approach to equilibrium from a supersaturated condition. Also, experiments studying clinoptilolite dissolution and phase equilibrium between analcime+clinoptilolite+aqueous-solution will be started by adding clinoptilolite grains to the mixtures ACDTIB, ACDTIIB, and ACDTIIIB. Results of the new experiments will be reported in the next quarterly research report.

2.1.3 Ion-Exchange Isotherm Experiments

Ion-exchange behavior of zeolites depends on several factors, including solid and aqueous phase compositions as well as aqueous solution concentrations (Barrer, 1978). Under Task 3 of this research project, ion-exchange isotherm experiments were previously conducted between well-characterized specimens of clinoptilolite and aqueous solutions of Na^+, K^+, and Ca^{2+} (Pabalan, 1991b, 1991b). These experiments were designed to investigate the effects on the exchange equilibrium of changes in total aqueous solution concentration and the relative concentration of the different exchangeable ions initially found in solution. The experimental data were interpreted using excess Gibbs energy models for the aqueous and zeolite phases to account for nonideality in the system. The data were also used to test model predictions of isotherm shapes and selectivities at some value of total solution concentration based on a single isotherm measured at another solution concentration. The results of the modeling efforts indicated that thermodynamic methods that account for nonideal behavior in aqueous solutions and zeolite phases are useful in describing and predicting the solid solution and ion exchange properties of the zeolite mineral clinoptilolite. These models provide a foundation for understanding ion exchange equilibria in multicomponent geochemical systems such as that expected at Yucca Mountain, Nevada (Pabalan, 1991b, 1991c).

Based on the results of the experimental and modeling work, a more extensive set of ion exchange experiments was planned and initiated. These experiments were designed to use a wider range of total solution concentrations and to evaluate the effects of temperature and anionic composition. Because the amount of Na-clinoptilolite prepared previously (Pabalan, 1991b, 1991c) is insufficient for this more extensive set of experiments, a new batch of Na-clinoptilolite was prepared from the specimens of clinoptilolite-rich zeolitized tuff which came from Death Valley, California. The preparation of the Na-clinoptilolite was reported previously (Pabalan and Turner, 1991). The same material is being used to study the sorption of uranium on zeolites (see Chapter 9 of this report).

This section reports the results of the studies performed during the third quarter of 1991. Ion-exchange experiments were conducted between clinoptilolite and aqueous mixtures of NaCl/KCl and $NaCl/CaCl_2$. Experiments previously reported (Pabalan, 1991b, 1991c) were conducted at total solution concentrations of 0.05 and 0.5 N. Some studies suggested that results of ion-exchange experiments are affected by the method used in preparing the zeolite material (e.g., Semmens and Seyfarth, 1978). Therefore, the current experiments also used solution concentrations of 0.05 and 0.50 N in order to check the reproducibility of the previous isotherms which were derived using differently prepared Na-clinoptilolite. In addition, experiments at

0.005 total normality were conducted to provide data for testing the predictive ability of thermodynamic models at ionic strengths closer to those of Yucca Mountain groundwaters.

The procedures used in the current set of experiments are similar to those described before (Pabalan, 1991b, 1991c). The points on the isotherm were obtained by equilibrating accurately weighed amounts of the near homoionic Na-clinoptilolite with a series of solutions of known volumes containing the two competing cations in different concentration ratios, but at constant total normality of 0.005, 0.05, or 0.50 N. The 0.50 N aqueous mixtures were prepared by weight from reagent grade chloride salts of the respective cations. The 0.005 and 0.05 N solutions were prepared by ten factor dilutions of the 0.05 and 0.50 N mixtures, respectively. The weights of the clinoptilolite powder and the volumes and initial compositions of the solutions used in the experiments are given in Tables 2-6 to 2-11. These values were somewhat optimized based on previously derived isotherm data in order to yield significant differences in the initial and final solution concentrations and to yield a relatively complete range of isotherm compositions. The clinoptilolite+solution mixtures were contained in 5 to 250 ml screw-cap polypropylene bottles, which were kept agitated and thermostatted at 25°C in a shaker water bath for at least one week.

After equilibrium was established, aliquots of the reference and experimental solutions were taken. In contrast to previous experiments in which concentrations of only one cation were analyzed, the procedures used in the current studies analyzed both cations participating in the exchange reaction. By charge balance calculations, this method could demonstrate that the exchange reaction is binary in nature, and that the participation of H^+ or of cations initially present with Na^+ in the zeolite are negligible. The aqueous samples were analyzed for Na^+, K^+, and Ca^{2+} concentrations using Orion ion selective electrodes and an Orion 920A pH/mV/ISE/°C meter. Calibration was done using five standard solutions of the cation of interest. The results of the chemical analysis are given in columns 4 to 7 of Tables 2-6 to 2-11.

The equivalent mole fractions of K^+ and Ca^{2+} in the solid and aqueous phases were calculated from the initial and final aqueous concentrations of the cation of interest, and from the weight of clinoptilolite powder and the volume of solution used in the exchange experiments. The equivalent mole fraction of K^+ and Ca^{2+} *in the zeolite* are defined, respectively, as follows:

$$E_{KZ} = \frac{(\text{equivs. } K_{zeol})}{(\text{equivs. } K_{zeol} + \text{equivs. } Na_{zeol})} = \frac{(\text{moles } K_{zeol})}{(\text{moles } K_{zeol} + \text{moles } Na_{zeol})} \quad (2\text{-}1)$$

Table 2-6. EXPERIMENTAL DATA AND CALCULATED EQUIVALENT FRACTIONS OF POTASSIUM IN THE SOLID (E_{KZ}) AND IN THE AQUEOUS PHASE (E_{KS}) FOR ION EXCHANGE BETWEEN CLINOPTILOLITE AND AN NACL/KCL SOLUTION WITH A TOTAL NORMALITY OF 0.50N

Soln. #	Wt. zeol. (gm)	Vol. Soln. (ml)	Initial Concentration (ppm)		Final Concentration (ppm)		Based on K^+ data		Based on Na^+ data	
			Na^+	K^+	Na^+	K^+	E_{KZ}	E_{KS}	E_{KZ}	E_{KS}
1	1.0371	10	10360	1900	11480	116.5	0.203	0.0060	0.216	0.0013
2	0.6143	10	10360	1900	11380	240.5	0.318	0.0123	0.333	0.0100
3	0.4031	10	10360	1900	11260	504.5	0.408	0.0258	0.447	0.0204
4	0.2259	10	10360	1900	11080	955	0.493	0.0489	0.639	0.0361
5	0.4801	10	9220	3805	10640	1485	0.570	0.0760	0.593	0.0744
6	0.3960	10	9220	3805	10560	1695	0.628	0.0867	0.678	0.0813
7	0.3518	10	9220	3805	10440	1915	0.633	0.0980	0.695	0.0918
8	0.2306	10	9220	3805	10020	2515	0.659	0.129	0.696	0.128
9	0.4737	10	7920	5790	9760	3010	0.692	0.154	0.779	0.151
10	0.3686	10	7920	5790	9240	3635	0.689	0.186	0.718	0.196
11	0.2991	10	7920	5790	9160	3885	0.751	0.199	0.831	0.203
12	0.4606	10	6860	7695	8760	4805	0.740	0.246	0.827	0.238
13	0.2794	10	6860	7695	8040	5825	0.789	0.298	0.847	0.301
14	0.4067	10	5710	9450	7410	6845	0.755	0.350	0.838	0.355
15	0.5295	10	4580	11450	6880	7650	0.846	0.391	0.874	0.401
16	0.5150	10	3440	13120	5670	9410	0.849	0.481	0.868	0.507
17	0.7517	10	1170	17530	4610	11740	0.908	0.601	0.918	0.599
18	0.7354	10	0	19310	3300	13530	0.926	0.692	0.899	0.713
19	0.6064	10	0	19310	2760	14470	0.941	0.740	0.912	0.760
20	0.4800	10	0	19310	2190	15560	0.921	0.796	0.915	0.809
21	0.2353	10	0	19310	1060	17850	0.731	0.913	0.904	0.908

Table 2-7. EXPERIMENTAL DATA AND CALCULATED EQUIVALENT FRACTIONS OF POTASSIUM IN THE SOLID (E_{KZ}) AND IN THE AQUEOUS PHASE (E_{KS}) FOR ION EXCHANGE BETWEEN CLINOPTILOLITE AND AN NACL/KCL SOLUTION WITH A TOTAL NORMALITY OF 0.05N

Soln.#	Wt. zeol.(gm)	Vol. Soln. (ml)	Initial Concentration (ppm)		Final Concentration (ppm)		Based on K^+ data		Based on Na^+ data	
			Na^+	K^+	Na^+	K^+	E_{KZ}	E_{KS}	E_{KZ}	E_{KS}
1	0.2592	25	1060	199	1110	9.69	0.215	0.0050	0.0967	0.0344
2	0.1535	25	1060	199	1140	24.15	0.337	0.0124	0.261	0.0083
3	0.1007	25	1060	199	1120	44.95	0.451	0.0230	0.299	0.0257
4	0.1695	25	922	390	1100	86.4	0.528	0.0442	0.526	0.0431
5	0.2160	25	802	581.5	1060	142.5	0.599	0.0729	0.599	0.0779
6	0.1891	25	802	581.5	1060	183	0.621	0.0936	0.684	0.0779
7	0.1760	25	802	581.5	1040	196	0.645	0.100	0.678	0.0953
8	0.1398	25	802	581.5	1000	254	0.690	0.130	0.710	0.130
9	0.1972	25	692	773	980	303	0.702	0.155	0.732	0.147
10	0.1691	25	692	773	945	359.5	0.721	0.184	0.750	0.178
11	0.1495	25	692	773	920	388.5	0.758	0.199	0.764	0.200
12	0.1151	25	692	773	874	480.5	0.749	0.246	0.792	0.240
13	0.1396	25	573	986.5	788	588.5	0.840	0.301	0.772	0.314
14	0.1693	25	459	1150	751	713	0.761	0.365	0.864	0.347
15	0.1897	25	349	1330	672	815.5	0.799	0.417	0.853	0.415
16	0.1932	25	-	1525	570	932.5	0.904	0.477	-	0.504
17	0.1880	25	116	1720	447	1135	0.917	0.581	0.882	0.611
18	0.1837	25	0	1945	333	1375	0.914	0.703	0.908	0.710
19	0.1518	25	0	1945	271	1460	0.941	0.747	0.895	0.764
20	0.1199	25	0	1945	221	1555	0.958	0.795	0.924	0.808
21	0.0587	25	0	1945	112	1650	1.481	0.844	0.956	0.903

Table 2-8. EXPERIMENTAL DATA AND CALCULATED EQUIVALENT FRACTIONS OF POTASSIUM IN THE SOLID (E_{KZ}) AND IN THE AQUEOUS PHASE (E_{KS}) FOR ION EXCHANGE BETWEEN CLINOPTILOLITE AND AN NACL/KCL SOLUTION WITH A TOTAL NORMALITY OF 0.005N

Soln. #	Wt. zeol. (gm)	Vol. Soln. (ml)	Initial Concentration (ppm)		Final Concentration (ppm)		Based on K^+ data		Based on Na^+ data	
			Na^+	K^+	Na^+	K^+	E_{KZ}	E_{KS}	E_{KZ}	E_{KS}
1	0.1093	50	92.3	36.8	114	1.03	0.193	0.0053	0.199	0.0083
2	0.1077	50	81.5	55.1	114	2.39	0.288	0.0122	0.302	0.0083
3	0.0777	50	81.5	55.1	113	4.46	0.384	0.0228	0.406	0.0170
4	0.0790	50	68.8	73.7	110	8.35	0.488	0.0427	0.523	0.0431
5	0.0817	50	57.4	93.6	107	14.6	0.570	0.0744	0.608	0.0692
6	0.0738	50	57.4	93.6	103	18.1	0.603	0.0923	0.619	0.104
7	0.0880	50	45.7	112	103	20.8	0.608	0.106	0.653	0.104
8	0.0774	50	45.7	112	99.2	28.1	0.635	0.144	0.693	0.137
9	0.0867	50	34	132	95.7	32.3	0.678	0.165	0.713	0.167
10	0.0799	50	34	132	92.7	37.1	0.700	0.190	0.736	0.194
11	0.0899	50	22.5	152	90.5	41.4	0.725	0.212	0.758	0.213
12	0.0806	50	22.5	152	83.9	50.6	0.741	0.259	0.763	0.270
13	0.0838	50	11	170	78.1	61.6	0.759	0.315	0.803	0.321
14	0.0745	50	11	170	71.6	72.2	0.770	0.369	0.815	0.377
15	0.0795	50	0	188	65.3	78.4	0.809	0.401	0.823	0.432
16	0.0645	50	0	188	54.8	96.7	0.831	0.494	0.852	0.523
17	0.1002	100	0	188	44.2	116	0.847	0.591	0.884	0.615
18	0.0736	100	0	188	32.9	136	0.833	0.693	0.896	0.714
19	0.1202	250	0	188	22.0	156	0.772	0.798	0.917	0.809
20	0.0589	250	0	188	11.0	169	0.926	0.864	0.936	0.904

Table 2-9. EXPERIMENTAL DATA AND CALCULATED EQUIVALENT FRACTIONS OF CALCIUM IN THE SOLID (E_{CaZ}) AND IN THE AQUEOUS PHASE (E_{CaS}) FOR ION EXCHANGE BETWEEN CLINOPTILOLITE AND AN $NaCl/CaCl_2$ SOLUTION WITH A TOTAL NORMALITY OF 0.50N

Soln. #	Wt. zeol. (gm)	Vol. Soln. (ml)	Initial Concentration (ppm)		Final Concentration (ppm)		Based on Ca^{2+} data		Based on Na^+ data	
			Na^+	Ca^{2+}	Na^+	Ca^{2+}	$E_{Ca,Z}$	$E_{Ca,S}$	$E_{Ca,Z}$	$E_{Ca,S}$
1	1.5359	5	10400	953	11400	237	0.0536	0.0237	0.0653	0.0083
2	1.843	5	9110	1920	11040	492	0.0891	0.0491	0.105	0.0396
3	1.3441	5	9110	1920	10700	667	0.107	0.0666	0.119	0.0692
4	0.8639	5	9110	1920	10520	951	0.129	0.0949	0.164	0.0848
5	1.2801	5	8230	2890	10280	1210	0.151	0.121	0.161	0.106
6	1.3072	5	8230	2890	9840	1400	0.131	0.140	0.123	0.144
7	0.7680	5	8230	2890	9700	1610	0.192	0.161	0.192	0.156
8	0.9599	5	7030	3860	8920	2090	0.212	0.209	0.197	0.224
9	0.6399	5	7030	3860	8560	2430	0.257	0.243	0.240	0.255
10	0.7946	5	5770	4890	7960	3050	0.266	0.304	0.276	0.307
11	0.6876	5	4670	5850	6820	3890	0.328	0.388	0.313	0.407
12	0.5984	5	3510	6960	5680	4970	0.382	0.496	0.363	0.506
13	0.5240	5	2350	7870	4520	5900	0.432	0.589	0.415	0.607
14	0.3677	5	2350	7870	3840	6460	0.441	0.645	0.406	0.666
15	0.4653	5	1180	8980	3480	6980	0.494	0.697	0.495	0.697
16	0.3292	5	1180	8980	2840	7470	0.527	0.746	0.505	0.753
17	0.4191	5	0	10100	2320	8140	0.538	0.812	0.555	0.798
18	0.3377	5	0	10100	1968	8340	0.599	0.832	0.584	0.829
19	0.4911	10	0	10100	1500	8460	0.768	0.844	0.612	0.870
20	0.3439	10	0	10100	1120	8940	0.776	0.892	0.653	0.903
21	0.2209	10	0	10100	785	9340	0.791	0.932	0.712	0.932
22	0.1459	10	0	10100	547	9540	0.883	0.952	0.752	0.952

Table 2-10. EXPERIMENTAL DATA AND CALCULATED EQUIVALENT FRACTIONS OF CALCIUM IN THE SOLID (E_{CaZ}) AND IN THE AQUEOUS PHASE (E_{CaS}) FOR ION EXCHANGE BETWEEN CLINOPTILOLITE AND AN NaCl/$CaCl_2$ SOLUTION WITH A TOTAL NORMALITY OF 0.05N

Soln. #	Wt. zeol. (gm)	Vol. Soln. (ml)	Initial Concentration (ppm)		Final Concentration (ppm)		Based on Ca^{2+} data		Based on Na^+ data	
			Na^+	Ca^{2+}	Na^+	Ca^{2+}	$E_{Ca,Z}$	$E_{Ca,S}$	$E_{Ca,Z}$	$E_{Ca,S}$
1	0.2446	25	1030	94.4	1130	19.4	0.176	0.0194	0.205	0.0170
2	0.1492	25	1030	94.4	1120	36	0.225	0.0359	0.302	0.0257
3	0.2879	25	919	195	1090	56.1	0.277	0.0560	0.298	0.0518
4	0.2034	25	919	195	1060	81.7	0.320	0.0815	0.347	0.0779
5	0.1555	25	919	195	1040	102	0.344	0.102	0.390	0.0953
6	0.2057	25	810	296	950	154	0.397	0.154	0.341	0.174
7	0.2559	25	696	391	920	203	0.422	0.203	0.439	0.200
8	0.1800	25	696	391	860	249	0.454	0.249	0.457	0.252
9	0.2304	25	584	481	810	295	0.464	0.294	0.492	0.295
10	0.2174	25	466	585	690	386	0.526	0.385	0.516	0.400
11	0.2022	25	349	693	580	488	0.583	0.487	0.573	0.495
12	0.1465	25	349	693	520	542	0.593	0.541	0.585	0.548
13	0.1858	25	234	813	460	587	0.699	0.586	0.610	0.600
14	0.2321	25	117	905	400	642	0.651	0.641	0.611	0.652
15	0.2541	25	0	1020	350	694	0.738	0.693	0.690	0.696
16	0.1999	25	0	1020	290	744	0.794	0.743	0.727	0.748
17	0.1516	25	0	1020	230	804	0.819	0.802	0.760	0.800
18	0.2136	50	0	1020	170	862	0.850	0.860	0.798	0.852
19	0.1356	50	0	1020	120	917	0.873	0.915	0.887	0.896
20	0.0640	50	0	1020	60	953	1.204	0.951	0.940	0.948

Table 2-11. EXPERIMENTAL DATA AND CALCULATED EQUIVALENT FRACTIONS OF CALCIUM IN THE SOLID (E_{CaZ}) AND IN THE AQUEOUS PHASE (E_{CaS}) FOR ION EXCHANGE BETWEEN CLINOPTILOLITE AND AN NaCl/$CaCl_2$ SOLUTION WITH A TOTAL NORMALITY OF 0.005N

Soln. #	Wt. zeol. (gm)	Vol. Soln. (ml)	Initial Concentration (ppm)		Final Concentraton (ppm)		Based on Ca^{2+} data		Based on Na^{+} data	
			Na^{+}	Ca^{2+}	Na^{+}	Ca^{2+}	ECaZ	ECaS	ECaZ	ECaS
1	0.1453	50	80.45	30.45	113.5	1.935	0.226	0.0193	0.228	0.0126
2	0.0916	50	80.45	30.45	112.5	3.065	0.344	0.0306	0.351	0.0213
3	0.1008	50	69	40.4	107	5.815	0.394	0.0580	0.378	0.0692
4	0.0802	50	69	40.4	108	7.2	0.476	0.0719	0.487	0.0605
5	0.0940	50	57.6	50.4	104.5	9.835	0.496	0.0981	0.500	0.0909
6	0.0806	50	57.6	50.4	99.95	13.15	0.531	0.131	0.527	0.130
7	0.0803	50	45.9	61.4	94.95	17.9	0.623	0.179	0.612	0.174
8	0.0711	50	45.9	61.4	91.25	21.1	0.652	0.211	0.639	0.206
9	0.0902	50	34.25	70.95	90.3	21.5	0.630	0.215	0.623	0.214
10	0.0800	50	34.25	70.95	85.35	24.9	0.662	0.249	0.640	0.258
11	0.0914	50	22.6	81.15	82.8	27.85	0.670	0.278	0.660	0.280
12	0.0798	50	22.6	81.15	76.7	32.15	0.706	0.321	0.679	0.333
13	0.0862	50	11.15	91.1	70.35	31.95	0.789	0.319	0.688	0.388
14	0.0759	50	11.15	91.1	64.8	42.7	0.733	0.426	0.708	0.436
15	0.0822	50	0	99.2	57.8	48.5	0.709	0.484	0.705	0.497
16	0.0624	50	0	99.2	46.6	58.5	0.750	0.584	0.748	0.595
17	0.1055	100	0	99.2	40.15	63.8	0.772	0.637	0.763	0.651
18	0.0888	100	0	99.2	34.5	67.95	0.809	0.678	0.779	0.700
19	0.0712	100	0	99.2	28.6	72.6	0.859	0.725	0.805	0.751
20	0.0555	100	0	99.2	22.15	79.6	0.812	0.794	0.800	0.807
21	0.0992	250	0	99.2	16.45	84.15	0.872	0.840	0.831	0.857
22	0.0640	250	0	99.2	10.85	90.05	0.822	0.899	0.850	0.906
23	0.0308	250	0	99.2	5.46	93.55	1.055	0.934	0.888	0.953

$$E_{CaZ} = \frac{(\text{equivs.Ca}_{zeol})}{(\text{equivs.Ca}_{zeol} + \text{equivs.Na}_{zeol})} = \frac{(2 * \text{moles Ca}_{zeol})}{(2 * \text{moles Ca}_{zeol} + \text{moles Na}_{zeol})} \quad . \quad (2\text{-}2)$$

The equivalent mole fraction of K^+ and Ca^{2+} *in the solution* phase are defined, respectively, as

$$E_{KS} = \frac{(\text{equivs.K}_{soln.})}{(\text{equivs.K}_{soln.} + \text{equivs.Na}_{soln.})} = \frac{(\text{moles K}_{soln.})}{(\text{moles K}_{soln.} + \text{moles Na}_{soln.})} \quad (2\text{-}3)$$

$$E_{CaS} = \frac{(\text{equivs.Ca}_{soln.})}{(\text{equivs.Ca}_{soln.} + \text{equivs.Na}_{soln.})} = \frac{(2 * \text{moles Ca}_{soln.})}{(2 * \text{moles Ca}_{soln.} + \text{moles Na}_{soln.})} \quad . \quad (2\text{-}4)$$

E_{KZ}, E_{KS}, E_{CaZ} and E_{CaS} were calculated from the zeolite weight, the solution volume, and the analytical concentrations of K^+ or Ca^{2+} using the following equations:

$$E_{KZ} = \frac{(K_i - K_f) \cdot (\text{vol. soln.})}{(AW_K) \cdot (10^6) \cdot (\text{CEC}) \cdot (\text{wt. zeol.})} \quad (2\text{-}5)$$

$$E_{KS} = \frac{K_f}{(AW_K) \cdot (10^3) \cdot (\text{TN})} \quad (2\text{-}6)$$

$$X_{CaZ} = \frac{2 \cdot (Ca_i - Ca_f) \cdot (\text{vol. soln.})}{(AW_{Ca}) \cdot (10^6) \cdot (\text{CEC}) \cdot (\text{wt. zeol.})} \quad (2\text{-}7)$$

$$E_{CaS} = \frac{2 \cdot (Ca_f)}{(AW_{Ca}) \cdot (10^3) \cdot (\text{TN})} \quad (2\text{-}8)$$

where K_i and Ca_i are the initial concentrations (in ppm) of K^+ and Ca^{2+} in the aqueous phase, respectively, and K_f and Ca_f are their final concentrations in solution. AW_K and AW_{Ca} are the atomic weights of potassium and calcium, respectively; CEC is the cation exchange capacity (in equivs./gm. of zeolite) of the Na-clinoptilolite; and TN is the total normality (equivs./liter of

solution) of the aqueous phase. The volume of solution and the weight of zeolite have units of milliliters and grams, respectively. The values of E_{KZ} and E_{KS} are given in columns 8 and 9, respectively, of Tables 2-6 to 2-8; and those of E_{CaZ}, and E_{CaS} are listed in columns 8 and 9, respectively, of Tables 2-9 to 2-11. Those values were calculated *assuming* that CEC is the same as that of the Na-clinoptilolite used in the previous experiments (Pabalan, 1991b,1991c) and is equal to 0.00217 equivs./gm. of zeolite.

E_{KZ}, E_{KS}, E_{CaZ} and E_{CaS} were *independently* calculated from the analytical concentrations of Na^+, using the following equations:

$$E_{KZ} = \frac{(Na_f - Na_f) \cdot (\text{vol. soln.})}{(AW_{Na}) \cdot (10^6) \cdot (CEC) \cdot (\text{wt. zeol.})} \qquad (2\text{-}9)$$

$$E_{KS} = 1 - \frac{Na_f}{(AW_{Na}) \cdot (10^3) \cdot (TN)} \qquad (2\text{-}10)$$

$$E_{CaZ} = \frac{(Na_f - Na_i) \cdot (\text{vol. soln.})}{(AW_{Na}) \cdot (10^6) \cdot (CEC) \cdot (\text{wt. zeol.})} \qquad (2\text{-}11)$$

$$E_{CaS} = 1 - \frac{Na_f}{(AW_{Na}) \cdot (10^3) \cdot (TN)} \qquad (2\text{-}12)$$

where Na_i and Na_f are the initial and final concentrations (in ppm), respectively, of Na^+ in the solution and AW_{Na} is the atomic weight of sodium. The values of E_{KZ} and E_{KS} calculated from the Na^+ data are given in columns 10 and 11, respectively, of Tables 2-6 to 2-8; and those of E_{CaZ} and E_{CaS} are listed in columns 10 and 11, respectively, of Tables 2-9 to 2-11.

The isotherm data for the NaCl/KCl mixtures at various total solution normalities are plotted in Figures 2-1 to 2-3, whereas the isotherm data for the NaCl/$CaCl_2$ mixtures are plotted in Figures 2-4 to 2-6. In these figures, the solid circles are equivalent mole fractions calculated from either the K^+ or Ca^{2+} analytical data, whereas the solid squares are equivalent mole fractions calculated from the Na^+ analytical results. The isotherm data given in Tables 2-6 to 2-11 and illustrated in Figures 2-1 to 2-6 indicate that equivalent mole fractions calculated from solution concentrations of either cation participating in the exchange reaction agree within analytical uncertainty. This demonstrates that the exchange reaction is essentially binary in nature, and that participation of H^+ or other cations initially present with Na^+ in the Na-

clinoptilolite is negligible. In addition, the concentration-valency effect which was demonstrated previously in experiments involving solution normalities of 0.5 and 0.05 N is verified by additional experiments at 0.005 N. Thus, for ion exchange reactions involving cations of the same ionic charge, the dependence of the isotherm on changes in total solution normality (e.g., Na^+/K^+ in Figures 2-6 to 2-8) is small. On the other hand, isotherms of ion exchanges involving cations of different valences show a strong dependence on the total solution normality (e.g., Na^+/Ca^{2+} in Figures 2-9 to 2-11).

An evaluation of thermodynamic models using the experimental data presented here will be conducted in the succeeding quarter, and results of modeling efforts will be reported in the next quarterly research report. In addition, experiments at 80°C are being conducted to determine the effect of temperature on the ion exchange equilibria. Results of these experiments will also be reported next quarter.

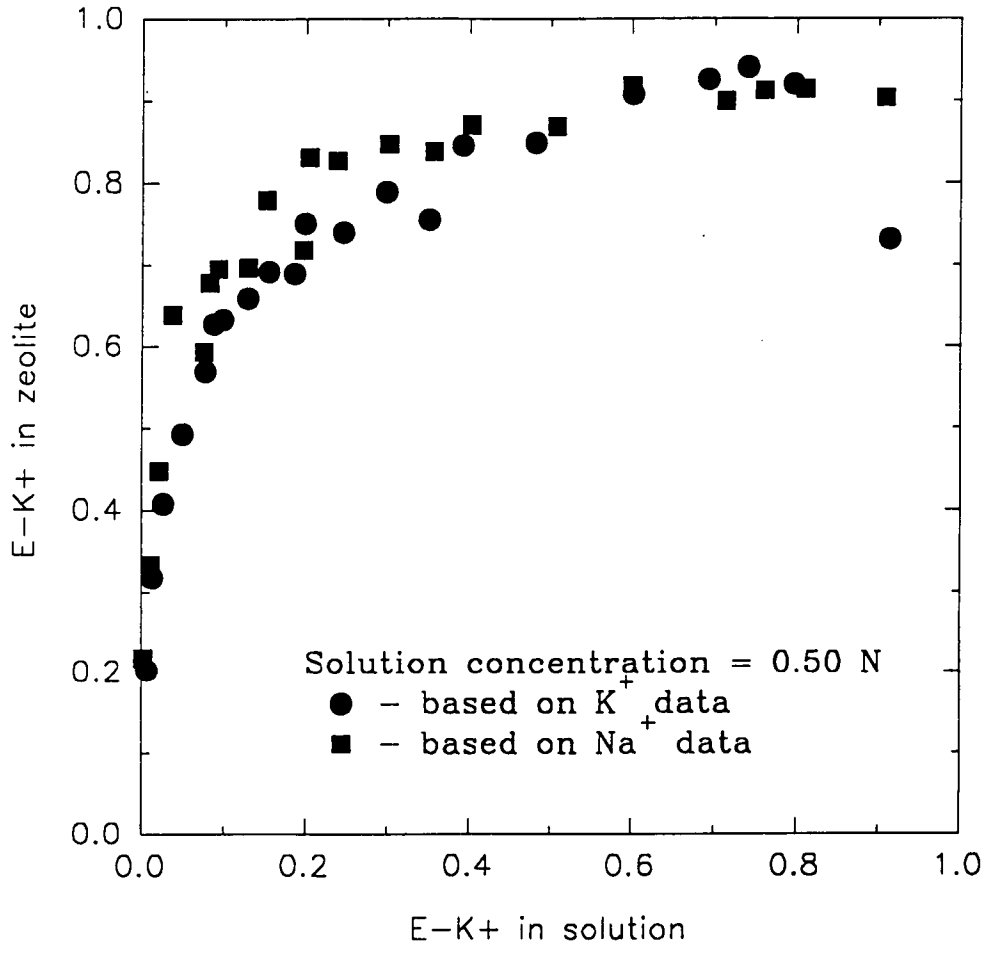

Figure 2-1. Isotherm at 25°C for ion exchange between clinoptilolite and aqueous mixtures of NaCl/KCl at a total solution concentration of 0.50N

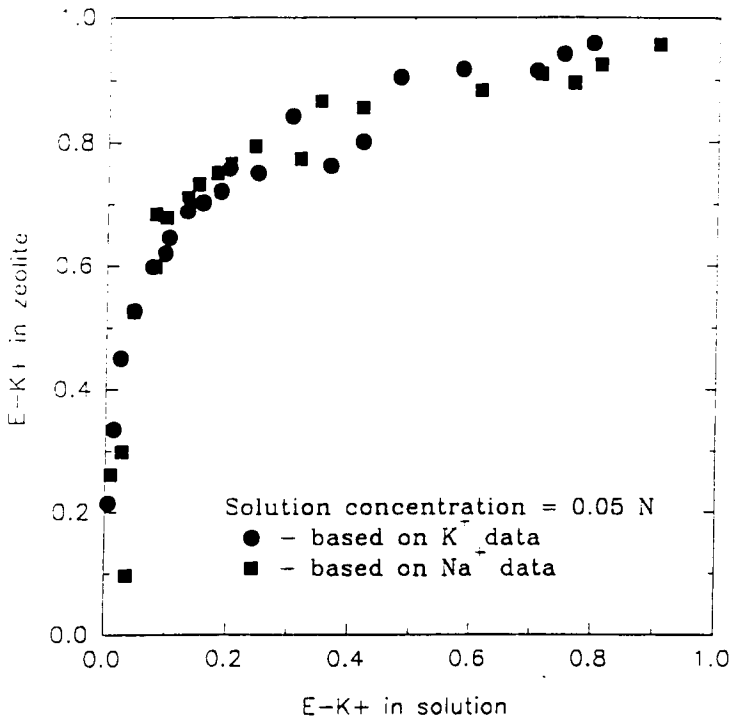

Figure 2-2. Isotherm at 25°C for ion exchange between clinoptilolite and aqueous mixtures of NaCl/KCl at a total solution concentration of 0.05N

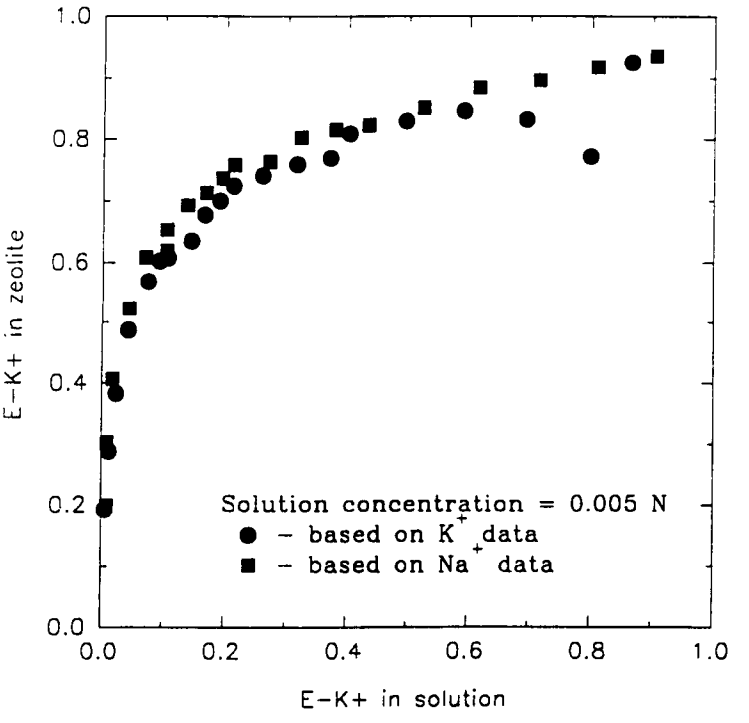

Figure 2-3. Isotherm at 25°C for ion exchange between clinoptilolite and aqueous mixtures of NaCl/KCl at a total solution concentration of 0.005N

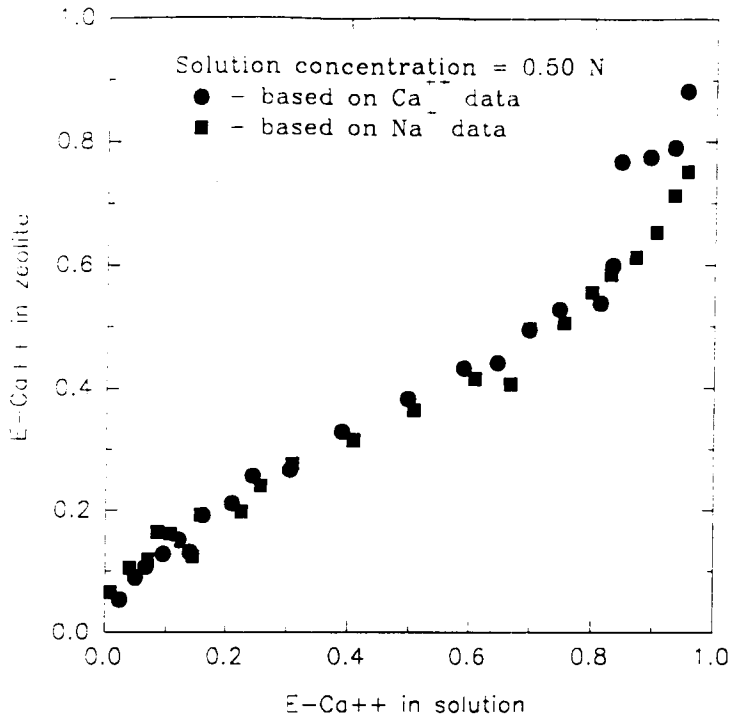

Figure 2-4. Isotherm at 25°C for ion exchange between clinoptilolite and aqueous mixtures of NaCl/$CaCl_2$ at a total solution concentration of 0.50N

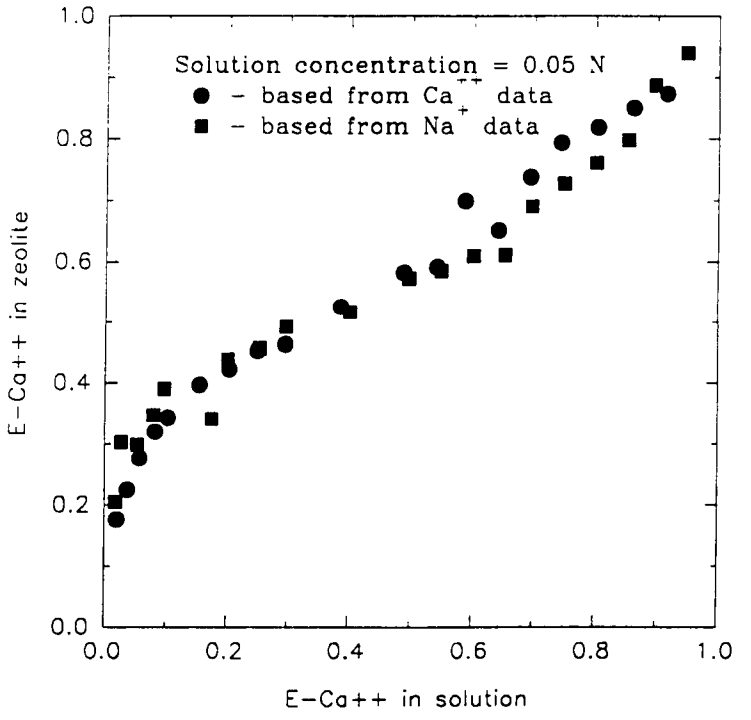

Figure 2-5. Isotherm at 25°C for ion exchange between clinoptilolite and aqueous mixtures of NaCl/$CaCl^2$ at a total solution concentration of 0.05N

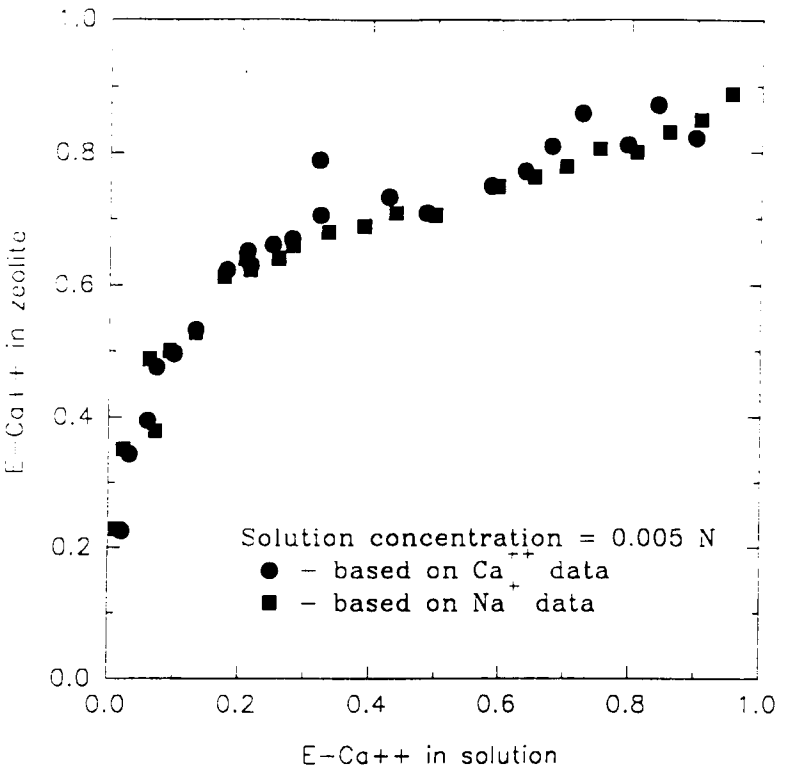

Figure 2-6. Isotherm at 25°C for ion exchange between clinoptilolite and aqueous mixtures of $NaCl/CaCl_2$ at a total solution concentration of 0.005N

2.2 GEOCHEMICAL MODELING by William M. Murphy

2.2.1 Technical Objectives

The technical objective of the modeling task of the Geochemistry Research Project is to apply principles of thermodynamics, kinetics, and mass balance to the interpretation of natural and experimental systems pertinent to ambient and repository geochemical conditions at Yucca Mountain and to the prediction of the evolution of these systems. One specific objective is the interpretation of data generated in the experimentation task of the project. Theoretical interpretation permits extraction of meaningful and useful parameters from the experimental data, assists design of future experiments, and provides a method to evaluate aspects of the models including theory and codes.

2.2.2 Thermodynamic and Kinetic Analysis of Analcime Dissolution Data

The theoretical basis for analcime-clinoptilolite equilibration experiments and laboratory techniques and initial data from scoping tests have been reported previously (Murphy, 1991a; Pabalan, 1991b). A kinetic and thermodynamic interpretation of the laboratory data from the initial series of experiments was presented by Murphy (1991b). This report summarizes progress in similar theoretical analyses of the more detailed analcime dissolution studies

ADCTIA, ADCTIIA, ADCTIIIA, for which data are reported in Pabalan (1991a) and in the preceding subsection 2.1.

2.2.2.1 Mass and stoichiometry analyses

Analytical data of the analcime dissolution experiments for aqueous concentrations as a function of time must be corrected for diminishing solvent mass and solute removal due to sampling and evaporation to properly evaluate reaction progress (Murphy, 1991b). These corrections are facilitated in the ADCT series experiments because solution mass and the mass of solution extracted at each sampling point were measured in the laboratory. Appropriate corrections to the ADCT series data were applied using the relation (Murphy, 1991b)

$$n_{I,R}(t_s) = m_I(t_s)\ W(t_s) + n_{I,E}(t_s) \qquad (2\text{-}13)$$

where $n_{I,R}(t_s)$ stands for the total number of moles of a particular component I (e.g., Si or Al) released to solution at the time of sampling t_s, $m_I(t_s)$ denotes the total molality of component I at time t_s, $W(t_s)$ stands for the mass of the solution in the reaction vessel prior to sampling at time t_s, and $n_{I,E}$ denotes the number of moles of component I removed from the experiment in all samples taken prior to time t_s, which is given by

$$n_{I,E} = \sum_{t_p<t_s} m_I(t_p)\ W_E(t_p) \qquad (2\text{-}14)$$

where $W_E(t_p)$ stands for the mass of water extracted at time t_p.

The cumulative release of Si and Al in the ADCT series experiments, $n_{I,R}$, calculated using Eqns. (2-13) and (2-14) is shown in Figures 2-7, 2-8, and 2-9 as a function of time for the first 600 hours of reaction. Data from the initial period of reaction progress are appropriate for an evaluation of the dissolution rate under conditions that are far from equilibrium. This rate should be independent of the small variations in solution composition in these experiments (Murphy, 1991b). Aqueous speciation analyses of the experimental solutions using EQ3NR indicate that samples collected after 200 hours of reaction have saturation indices with respect to analcime of several percent, signifying that the rate of reaction at this stage of reaction progress may be detectably affected by the approach to equilibrium. Interpretations of the initial rate data are represented by straight lines in Figures 2-7, 2-8, and 2-9, with slopes that correspond to dissolution rates in units of moles released per hour. The lines are constrained to have relative slopes representing stoichiometric release of Si and Al (i.e., rate of Si release equal to twice the rate of Al release) in each of the three experiments. The lines approximate the experimental data in the initial 200 hours of reaction. The intercepts of the lines are not

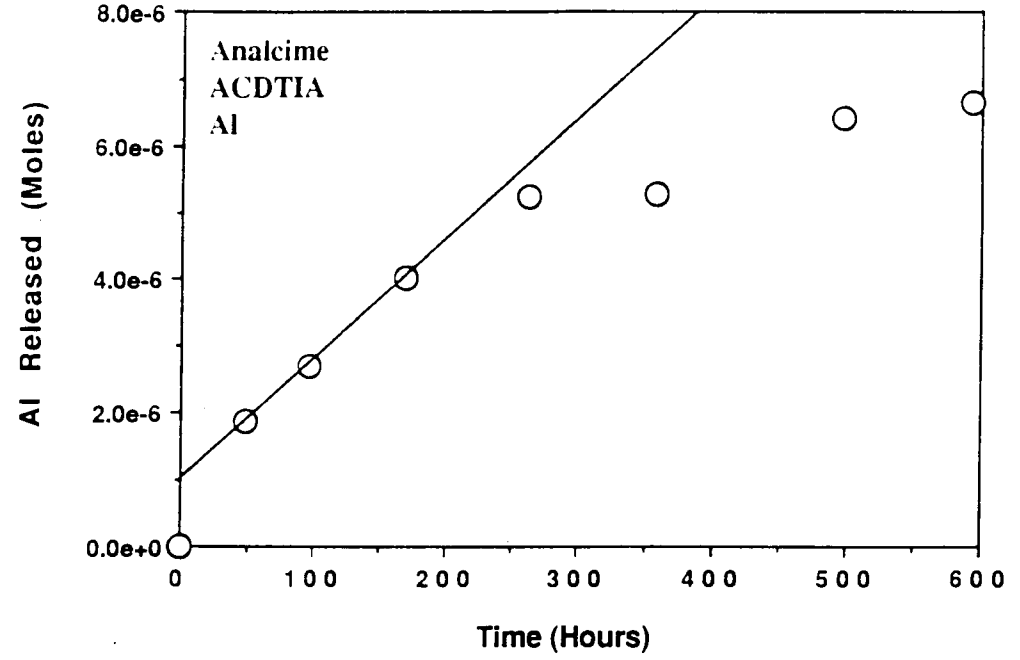

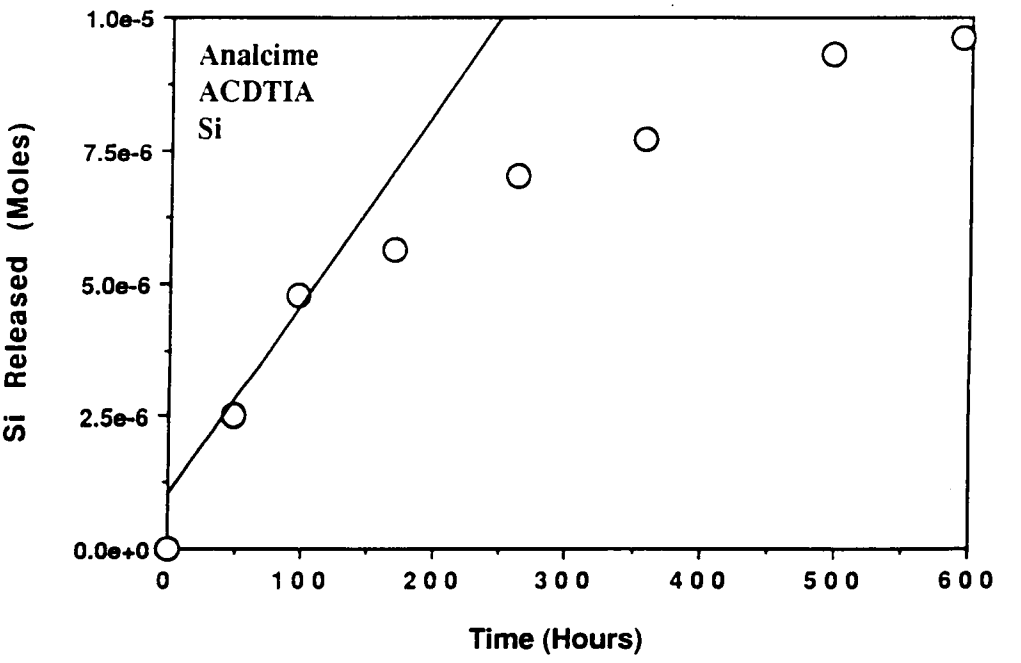

Figure 2-7. Total moles of Al and Si released as a function of time in analcime dissolution experiments ADCT-IA. Lines represent interpretations of the initial stoichiometric dissolution.

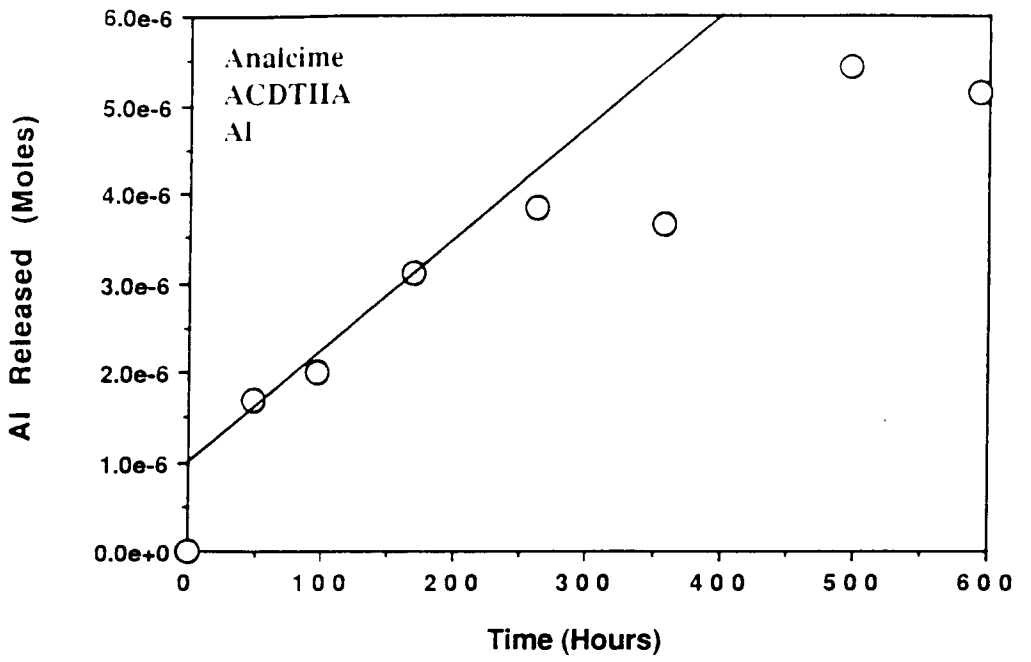

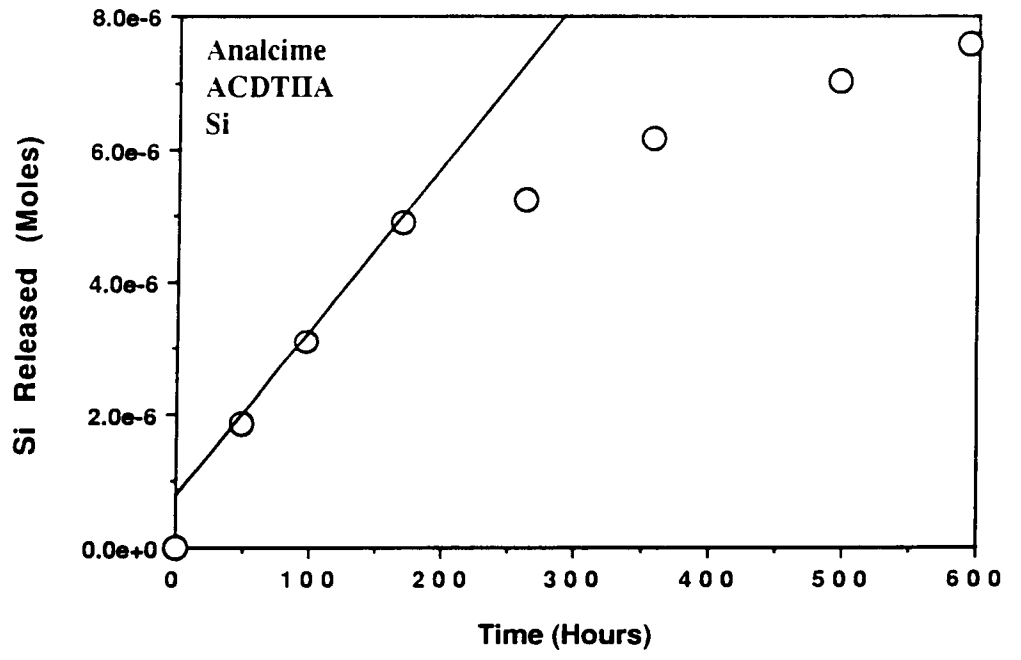

Figure 2-8. Total moles of Al and Si released as a function of time in analcime dissolution experiments ADCT-IIA. Lines represent interpretations of the initial stoichiometric dissolution.

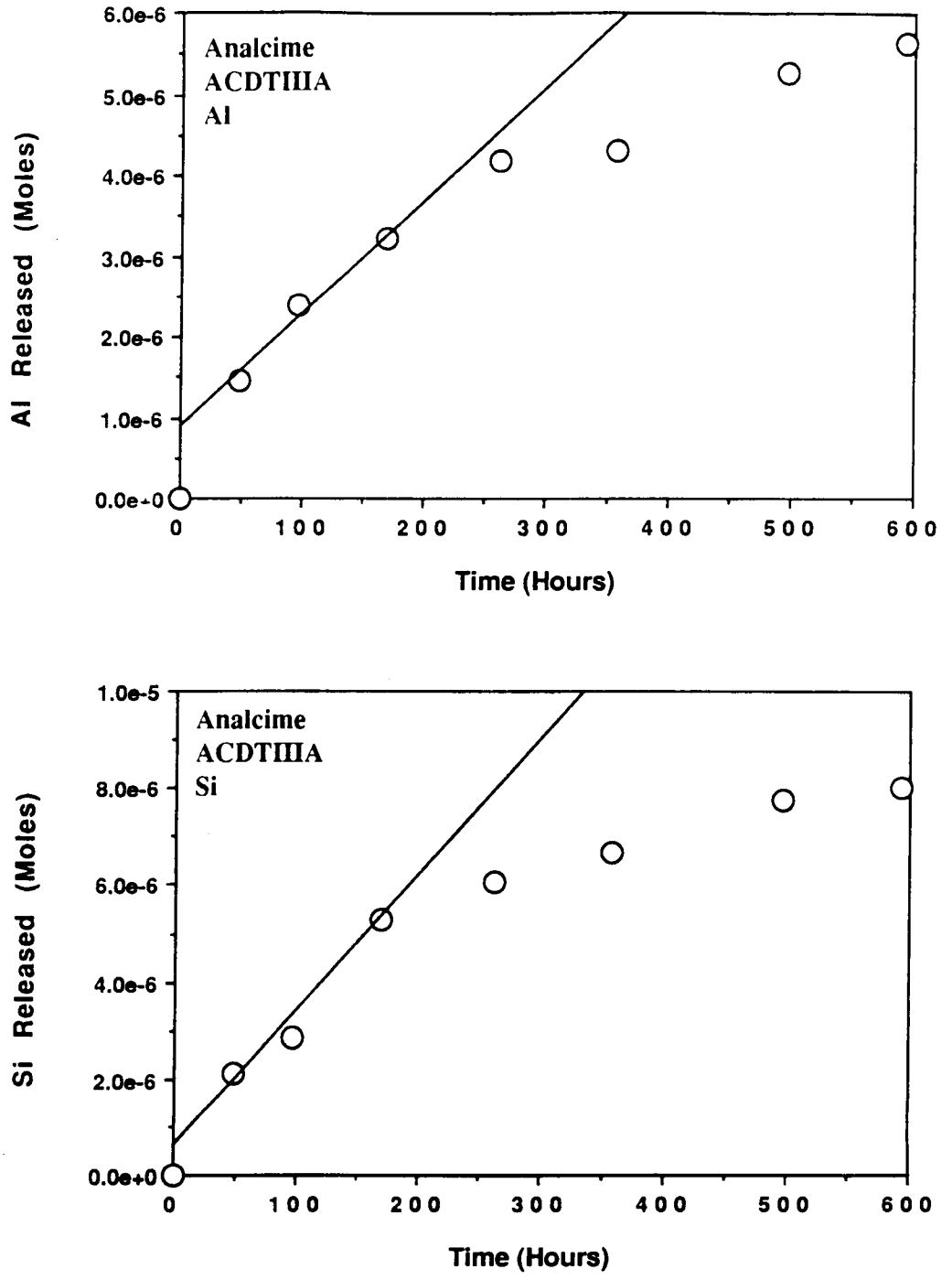

Figure 2-9. Total moles of Al and Si released as a function of time in analcime dissolution experiments ADCT-IIIA. Lines represent interpretations of the initial stoichiometric dissolution.

limited to be zero or to represent ideal stoichiometry, allowing for initial rapid dissolution of surface material and initial variations in surface composition[1]. Reaction rates derived from the lines in Figures 2-7, 2-8, and 2-9 are given in Table 2-6, together with solid sample masses and specific rates of release (moles released per time per sample mass). Variations in the specific rates among the experiments are due in part to differences in the specific surface areas of the analcime reactants.

The overall stoichiometry of Al and Si release from analcime in the ACDT series experiments is illustrated in Figures 2-10 and 2-11 for all data collected up to 3209 hours of reaction time. The correspondence between the slopes of the lines in these figures, which reflect the stoichiometric ratio of Al and Si in analcime, and the trend of the experimental data indicate that release of Si and Al occurred stoichiometrically following an initial period of preferential Al release. Despite calculated supersaturations with respect to secondary aluminum phases such as gibbsite, no incongruent precipitation is indicated by the stoichiometric release relations.

2.2.2.2 Theoretical rate analysis

The analcime-solution equilibrium reaction can be written as

$$NaAlSi_2O_6 \cdot H_2O \rightleftharpoons Na^+ + AlO_2^- + SiO_2 + H_2O \ . \qquad (2\text{-}15)$$

A theoretical rate equation for stoichiometric analcime dissolution corresponding to the net irreversible forward variant of reaction (2-3), and its analytical integration were presented in Murphy (1991b). It was derived from the basic rate equation

$$\frac{d\xi}{dt} = k^* s \, (1 - Q/K) \qquad (2\text{-}16)$$

where ξ stands for the number of moles of dissolved reactant, t represents time, s denotes the surface area of the reactant, K stands for the equilibrium constant for the dissolution reaction, and Q denotes the reaction quotient for this reaction. Preliminary analyses indicate that an alternate form for the rate expression given by

[1] resulting from adjustments to the matrix solution

Table 2-12. INTERPRETATION OF INITIAL ANALCIME DISSOLUTION RATE

Experiment	Analcime Dissolution Rate (moles per hour)	Analcime Mass (grams)	Specific Dissolution Rate (moles per hour per gram)
ADCT-1A	1.8×10^{-8}	3.75	1.33×10^{-12}
ADCT-2A	1.25×10^{-8}	2.50	1.39×10^{-12}
ADCT-3A	1.4×10^{-8}	2.25	1.73×10^{-12}

$$\frac{d\xi}{dt} = k^* s \left[1 - (Q/K)^{1/2}\right] . \qquad (2\text{-}17)$$

may provide a better representation of the experimental data. Rates given by Eqns. (2-16) and (2-17) are equivalent for conditions that are far from equilibrium (i.e., $Q << K$). However, as equilibrium is approached, the rate equations give different results. The formulation for reaction rates near equilibrium depends in part on the mechanisms of the rate-limiting elementary reactions. The formulation in Eqn. (2-17) is consistent with a rate-limiting step that involves one silicon rather than two as in the conventionally written reaction (2-15).

In a manner similar to that given in Murphy (1991b) and that employs the same assumptions and approximations, an analytical solution can also be obtained for the integral of the rate equation given in Eqn. (2-17). The result is

$$\int_{t_i}^{t_{i+1}} dt = \qquad (2\text{-}18)$$

$$\frac{2}{3Bk}\left[\frac{1}{2}\log_e\left[\frac{(A+Bx^{1.5})}{(k+\sqrt{x})^3}\right] + \sqrt{3}\tan^{-1}\left[\frac{2\sqrt{x}-k}{k\sqrt{3}}\right]\right]\Bigg|_{x(t_i)}^{x(t_{i+1})}$$

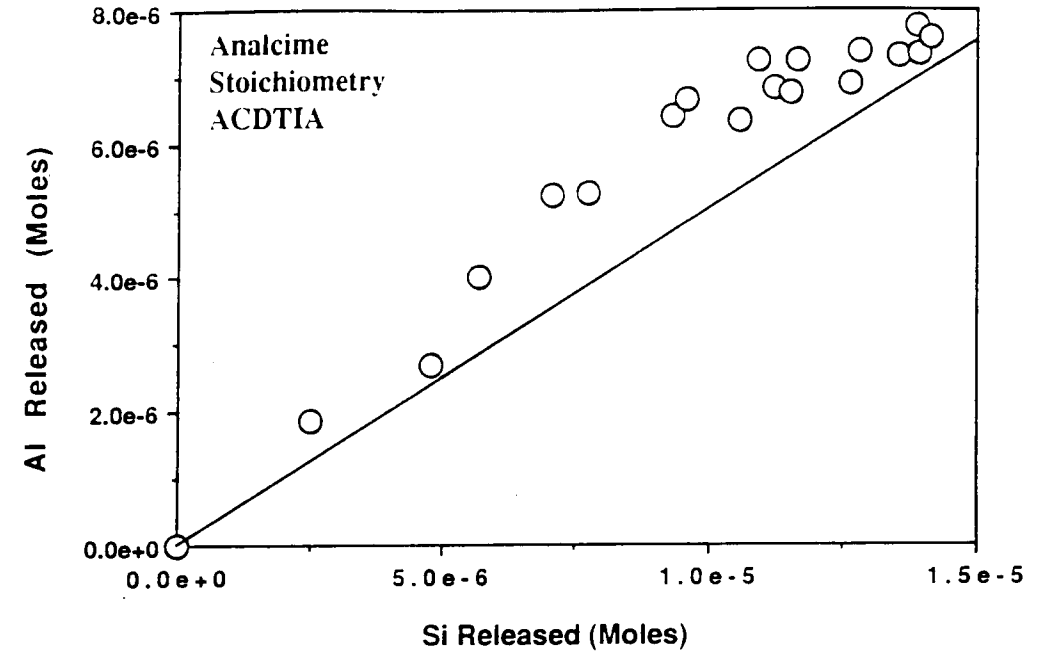

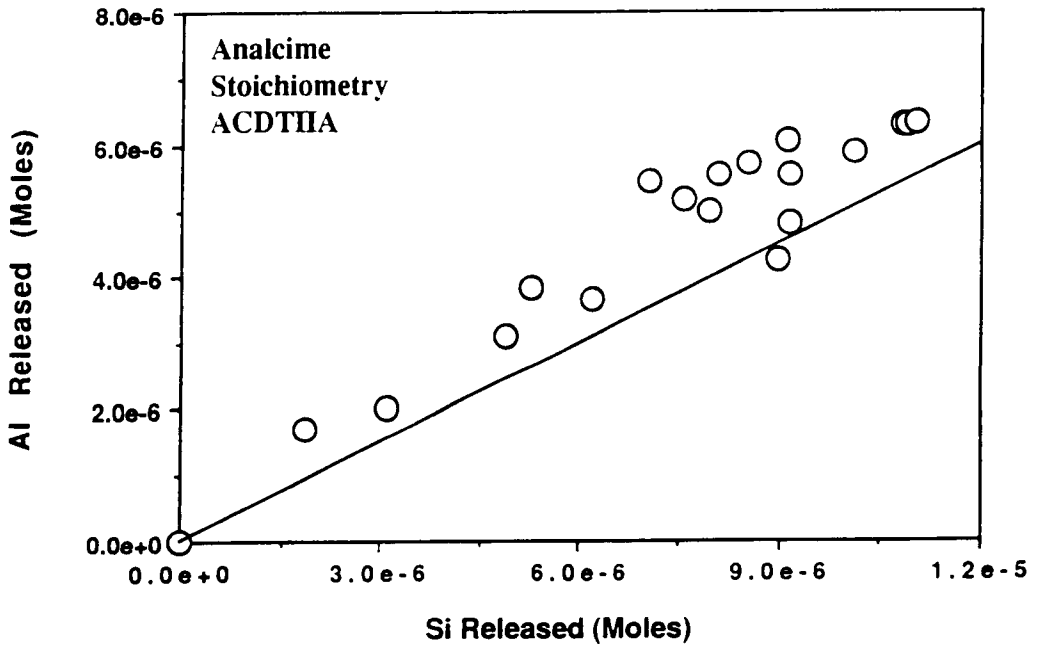

Figure 2-10. Moles of Al released versus moles of Si released representing the stoichiometry of analcime dissolution in experiments ADCT-IA and ADCT-IIA. Lines represent stoichiometric release.

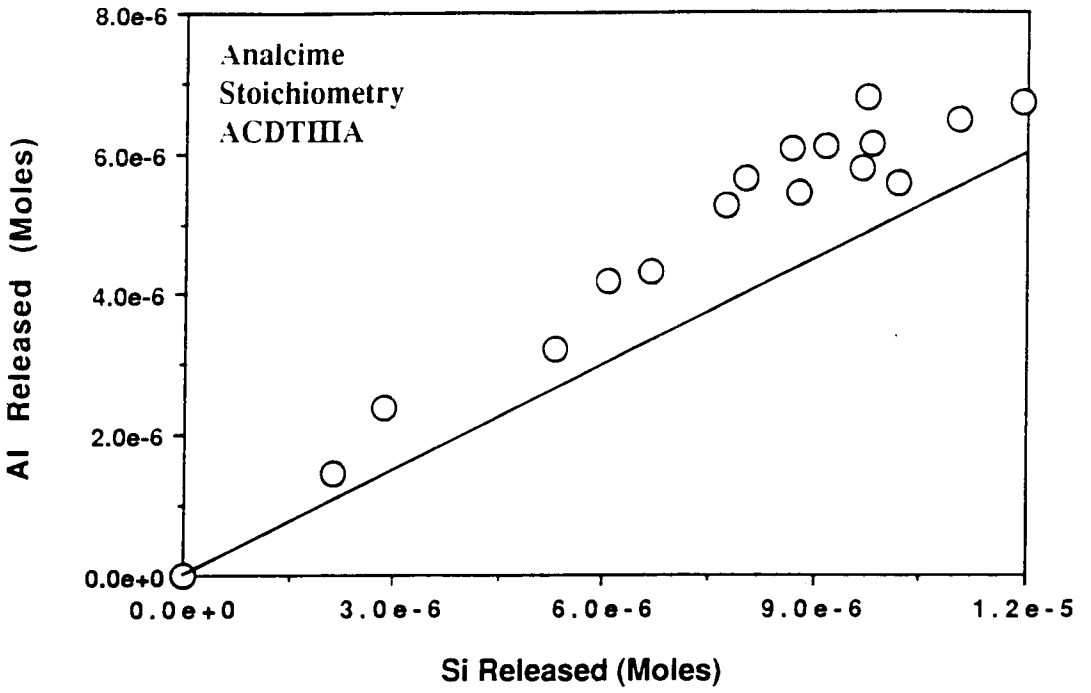

Figure 2-11. Moles of Al released versus moles of Si released representing the stoichiometry of analcime dissolution in experiment ADCT-IIIA. The line represents stoichiometric release.

where A = k*s,

$$B = -2\,A\gamma_{SiO_2}X_{SiO_2}\sqrt{a_{Na+} + \gamma_{AlO_2^-}\frac{X_{AlO_2^-}}{KW^3}}\ ,$$

$$k = 3\sqrt{\frac{A}{B}}\ ,$$

$$X = n_{Al,R} - n_{Al,E} ,$$

and γ_i represents the activity coefficient of the subscripted species, X_i stands for the fraction of the total molality of the component corresponding to the subscripted species that is in the form of the subscripted species, and a_i denotes the activity of the subscripted species (Murphy, 1991b). Regressions of the dissolution rate data using the alternate rate expressions will be conducted on completion of the dissolution experiments.

2.2.2.3 Thermodynamic analysis

The ACDT series experiments proceeded sufficiently far to approach equilibrium as indicated by data for Al and Si concentrations that are nearly constant as a function of time (Pabalan, 1991a; Section 2.1 above) within the apparent analytical error. The final solution compositions can be interpreted to give limits on the equilibrium solubility as approached from undersaturation. The experimental data indicate that ADCT-IA and ADCT-IIIA progressed further than ADCT-IIA in the first 3209 hours of reaction. Average concentrations of duplicate samples for ADCT-IA and ADCT-IIIA taken at 3209 hours were assumed to represent bulk SiO_2 and Al concentrations (1163.5 and 241.2 ppb, respectively) close to equilibrium with analcime. Equilibrium aqueous speciation calculations have been performed for this average solution using the program EQ3 (version EQ3NR.3245R124) with its composite thermodynamic data base (version DATA0.COM.R7) (Wolery, 1983). The total Na content was fixed in the calculation at 1.1×10^{-1} molal, which was the initial Na content in the experiments. Evaporation and analcime dissolution increased this value negligibly. The pH was fixed at the analytical value (9), and the total carbonate content was obtained by adjusting its concentration to achieve charge balance in the speciated solutions. The resulting carbonate concentration corresponds to an equilibrium CO_2 gas fugacity of $10^{-3.42}$ bar. This pressure corresponds closely to the atmospheric CO_2 pressure, which was used to buffer the solutions.

The EQ3 calculations provide values for the parameters required to calculate a preliminary value for the equilibrium constant, K, according to the relation

$$K = \left(a_{Na^+}\right)\left(a_{AlO_2^-}\right)\left(a_{SiO_2}\right)^2 \qquad (2\text{-}19)$$

which is consistent with the reaction in Eqn. (2-15). Calculated values for the activities and equilibrium constant are: $a_{Na^+} = 8.334 \times 10^{-2}$; $a_{AlO_2^-} = 6.882 \times 10^{-6}$; $a_{SiO_2} = 9.998 \times 10^{-6}$; and $K = 10^{-16.24}$. Uncertainties in the thermodynamic data in the EQ3 data base for aqueous speciation reactions, as well as uncertainties in the equilibrium aluminum and silica concentrations, are reflected in the calculated value of K. Furthermore, this value

represents a lower limit because equilibrium was only approached from a state of undersaturation. A more detailed analysis of the analcime dissolution equilibrium constant will be presented on completion of the experimentation. Plans are being made to add a synthetic solution metastably supersaturated with respect to analcime to the reaction vessels containing the nearly equilibrated analcime and residual solution, following the dissolution stage in the ADCT-A series of experiments. This should permit experimental reversals of the analcime solubility measurements.

2.2.3 Conclusions

Kinetic and thermodynamic interpretations of data from the ADCT-A series of analcime dissolution experiments permit an evaluation of the reaction stoichiometry, initial dissolution rate, and a lower limit on the analcime solubility. Dissolution in the experiments was apparently stoichiometric with respect to Si and Al release, and congruent with absence of secondary phase growth. Provisional calculations of values for the reaction rates and equilibrium constant will be refined on completion of the experiments.

2.3 REFERENCES

Barrer, R. M. 1978. Cation-exchange equilibria in zeolites and feldspathoids. L. B. Sand and F. A. Mumpton, eds. *Natural Zeolites: Occurrence, Properties, Use.* New York: Pergamon Press: 385-395.

Murphy, W. M. 1991a. Unsaturated mass transport (Geochemistry): Geochemical modeling. *Report on Research Activities for Calendar Year 1990.* W. C. Patrick, ed. CNWRA 90-01A. San Antonio, Texas: CNWRA: 2-25 to 2-55.

Murphy, W. M. 1991b. Unsaturated mass transport (Geochemistry): Geochemical modeling. *Report on Research Activities for the Quarter April 1 through June 30, 1991.* W. C. Patrick, ed. CNWRA 91-02Q. San Antonio, Texas: CNWRA: 2-6 to 2-25.

Pabalan, R. T. 1991a. Unsaturated mass transport (Geochemistry): Experimental studies. *Report on Research Activities for the Quarter April 1 Through June 30, 1991.* W. C. Patrick, ed. CNWRA 91-02Q. San Antonio, Texas: CNWRA.

Pabalan, R. T. 1991b. Unsaturated mass transport (Geochemistry): Experimental studies. *Report on Research Activities for Calendar Year 1990.* W. C. Patrick, ed. CNWRA 90-01A. San Antonio, Texas: CNWRA.

Pabalan, R. T. 1991c. Nonideality effects on the ion exchange behavior of the zeolite mineral clinoptilolite. T. Abrajano, Jr. and L. H. Johnson, eds. *Scientific Basis for Nuclear Waste Management XIV.* MRS Symp. Proc. 212, Pittsburgh, PA: Materials Research Society: 559-567.

Pabalan, R. T., and D. R. Turner. 1991. Sorption modeling for HLW performance assessment. *Report on Research Activities for the Quarter April 1 through June 30, 1991*. W. C. Patrick, ed. CNWRA 91-02Q. San Antonio, Texas: CNWRA.

Semmens, M. J., and M. Seyfarth. 1978. The selectivity of clinoptilolite for certain heavy metals. L. B. Sand and F. A. Mumpton, eds. *Natural Zeolites: Occurrence, Properties, Use*. New York: Pergamon: 517-526.

Wolery, T. J. 1983. EQ3NR A computer program for geochemical aqueous speciation-solubility calculations: User's guide and documentation. UCRL-53414. Livermore, California: Lawrence Livermore National Laboratory.

3 THERMOHYDROLOGY

by Ronald T. Green (CNWRA) and Win Pe (CNWRA)

Investigators: Franklin T. Dodge (SwRI), Ronald T. Green (CNWRA), Randall D. Manteufel (CNWRA), Ronald H. Martin (CNWRA), Win Pe (CNWRA), and Steve J. Svedeman (SwRI)

3.1 INTRODUCTION

Technical issues and uncertainties for the proposed Yucca Mountain HLW repository site indicate a need for research on thermohydrological phenomena (i.e., phenomena associated with heat and fluid flow) to provide information relevant to performance assessment (PA) and design criteria. The class of thermohydrological phenomena examined in this project includes phenomena driven by heat emanating from HLW emplaced in a geologic repository. Information derived principally from research is used to establish a knowledge base of thermohydrologic phenomena which will be utilized to assess models of processes used in PAs. This report summarizes the progress of the Thermohydrology Research Project performed during the third quarter of 1991.

3.2 TECHNICAL OBJECTIVES

The specific objectives of the Thermohydrology Research Project are summarized as follows:

- Perform a critical assessment of the state-of-knowledge of thermohydrology in unsaturated fractured media, in the context of present HLW-NRC program activities. This assessment will require an in-depth review of existing literature and on-going programs. The assessment will focus on flow processes, heat-transfer mechanisms, and state-of-the-knowledge experimental methods in porous media.

- Perform a detailed dynamic similarity or similitude analysis on the complete set of governing equations relevant to unsaturated flow and determine the set of dimensionless parameters required to conduct appropriate laboratory simulations. In this analysis of modeling parameters, the range of parameter applicability and limitation on the magnitude of these parameters, as constrained by the principles of dynamic similarity, will be determined.

- Identify potential problems associated with the design and performance of laboratory simulations with scaled geometry, fluid, media, and other relevant properties subject to modeling distortion.

- Perform a series of separate-effects experiments in order to identify and understand the role of each effect in the overall coupled processes involved in thermohydrologic phenomena.

- Design and perform comprehensive experiments whose results will continue to identify key dependent and independent parameters and their relationships to each other in the context of thermohydrologic issues.

- Develop the laboratory facilities, experimental methods, measurement techniques, and associated analytic skills to evaluate and validate other program results and to provide a high quality of technical assistance and research in support of NRC's licensing of a HLW repository.

- Examine and correlate laboratory results with field data to aid in the design of future field experiments.

A revised Project Plan for the Thermohydrology Research Project has been submitted to NRC/RES. The revised work plan was modified for the purpose of redefining the project tasks so that the objectives of the project could be pursued in a more direct fashion. These modifications were written to reflect in the project plan the greater understanding of thermohydrologic phenomena that has been achieved through the course of the research project to date. Accordingly, selected portions of the revised plan have received greater attention than they were afforded in the original work plan. These include the investigation of matrix/fracture hydraulic properties; a higher involvement in numerical simulations of two-phase flow phenomena; and the execution of highly-instrumented, two-dimensional experiments. The seven tasks of the revised Project Plan are as follows:

- Task 1 - Assessment of the State-of-Knowledge on Thermohydrology in Unsaturated Media

- Task 2 - Design and Execution of Preliminary Separate-Effects Experiments

- Task 3 - Design and Execution of Thermohydrological Experiments in Unsaturated Media

- Task 4 - Numerical Analysis of the Thermohydrological Phenomena Observed during Execution of the Laboratory Experiments (not funded at this time)

- Task 5 - Investigation of Matrix and Fracture Hydraulic Properties (not funded at this time)

- Task 6 - Collaboration with the University of Arizona Hydrology Department on the Field Heater Test at the Apache Leap Site (not funded at this time)

- Task 7 - Quarterly and Annual Research Report Preparation.

Task 1 of the Project Plan was previously completed. Task 2, Design and Execution of Separate Effect Experiments, was completed during this reporting period. Task 3, Design and Execution of Thermohydrological Experiments in Unsaturated Media, has been started with the initiation of Test 7.

3.3 SEPARATE-EFFECTS EXPERIMENTS

Results from Test 6, the last of the separate-effects experiments, have been investigated in greater detail. Test 6 was a two-dimensional, vertically upright configured, nonisothermal experiment conducted in a test container filled with silica beads. A fracture simulated with coarse silica beads was located midway between the two vertical heat-exchanger boundaries. The right heat exchanger was maintained at 60°C, and the left was maintained at 20°C for the 120-day duration of the experiment.

Vector plots of suction pressures were prepared from moisture-saturation measurements collected on days 25, 75, and 113 of Test 6. Moisture-content values were determined using the gamma-ray densitometer measurements, and the calculation method with the resulting values (Green and Svedeman, 1991a) was reported.

To determine suction pressures from moisture content or saturation values, van Genuchten's equation (van Genuchten, 1978), that is,

$$S=(1-S_r)\left[\frac{1}{1+|\alpha\psi|^{\beta}}\right]^{1-\frac{1}{\beta}}+S_r\ , \tag{3-1}$$

was solved for suction pressure as follows:

$$\psi=\frac{1}{\alpha}\left[\left(\frac{S}{1-S_r}\right)^{\frac{\beta}{1-\beta}}-1\right]^{\frac{1}{\beta}} \tag{3-2}$$

where ψ is suction pressure, α and β are the van Genuchten parameters, and S is saturation. The subscript r denotes residual. Note that isothermal conditions are assumed in this expression.

The van Genuchten parameters had been determined in the laboratory using a positive-pressure experiment conducted with a Tempe cell. Since the medium tested using the Tempe

cell was the same as that in the Test 6 container, the measured van Genuchten parameters that were used to calculate the suction pressures should be appropriate.

Two sets of vector plots have been prepared from the results of Test 6. Figures 3-1 through 3-3 illustrate vector plots of the suction pressure gradient at 25, 75, and 113 days, respectively. Figures 3-4 through 3-6 illustrate the gradient of the combined total of suction pressure and pressure resulting from the gravity at the same time intervals (up is toward 1-5 on the vertical scale).

Interesting pressure regimes are illustrated in these vector plots. As presented in both vector plots at 25 days (Figures 3-1 and 3-4), there is no obvious effect upon water potential by the heated boundary at this time in the experiment. The effect of gravity, however, appears to dominate the potential of liquid water. Based on this observation, significant time (greater than 25 days) is required for the moisture in the container to attain equilibrium with respect to gravity.

The effect of gravity is still apparent at 75 and 113 days, but the effect of the heated vertical boundary is also manifested. Even at the end of the experiment (day 113), the effect of the heated boundary upon suction pressure is apparent only within about 3 to 5 cm from the heated boundary, except along the lower boundary where thermal effects upon suction pressure approach the mid point of the container (about 6 to 7 cm) (Figure 3-6).

3.4 THERMOHYDROLOGICAL EXPERIMENTS IN UNSATURATED MEDIA

The first experiment as part of Task 3, Design and Execution of Thermohydrological Experiments in Unsaturated Media, has been started. This experiment, designated as Test 7, is a continuation of the series of two-dimensional experiments that were conducted as part of the scoping portion of the research project and as part of Task 2, Design and Execution of Preliminary Separate Effects Experiments. A schematic of the test-container dimensions and locations of the measurements is illustrated in Figure 3-7.

The objective of the experiments has been to investigate thermohydrological phenomena using experiments that exhibit these phenomena and provide a means to observe and quantify the processes of interest. Experiments conducted in the course of this research project have been designed to incorporate features expected in a geologic, HLW disposal environment (e.g., a fractured, porous medium) at partially saturated, nonisothermal conditions.

Experiments that are two dimensional in scope have proven to be amenable to observation using instrumentation and measurement techniques currently available. In the two-dimensional experiment performed as part of this research project, gamma-ray densitometry has been a useful technique to measure density differences and infer changes in moisture content from these measurable differences. The series of two-dimensional experiments has continued because useful and insightful information has been provided and also because similarly useful data are not

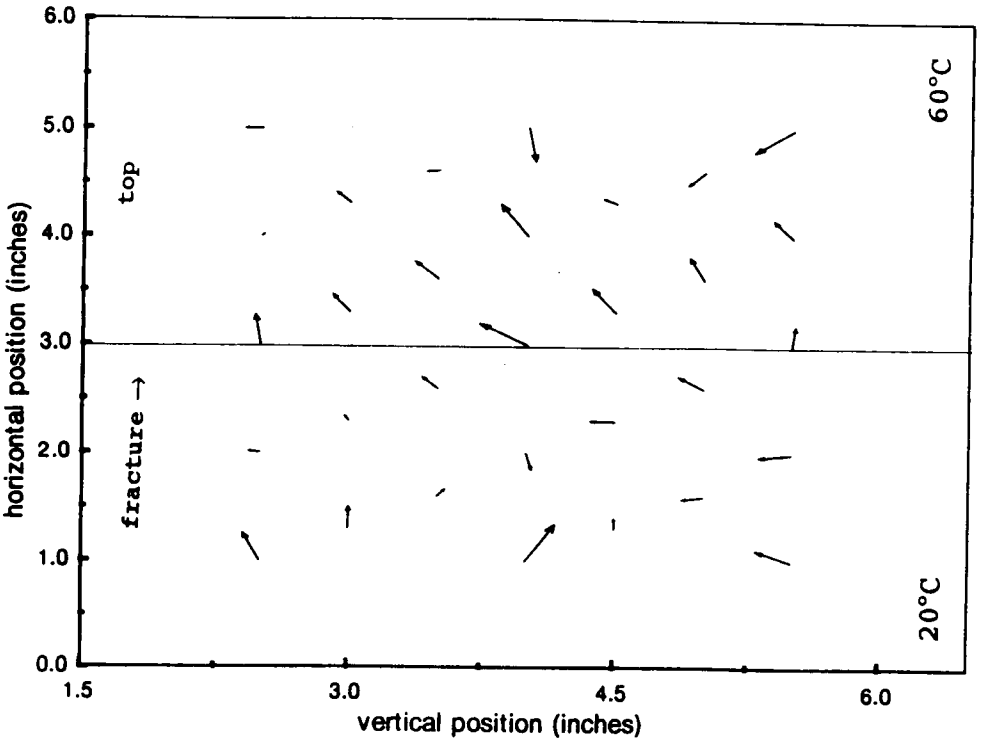

Figure 3-1. Suction vector plot after 25 days

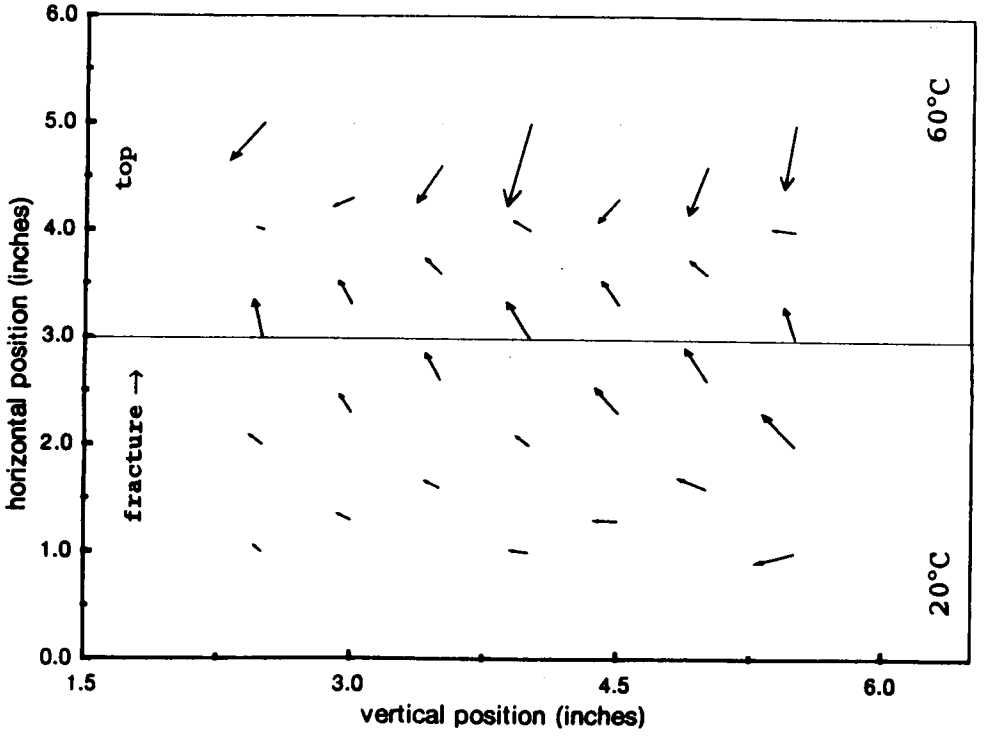

Figure 3-2. Suction vector plot after 75 days

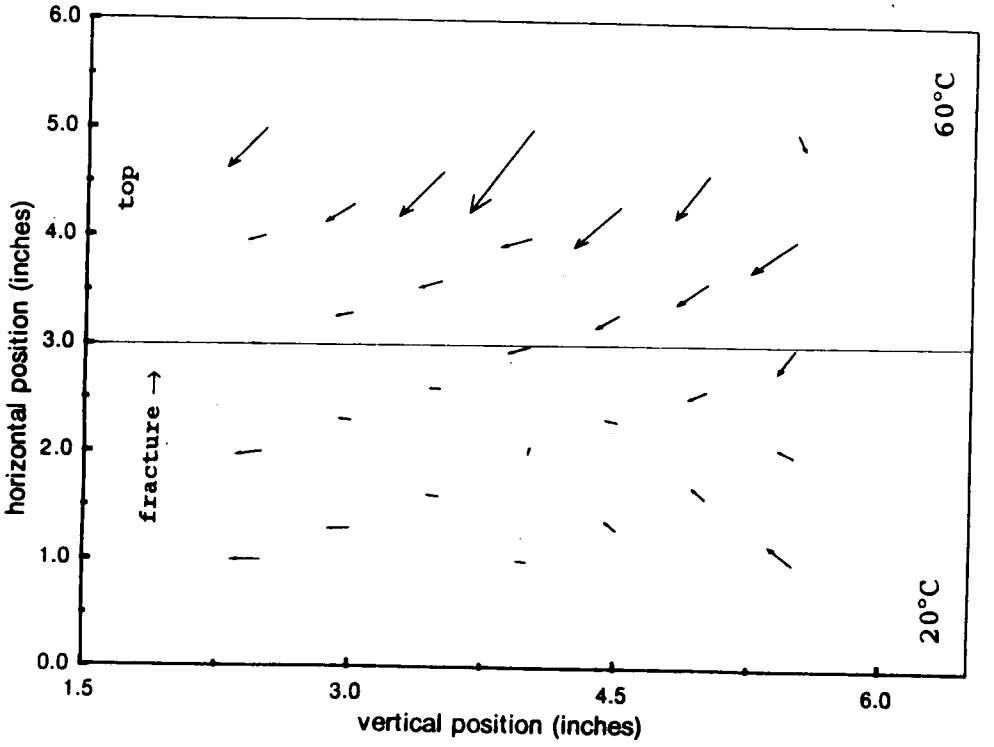

Figure 3-3. Suction vector plot after 113 days

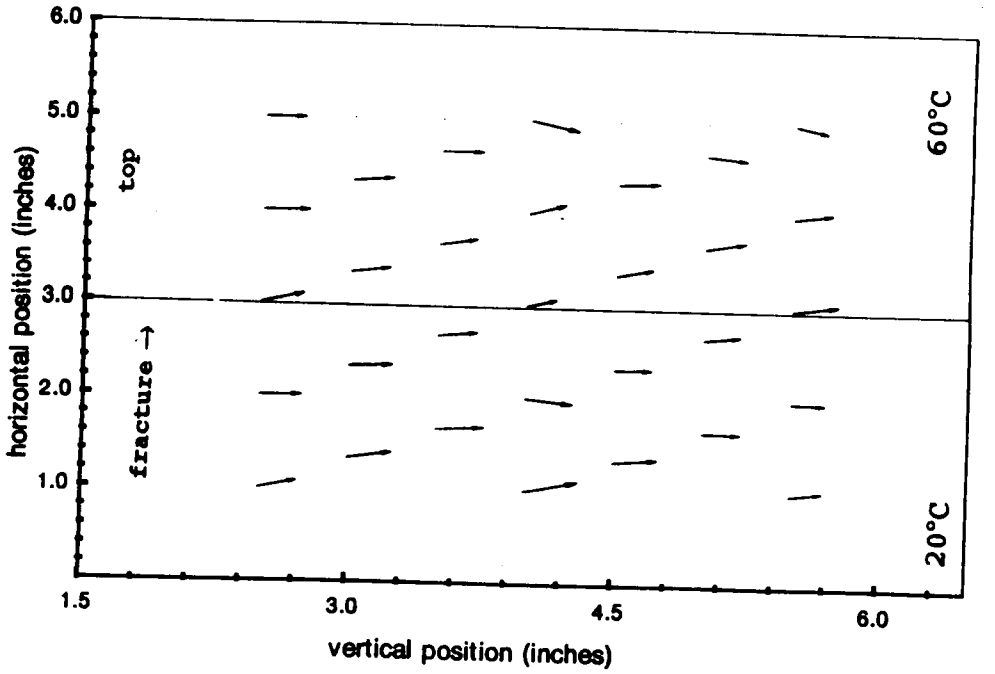

Figure 3-4. Total pressure gradient after 25 days

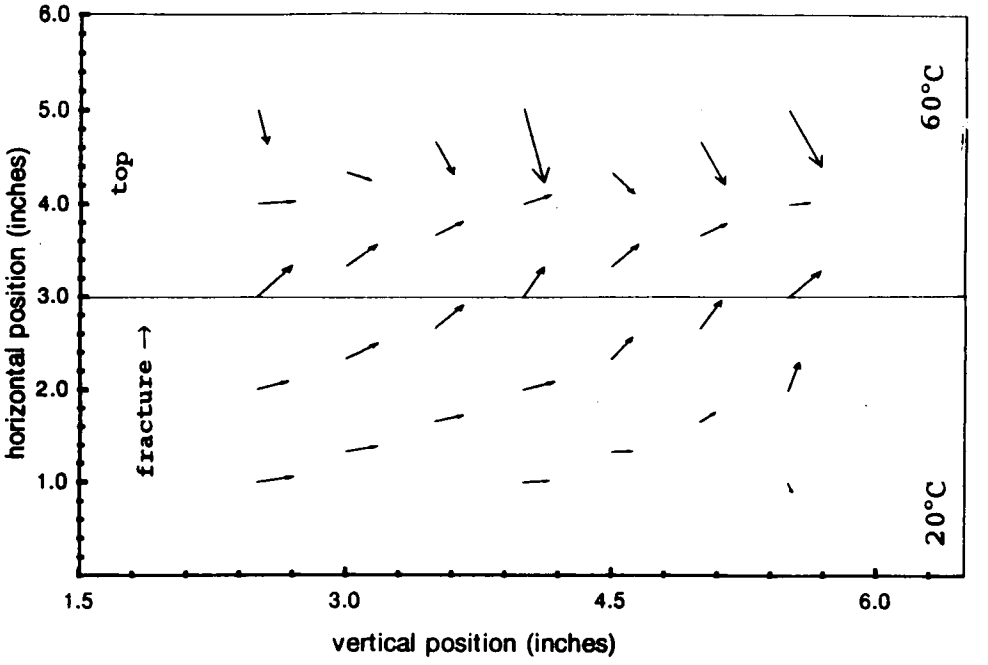

Figure 3-5. Total pressure gradient after 75 days

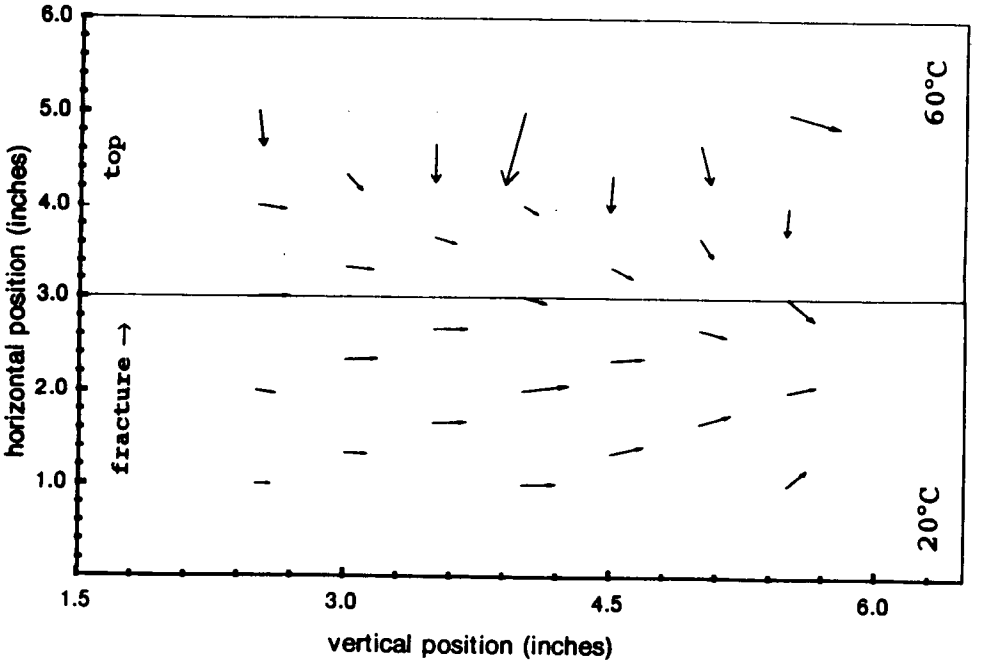

Figure 3-6. Total pressure gradient after 113 days

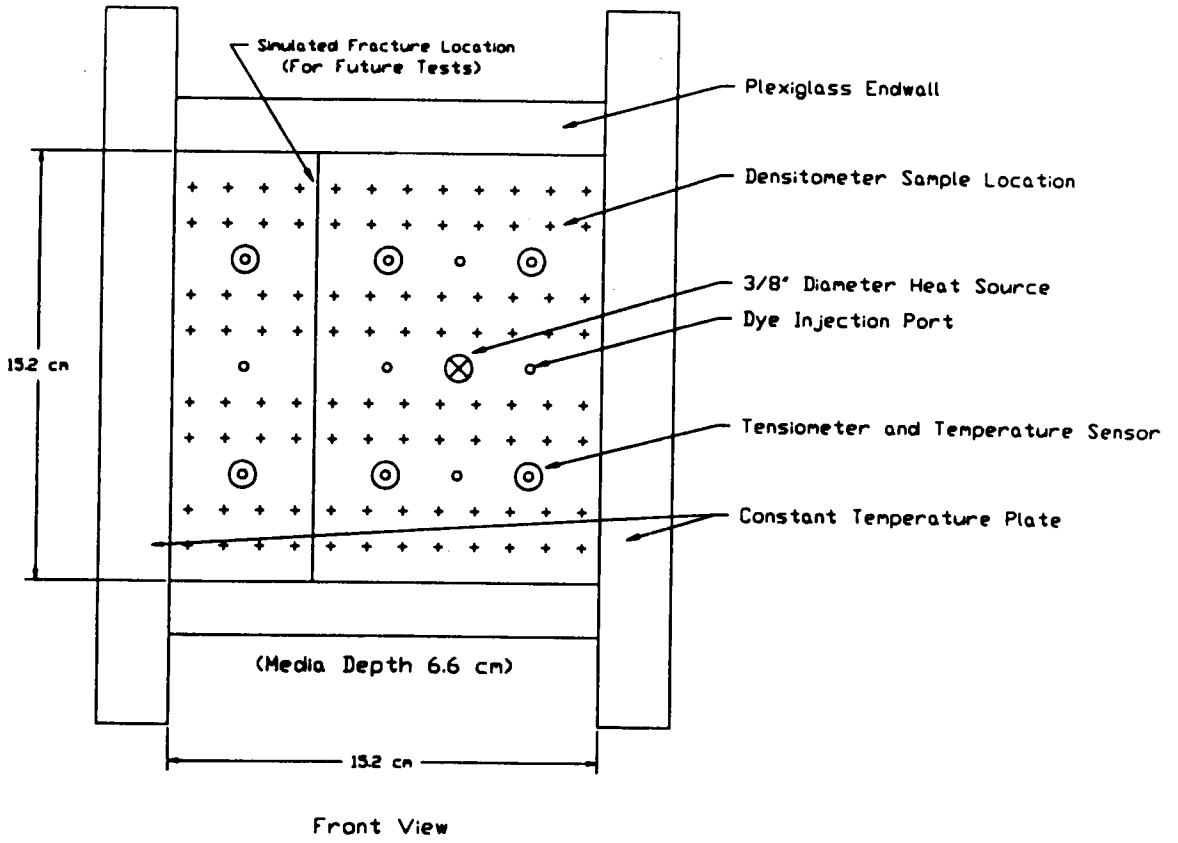

Figure 3-7. Schematic of Test 7

reasonably obtainable from experiments conducted at three dimensions using the currently available technology.

The design of Test 7 is similar to Test 6 and earlier tests. In essence, Test 7 consists of a vertical two-dimensionally configured test container filled with a uniform mix of alumina powder. The alumina powder was sieved between 100 and 325 mesh (150 to 45 microns) to provide a controlled uniform medium.

Alumina powder was used to avoid difficulties resulting from the dissolution of silica and bead degradation associated with the glass beads used in previous experiments. As was demonstrated in earlier tests, the prolonged duration of the thermohydrological tests, especially under nonisothermal conditions, can result in degradation of the medium, thus introducing at

least one additional unknown into the experiment: a medium with time-varying hydraulic properties. Use of alumina beads probably will eliminate medium degradation as a variable from the experiments using synthetic materials.

Although the entire medium in this experiment is uniform, future experiments, including Test 8, are being designed to contain a simulated or actual fracture. A fracture has not been incorporated into the design of Test 7 purposely to permit an examination of fluid movement not affected by a simulated or actual fracture. Results from Test 8, which will incorporate a fracture, will be evaluated vis a vis Test 7 to assess the effect of the fracture.

The temperature of both the left and right vertical boundaries of the container in Test 7 has been held constant at 20°C. A point heat source held constant at 60°C has been placed in the mid-level right portion of the test container. The heat source actually spans the entire short dimension of the container; therefore, even though it is a finite-length line source in the container, it is effectively a point source in the two-dimensional configuration. The temperature of the heat source may be raised during later stages of the experiment.

The front and back vertical walls were constructed of clear plexiglass to permit visual inspection of the medium for the duration of the experiment. Tensiometers were installed at six locations in the container. Unfortunately, one of the tensiometers in the Test 7 container was damaged during start-up and does not appear to be functional for this experiment. Six ports permit the introduction of dye as a tracer of liquid water flow. Thermistors were attached to the two vertical-boundary heat exchangers and to each of the six tensiometers, thereby providing temperature measurement at a total of eight locations in the test container.

The gamma-ray densitometer will again be used to measure changes in density of the test container. The moisture content of the medium will be calculated from the density measurements in a procedure similar to that used in the evaluation of data collected during Test 6. Gamma-ray densitometer measurements will be recorded at a total of 96 locations during Test 7. This increase in measurement locations will provide greater resolution in moisture-content values than was available in earlier tests. Gamma-ray measurements will also be made of a stationary aluminum block prior to and subsequent to each set of gamma-ray measurements to permit removal of instrument drift during the course of the experiment. Instrument drift resulting from thermal and barometric fluctuations has been detected during previous experiments.

Variables measured during Test 7 are temperature, barometric pressure, suction pressure, and moisture content (indirectly measured using a gamma-ray densitometer). Barometric pressure and temperature are measured at ambient conditions. All measurements will be collected using an automated data acquisition system (DAS). Additionally, dye is being injected

into the container at six points to indicate the direction of liquid water flow. Photographs of the dye are periodically taken through the clear plexiglass side walls to help ascertain and document liquid water movement.

The test medium was initially saturated at 75 percent. The total duration of Test 7 is not precisely known at this time but is anticipated to be similar to Test 6, which ran for about 120 days.

3.5 REFERENCES

van Genuchten, M. Th. 1980. A closed-form equation for predicting the hydraulic conductivity of unsaturated soils. *Sci. Am. Journal.* 44: 892-898.

4 SEISMIC ROCK MECHANICS

by Simon M. Hsiung and Asadul H. Chowdhury

Investigators: Mikko P. Ahola (CNWRA), Asadul H. Chowdhury (CNWRA), Jaak J. Daemen (University of Nevada), Roger Hart (ITASCA), Simon H. Hsiung (CNWRA), Daniel D. Kana (SwRI)

4.1 TECHNICAL OBJECTIVES

Six specific objectives have been identified for the Seismic Rock Mechanics Research Project. These are as follows:

- Develop a good understanding of the information currently available of seismic effects on underground structures.
- Assess, by conceptual models and experimental studies, the capabilities and limitations of rock-joint models and computer codes currently in use.
- Demonstrate by laboratory model studies and instrumented field studies the degree of accuracy (validation) for the rock-joint models and computer codes used for seismic analysis in a tuff medium.
- Assess by instrumented field studies the significance of seismic pumping and demonstrate the degree of validation for the rock-joint models and computer codes for simulation of seismic effects on groundwater hydrology.
- Identify and assess the key seismic-related parameters that are applicable to the Yucca Mountain site.
- Generate technical data for preparing licensing-related positions as they relate to the effect of seismic action on the underground repository in a tuff medium.

The objectives are to be addressed in the following eight tasks.

- Task 1 - Focused Literature Search
- Task 2 - Laboratory Characterization of Jointed Rock
- Task 3 - Assessment of Analytical Models/Computer Codes
- Task 4 - Rock Dynamics Laboratory and Field Studies and Code Validation
- Task 5 - Groundwater Hydrology Field Studies and Code Validation

- Task 6 - Yucca Mountain Scoping Analysis
- Task 7 - Technical Report
- Task 8 - Quarterly Research Report

During this reporting period, most of the research activities were on hold due to budget constraint; and as a result, the milestones schedule will be altered. These changes will be reflected in a revised project plan. Only data collection on instrumented field studies at the Lucky Friday Mine, Mullan, Idaho, for dynamic effects on underground openings and seismic effects on the geohydrologic regime water was carried out. Data reduction was performed on part of the data collected and is reported in the following section. Analysis of these data will be conducted and reported at a later date.

4.2 INSTRUMENTED FIELD STUDIES

4.2.1 Excavation Response

Two sites about 5,210 feet below the ground level were selected for the study of excavation response to mining-induced seismic events. One site (LFM95-C1) is about 250 feet from the orebody that is currently being mined, and the other site (LFM95-C2) is about 100 feet from the orebody. Data collected at the two sites include: (1) opening closure, (2) long-term displacements in the rock around openings, and (3) transient response of the rock at opening surfaces due to the propagation of seismic waves. Figure 4-1 shows instrumentation layouts for the two sites. The two cross sections are as viewed facing the orebody. Five extensometers for long-term displacement measurement at each site were numbered clockwise with the first extensometer on the floor. Data collection from the three types of instruments started on December 19, 1990. Extensometer readings were monitored through the Center for Nuclear Waste Regulatory Analyses' (CNWRA) automatic data acquisition system and were collected at a 2.25 hour preset rate. Closure measurements were taken manually using tape extensometer every two weeks. Transient vibration-response data (velocity waveform data) were collected through the Bureau of Mines' seismic data acquisition system. For detailed discussion regarding field instrumentation please refer to the "Report on Research Activities for Calendar Year 1990," prepared by CNWRA (CNWRA, 1991).

Figures 4-2 to 4-11 show the results of the extensometer measurements. The data are presented in terms of Julian days from the beginning of 1991. The data for the first thirteen days (from December 19 to 31, 1990) are not included in the figures. These data are negligibly small compared to the ones shown in the figure. Position (Pos) Nos. 1 through 5 in each of the figures indicate the anchor positions for an individual extensometer with Pos No. 1 closest to and Pos No. 5 farthest from the opening. Displacements shown in the figures are measured relative to the assembly head of the extensometer, which is near the opening surface. The reported displacements are the results of mining activities and mining-induced events. Positive values indicate that an anchor and its corresponding assembly head move

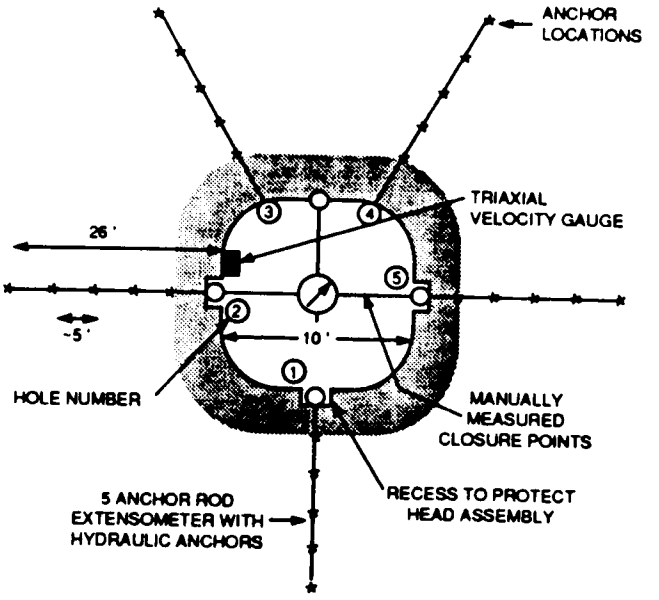

(a) LFM95-C1 Site

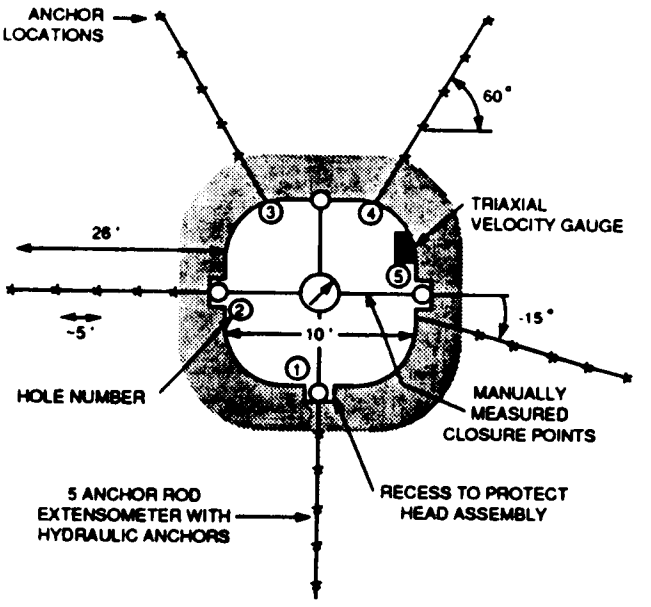

(b) LFM95-C2 Site

Figure 4-1. Instrumentation array for excavation response at the 5200 level, Lucky Friday Mine

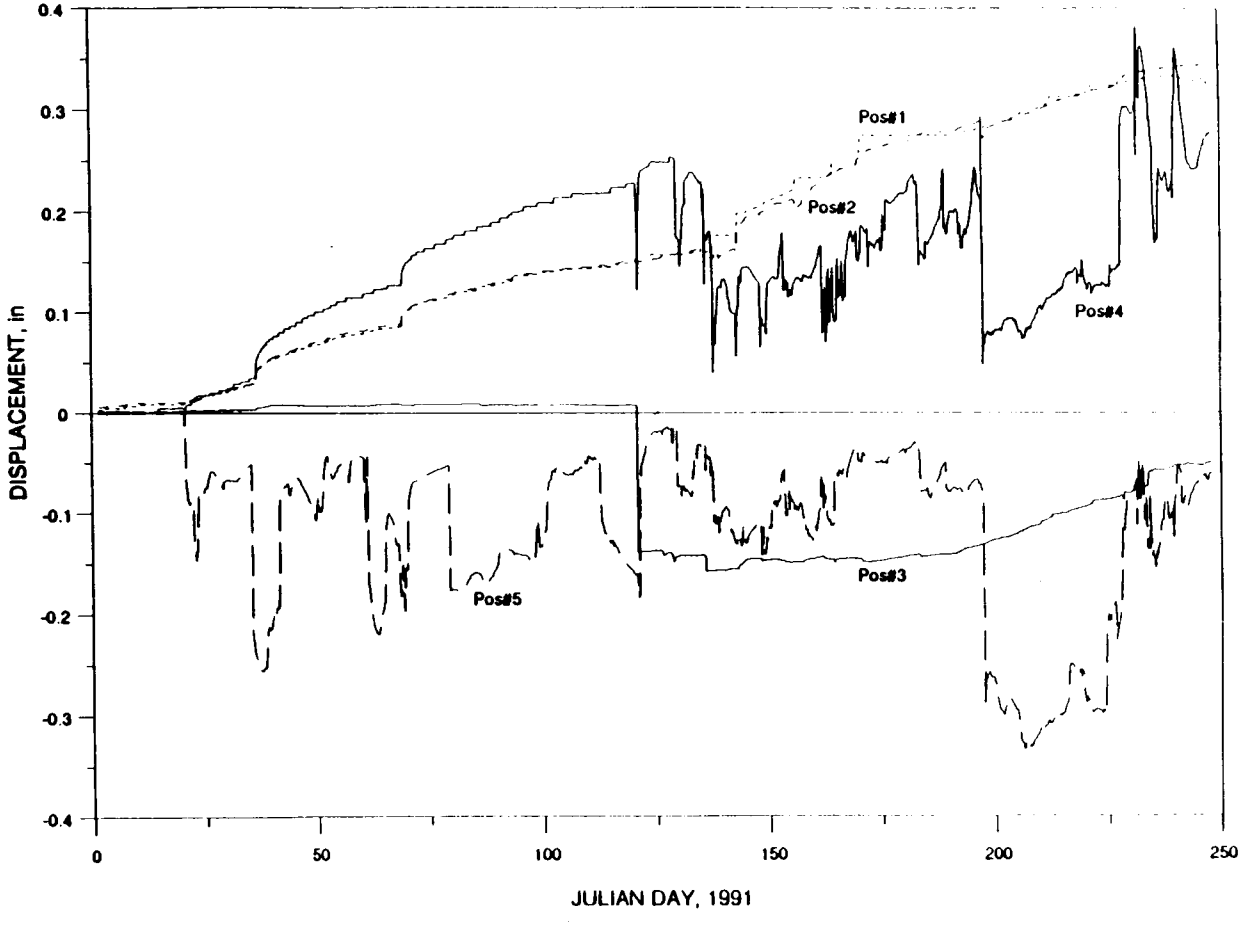

Figure 4-2. Relative anchor displacements from extensometer No. 1 at LFM95-C1 Site

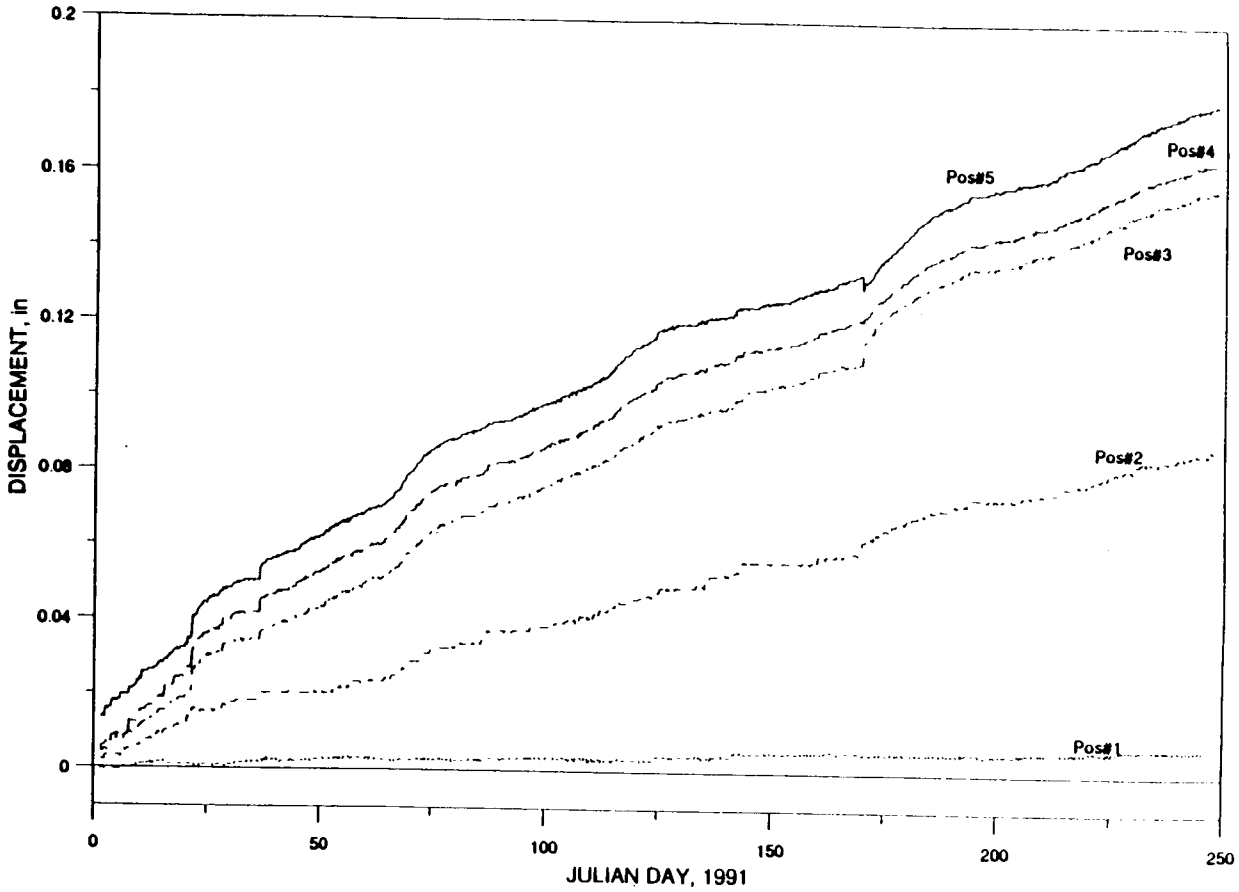

Figure 4-3. Relative anchor displacements from extensometer No. 2 at LFM95-C1 Site

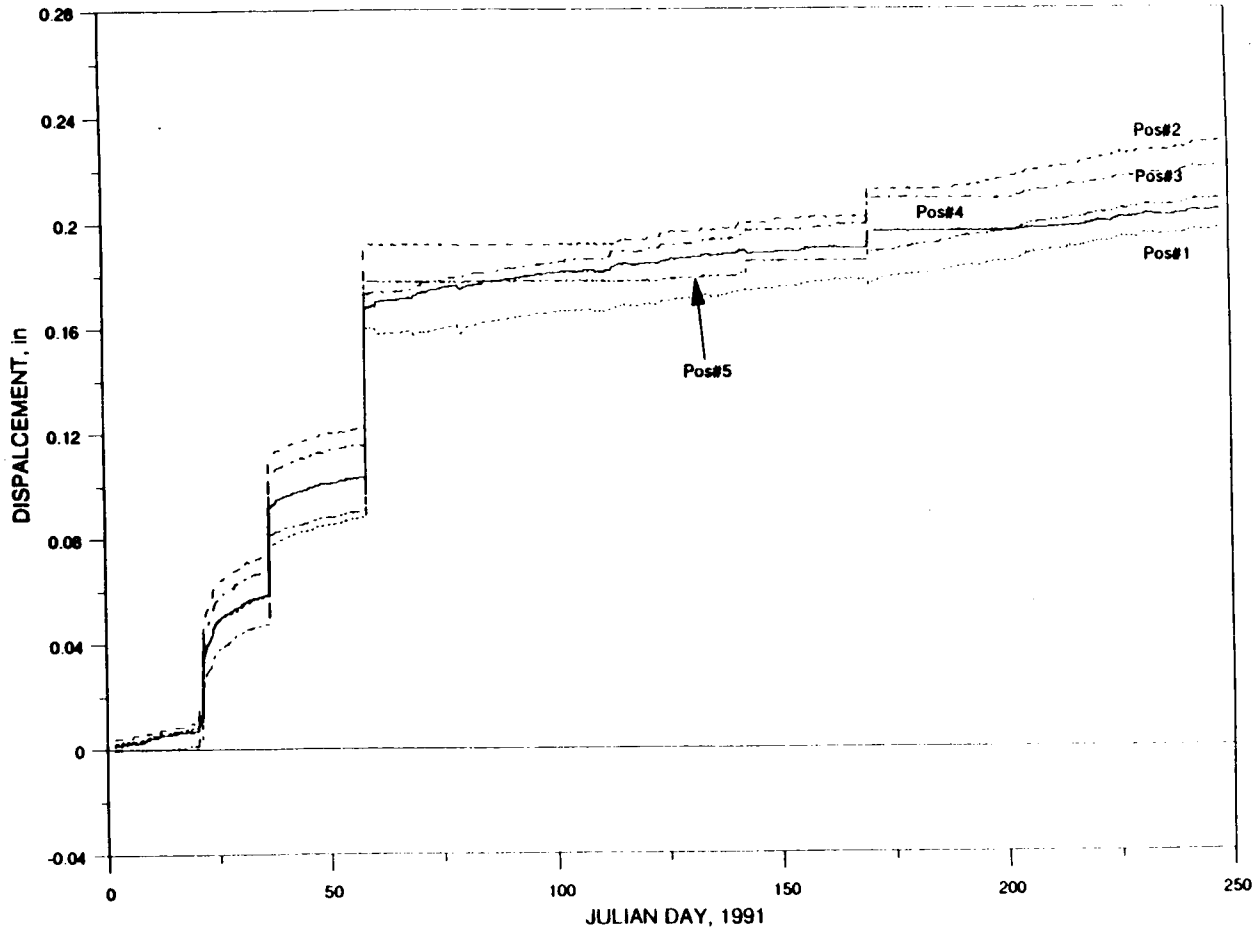

Figure 4-4. Relative anchor displacements from extensometer No. 3 at LFM95-C1 Site

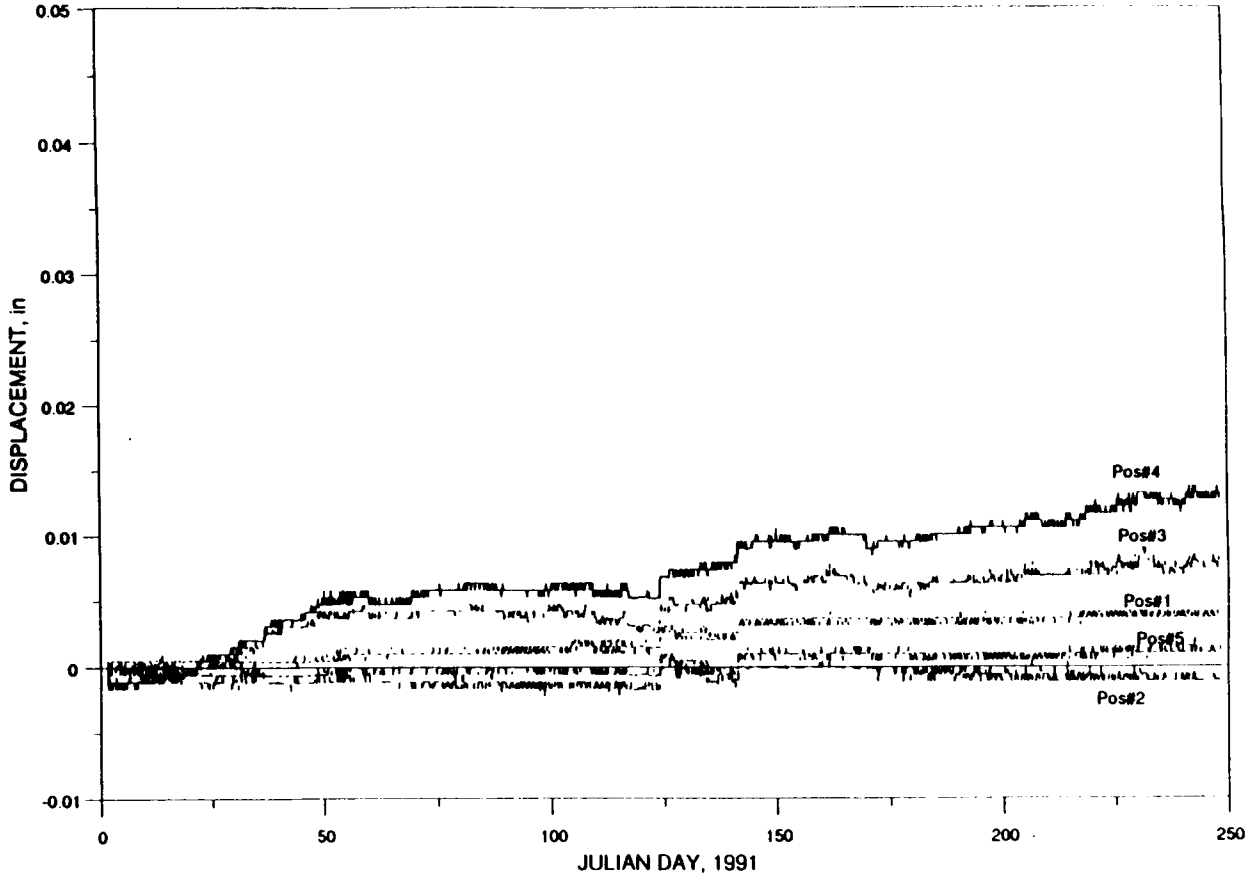

Figure 4-5. Relative anchor displacements from extensometer No. 4 at LFM95-C1 Site

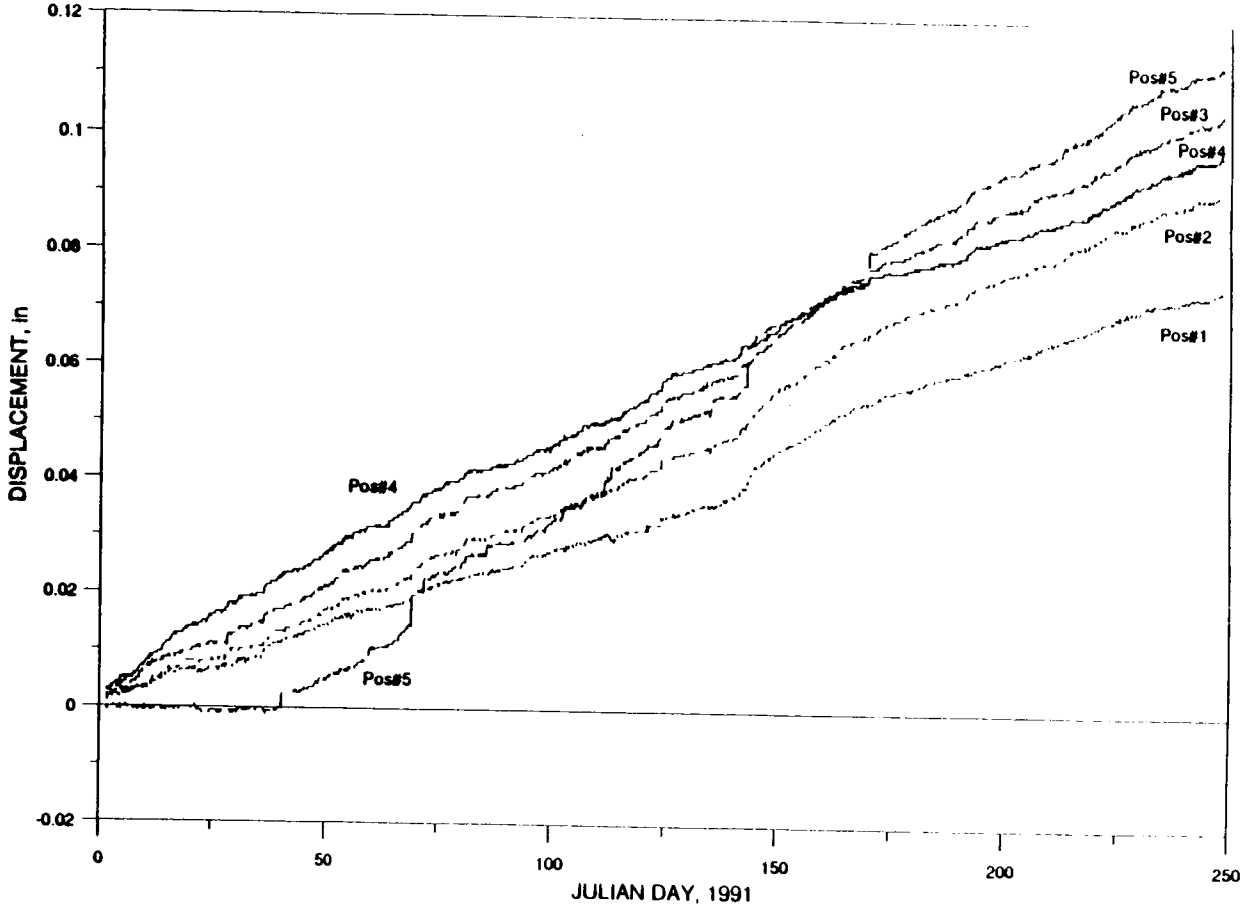

Figure 4-6. Relative anchor displacements from extensometer No. 5 at LFM95-C1 Site

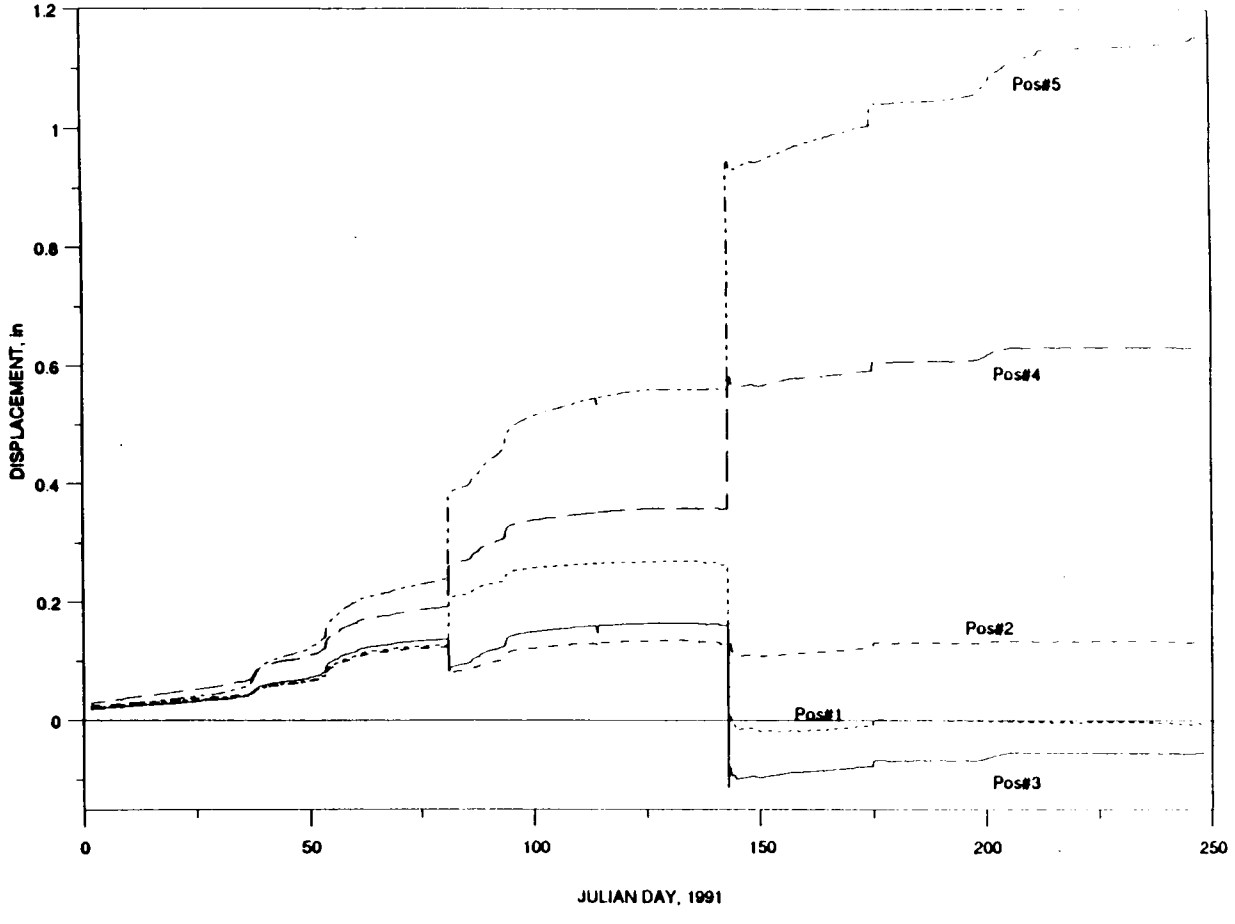

Figure 4-7. Relative anchor displacements from extensometer No. 1 at LFM93-C2 Site

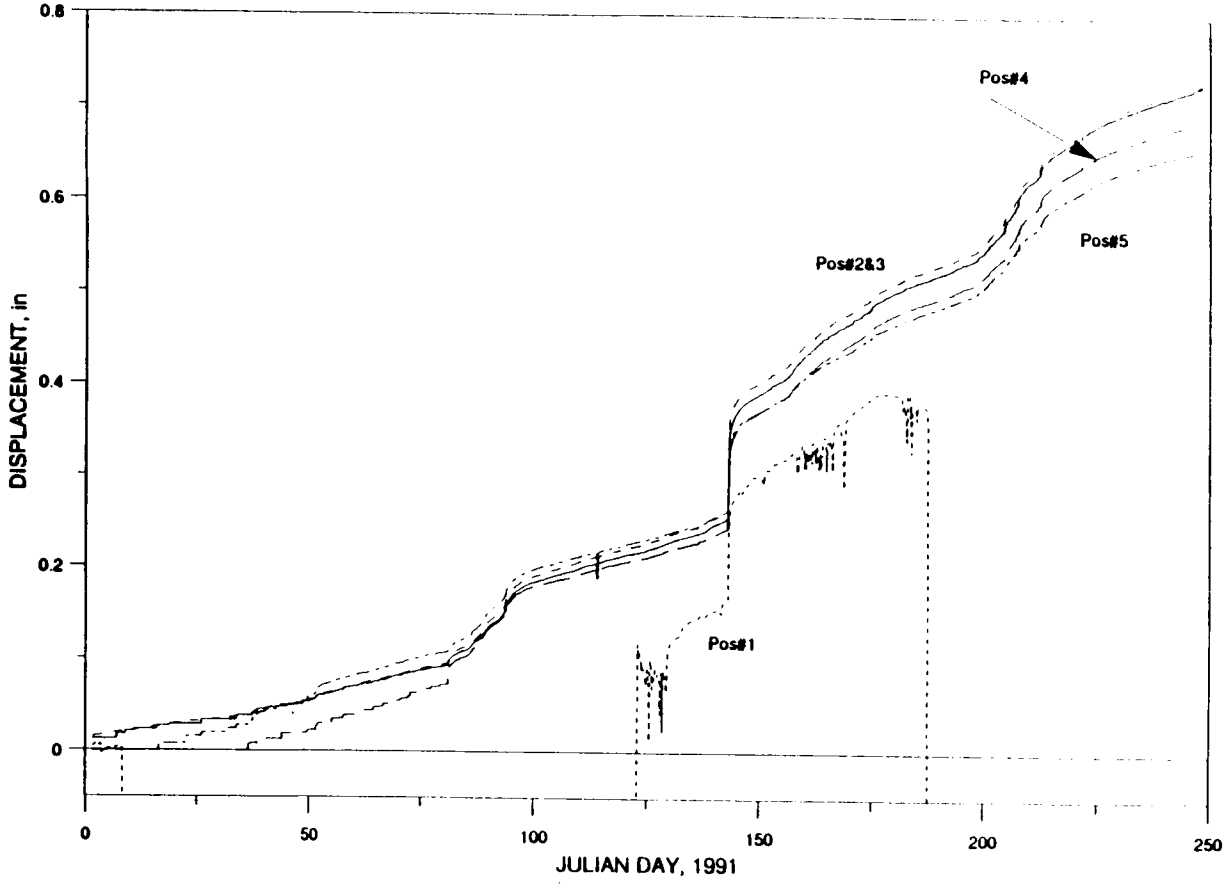

Figure 4-8. Relative anchor displacements from extensometer No. 2 at LFM95-C2 Site

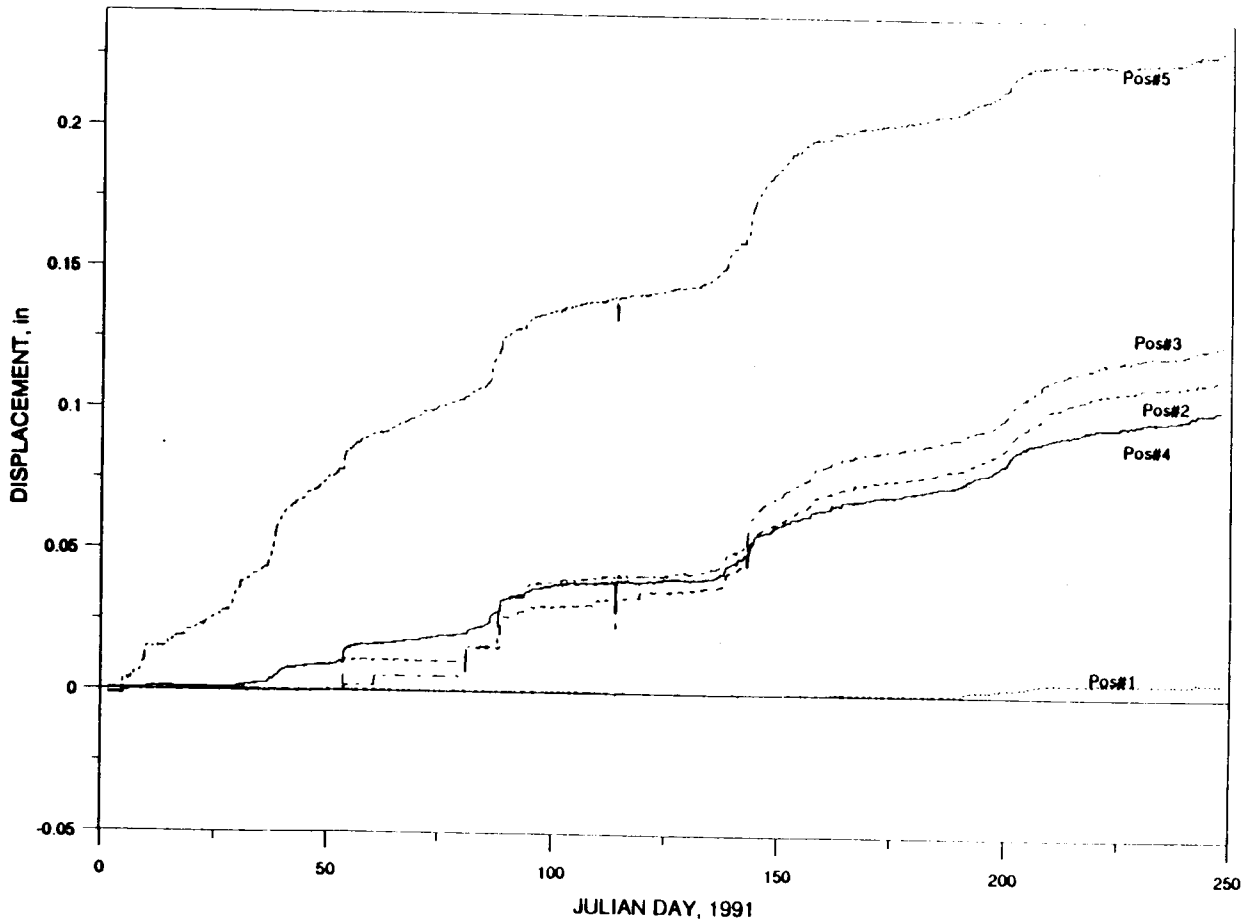

Figure 4-9. Relative anchor displacements from extensometer No. 3 at LFM95-C2 Site

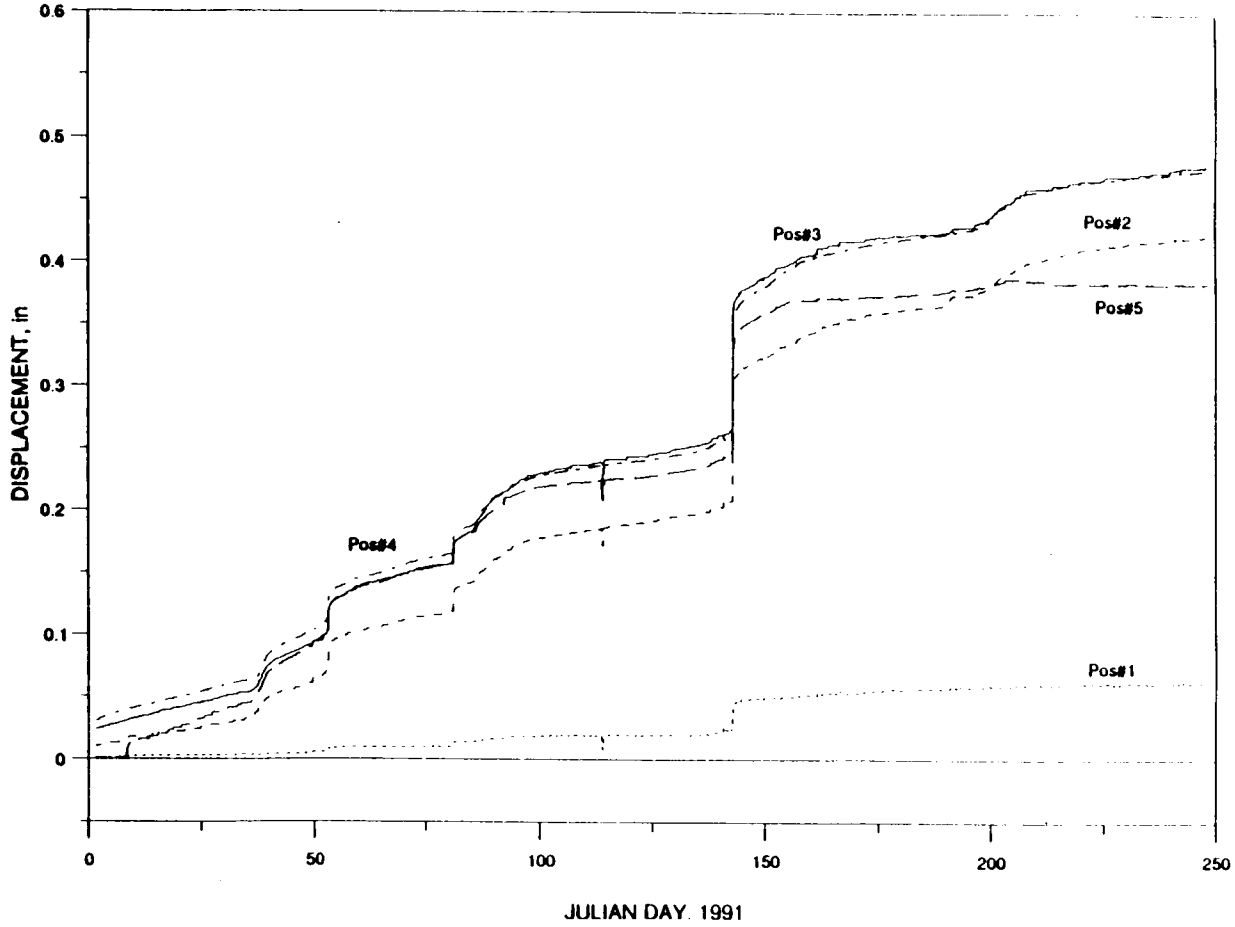

Figure 4-10. Relative anchor displacements from extensometer No. 4 at LFM95-C2 Site

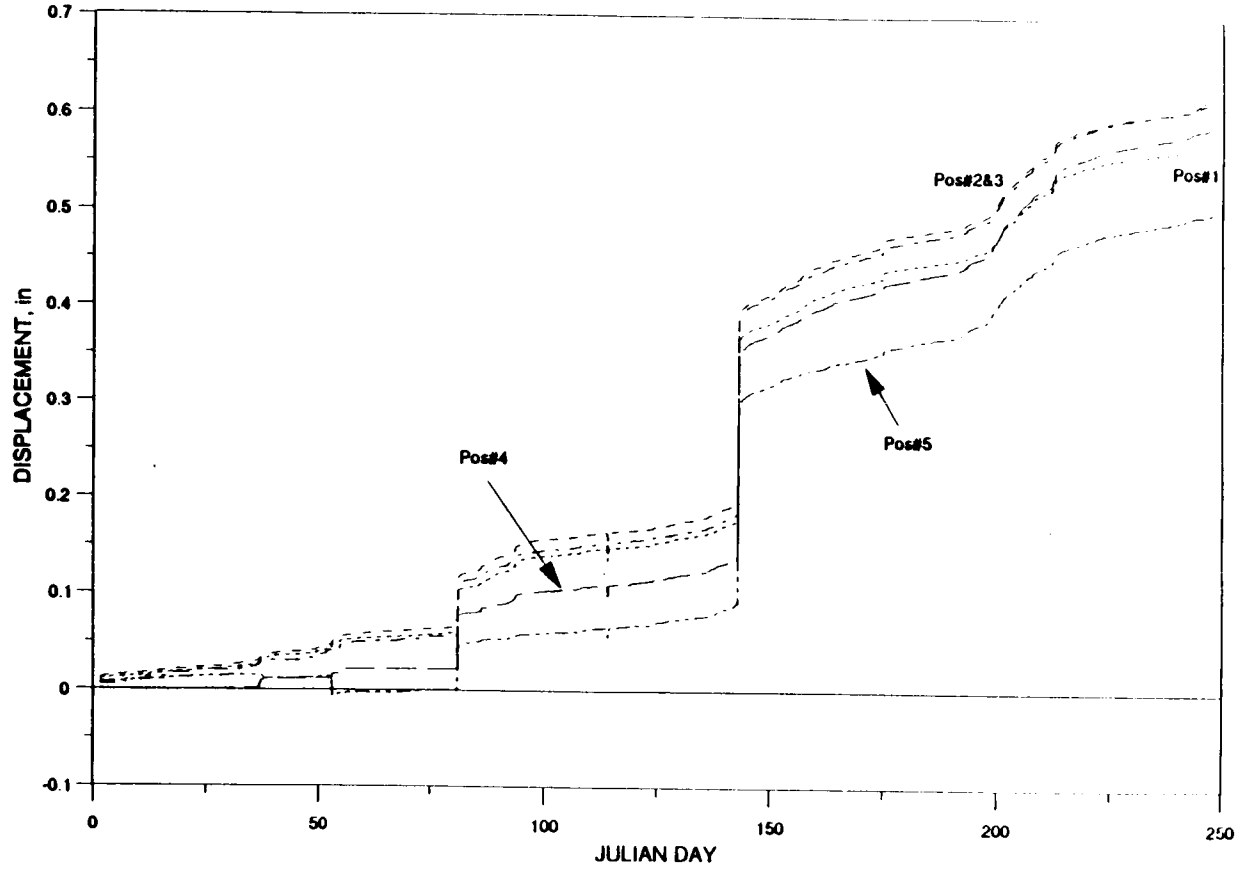

Figure 4-11. Relative anchor displacements from extensometer No. 5 at LFM95-C2 Site

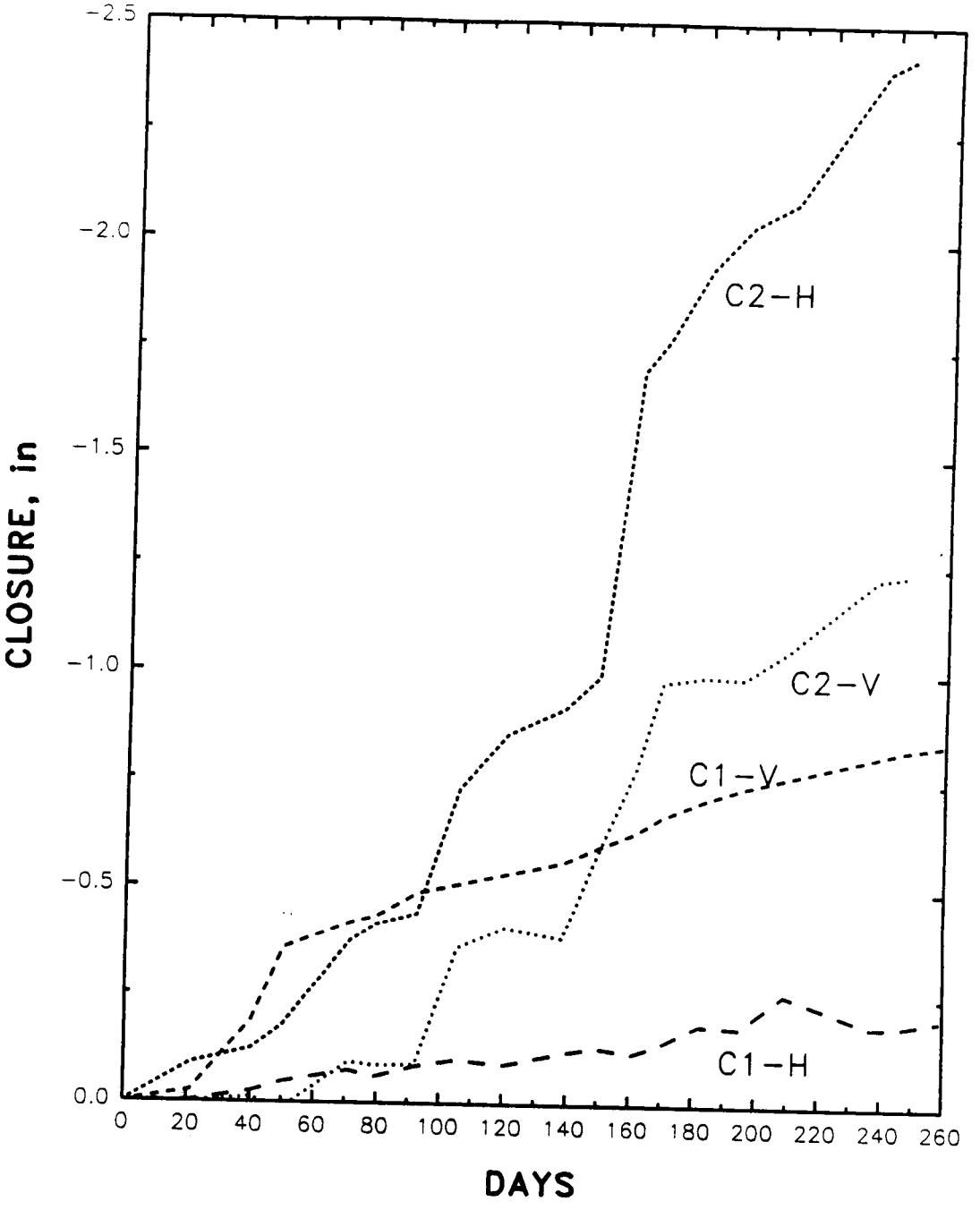

Figure 4-12. Closure measurements at both LFM95-C1 and LFM95-C2 sites (December 19, 1990, through September 4, 1991

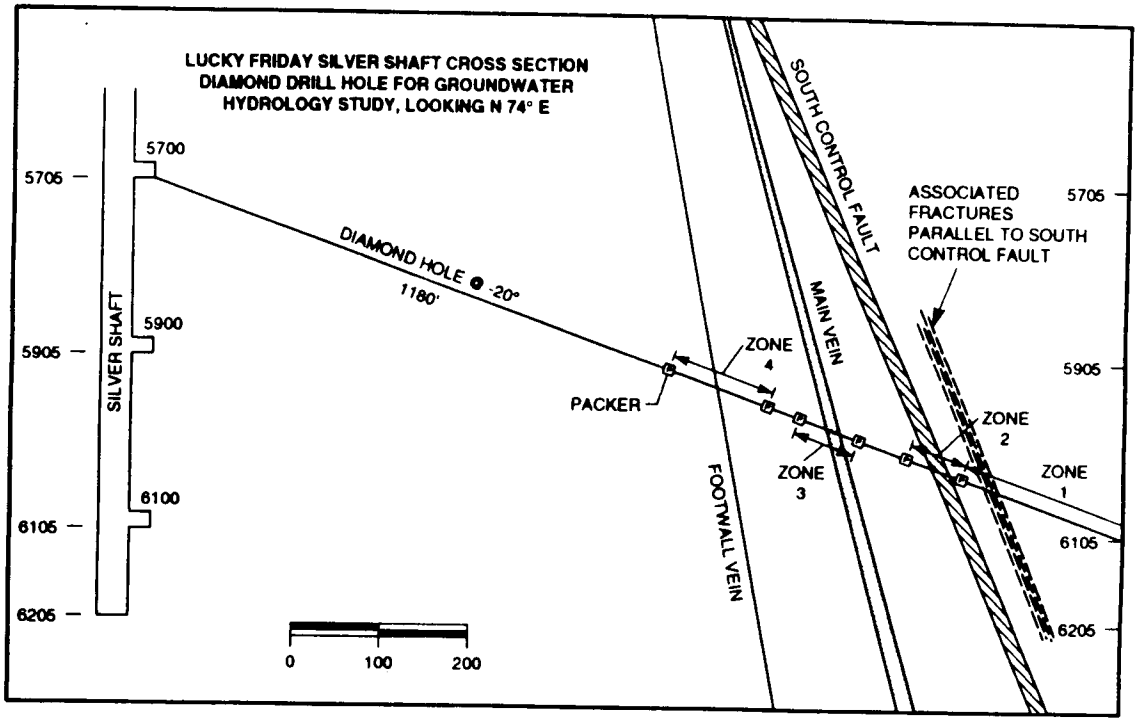

Figure 4-13. Packed-off zones for water-pressure monitoring

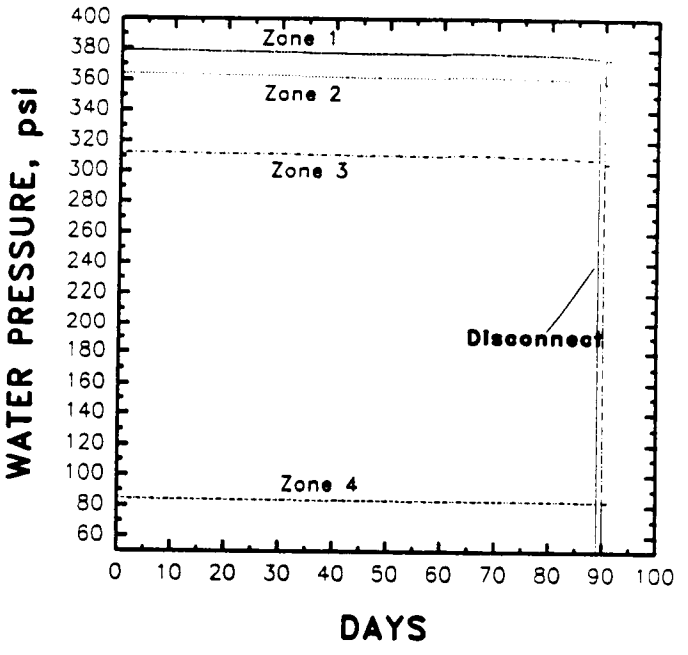

Figure 4-14. Measured water pressures at the four packed-off zones

away from each other while negative values mean that the two move toward each other. In general, the long-term displacements (both induced by mining and seismicity) around the opening at the LFM95-C1 site are smaller than those at the LFM95-C2 site. This observation is in agreement with the relative distances of the two sites from the orebody, since the LFM95-C2 site is about 150 feet closer to the orebody currently being mined than the LFM95-C1 site. Observations show that the LFM95-C1 site is relatively insensitive to seismic events induced by mining activities compared to the responses of the opening at the LFM95-C2 site. This, too, is judged to be differences in distance from the sources of the seismic events. In general, most step increases or decreases in displacements shown in Figures 4-2 to 4-11, but not all of them, are the responses of the rock around openings to seismic events (including rockbursts). For instance, two of the first three step-displacement increases in Figure 4-3 were results of backfilling of a nearby stope. The borehole used for backfilling was drilled very close to extensometer No. 3 at the LFM95-C1 site. Water and possibly some backfill materials from the backfill borehole caused the step increases in displacement. One step displacement increase associated with extensometer No. 1 at the LFM95-C2 site can not be related to any seismic event. Further, not all seismic events induced step-displacement increase responses. A related detail discussion will be presented in the future.

Figure 4-12 represents the closures of the mined openings for the two sites for the first 170-day measurement beginning from December 19, 1990. The legends C1-H and C1-V denote the horizontal and vertical closures at the LFM95-C1 site, respectively, and C2-H and C2-V are for closures at the LFM95-C2 site. For LFM95-C1, vertical closure dominates while horizontal closure is larger than the vertical one at the LFM95-C2 site.

4.2.2 Pore-Water Pressure Measurement

For pore-water measurement, four selected zones with geologic features such as faults, orebodies (veins), and fractures were identified in an NX-size borehole drilled at a location 5,700 feet below ground level with a 20-degree angle inclined downward. Each of the selected zones was packed off using a pair of packers. One piezometer was placed in each zone. Figure 4-13 indicates the cross-section view of the borehole showing the packed-off zones. Hydrologic (water pressure) data were collected using CNWRA's data acquisition system. Rate of collection was originally set at a 2.25-hour interval and was later changed to collect data every 60 seconds. Water-pressure monitoring started at the end of January, 1991. Pore-water pressure monitoring so far showed that seismic activities in Lucky Friday Mine did not cause any noticeable hydrologic water-pressure change. Figure 4-14 shows water pressures at the four zones for the first 90 days of monitoring. Water pressures measured in the following days are essentially the same as those presented in Figure 4-14. A sharp drop in water pressure at the right-hand side of the figure was due to disconnection of piezometer cables from the data acquisition system. Water pressures recorded after the cables were reconnected were essentially the same as those before disconnection.

4.3 REFERENCES

CNWRA. 1991. *Center for Nuclear Waste Regulatory Analyses Report (CNWRA) on Research Activities for Calendar Year 1990.* W. C. Patrick, ed. CNWRA 90-01A. San Antonio, Texas: CNWRA: 4-1 to 4-97.

5 INTEGRATED WASTE PACKAGE EXPERIMENTS

by Gustavo Cragnolino and Narasi Sridhar

Investigators: *Narasi Sridhar (CNWRA), Gustavo Cragnolino (CNWRA)*
Walter Machowski (SwRI), and Thomas Page (CNWRA)

5.1 TECHNICAL OBJECTIVES

The overall technical objectives of the Integrated Waste Package Experiments (IWPE) Project are as follows:

- Develop a good understanding of the information currently available on metal corrosion and on other metal degradation processes.
- Assess the current status of Yucca Mountain Project (YMP) Waste-Package Programs.
- Conduct waste-package experiments to scope and study the key parameters affecting long-term material performance.
- Assess experimentally YMP selected waste-package materials and designs and provide independent evaluation for reasonable assurance of long-term performance.
- Facilitate a continuous technical integration support to NRC and the CNWRA in the area of waste-package performance.

The objectives of the IWPE are planned to be accomplished under the following tasks, which are consistent with Revision 3 of the Project Plan:

- Task 1 - Corrosion, including Localized, Uniform, and Internal Corrosion
- Task 2 - Stress Corrosion Cracking
- Task 3 - Materials Stability
- Task 4 - Microbiologically Influenced Corrosion
- Task 5 - Other Degradation Modes
- Task 6 - Periodic Reporting

The current report focuses on work performed in Task 1. The experimental programs have been initiated in Tasks 2 and 3 in this reporting period.

5.2 TASK 1 - CORROSION OF CONTAINER MATERIALS

5.2.1 Short-term Experiments on CDA-715

In previous quarterly reports (Cragnolino, 1990, 1991a), the effect of environmental factors on the localized corrosion behavior of Fe-Ni-Cr-Mo alloys was presented. The main environmental factors examined were: chloride, nitrate, sulfate, fluoride, bicarbonate, and temperature. A statistical experimental design was used in which the localized corrosion behavior was determined by the cyclic, potentiodynamic, polarization technique. The copper-based alloys have been examined using the same short-term, electrochemical test technique. Of the three copper-based alloys currently under consideration as candidate container materials, attention was focused on CDA-715 (copper-30% nickel alloy) and CDA-102 (oxygen-free copper). The copper-aluminum bronze, CDA-613, is not currently regarded as the most desirable of the copper-based alloys because of its potential failure by thermal instability and de-alloying. Consequently, testingof this alloy was deferred.

The environmental factors that influence the corrosion mode of copper and copper-nickel alloys are quite different from those for Fe-Ni-Cr-Mo alloys (Cragnolino, 1991b). Traditionally, the localized corrosion in copper has been classified as Type 1 pitting, which is a shallow, wide pitting occurring in hard waters at low temperatures (about 25°C), and Type 2 pitting, which is narrow, deep pitting occurring in soft waters at relatively high temperatures (about 75°C). The environmental factors leading to one or the other type of pitting have not been well defined. Indeed, Shalaby et al. (Shalaby, 1989) found Type 1 pitting in relatively soft water at moderate temperatures (50°C). In the case of the classical Type 2 pitting, the environmental factors shown to be important are SO_4^{2-} (promoter of pitting) and HCO_3^- (inhibitor) (Mattson, 1968). Chloride was not an important factor in localized corrosion. The effects of HCO_3^- and Cl^- as sodium salts, and also that of temperature on the localized corrosion of copper were investigated more systematically by Thomas and Tiller (1972a, 1972b), who found that bicarbonate was an important factor in passivation and localized corrosion. Chloride solutions at high concentrations corroded copper uniformly. In contrast to the Fe-Ni-Cr-Mo alloys, increasing the temperature from 25°C to 90°C resulted in a decrease in localized corrosion of copper when tested in a solution containing only HCO_3^-. Thomas and Tiller did not perform reverse scan polarization, and hence did not evaluate the repassivation behavior of copper. They also did not study Cu-Ni alloys.

Beavers and Durr (Beavers, 1990) examined the effect of various anions including HCO_3^-, Cl^-, SO_4^{2-}, NO_3^- and F^-, and temperature on the breakdown and repassivation potentials of alloy CDA-715 using a statistical, experimental matrix. They found that HCO_3^- increased the breakdown potential, NO_3^- decreased it, and Cl^- did not have any significant effect. An increase in pH increased the breakdown potential. HCO_3^- also increased the repassivation potential while Cl^- and NO_3^- decreased it. Temperature in the range of 50-90°C did not have any effect on the breakdown and pitting potentials. They also noted that, in many solutions, large differences among breakdown and repassivation potentials occurred without concurrent development of

localized corrosion as observed visually. Their experimental matrix did not permit determination of interactions between the various environmental parameters.

Based on a literature survey (Cragnolino, 1991b) and some preliminary experiments, it was decided to test the copper-based alloys using a different environmental matrix than that used for the Fe-Ni-Cr-Mo alloys. Bicarbonate was included as one of the factors, and the range of bicarbonate concentration was increased. Similarly, the range of temperature was increased so that the classical Type 1 pitting could be reproduced at 25°C. The test technique used was the same as reported previously (Cragnolino, 1990). The solutions were prepared with sodium salts and contained a constant initial concentration of F^- (2 ppm) and NO_3^- (10 ppm). The solutions were deaerated by purging argon for 1 hour prior to the start of cases and throughout the test periods. The pH of the solutions was measured at room temperature before and after the test. The initial pH of all solutions was 8.4 with a standard deviation of 0.2, which is reasonably close to the predicted pH (8.14) for solutions in equilibrium with atmospheric CO_2 (Pabalan, 1990). The final pH after the test increased in all tests, but was more pronounced for the 95°C tests. In a previous report, the increase in pH for tests on alloy 825 conducted at 95°C related to the exsolution of CO_2 at the higher temperature (Pabalan, 1990). However, since an increase in pH was observed even for tests conducted at 30°C, it is unlikely to be due to exsolution of CO_2. Other factors that may raise the pH include deaeration by argon, which can lower the partial pressure of CO_2 in equilibrium with the solution, and cathodic reduction of water. The greater increase in pH for tests carried out on CDA-715 and 102 than for tests carried out on alloy 825 at 95°C may be a result of either greater cathodic currents or anodic reactions involving copper-carbonate complexes. The evolution of the pH during the tests will be investigated further. The bicarbonate concentration measurements were in reasonable agreement with the calculated additions (Cragnolino, 1991a). The samples were observed visually at the end of the test under a stereoscope.

5.2.2 Effect of Anionic Concentration

The results of the experiments on CDA-715 are shown in Table 5-1. The corrosion potential was not greatly affected by the variations in anionic species, but was more negative for the 95°C tests. Since the behavior of the copper-based alloys with varying environmental factors was more complex than that of the Fe-Ni-Cr-Mo alloys, simple characterization in terms of the extent of localized corrosion or critical potentials is inadequate. Hence, a more complete, albeit qualitative, description of the post-test sample surface is provided in Table 5-1. The potential at which a sudden increase in current is observed could not be associated uniquely with localized corrosion. Therefore, this potential is described as breakdown potential (E_{break}) rather than pitting potential. In some cases, the reverse scan did not produce any hysteresis or the current in the reverse scan was lower than that in the forward scan. Therefore, a repassivation potential could not be assigned to these tests and are so indicated in Table 5-1.

It can be seen from Table 5-1 that in environments containing 85 ppm HCO_3^-, the corrosion was mostly uniform and often associated with red, flaky film. Examples of

Table 5-1. RESULTS OF FACTORIAL EXPERIMENTS ON ALLOY CDA-715 (solutions contained 10 ppm NO_3^- and 2 ppm F^-)

Trial	HCO_3^- (ppm)	Cl^- (ppm)	SO_4^{2-} (ppm)	T (°C)	pH, 25°C		E_{corr} (mV_{SCE})	E_{break} (mV_{SCE})	E_{rp} (mV_{SCE})	Comments
					Initial	Final				
1	85	6	20	30	8.04	9.46	-229	56	56	U.C., brown film
2	8500	6	20	30	8.29	9.08	-230	831	799	U.C., Ni-color
3	85	1000	20	30	8.49	9.18	-261	NA*	NA	U.C., Ni-color
4	8500	1000	20	30	8.52	9.17	-280	845	13	L.C., green deposit
5	85	6	1000	30	8.54	9.24	-232	NA	NA	U.C., red film
6	8500	6	1000	30	8.34	9.25	-249	820	56	L.C., green deposit
7	85	1000	1000	30	8.05	9.24	-283	NA	NA	U.C., red film
8	8500	1000	1000	30	8.52	9.42	-259	506	26	L.C., green deposits
8R	8500	1000	1000	30	8.25	9.13	-237	678	54	L.C., green deposits
9	85	6	20	95	8.5	9.78	-299	198	-18	U.C., red film
10	8500	6	20	95	8.42	10.16	-427	602	530	No corrosion, dark brown stain
11	85	1000	20	95	8.15	9.78	-338	-29	-242	U.C., red film
12	8500	1000	20	95	8.41	9.87	-365	628	552	No corrosion, tarnished
13	85	6	1000	95	8.26	9.99	-343	74	-162	Shallow L.C.
14	8500	6	1000	95	8.43	-	-350	611	551	L.C. at crevice
15	85	1000	1000	95	-	10.02	-293	-24	-241	U.C., red film
16	8500	1000	1000	95	8.38	10.08	-425	612	525	Minor L.C., Ni-color

U.C.: Uniform Corrosion L.C.: Localized Corrosion

* Not applicable
** Was not measured

polarization curves for CDA-715 in 85 ppm HCO_3^- environment at 30°C and 95°C are shown in Figure 5-1. At 30°C, the polarization curves were typical of actively corroding metals exhibiting a rather monotonic increase in current density with potential with little hysteresis in the reverse scan. As noted in Table 5-1, these samples exhibited uniform corrosion with a weakly adherent red film, which may be Cu_2O. At 95°C, the polarization curves showed signs of active-passive transition and significant hysteresis in the reverse scan (Figure 5-1). This active-passive transition may be related to an adherent film/scale. However, except in one case, no localized corrosion was noted upon visual observation at 70X. One of the samples was immersed for about two minutes in 1M H_2SO_4 to remove the scale and was reexamined; no pitting was found. It must also be noted that the breakdown potentials in all the 85 ppm HCO_3^- solutions were rather low (-24 to 200 mV_{SCE}). Comparison of Trial 9 with Trials 11, 13, and 15, indicates that the addition of Cl^-, SO_4^{2-}, or both decreases the breakdown potential significantly, although no localized corrosion was observed visually. It is possible that

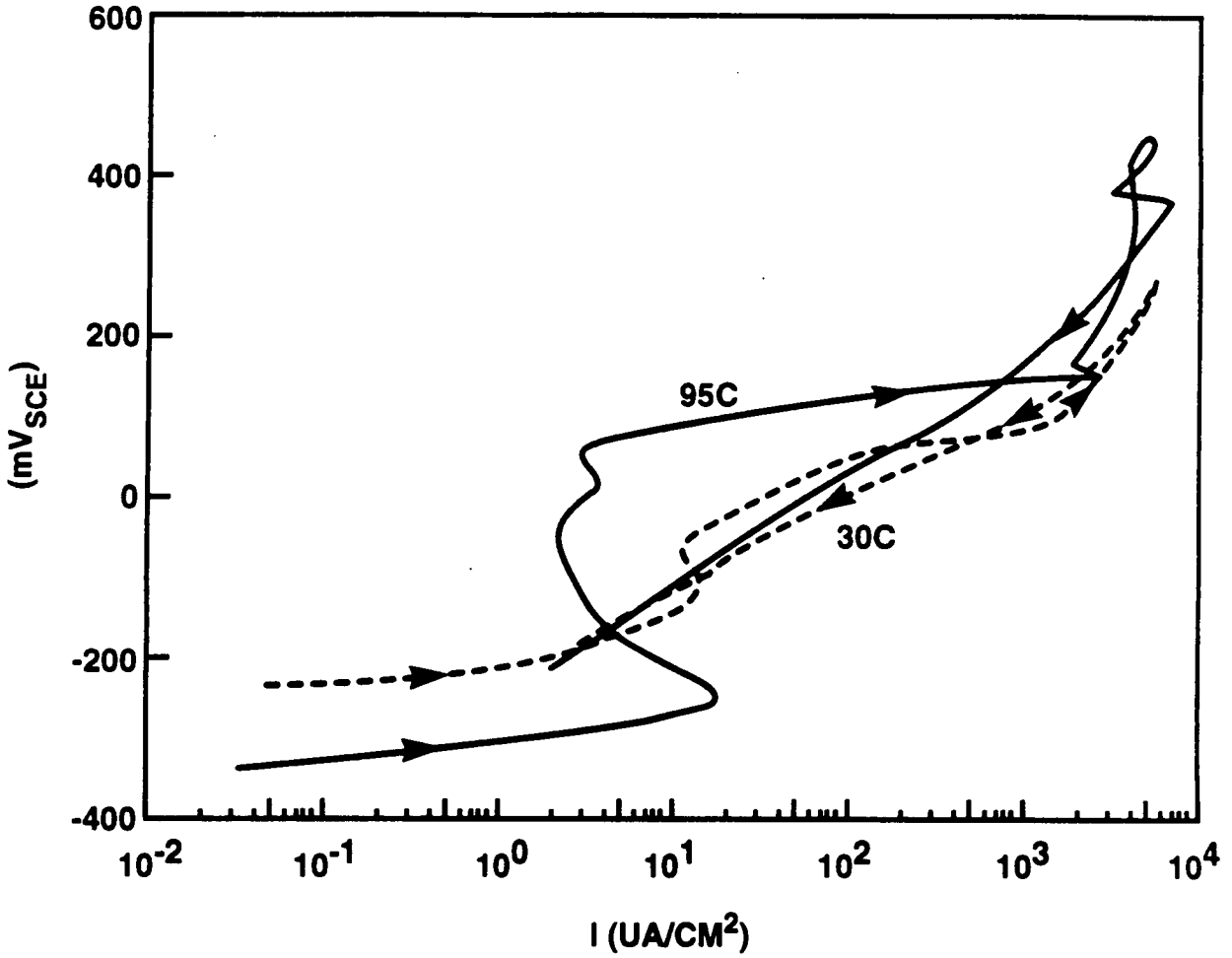

Figure 5-1. Effect of temperature on cyclic potentiodynamic polarization curves for CDA-715 in solutions containing: 85 ppm HCO_3^-, 6 ppm Cl^-, 1000 ppm SO_4^{2-}, 10 ppm NO_3^-, and 2 ppm F^-. Scan rate: 0.17 mV/sec.

microscopic pits (less than about 10 μm in diameter) escaped detection at a magnification of 70X. Selected samples will be examined in the scanning electron microscope during the next reporting period.

As shown in Table 5-1, the addition of 8500 ppm HCO_3^- resulted in a significant increase in passive current density range, with the breakdown potential increasing to greater than 600 mV_{SCE}. Correspondingly, the samples exhibited formation of a thin, surface film. Additionally, in tests conducted at 30°C, localized corrosion was observed to be covered by green deposits of corrosion product. However, when localized corrosion was not observed, as was the case at 95°C, the samples exhibited no coloration, indicating that the protective film was quite thin. The effect of the addition of Cl^- and SO_4^{2-} is shown in Figure 5-2 for tests conducted at 30°C. As shown, the addition of Cl^- and SO_4^{2-} decreased the repassivation potential but not the breakdown potential. However, when both Cl^- and SO_4^{2-} were added, the breakdown potential decreased significantly. In all these cases, considerable localized corrosion was observed, which was overlaid by mounds of green deposit covering a loose, red deposit. This appearance of localized corrosion is similar to that of Type 1 pitting reported for copper (Campbell, 1974).

5.2.3 Effect of Temperature

Because localized corrosion occurred to a greater extent at 30°C than at 95°C in the solutions containing 8500 ppm HCO_3^-, tests at intermediate temperatures were conducted. The effect of temperature on localized corrosion of CDA-715 in the 8500 ppm HCO_3^- solution is shown in Table 5-2. As shown, an increase in temperature from 40 to 80°C resulted in a progressive decrease in the extent of localized corrosion until about 80°C, beyond which only minor localized corrosion was observed. Also shown is that the increase in temperature resulted in an increase in breakdown potential with a maximum at 60°C. The increase in breakdown potential with increasing temperature was observed by Thomas and Tiller for pure copper (Thomas, 1972b) only in pure 0.01M bicarbonate solutions, whereas a decrease in breakdown potential was observed by them in 0.01M bicarbonate solutions containing 0.01M chloride. Increasing the temperature did not result in any significant change in repassivation potential up to 80°C. Beyond this temperature, a significant increase in repassivation potential increased by almost an order of magnitude. At all the temperatures, the localized corrosion was similar to Type 1 pitting. It must be emphasized that these are observations arising from short-term tests, and long-term tests may result in a more uniform type of corrosion (Thomas, 1972a).

5.2.4 Discussion

There is a dearth of information on the effect of environmental factors relevant to the proposed repository site at Yucca Mountain on the localized corrosion behavior of Cu-Ni alloys such as CDA-715. In the current project, selected anionic species present in the groundwater in the vicinity of the proposed site were evaluated over a broad range of concentrations. The concentration of species such as HCO_3^- under conditions of evaporation or in crevices is not known. However, the current investigation suggests that localized corrosion

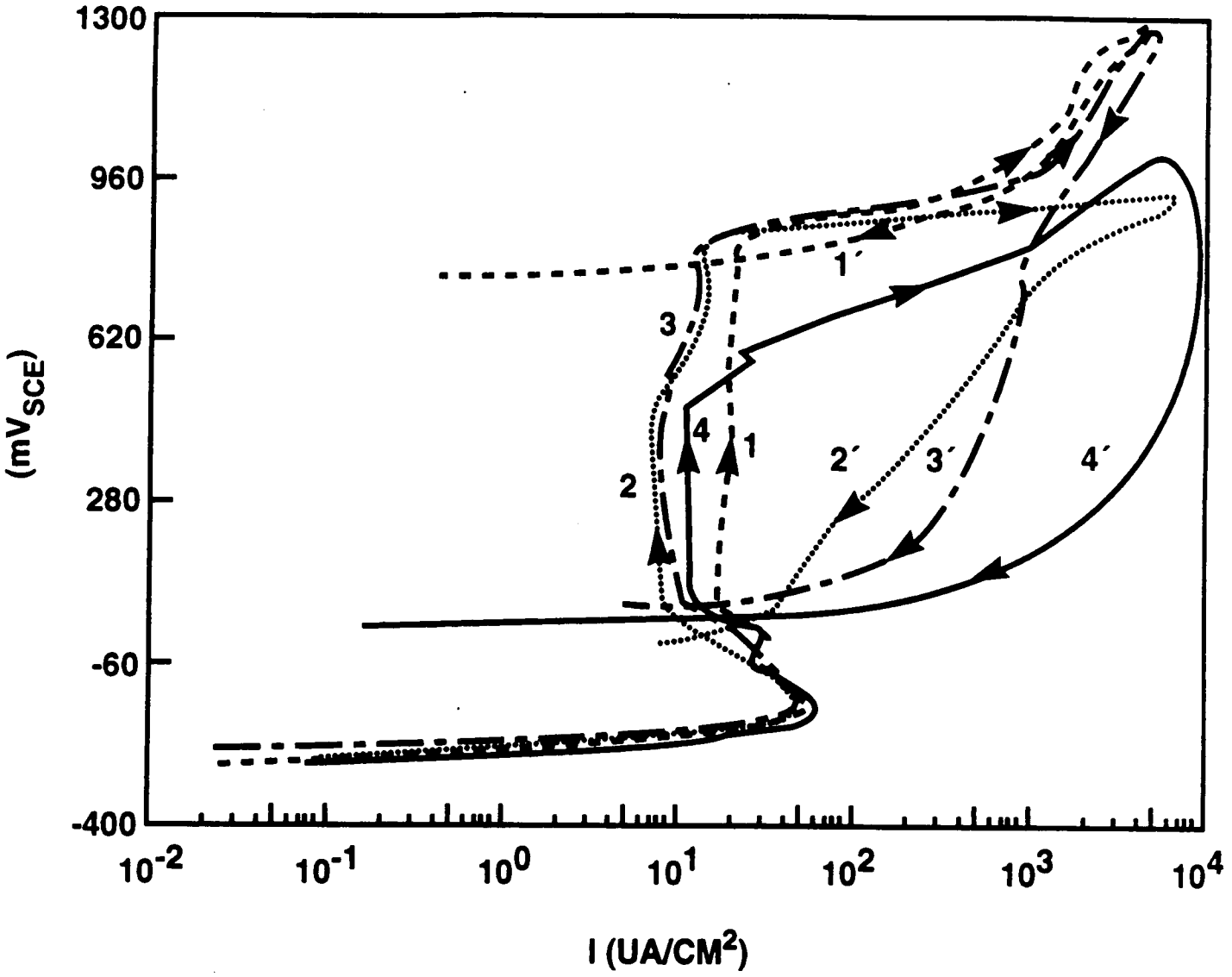

Figure 5-2. Effect of addition of Cl^- and SO_4^{2-} to a solution containing 8500 ppm HCO_3^-, 10 ppm NO_3^-, and 2 ppm F^- at 30°C on polarization behavior of CDA-715. Curve 1 and 1': no addition; curve 2 and 2': + 1000 ppm Cl^-; curve 3 and 3': + 1000 ppm SO_4^{2-}; and curve 4 and 4': 1000 ppm Cl^- + 1000 ppm SO_4^{2-}.

Table 5-2. EFFECT OF TEMPERATURE ON ELECTRO-CHEMICAL PARAMETERS OF ALLOY CDA-715 (Solution: 8500 ppm $HCO3^-$ + 1000 ppm SO_4^{2-} + 10 ppm NO_3^- + 2 ppm F^-)

T (°C)	E_{corr} (mV_{SCE})	E_{break} (mV_{SCE})	E_{rp} (mV_{SCE})	Comments
30	-259	506	26	Localized corrosion, green deposit
40	-266	499	38	Localized corrosion, green deposit
60	-279	718	49	Minor localized corrosion, green deposit
80	-331	602	58	Minor localized corrosion
95	-425	612	525	Minor localized corrosion

is of concern mainly in the high HCO_3^- environments in the presence of Cl^- and SO_4^{2-} at low temperatures. This finding compares at least qualitatively with that of Thomas and Tiller for copper (Thomas, 1972a, 1972b). The results of Beavers and Durr (Beavers, 1990) did not indicate any effect of temperature. This is because the fractional factorial matrix used by them did not permit evaluation of any interactions among the factors evaluated. Additionally, because they used SO_4^{2-} to balance the stoichiometry, the effect of this anion is difficult to quantify.

During the present investigation, no change occurred in the type of localized corrosion observed at various temperatures. While most experimental studies and modeling of the corrosion of copper containers have concentrated on the uniform corrosion behavior of this material, the current experimental results point to the need to better understand the localized corrosion behavior of these alloys. The critical question raised by the current investigation is the long-term growth rate of the Type 1 pits in the high HCO_3^--containing environments. Additional questions that must be answered by short-term and long-term experiments are the critical concentrations of HCO_3^-, Cl^-, and SO_4^{2-} required for the initiation of localized corrosion.

5.3 SUMMARY

A full-factorial experimental design was used to study the effects of environmental factors on the localized corrosion of Cu-30%Ni (CDA-715) alloy. The short-term, electrochemical tests conducted thus far indicate that:

(1) Localized corrosion did not occur in environments containing low concentrations of HCO_3^- (85 ppm). The electrochemical response was indicative of active corrosion at 30°C and an active-passive behavior at 95°C. However, no

significant localized corrosion was observed at either of these temperatures. The hysteresis in the polarization curves did not correlate with the observed lack of localized corrosion.

(2) An increase in HCO_3^- concentration from 85 to 8500 ppm increased the passive range of the alloy both at 30°C and 95°C. A four-way interaction between HCO_3^-, temperature, Cl^-, and SO_4^{2-} was observed qualitatively. The addition of Cl^- and SO_4^{2-} resulted in a decrease in repassivation potential and a greater incidence of pitting only at 30°C, but not at 95°C. Simultaneous presence of Cl^- and SO_4^{2-} decreased both the breakdown and repassivation potential. The observed hysteresis in the polarization curves correlated reasonably well with the observed localized corrosion in the 8500 ppm HCO_3^- solutions.

(3) In a solution containing 8500 ppm HCO_3^-, 1000 ppm Cl^-, and 1000 ppm SO_4^{2-}, localized corrosion was observed at temperatures up to 80°C, but not at 95°C. The hysteresis in the polarization curves in this environment correlated well with the observed localized corrosion.

5.4 REFERENCES

Beavers, J. A., and C. L. Durr. 1990. *Container Corrosion in High-level Waste Repositories*. NRC Contract No. NRC-04-87-009. Year 3, First Semi-Annual Report. September 1989-February 1990. Columbus, Ohio: Cortest Columbus.

Campbell, H. S. 1974. A Review: Pitting Corrosion of Copper and Its Alloys. *Localized Corrosion*. R. W. Staehle et al., eds. Houston, Texas: NACE: 625-638.

Cragnolino, G. A., and N. Sridhar. 1990. Integrated waste-package experiments. *Report on Research Activities for the Quarter July 1 through September 30, 1990.* W. C. Patrick, ed. CNWRA 90-03Q. San Antonio, Texas: CNWRA.

Cragnolino, G. A., and N. Sridhar. 1991a. Integrated waste package experiments. *Report on Research Activities for the Quarter April 1 through June 30, 1991.* W. C. Patrick, ed. CNWRA 91-02Q. San Antonio, Texas: CNWRA.

Cragnolino, G. A., and N. Sridhar. 1991b. *A Review of Localized Corrosion of High-level Nuclear Waste Container Materials - I.* CNWRA 91-004, San Antonio, Texas: CNWRA.

Pabalan, R. T., and W. M. Murphy. 1990. Unsaturated mass transport (Geochemistry). *Report on Research Activities for the Quarter July 1 through September 30, 1990.* W. C. Patrick, ed. CNWRA 90-03Q. San Antonio, Texas: CNWRA.

Shalaby, H. M., F. M. Al-Kharafi, and V. K. Gouda. 1989. A morphological study of pitting corrosion of copper in soft tap water. *Corrosion*. 45: 536-547.

Thomas, J. G. N., and A. K. Tiller. 1972a. Formation and breakdown of surface films on copper in sodium hydrogen carbonate and sodium chloride solutions - effects of anion concentrations. *British Corrosion J.* 7: 256-262.

Thomas, J. G. N., and A. K. Tiller. 1972b. Formation and breakdown of surface films on copper in sodium hydrogen carbonate and sodium chloride solutions - effects of temperature and pH. *British Corrosion J.* 7: 263-267.

6 STOCHASTIC ANALYSIS OF UNSATURATED FLOW AND TRANSPORT

by Rachid Ababou, Gordon Wittmeyer, and Budhi Sagar

Investigators: ***Rachid Ababou (CNWRA), Budhi Sagar (CNWRA), and Gordon Wittmeyer (CNWRA)***

6.1 TECHNICAL OBJECTIVES

The objectives of this project are the following:

- Review the literature on theoretical and experimental approaches, and assess the status of available data in relation to simulation needs;
- Select a global approach for stochastic modeling of large-scale flow and transport in naturally heterogeneous unsaturated fractured rock;
- Develop submodels, analyze simplified separate effects, and incorporate these submodels and analyses into the global modeling approach;
- Implement large-scale flow and radionuclide transport simulations under realistic conditions, and interpret the results using statistical analysis and other tools; and
- Develop interactions with related and pertinent activities at the CNWRA and from outside the CNWRA towards the validation of flow and transport models for the proposed Yucca Mountain repository.

The work described in this section relates to the fifth objective stated above. Since the Performance Assessment Research Project has a task with a similar objective, this work was performed in cooperation with that project. This chapter summarizes work reported by Ababou and Sagar (1991).

6.2 INTRODUCTION

The need to ensure the quality of predictions obtained from flow and transport models used to assess the performance of the proposed high-level radioactive repository at Yucca Mountain, Nevada, requires the development of concise working definitions of model consistency and validity which can be both readily applied by modelers and easily understood by those persons responsible for reviewing the license application. Owing to the differing degree of spatial variability of the geologic setting, hydrologic regime and geochemistry, multitude of near-field processes which must be studied, and relatively large spatial and temporal scales characteristic of the radioactive waste disposal problem, the predictive models to be used may vary considerably in their degree of complexity. Thus type of model validation strategy must

be consistent with the nature of the physical processes modeled and with the specific question that the results of the model will be used to resolve.

Specific methods were developed for assessing model complexity, measuring model consistency, and testing model validity for the case of water flow in unsaturated porous media. The following discussion addresses several aspects of unsaturated flow-model testing, including numerical formulation; internal consistency; intercomparison of models; in-situ experiments; performance measures; and underlying concepts of probabilistic induction, and parameter estimation. These aspects of testing may be used to select appropriate experimental tests and evaluate the degree to which the model is validated or refuted.

6.3 UNSATURATED FLOW EQUATIONS

In the following subsection the fundamental governing equations which describe the flow of water in unsaturated porous media are briefly outlined. The governing equations are themselves simply models of the physical processes of interest and should be carefully scrutinized for their validity or applicability to a specific physical situation.

The fundamental equation that describes water flow in saturated porous media was empirically derived by Henri Darcy in 1856. Darcy's law, which proposes a linear relationship between the flux of water and the mean hydraulic gradient, may also be derived directly by averaging the Navier-Stokes equation over assemblages of capillary tubes or fracture networks (Bear 1972). The Darcy equation was extended by Buckingham (1907) and Richards (1931) to the case of unsaturated flow, assuming that the movement of the air phase has no effect on liquid flow and that air is freely connected to the atmosphere. The generalized Darcy-Buckingham equation for isotropic porous media takes the form:

$$\vec{q} = -K(h)\vec{\nabla}(h+z) \tag{6-1}$$

where $h = P/\rho g$ is the water pressure head relative to atmosphere air pressure, $h+z = H$ is hydraulic head, z is vertical upwards, and K(h) is the unsaturated hydraulic conductivity. For convenience, K(h) is generally decomposed as follows:

$$K = K(h) = K_s \cdot K_r(h) \tag{6-2}$$

where K_s is saturated hydraulic conductivity and $K_r(h)$ denotes the "relative" unsaturated conductivity function. Since $0 \leq K(h) \leq K_s$, it follows that $0 \leq K_r \leq 1$. Conservation of mass requires that the rate of decrease of moisture content per unit volume of porous medium equal the divergence of the flux. Assuming the density of water remains constant, the equation of mass conservation reduces to

$$\frac{\partial\theta}{\partial t} = -\vec{\nabla} \cdot \vec{q} = +\vec{\nabla}(K(h)\vec{\nabla}(h+z)) \quad . \tag{6-3}$$

Since Eqn. (6-3) two unknowns (volumetric water content Θ, and pressure head h) a second constitutive relation is needed for moisture content as a function of pressure:

$$\theta = \theta(h) = \theta_r+(\theta_s-\theta_r)S(h) \quad . \tag{6-4}$$

In this equation, θ represents the volumetric moisture content (volume of water per volume of medium), θ_s is the saturated water content (which is equivalent to porosity), θ_r is the residual water content, and S represents the degree of saturation. The specific moisture capacity,

$$C(h) = \frac{\partial\theta}{\partial h} \quad , \tag{6-5}$$

can then be used to convert Eqn. (6-3) to the head-based Richards equation:

$$C(h)\frac{\partial h}{\partial t} = \vec{\nabla}(K(h)\vec{\nabla}(h+z)) \quad . \tag{6-6}$$

The mixed-form Eqn. (6-3) may be preferable for modeling purposes, however, as it is more directly expressed in mass-conservation form.

The Darcy-Buckingham-Richards equations described above model variably saturated flow in porous media in a *generic fashion*. This model has been extensively tested under a variety of conditions, usually based on centimeter to decimeter scale measurement of volumetric water content and thermodynamic water potential ("pressure"). The basic postulates of the local Darcy-Buckingham-Richards model are as follows:

- Porous medium can be represented as a continuum, in terms of macroscopic variables such as areal flux density (specific discharge rate), water potential (pressure), volumetric water content, and porosity - all defined over scales much larger than the scales of the largest voids (much larger than pore-scale).

- Air phase is well connected throughout the unsaturated domain and is stationary.

- Specific discharge rate, $\vec{q}$, is related to the gradient of total hydraulic potential in a quasi-linear fashion, such that the coefficient of proportionality (hydraulic conductivity) depends on the state variable (pressure) but not on specific discharge rate, or on hydraulic gradient (Darcy-Buckingham). In addition, it is

also assumed that water content depends on the state variable (pressure), but not on specific discharge rate or on hydraulic gradient.

While the latter postulate of a quasi-linear relation between specific flux and hydraulic gradient is quite general, only specialized versions have been tested experimentally. The simplest formulation of the Darcy-Buckingham-Richards model is that given above. This special formulation is *local* in space, *nonhysteretic*, and *isotropic*:

- *Locality*: The local hydraulic conductivity at a given point depends only on local macroscopic variables, such as water pressure or water content, not on the values of these variables at other points in space.

- *Nonhysteresic*: The local hydraulic conductivity at a given point in time depends only on the value of local variables at the same point in time, not on their rate of change at the same point in time (rate-dependence), and not on their past values (memory).

- *Isotropy*: The local hydraulic conductivity at a given point in space is invariant under rotations of the coordinate system attached to the porous medium at that point.

The locality assumption is key to the application of Darcy-Buckingham model. Hysteresis has been frequently observed, and auxiliary models have been proposed to express the dependence of hydraulic conductivity and moisture content on the past history of wetting and drying observed (scanning curves). Finally, in the case of anisotropic media, the unsaturated conductivity function is expected to be generally direction-dependent. A simple extension of the Darcy-Buckingham Eqn. (6-1), assuming that hydraulic conductivity is a pressure-dependent tensor, is

$$\vec{q} = -\overline{\overline{K}}(h) \cdot \vec{\nabla}(h+z) \ . \qquad (6\text{-}7)$$

However, this may be too restrictive. Other types of orientation-dependent conductivity functions may be more realistic. Consider for instance the case where K_s depends on the orientation of hydraulic gradient, and $K_r(h)$ is a directional functional of h. If K_s and $K_r(h)$ are second-rank tensors, then $K(h) = K_s K_r(h)$ will not necessarily be a second-rank tensor. One possible point of view is that K(h) is approximately a second-rank tensor as well as $K_s = K(0)$. Adopting this point of view precludes the use of a tensor for *relative* conductivity.

Several functional forms have been proposed in the literature for isotropic K(h) and S(h), some based on semiempirical models of unsaturated flow through idealized granular and porous media. Commonly used functional forms include the exponential Gardner model for K(h), the Burdine and Mualem functional models for $K(\theta)$ and K(h), the van Genuchten model for $\theta(h)$, the Brooks-Corey model for $\theta(h)$, and combinations of van Genuchten and Brooks-Corey with the Mualem functional model. See Ababou (1991a) for a review.

6.4 SPACIALLY DISTRIBUTED MODELS

6.4.1 Local and Spatially Distributed Models

The Darcy-Buckingham-Richards model applies locally and is space-independent with respect to macroscopic variables and coefficients. Methods have been developed to measure water pressure, moisture content, flux, and hydraulic conductivity. Local measurements have been used to test the validity and limitations of the model, and to characterize the functional form of constitutive relations such as conductivity and saturation versus pressure. To investigate natural flow systems at scales much larger than the scale of measurement, however, the generic constitutive model must be incorporated into a more specific model capable of representing or simulating spatially distributed flow processes for a given site under prescribed boundary conditions.

Spatially distributed models are obtained by allowing the local constitutive relations K(h) and $\Theta(h)$ to vary in space, by defining the geometry and size of the domain of interest, and by prescribing spatially distributed initial and boundary values of state variables.

6.4.2 Spatially Distributed Modeling and Degrees of Freedom

Spatially distributed models differ greatly by the degree of freedom allowed for flow pathways, depending on assumed spatial dimensionality, degree of detail of material heterogeneity, and degree of detail of boundary value heterogeneity. For example, the degree of freedom of fluid pathways and fluid velocities is virtually zero ($n_F = 0$) in the case of a unidimensional steady-state flow column, as mass conservation imposes a constant unidimensional flux vector throughout the column. For a black-box model such as represented in Figure 6-1, the only degree of freedom allowed is that of time variations ($n_F = 1$). In spite of their apparent simpilicity, black-box models can require a large number of in-situ experiments for calibration, since they rely less on physical principles and more on site-specific adjustment parameters. At the other end of the spectrum is the case of detailed models of transient flow through a three-dimensional domain, with localized boundary conditions and fully three-dimensional spatially distributed heterogeneity. In this case, the degree of freedom is much larger than one, and increases with the number of heterogeneities.

While having a large degree of freedom allows for more realistic modeling of naturally heterogeneous flow paths and dispersive contaminant transport, there is an obvious trade-off between degree of freedom on the one hand, and data requirements and model tractability on the other hand. In some cases, the use of stochastic concepts alleviate parts of the problems associated with data requirements and model tractability, while maintaining a large degree of freedom for fluid particles.

Figures 6-1 and 6-2 depicts schematic representations of a few typical flow configurations and the associated degrees of freedom (N_F). The latter can be thought of alternatively as the effective number of heterogeneities, or as the quantity of information which

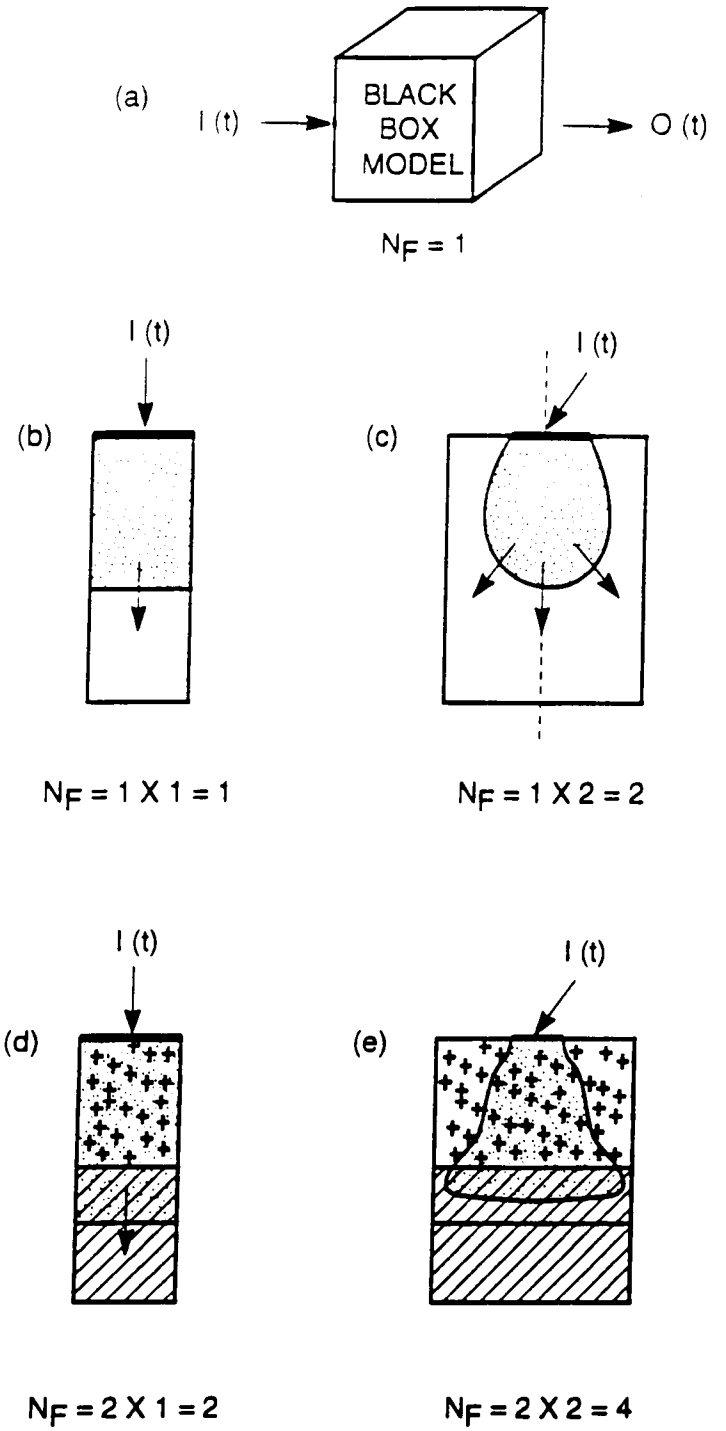

Figure 6-1. Degrees of freedom of unsaturated flow systems: (a) black box model, (b) one-dimensional flow in a homogeneous column, (c) two-dimensional flow in a homogeneous medium, (d) one-dimensional flow in a layered medium, and (e) two-dimensional flow in a layered medium

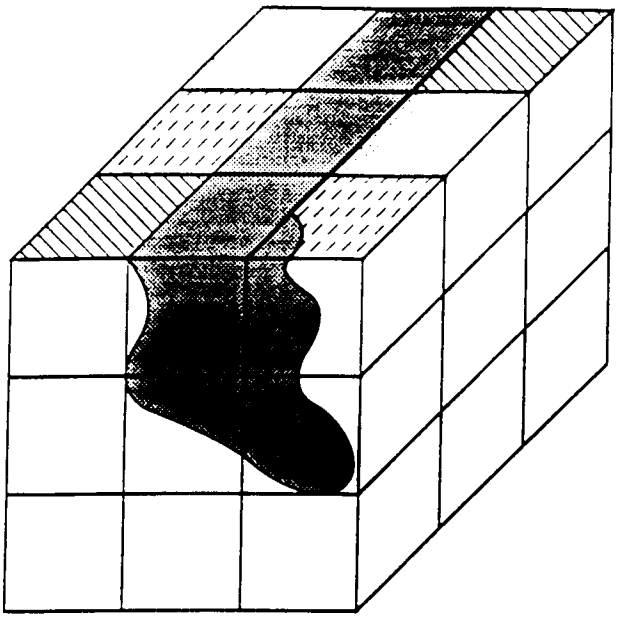

$N_F = 3^3 \times 2 = 54$

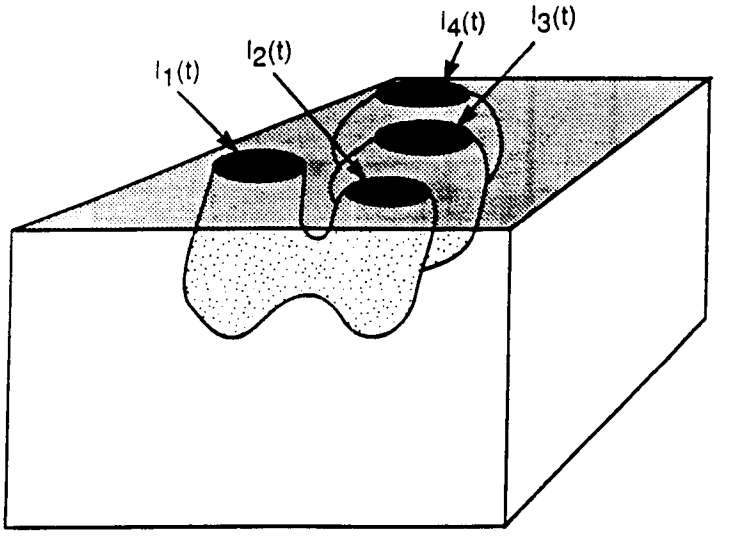

$N_F = 1 \times 4 \times 2.5 = 10$

Figure 6-2. Degrees of unsaturated flow systems: three-dimensional examples

the model makes available. Uniformity decreases N_F, while heterogeneity increases N_F. In the general case of transient flow, the degree of freedom can be defined in an ad hoc fashion as the effective number of elementary cells having distinct material properties (1 for a homogeneous column, 2 for a uniformly bi-layered medium, etc.) times the effective number of distinct flow regions caused by heterogeneity in boundary conditions (1 for a uniform boundary flux, 2 for a single plane-symmetric strip source, 2.5 for a final axi-symmetric disc source, 3 for a single arbitrarily shaped connected source).

While this definition is admittedly subjective, it does account for the effects of spatial dimensionality, multiplicity and symmetries of flow regions due to boundary conditions, and symmetry-breaking heterogeneity. These effects are summarized by

$$N_F = n_B D_E N_E \tag{6-8}$$

where N_E is the effective number of elementary cells (material heterogeneity), n_B the number of flow regions originating from boundary sources, and D_E the effective spatial dimension of the flow regions thus defined. In the case of randomly generated material heterogeneity, N_E can be replaced by the equivalent number of statistically independent samples given by

$$N_E^* = \prod_{i=1,\ldots,D} \left(\frac{L_i}{\lambda_i}\right) \tag{6-9}$$

where D is space dimension, L_i is domain size along each axis, and λ_i is the fluctuation scale or correlation scale of the D-dimensional random field along each axis.

For example, Figure 6-3 shows a three-dimensional view of a simulated strip-source moisture plume during infiltration. This numerical simulation was based on a finite-difference discretization of a domain divided into 52 x 76 x 76 $\approx$ 300,000 cells, each with distinct material properties. As a consequence, the number of distinct material cells is N_E = 300,000. However, owing to numerical resolution requirements, mesh size was taken smaller than correlation scales, in ratios (2/5, 1/5, 1/5). As a result, the total number of correlation scales for Figure 6-3 is 20 x 15 x 15 = 4500, which yields a measure of effective number of statistically independent samples, N_E^* = 4500. Finally, observing that the strip source does not extend all the way throughout the domain, the effective dimension of the flow region is three (not two). Based on Eqn. (6-8), this yields for the flow system of Figure 6-3:

$$N_F = 3 \text{ X } 300{,}000 = 900{,}000 \tag{6-10a}$$

$$N_F^* = 3 \text{ x } 4{,}500 = 13{,}500 \text{ .} \tag{6-10b}$$

In other words, the effective degree of freedom is about 10^6 if defined deterministically, and about 10^4 if defined statistically.

One disadvantage of using this definition of degrees of freedom to assess model complexity is that the effect of the variability of material properties is not incorporated. Note that the effective number of "material heterogeneities," N_E, was used to measure spatial heterogeneity. However, this definition does not distinguish between a multilayer system in which the properties vary so mildly from layer to layer as to appear homogeneous, and a multilayer system in which the material properties vary greatly. This can be taken into account by using the concept of entropy or, conversely, information content as a measure of the degree of variability of the physical system (Ababou and Sagar, 1991).

6.5 SPATIALLY DISTRIBUTED MODELING GUIDELINES AND CRITERIA

Development of models follows three stages: (1) defining the physically identifiable variables and parameters (2) formulating specific governing equations and (3) solving the equations for prescribed values of model parameters. In the case of spatially distributed models, this last step is to be implemented numerically, since we do not expect to obtain analytical

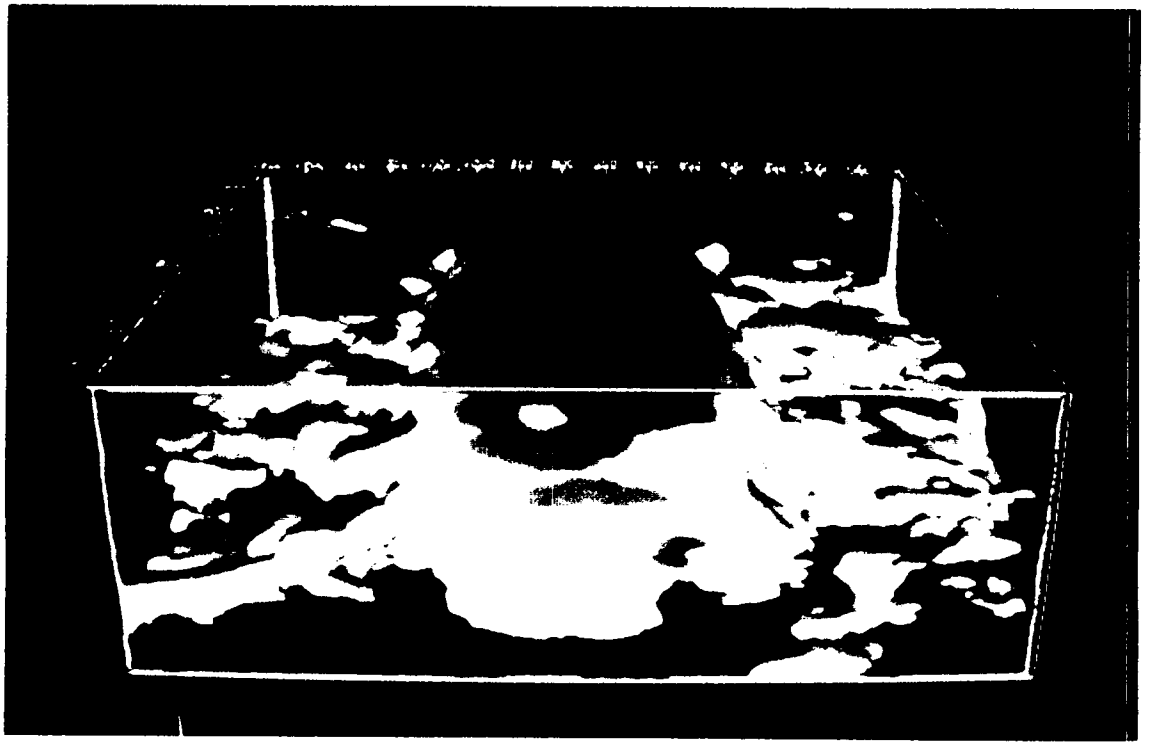

Figure 6-3. Degrees of freedom of unsaturated flow systems: (a) simulated three-dimensional moisture plume in a heterogeneous medium during constant flux strip-source infiltration (time t = 10 days). The simulation was done with the BIGFLO code. Domain size is 15 x 15 x 5 meters, and strip size is 4 x 9 meters. Dry zones were peeled off to reveal the 3D structure of the moisture plume.

solutions except under highly idealized conditions. It is, however, important to keep in mind the distinction between the conceptual model and its numerical implementation (sometimes dubbed "numerical model"). Both aspects are examined in this work. In our view the merits and disadvantages of a particular modeling approach to subsurface flow should be first assessed qualitatively, based on the criteria listed below.

6.5.1 Equations

The governing equations and auxiliary models, including constitutive equations, should be physically based and generic, rather than empirical.

6.5.2 Simplifying assumptions

The necessary simplifications introduced at various stages should be consistent with the objectives of modeling, and should capture the known characteristics of the field site. Assumptions aimed at simplifying the three-dimensionality, discontinuity, fracture density, stratification, anisotropy, and nonlinearity of hydraulic coefficients may not be justifiable if the objective is to identify the entire distribution of travel times and/or to identify the fastest flow paths. In addition, it may not be consistent to proceed with a high-resolution representation of heterogeneities in less than three dimensions, as this would artificially limit the degree of freedom of fluid and contaminant pathways. The steady-state assumption may be justifiable provided that it does not conflict with the imposed boundary conditions. Indeed, steady solutions can be either unbounded or unstable under certain conditions, and transient simulations may be required to verify the steady-state calculations.

6.5.3 Model inputs

The model should be parsimonious in terms of input parameters, particularly in the absence of high-quality data. This requirement puts a bound on the allowed degree of sophistication of the model. In the direct simulation approach to stochastic modeling, a few statistical parameters are used to generate a large number of hydrogeologic coefficients. The statistical parameters need not be precisely evaluated; they should be estimated by combining site-specific data with indirect, nonspecific information from related experiments and sites. In this way, relatively parsimonious stochastic models can be used to simulate highly heterogeneous flow systems in detail. In principle this could also be achieved using purely descriptive models, but at the cost of collecting a very large quantity of data in-situ. On the other hand, the model should not be so under-parameterized that it ignores significant and singular features of the subject site.

6.5.4 Computational feasibility

It should be demonstrated that the numerical solution of model equations is computationally feasible with current computing hardware, such as workstations and supercomputers. Owing to the complexity of unsaturated flow processes in highly heterogeneous

and fractured media, it is expected that the numerical implementation of any realistic model of these processes will be nontrivial. Therefore, the judicious selection or development of efficient algorithms may be key to the whole modeling approach.

6.6 DIRECT AND INDIRECT APPROACHES TO SPATIAL VARIABILITY

It is now recognized that accurate modeling of hydrogeologic flow and transport systems over large space-time scales requires adequate representation of a whole hierarchy of natural heterogeneities, discontinuities, and/or fractures having many sizes and shapes. See for instance Cushman (1990) for a recent collection of works in this area. Moreover, in the case of partially saturated or unsaturated flow, the complex spatial features of the geologic medium must be represented through nonlinear matrix/fracture hydrodynamic properties according to the unsaturated flow Eqn. (6-3). Therefore, the difficulty in modeling heterogeneous processes is compounded by the nonlinear nature of the governing equations.

Scientific approaches to field-scale flow modeling can be broadly classified in two types. The first approach is direct simulation of the detailed hydrodynamics based on the classical Darcy-Richards equations. This requires an explicit representation of fine-scale heterogeneities, stratification, and/or fracture density of the geologic medium based on a combination of geostatistical models and hydrogeologic data. The second approach, coarse-scale or effective modeling, makes use of physically-based auxiliary sub-scale models for describing in a simplified way the detailed hydrodynamics processes not explicitly accounted for in the coarse-scale simulation model. Combinations of these two approaches are also conceivable, as will be explained below.

A clear advantage of direct simulation is that it requires only the basic phenomenological equations to model the flow system and, if needed, subsidiary constitutive relations for fractures. While fine-scale spatial variations of groundwater velocity are known to play a significant role in radionuclide transport and dispersion (Gelhar and Axness, 1983; Winter et al, 1984; Dagan, 1987), there are limits to how extensively and explicitly the broad spectrum of geologic heterogeneities can be represented in a flow model. First, site-specific data are not likely to be available with the required degree of detail, so that much effort is required for auxiliary analyses such as statistical interpolation and conditioning and statistical continuum models of heterogeneous porous media. Second, the computational demands are great. The computational demands in the case of fractured porous media, with both continuum and discontinuum-type heterogeneity, are likely to be even higher owing to the extreme disparity of active fluctuation scales. The following models, while spatially distributed, avoid explicit representation of detailed medium heterogeneity:

(1) *Single Equivalent Continuum*: The heterogeneous and/or fractured medium is treated as a single homogeneous continuum with unique effective hydraulic properties. This approach captures the pressure-dependent anisotropy due to stratification, but not that due to fractures.

(2) *Dual Equivalent Continuum (Double Porosity)*: The fractured medium is treated as a mixture of two distinct continua of unspecified geometry, a homogeneous matrix and a homogeneous fracture continuum. Each continuum is characterized by distinct pressure, flux, and hydrodynamic parameters and an effective transfer term to account for mass movement between the two continua (Barenblatt et al., 1990; Shapiro 1987).

(3) *Combination of Single and Dual Equivalent Continua*: The dual equivalent continuum model has been traditionally implemented assuming spatially uniform properties for each continuum. However, if effective flow models are made available for each type of equivalent continuum, then it may be possible to improve the overall model by combining (1) and (2) above.

In fact, the indirect approach to heterogeneous flow modeling can be used in combination with explicit modeling of certain types of heterogeneities that either are not accounted for by the auxiliary models, or are too important to be treated implicitly. This is the case for major geologic features such as faults, major fractures, bedding sequence of large geologic units, and large-scale trends in hydraulic properties.

In conclusion, when indirect modeling methods are implemented to obtain representative field-scale simulations of site-specific processes, direct representation of heterogeneities may still be needed to capture essential site-specific features. As a consequence, only a limited part of the modeling effort can be transferred from the global model to the submodel(s), where the submodel may be the matrix-fracture transfer term used in dual porosity methods, or the effective conductivity functions employed in single equivalent continuum methods. There are pending questions regarding the conceptual/empirical basis of such submodels, their consistency with the global model, their intrinsic range of validity, and the identifiability of their internal parameters. The physical basis of effective continuum and double-porosity continuum models needs to be better ascertained in particular for the case of unsaturated flow.

As an alternative, emphasis was placed on the case of direct simulation approaches of spatially distributed processes based on the local Darcy-Buckingham-Richards model (Richards equation). It is assumed that the model is implemented numerically, which leads to additional approximations.

6.7 INTERNAL AND COMPARATIVE TESTS OF CONSISTENCY

Spatially distributed models can be tested using specific methods. It is convenient to distinguish between testing procedures, aimed at verifying the consistency of well-defined components of the model, and groundtruth experiments, which aim at an overall assessment of the model under real field conditions. While the consistency tests purposely limit the scope of testing in order to focus on the validity of particular solutions for well-known model inputs, the latter tests attempt to assess the validity of the postulated model under conditions that are not fully controlled and that may lie outside the accepted range of validity of specific model

postulates. This subsection focuses on methods for testing internal model consistency in the sense defined above. Groundtruth testing is discussed in the next subsection.

6.7.1 Internal Numerical Testing

Numerical tests are designed to check the internal consistency of the numerical implementation, without questioning the basic governing equations or postulated constitutive relations. Internal numerical testing is based on results of numerical analysis. Space-time discretization methods must be selected so as to be theoretically consistent with governing equations in the sense that the discretized equations must converge to governing equations as space-time mesh size goes to zero. Typically, however, numerical analysis does not give sufficient information on the rate of convergence of discrete approximations to governing equations.

Consider an implicit finite-difference approximation of Richards' equation for the case of transient one-dimensional infiltration through a homogeneous soil column. The original partial differential operator corresponding to the Darcy-Buckingham-Richards model is

$$\mathcal{L}(h) = -C(h)\frac{\partial h}{\partial t} + \frac{\partial}{\partial x_1}\left(K(h)\left(\frac{\partial h}{\partial x_1} + \cos\Theta_1\right)\right) = 0 \qquad (6\text{-}11)$$

where x_1 is the axis of the soil column and $\Theta_1 = \pi$ if x_1 is vertical downwards. Implicit space-time finite-difference approximation of this operator yields a discrete system of algebraic equations of the form:

$$L(h) = -C_i^n \frac{h_i^n - h_i^{n-1}}{\Delta t} + \frac{K_{i+1/2}^n}{\Delta x_1}\left[\frac{h_{i+1}^n - h_i^n}{\Delta x_1} + \cos\Theta_1\right] - \frac{K_{i-1/2}^n}{\Delta x_1}\left[\frac{h_i^n - h_{i-1}^n}{\Delta x_1} + \cos\Theta_1\right] \approx 0 \qquad (6\text{-}12)$$

where h_i^n stands for $h((i-1)\Delta x_1, n\Delta t)$ and $K_{i+1/2}^n$ stands for $K(h((i+1/2)\Delta x_1, n\Delta t))$.

The truncation error defined by

$$E(h) = L(h) - \mathcal{L}(h) \qquad (6\text{-}13)$$

can be evaluated theoretically to first-order in time and to second-order in space in terms of pressure (h) and flux ($q_1 = -K(\partial h/\partial x_1 + \cos\Theta_1)$) at the nodes of the space-time grid. In

the special case of an exponential conductivity function $K(h) = K_s \exp(\alpha h)$, the result is (Ababou, 1990):

$$E(h) = \Delta t\left\{\frac{\partial}{\partial x_1}\left[K\frac{\partial}{\partial t}\left(\frac{\partial h}{\partial x_1}\right)\right] - \frac{C}{2}\frac{\partial^2 h}{\partial t^2}\right\}$$

$$+ \frac{\Delta x_1^2}{24}\left\{\frac{\partial}{\partial x_1}\left[K\frac{\partial^3 h}{\partial x_1^3}\right] - \frac{\partial^3 q_1}{\partial x_1^3} - 3\alpha\frac{\partial}{\partial x_1}\left[q_1\frac{\partial^2 h}{\partial x_1^2}\right]\right\} \qquad (6\text{-}14)$$

$$+ \text{h.o.t.}$$

The point to be emphasized here is that, while Eqn. (6-14) is indicative of the order of accuracy of the discretization, it does not give sufficiently reliable information on the accuracy to be expected for finite space-time mesh size. Indeed, higher order terms (h.o.t.) have been dropped. Moreover, the magnitude of the coefficients in braces cannot be determined in advance except for trivial cases where closed-form solutions are known. For these reasons, numerical experimentation is required in order to better evaluate the effects of space-time mesh size.

In addition to discretization errors, numerical implementation of spatially distributed flow models entails errors due to approximate solution of nonlinear discrete systems, and round-off errors due to limited machine precision for floating-point operations. When using iterative solution schemes, the combined solution errors and round-off errors can be estimated numerically by computing "on-line" the norm of the residual, or incremental solution between consecutive iterations. The magnitude of this error norm, and its rate of convergence toward zero, give approximate indications of the errors incurred in the solution process (see for instance Ababou et al., 1989, for the case of iterative solution of large linear systems). The combined numerical errors defined above can also be assessed indirectly through global internal tests such as preservation of fundamental symmetries, conservation of total mass, and other global conservation principles.

Global conservation principles such as mass balance are useful as internal checks of overall accuracy in the following restricted sense. Since the exact solution must satisfy exactly global mass conservation, the accuracy of the numerical solution can be assessed by evaluating the discrepancy between the net discharge rate entering the system and the rate of change of mass (converted to volume) of water present in the system [for example, involving large 3D simualtions (see for instance Ababou, 1991b)]. However, even if global mass balance is satisfied accurately, this does not rule out the possibility of significant local errors which cancel out on average (e.g., spatial oscillations). On the other hand, in the case where significant mass-balance discrepancies are found, it is not known whether these errors are from spatial discretization, time discretization, nonlinear solutions, and/or round-off. In the case

where nonlinear-solution and round-off errors are thought to be under control through iterative convergence rate analysis, persistent mass-balance errors can still be caused by overly coarse space and/or time discretization.

6.7.1.1 Boundary Conditions

In steady-state models, boundary conditions should be compatible with the steady-state assumption; that is, a stable and physically realizable steady-state solution should exist under the prescribed boundary conditions. However, in the case of more complex boundary conditions such as seepage faces, the existence of a steady state may depend upon stability properties of the full transient equation.

6.7.1.2 Initial Conditions

In transient simulations, initial conditions should be compatible with the class of solutions generated by the model. In the absence of sufficiently accurate in-situ measurements of the initial state, an internally consistent initial condition can be generated in principle for the special case of hydrostatic equilibrium in the 3D-heterogeneous medium, $(h(\vec{x}) = H_o+z)$. In practice, approximations such as $h(\vec{x}) = H_o$ may be satisfactory for representing hydrostatic equilibrium in the case of large negative H_o (dry initial state). Note that in a heterogeneous medium under hydrostatic equilibrium, the volumetric content may vary in space both horizontally and vertically.

6.7.2 Comparative Tests of Consistency

The consistency of a spatially distributed numerical model can also be tested by comparing the outputs of two codes based on governing equations, or by comparing code output to analytical solutions based on identical governing equations. In the first instance, model outputs can be tested for relatively complex hypothetical flow systems. The rationale of code-to-code comparison is that the probability of obtaining nearly identical *incorrect* solutions is presumably low in the case where the benchmarked codes were developed independently. Independence is, however, not perfect; the level of significance of code-to-code comparison is presumably highest for codes which differ significantly in numerical implementation (discretization, variable transformations, etc.). On the other hand, comparison with exact analytical solutions provides a precise test of numerical solutions.

Unfortunately, exact analytical solutions are only known for simplified flow conditions, homogeneous material properties, and restricted classes of unsaturated constitutive relations. As a consequence, such comparisons only test specific algorithms of the numerical model, leaving untested several essential features such as nonlinear system solvers. To illustrate this point, consider the transient one-dimensional mixed-variable Richard's Eqn. (6- 3) with the following nonlinear constitutive relations:

$$K(h) = k_s \exp(\alpha h) \tag{6-15}$$

$$\Theta(h) = \Theta_s \exp(\beta h) \ . \tag{6-16}$$

It is easily seen that, in the special case $\alpha = \beta$, this equation becomes mathematically equivalent to the linear heat equation, with constant diffusion coefficient $D = K_s/\alpha\theta_s$, in terms of the total hydraulic head ($H = h + z$). Figure 6-4 shows the transient solution for fixed hydraulic heads at the two end-points, as obtained by the finite difference BIGFLO code using variable time-steps and a nonlinear system solver. The analytical and numerical solutions are indistinguishable. However, while the numerical solution was obtained in a nonlinear fashion, the perfect fit thus obtained does not fully test the accuracy of the nonlinear flow solver, since this particular flow problem is known to be intrinsically linear when formulated in terms of hydraulic heads.

Figure 6-5 illustrates a comparison of numerical solution from the finite difference model PORFLO-3 (Runchal and Sagar, 1989; Sagar and Runchal, 1990) with a one-dimensional analytic solution of Philip (1957). The PORFLO-3 solution was obtained using a $\Delta x = 0.15$ cm with a convergence criterion $R \leq \text{Max}\ ((P_{new} - P_{old})/P_{old}) \leq 10^{-5}$ and using the

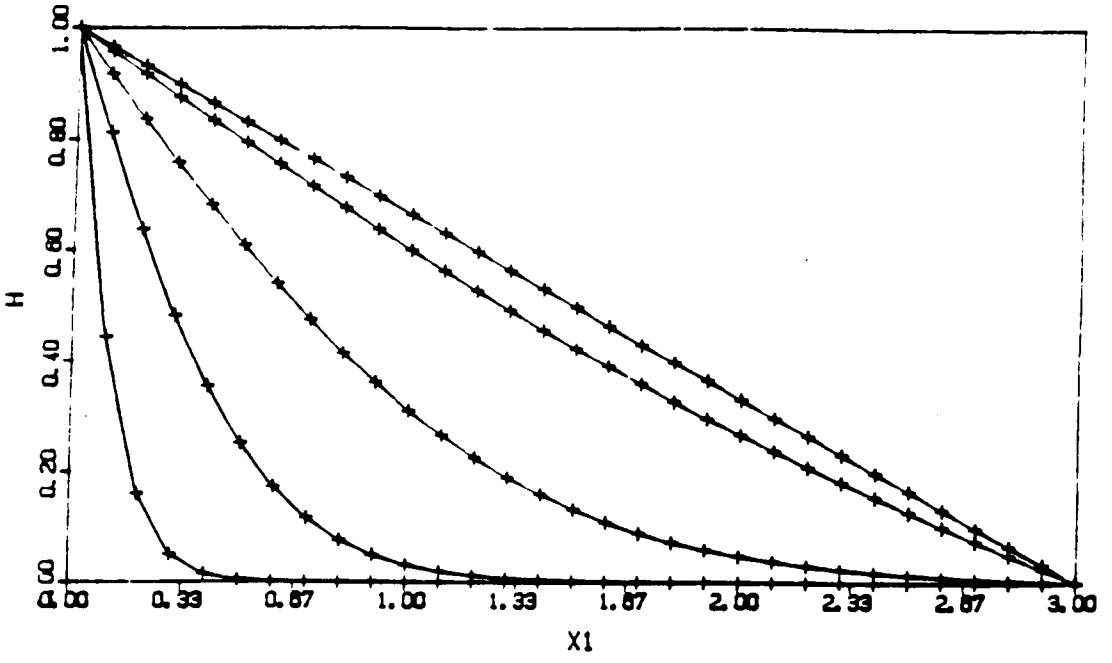

Figure 6-4. Numerical and analytical solutions for the transient 1D diffusion equation with constant coefficients. The numerical solutions obtained in the saturated or unsaturated modes, with fixed or variable time steps, were undistinguishable from the analytical solution. One of the numerical solutions is shown here for times t = 0.01, 0.10, 0.5, 1, and t ≥ 5 (quasi-steady state)

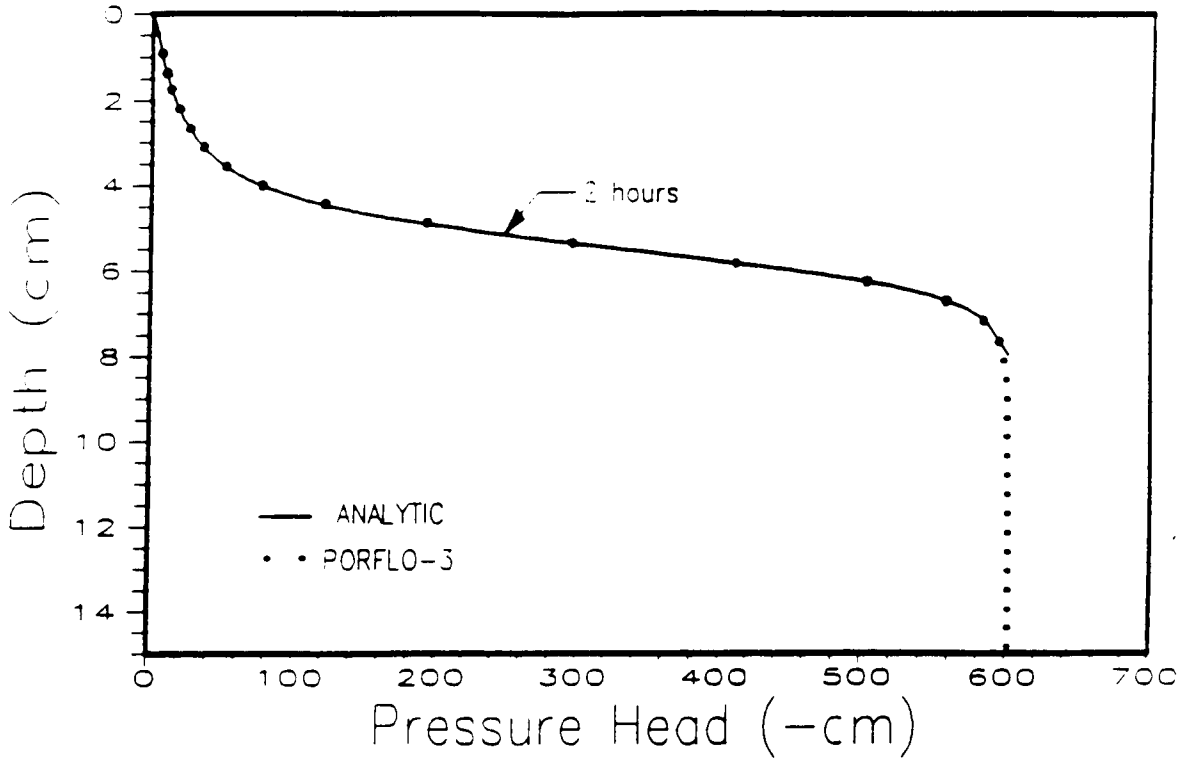

Figure 6-5. Comparison of numerical solution from PORFLO-3 with 1D analytic solution of Philip (1957)

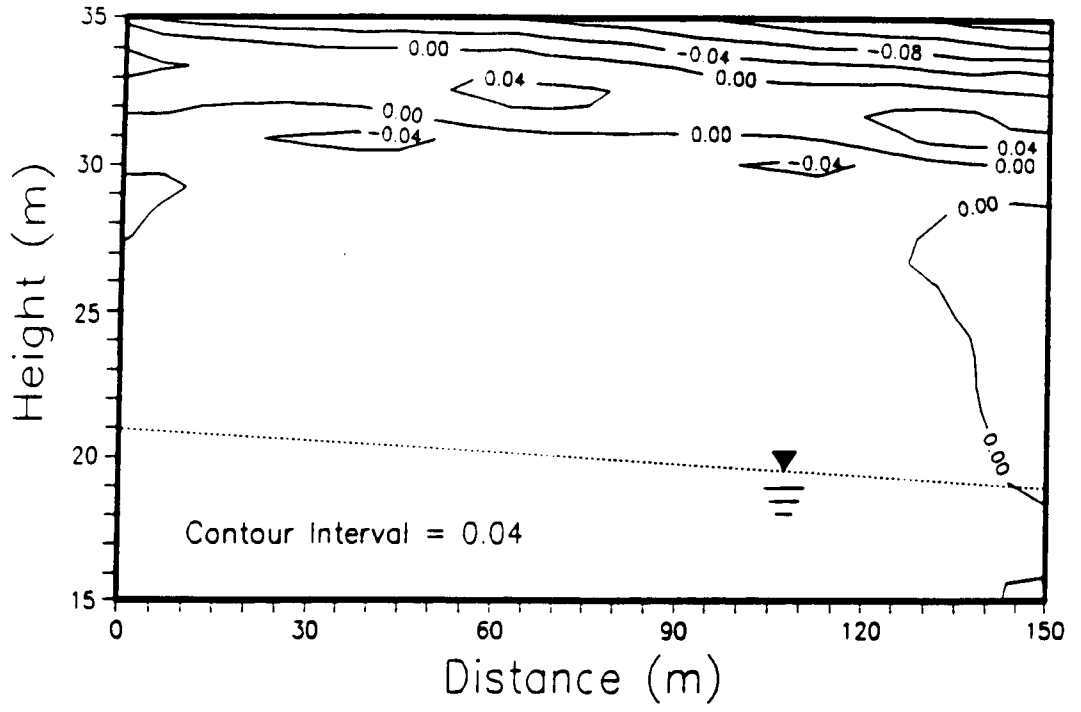

Figure 6-6. Comparison of PORFLO-3 and FEMWATER codes: Comparison of pressures

alternate direction implicit (ADI) solution algorithm. Figure 6-6 shows a comparison of a two-dimensional saturated-unsaturated flow problem simulated with PORFLO-3 and FEMWATER (Yeh and Ward, 1979). These two codes have different dimensionality, used different solvers, and were developed independently. As stated above, such comparisons are not conclusive to the correctness of either model. They do, however, provide some confidence in the results of both models. With regard to Figure 6-4, when conductivity-weighing schemes other than geometric (e.g., arithmetic, harmonic, or upstream) were used to calculated interfacial conductivities, the comparison was not as good as shown in this figure. The geometric-weighting scheme was also used in computing the detailed moisture plume shown earlier in Figure 6-3.

6.8 GROUNDTRUTH MODEL TESTING

6.8.1 Objectives, Scope, and Uncertainty of Groundtruth Tests

Groundtruth model testing differs from consistency checks in that model results are compared to imperfectly known flow systems generated in laboratory or in-situ field experiments. Another key difference is one of scope. Groundtruth experiments test the overall validity of models, including basic postulates and assumed governing equations. The scope and objectives of groundtruth experiments are much broader than tests of consistency.

Excluding the case of specialized laboratory experiments such as small-scale tests of the Darcy-Buckingham relation, interpretation of groundtruth experiments requires taking into account several areas of uncertainty:

- Uncertainty in spatially distributed material properties and nonlinear constitutive relations (not well known)
- Uncertainty in flow inputs and initial-boundary conditions (imperfectly controlled and subject to measurement errors)
- Uncertainty in the evolution of the flow system in time and space (sparsely monitored and subject to measurement errors)
- Limited resolution and limited range of measurements, tensiometers fail to measure suction above 0.8 bars; the spatial resolution of neutron moisture probes is generally coarser than that of tensiometers, and is highly dependent on moisture content.

In practice, these areas of uncertainties can be reduced in well-controlled laboratory experiments, e.g., using carefully homogenized sieved soils for 1D column and 2D slab experiments. However, such procedures also remove potential sources of discrepancies between model and field, such as natural heterogeneity and three-dimensionality. A trade-off then occurs between increased scope of testing and increased uncertainty of knowledge of the

experimental flow system. In this section the significance of experimental model validation approaches is analyzed, particularly with regard to the above mentioned limitations.

Internal-consistency tests aside, all other types of model testings use data either from laboratory experiments or from testing in-situ. Inconsistencies between simulation results and observations may be due to deficiency in the model, insufficient resolution of material properties, or lack of all-encompassing observations. Figure 6-7 shows a predicted tracer plume in which the points of observations are also shown. It seems obvious that in this particular case, the observation points are insufficient to prove or disprove the correctness of the model, specifically the thin parts of the plume.

Another important factor on the scope of model testing is the objective. On the one hand, the objective may be generic science, such as analysis of dispersive transport where fine-scale details of material heterogeneity are important. On the other hand, the objective may be operational, such as performance assessment of nuclear waste repositories, where specific performance measures are to be compared to socio-economic criteria and environmental standards. Criteria stated in terms of groundwater travel time require determining a large number of flow paths and therefore may require a model with a large number of degrees of freedom. An integrated measure such as a flux or cumulative release of a contaminant can probably be estimated at a coarse scale, although the validity of a coarse-scale approach needs to be ascertained in relation to site-specific heterogeneity.

6.8.2 Model Validation Versus Model Refutation

Goundtruth model testing faces two types of limitations: (1) incomplete knowledge or uncertainty regarding the experimental flow system and (2) limited scope of testing relative to the scope of the theoretical model. Here we focus on limitations of scope rather than uncertainties. That is, perfect control of system parameters, inputs, and outputs is assumed. In particular, the following questions were addressed: in what sense and to what degree can a model be "validated" through comparisons with one or several specific experiments?

The idea that a theoretical model can be "validated" experimentally has been criticized on logical grounds (Popper, 1935 and 1959). The concepts developed by Popper and followers were originally formulated for scientific theories of natural phenomena. The flow models discussed here can be considered as specialized theories. The crucial attribute of a theory or predictive model, such as the spatially distributed Darcy-Buckingham-Richards model, is that it makes a universal assertion on the behavior of the system as opposed to the singular nature of experimental observation. Thus, although a particular experiment can test a particular manifestation of the model, it should be recognized that there can be no *logical* inference from the particular (experiment) to the general (model). Accepting the rules of standard inference means rejecting the validity of inductive reasoning. This leaves only refutation as a viable way to assess models experimentally. Indeed, Popper's view implies that models should always be formulated in such a way as to be falsifiable (refutable). A proper model makes a universal statement about its potential falsifiers (that they are not true), but makes no assertions concerning

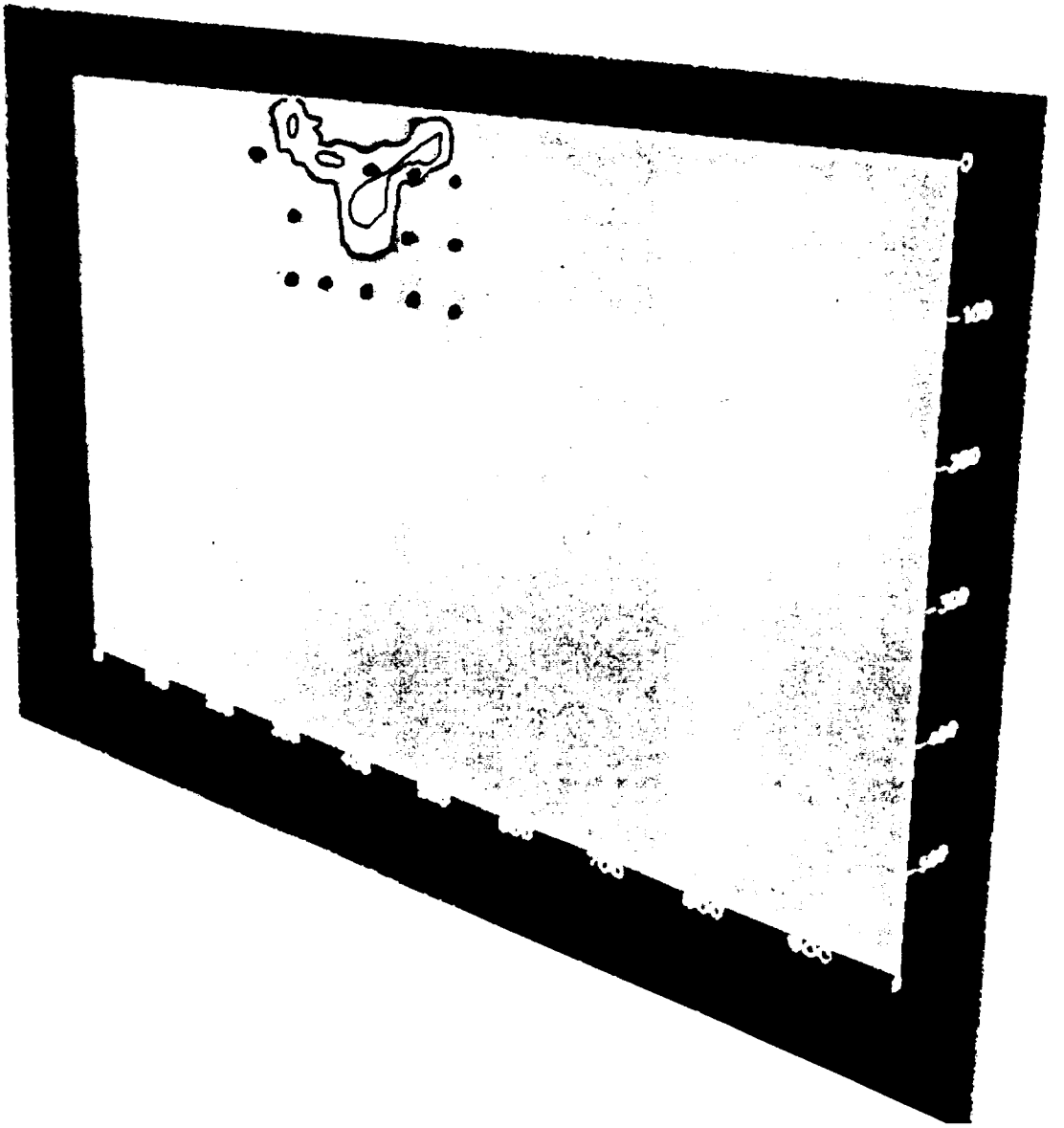

Figure 6-7. Simulated tracer plume for Las Cruces strip-source experiment No. 2, with superimposed locations of suction-cup concentration probes. Tracer plume was simulated with the PORFLO-3 code.

noncontradictory experimental observations. The potential falsifiers of the model are singular statements whose truth value can be verified experimentally. In other words, potential falsifiers are experiments that have the potential of invalidating the particular model at hand. Only these experiments are of interest in testing a theoretical model.

The value of Popper's approach lies not so much in its denial of the possibility of model validation, but rather in that it recognizes a fundamental dissimilarity between validation and refutation and between singular and universal assertions. Consider, for example, a simple black-box model such as represented schematically in Figure 6-8. I(t) could represent the inflow at the ground surface, and O(t) the outflow at a compliance boundary or the advance of a wetting front. For the black-box model, a causal, stationary, and linear relation between input and output was chosen. According to Wiener (1948), every causal, stationary, and linear operator can be expressed as the limit of a sequence of convolution integrals. With this in mind, a specific formulation of the postulated black-box model could be as follows. The model being tested asserts that "M is true," where M is the universal assertion:

$$M = \{O(t) = \int_0^t K(\tau; P)\, I\,(t-\tau)\, d\tau\} \,. \qquad (6\text{-}17)$$

The kernel function K is square-integrable, depends uniquely on the system parameters {P} in a predefined fashion, and is independent of the input function I. On the other hand, the outcome of a particular experiment can be expressed as "E_1 is true" where E_1 is the singular assertion:

$$E_1 = \{I(t) = I_1(t) \text{ and } P = P_1 \rightarrow O(t) = O_1(t)\} \,. \qquad (6\text{-}18)$$

It is easily seen that E_1 is a potential falsifier of model M. The transfer function for model M is

$$\frac{\hat{O}(s)}{\hat{I}(s)} = \hat{K}(s\,;\,P) \,. \qquad (6\text{-}19)$$

Therefore, if the experimental observations (E_1) are such that $\hat{O}_1(s)/\hat{I}_1(s)$ differs significantly from $\hat{K}(s;P)$, then model M is refuted. However, in case of a good fit, is model M validated? The crucial characteristic of model M is precisely its universality, as opposed to the specificity of empirical statements. For perfect validation of model M, it must be demonstrated that Eqn. (6-19) is satisfied for all input functions, and that the kernel function K depends on parameters (P) in the postulated manner for the whole specified range of parameters. The *degree* to which a single experiment (E_1) can validate the model depends on the subjective weight, or probability, assigned to that particular experiment.

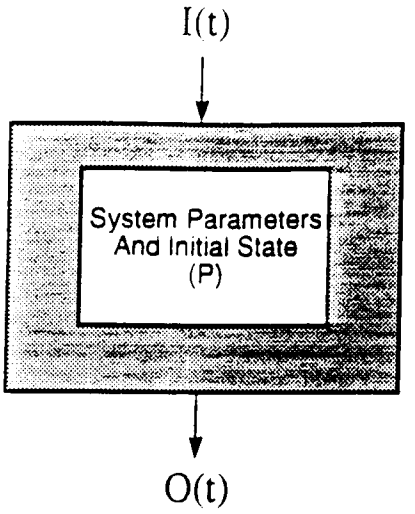

Model (M):

$$O(t) = \int_0^t K(\tau, P)\, I(t-\tau)\, d\tau$$

Figure 6-8. Schematic representation of a black-box model with casaul, stationary, and linear relation between input I(t) and output O(t)

6.8.3 Degree of Validation and Performance Measures

Having recognized that a single experiment can possibly refute a model but cannot validate it in a strict sense, it remains to be seen whether more lenient validation criteria can be defined. Assume as before that the parameters, inputs, and outputs of the experiment are perfectly known. In this hypothetical case, the extent to which one or several experiments partially validate or refute a spatially distributed model depends on the scope as well as the outcome (goodness-of-fit) of each experiment.

- *Scope*: In a subjective sense, a particular experiment is assigned more validation weight if the range of the input function and the range of material properties are both broad, so that the universal character of the model is efficiently put to test.

- *Outcome (Goodness-of-Fit)*: A particular experiment is assigned more subjective validation weight if the model prediction comes closer to

experimental observation according to some prescribed performance measure(s).

It is important to recognize that different experiments do not stand on an equal footing with respect to their potential validating value. In the simplified case of the black-box model of Figure 6-8, an experiment conducted with a highly fluctuating input function has more validating value than one for which the input function is smooth, constant, and small. Indeed, in the trivial case where $I(t) = 0$, one obtains $O(t) = 0$, i.e., the system is unperturbed and the experiment has virtually no validating value.

The goodness-of-fit of model prediction to experimental observation is somewhat easier to quantify than the scope of the experiment. Performance measures can be defined either by analogy with regulatory standards or with a view to characterizing physically meaningful features of the simulated/experimental flow system. For the case of unsaturated flow due to localized infiltration, the following multi-dimensional performance criteria based on the distribution of water content (θ) are of interest:

- Total Mass:

$$M(t) = \mathrm{Vol}(\Omega)\ \bar{\theta}(t) = \iiint_{\Omega} \theta(\vec{x},t)\, d\vec{x} \ . \qquad (6\text{-}20)$$

- Center of Mass of Moisture Plume:

$$X_i(t) = \iiint_{\Omega} x_i\ \theta(\vec{x},t)\, d\vec{x} \ . \qquad (6\text{-}21)$$

- Spatial Dispersion of Moisture Plume:

$$\Sigma_{ij}(t) = \iiint_{\Omega} (x_i - X_i(t))\ (x_j - X_j(t))\ \theta(\vec{x},t)\, d\vec{x} \ . \qquad (6\text{-}22)$$

It should be emphasized that these time-dependent spatial moments only require the space-time distribution of moisture contents for their evaluation. Moisture contents are more readily measured than water fluxes.

The proposed performance criteria can be interpreted as follows. $M(t)$ gives the total mass within the prescribed domain, and can also be used to evaluate the mass escaping or incoming through compliance boundaries if the surface flux is known. The migration of the moisture plume is characterized by the coordinates $X_i(t)$ of the center of mass of the plume. In particular, note that the left-right assymetry of the plume can be quantified in terms of $X_1(t)$, since $X_1(t)$ may be different from zero due solely to the presence of symmetry-breaking heterogeneity. The downward migration of the plume, during both infiltration and subsequent

redistribution, is quantified by $X_2(t)$. The second-rank tensor $\Sigma_{ij}(t)$ characterizes the multidimensional spatial dispersion of moisture around the center of the plume mass.

6.8.4 Probabilistic Validation and the Problem of Induction

Probabilistic approaches to model validation have been introduced at several levels. On a fundamental level, epistemologists and mathematicians have attempted to develop rules of inductive reasoning as an alternative to logical inference. Thus, new formalisms have been introduced to characterize the extent to which a universal statement (theory or model) can be validated by a singular statement of limited scope (experiment). Polya (1954) described informal rules of "plausible inference" or "shaded inference" based on assigning qualitative probability weights. His intent was to develop guidelines for proving theorems, that is, to justify inductive reasoning from the particular to the general (if $M \rightarrow E_1$ and E_1 is true, then M becomes more credible). More formal probabilistic verification theories have been advanced by logicians and philosophers, but examples of actual applications do not abound. These theories require, in effect, the construction of the collection of all models which might fit the data, or else the construction of all experimental tests which might validate the given model. They have been criticized, justifiably, on the grounds that the probability spaces of all models and all experimental tests cannot possibly be constructed. This position is based on the historical fact that truly crucial predictive models and validating experiments may never be identified if they are not part of the current scientific tradition (Kuhn, 1970).

However, more limited applications of probabilistic verification theories may be of interest. Burks (1977) developed a complex logical system of alternative approaches to inductive calculus. He made ample use of Bayes theorem of conditional probabilities in his "calculus of inductive probability" as a means of comparing two mutually exclusive and jointly exhaustive models. In his example, the models to be compared were the heliocentric and geocentric hypotheses, and the test was an observation of stellar parallax. If E_1 is the experimental observation, and M and $\bar{M}$ are the mutually exclusive, jointly exhaustive models by construction, the models satisfy approximately

$$\text{Prob}(M) + \text{Prob}(\bar{M}) = 1 \qquad \text{(exhaustive) and}$$

$$\text{Prob}(M)\ \text{Prob}(\bar{M}) = 0 \qquad \text{(exclusive)} \quad . \tag{6-23}$$

As a corollary to Bayes theorem, is the following equivalence theorem (Burks, 1977, theorem [22]):

$$\{\text{Prob}(M|E_1) > \text{Prob}(M)\} \leftrightarrow \{\text{Prob}(E_1|M) > \text{Prob}(E_1|\bar{M}\} \tag{6-24}$$

which always holds if $0 < \text{Prob}(M) < 1$ and $\text{Prob}(E_1/M) > 0$.

The above theorem states that the posterior probability of model M conditioned on experimental observation E_1 is larger than its prior probability if, and only if, the "degree of prediction " on model M is larger than the "degree of prediction" on the contradictory model $\bar{M}$. Here, the "degree of prediction" on model M is the probability that the observed event E_1 would occur, had model M been exactly true. For the example of a migrating contaminant plume, given E_1 = {"The observed concentration plume splits into slow-moving and fast-moving parts"}, the degree of prediction for model M = {"Fractured porous medium"} is higher than for the alternative model $\bar{M}$ = {"Nonfractured porous medium"}. As a consequence, the posterior probability, or "truth value," of model M is increased, while that of model $\bar{M}$ is decreased. In other words, Model M is validated to a degree, while model $\bar{M}$ is refuted to a degree.

Note that the effect of introducing the concept of inductive probability is to disguise the fundamental distinction between refutation, which is possible by logical inference, and validation, which is not possible by standard logical inference. The problem of induction from the particular to the general is also related to the limited scope, or testing power, of the experiment. The degree to which a particular experiment effectively tests the given model is difficult to quantify, although it can be defined formally in terms of Bayesian hypothesis testing. Thus, given a postulated model, the experimental test is required to have an adequately high probability of rejecting the model if the model is false.

The claim that any two models are mutually exclusive and exhaustive is, however, a somewhat subjective decision. Probabilistic tests can be applied either to select the best among a class of parameterized models or to decide upon the acceptance or rejection of a given model. In what follows, the focus was on the former approach. See Ababou and Sagar (1991) for a discussion of the acceptance/rejection approach based on Bayesian hypothesis testing (decision tests).

6.8.5 Probabilistic Model Validation Through Parameter Estimation

Consider the case of unsaturated transport based on the mobile-immobile model, whereby a fraction of the water is assumed immobile and exchanges solute with the mobile fraction. Let P be the parameter which characterizes the fraction of immobile water. Taking $P \rightarrow 0$ yields the standard advective-diffusive transport model. Having parametrized the model in this fashion, experimental observations of breakthrough curves can be used to estimate parameter P by the maximum likelihood method.

We assume here that no direct measurements of the adjustment parameters are available. Let θ be the observable, $\theta(P)$ the value predicted by the model for a prescribed value of parameter P, and θ^* the observed value. The discrepancy between observations and predictions at points in space and time is given by the residual vector

$$e(x_i,t_n) = \theta^*(x_i,t_n) - \theta(x_i,t_n,P) .$$

The likelihood of experimental observations for a given parameter P is proportional to the probability density function f(e,P) of residuals, which depends on the deterministic but unknown parameter P. In the case of the mobile-immobile model, observations may consist of measurement of the breakthrough curve in time. The residuals at different times could be assumed jointly Gaussian with a time-correlation function which decays with time lag. The unknown variance and correlation function could then be included in the set of parameters being estimated, in addition to the model parameter P.

The maximum likelihood method seeks to maximize the log-likelihood function:

$$\ln L(P) = \ln f(e,P) = \ln f(\theta^* - \theta(P)) \qquad (6\text{-}26)$$

with respect to parameter P. The maximizer, denoted $\hat{P}$, is therefore considered to be the best-fit estimate of parameter P. A measure of performance of the maximum-likelihood estimation is given by the Cramer-Rao lower bound:

$$\langle (\hat{P}-P)^2 \rangle \geq \langle \left(\frac{\partial \ln f(\theta,P)}{\partial P} \right)^2 \rangle^{-1} = I_\theta(P)^{-1} \qquad (6\text{-}27)$$

where $I_\theta(P)$ is the Fisher information matrix. In the Gaussian case, $I_\theta(P)$ is essentially an inverse variance of error, which is a measure of the information provided by the experiment. Information is high if the discrepancy between observations and predictions is low. The Cramer-Rao bound provides an asymptotic estimate of estimation variance.

If the optimal parameter P is found to be zero, then the optimal model is the simplest (e.g. no immobile water). The log-likelihood function in practice may be very nearly flat in parameter space. In such a case, the "best" model is justifiably the simplest model, that is, the one obtained by eliminating the corresponding parameter. This choice is one of parsimony rather than best fit. Carrera et al. (1989) applied this type of reasoning to select the best among a class of transport models involving parametrized dual-porosity transfer terms, matrix-diffusion terms, etc. One difficulty in applying maximum likelihood to a parametrized class of models, however, is the more or less arbitrary choice of the joint probability structure of residuals, particularly for nonlinear space-time distributed models.

6.9 SUMMARY AND CONCLUSIONS

The selection of a modeling approach is a rather subjective process, and requires maintaining a balance between parsimony and other imperatives related to the objectives of modeling. For instance, a large number of degrees of freedom, or a large amount of information, may be required for characterizing fast flow paths from contamination sources to

the accessible environment. Stochastic representation of material heterogeneity can simplify the task of maintaining a large degree of freedom. Testing the internal consistency of complex numerical models based on stochastic representations is a non trivial and important part of model validation. We emphasize the distinction between internal numerical tests, such as mass balance and fine-to-coarse mesh comparisons, and comparative numerical tests based on independently obtained analytical and numerical solutions.

Once the model has been selected and tested for internal consistency, it is quite another matter to demonstrate experimentally that the model is universally correct. In fact, the degree to which an experimental test can "validate" a generic predictive model depends, not only on the goodness-of-fit, but also on the conditions and scope of the experiment. One measure of "scope" may be the range and variability of material properties and inputs. In a strictly logical sense, a single experiment cannot validate a generic model, but it can refute the model. In practice, the conclusion that the model is refuted needs to be qualified, not only in terms of the observed discrepancies, but also in terms of the scope of the test. Unfortunately, quantitative methods to characterize the degree of validation or refutation in terms of the scope of the experimental test are currently lacking.

In a limited sense, comparative model validation is possible via parameter estimation techniques such as maximum likelihood. This approach tests a class of models that are closely related; that is, the models differ only by the values of one or a few adjustment parameters. An interesting case is one in which equating a parameter to zero eliminates a particular process in the model. In this indirect way, parameter estimation leads to comparisons of conceptually distinct models as well as estimates of goodness-of-fit. Again, as in Bayesian hypothesis testing, the probability structure of residuals must be known or assumed.

Measures of goodness-of-fit used in probabilistic validation approaches, such as described above, typically involve variances or sums-of-squares of the observed variables. While these performance measures have statistical significance, other integrated performances measures may be more adequate with regard to the actual in-situ processes at play or with regard to practical objectives and regulatory standards. Use of these integrated performance measures as acceptance criteria in probabilistic validation tests deserves further study.

6.10 REFERENCES

Ababou, R. 1988. *Three-Dimensional Flow in Random Porous Media.* PhD Thesis. 2 Vols. Cambridge, MA: Department of Civil Engineering, Massachusetts Institute of Technology.

Ababou, R. 1990. Numerical analysis of unsaturated flow equations. *Proceedings VIIIth Conference on Computational Methods in Water Resources.* G. Gambolati et al., eds. Venice, Italy: Computational Mechanics Publications and Springer-Verlag: A: 151-160.

Ababou, R. 1991a. *Approaches to Large-Scale Unsaturated Flow in Heterogenous, Stratified, and Fracturated Geologic Media.* NUREG/CR-5743. Washington, D.C.: NRC.

Ababou, R. 1991b. Three-dimensional flow in heterogeneous geologic media: high-resolution simulations. *Proceedings International Hydrology and Water Resources Symposium.* Oct. 2-4, 1991. Perth, Australia: 725-731.

Ababou, R., and B. Sagar. 1991. Testing procedures for variably saturated, spatially distributed flow models. San Antonio, Texas: CNWRA. Submitted to *Advances in Water Resources.*

Barenblatt, G. I., V. M. Entov, and V. M. Ryzhik. 1990. *Theory of Fluid Flows Through Natural Rocks.* Dordrecht, The Netherlands: Kluwer Academic Publishers.

Bear, J. 1972. *Dynamics of Fluids in Porous Media.* New York: American Elseiver.

Buckingham, E. 1907. *Studies on the Movement of Soil Moisture.* Bulletin No. 8. Washington, D. C.: U.S. Dept. Agric. Bureau of Soils.

Burks, A. W. 1977. *Chance, Cause, Reason: An Inquiry Into the Nature of Scientific Evidence.* Chicago, IL: The Univ. of Chicago Press: 694+.

Carrera, J., et al. 1989. INTRAVAL-*An International Project to Study Validation of Geosphere Transport Models.* Progress Report No. 4, March-October 1989. Stockholm, Sweden: Swedish Nuclear Power Inspectorate.

Cushman, J. 1990. *Dynamics of Fluids in Hierarchical Porous Media.* J. Cushman, ed. New York, NY: Academic Press: 505.

Dagan, G. 1987. Solute transport in groundwater. *Annual Review of Fluid Mechanics.* 19.

Gelhar, L. W., and C. L. Axness. 1983. Three-dimensional stochastic analysis of macrodispersion in aquifers. *Water Resour. Res.* 19(1): 161-180.

Kuhn, T. 1970. *The Structure of Scientific Revolutions.* Chicago, IL: The University of Chicago Press.

Philip, J. R. 1957. Numerical solution of equations of the diffusion type with diffusivity concentration-dependent II. *Australian Journal of Physics.* 10(2): 29-42.

Polya, G. 1954. *Mathematics and Plausible Reasoning: Vol. 2, Patterns of Plausible Inference*. Princeton, NJ: Princeton University Press.

Popper, K. R. 1935. *Logik der Forschung*. Vienna, Austria: Julius Springer.

Popper, K. R. 1959. *The Logic of Scientific Discovery*. London, England: Hutchinson Co.

Richards, L. A. 1931. Capillary conduction of liquids through porous medium. *Physics*. 1: 318-333.

Runchal, A. K., and B. Sagar. 1989. *PORFLO-3: A Mathematical Model For Fluid Flow, Heat, and Mass Transport in Variably Saturated Geologic Media, Users Manual, Version 1.0*. WHC-EP-0042. Richland, WA: Westinghouse Hanford Company.

Sagar, B., and A. K. Runchal. 1990. *PORFLO-3: A Mathematical Model For Fluid Flow, Heat, and Mass Transport in Variably Saturated Geologic Media, Theory and Numerical Methods, Version 1.0*. WHC-EP-0042. Richland, WA: Westinghouse Hanford Company.

Shapiro, A. M. 1987. Transport equations for fractured porous media. *Advances in Transport Phenomena in Porous Media*. J. Bear and M.Y. Corapcioglu, eds. NATO A.S.I. Series E, No. 128. Brussels, Belgium: North Atlantic Traty Organization: 405-471.

Winter, C. L., C. M. Newman, and S. P. Neuman. 1984. A perturbation expansion for diffusion in a random velocity field. *SIAM J. Appl. Math.* 24: 411-424.

Yeh, G. T., and D. S. Ward. 1979. *FEMWATER: A Finite-Element Model of Water Flow through Saturated-Unsaturated Porous Media*. ORNL-5567. Oak Ridge, TN: Oak Ridge National Laboratory.

7 GEOCHEMICAL NATURAL ANALOGS

by English C. Pearcy and William M. Murphy

Investigators: English C. Pearcy (CNWRA), William M. Murphy (CNWRA), Ronald T. Green (CNWRA), Bret W. Leslie (CNWRA), and James D. Prikryl (CNWRA)

7.1 TECHNICAL OBJECTIVES

The Geochemical Natural Analog Research Project is designed to provide knowledge of the state of the art in natural analog studies applied to contaminant transport, to conduct investigations of a specific site or sites, and to permit evaluation of the use of analog data to support modeling appropriate for performance assessment of a Yucca Mountain repository. Task 1 of the project, "Literature Review," was completed with the submission of the report entitled "Geochemical Natural Analog Literature Review" (Pearcy and Murphy, 1991a). The first activity within Task 2, "Identification of Site and Development of Workplan," has been completed with the submission of a workplan report for the Peña Blanca, Mexico, natural analog. The remainder of Task 2 will consist of field evaluation of the Akrotiri natural analog; this work is planned for 1992 when the Akrotiri site will next be available for direct observation.

Objectives of Task 2 included (1) selection of a site at which to conduct analog research likely to yield information relevant to processes and events controlling contaminant transport in the proposed high-level nuclear waste (HLW) repository at Yucca Mountain, Nevada, and (2) development of a workplan to obtain that information. These objectives were met through literature review (Pearcy and Murphy, 1991a) and the conduct of field and laboratory research (Pearcy and Murphy, 1991c). The Nopal I deposit in the Peña Blanca, Mexico, uranium district was selected for research.

The primary objective of Task 3 is to develop methodologies for data acquisition and to implement those methodologies for the Peña Blanca natural analog. This is the main data acquisition activity for the natural analog study and, as such, encompasses a wide variety of techniques such as sampling of water, rock, and gas; mapping of lithology, structure, mineralogy, and alteration; petrographic analysis of rocks; chemical analysis of water, rock, gases, and minerals; the isotopic analysis of waters, rocks, gases, and minerals. These data will provide the basis for development of conceptual and numerical models within Task 4.

7.2 RESEARCH RESULTS DURING THE THIRD QUARTER OF 1991

During this quarter, optical petrography, scanning electron microscopy, electron-microprobe energy-dispersive and wave-length dispersive analyses, and X-ray diffractometry were conducted on samples from the Peña Blanca analog site to characterize the ore and host-rock mineralogy, chemical composition, and phase relations. This report presents the results of these analyses and preliminary interpretations.

The primary mineral assemblage of the Nopal I deposit has been tentatively established as uraninite+kaolinite+pyrite. The hydrothermal fluids that deposited the uranium at Nopal I were essentially restricted to the permeable zone defined by the breccia body. This assemblage has undergone oxidative alteration, producing a suite of secondary uranyl silicate and uranyl oxy-hydroxide minerals. The altering fluids appear to have been restricted to migration along preexisting veinlets in some areas; in other areas, the altering fluids appear to have migrated through the matrix of the host tuffs. Radiometric surveys and field observations indicate that no extensive uranium migration has occurred laterally out of the breccia zone as a result of interaction with the fluids responsible for the secondary oxidation of the orebody.

7.3 PRIMARY AND SECONDARY URANIUM PHASES AT THE NOPAL I DEPOSIT

7.3.1 Uraninite

Uraninite (UO_{2+x}) was apparently the form in which uranium was originally precipitated from hydrothermal solutions moving through the breccia pipe at the Nopal I deposit. Uraninite crystals most commonly have a granular anhedral form with maximum dimensions on the order of 5μm and are intimately intergrown with well-formed crystals of kaolinite. Euhedral pyrite crystals also occasionally occur intergrown with the uraninite. Precipitation apparently took place in open fractures between breccia fragments with uraninite, pyrite, and kaolinite being co-deposited. The uraninite-bearing veinlets are quite small, with maximum widths of about 1-2 mm. There is no evidence of symmetric precipitation upon opposing fracture surfaces; mineral compositions, crystal sizes, and crystal morphologies are approximately constant across the veinlets.

In some veinlets, the uraninite has a colloform texture, with masses rimming formerly open voids which are now filled with secondary uranium minerals. The colloform uraninite has both radial and concentric microfractures along which the uraninite is altered to secondary uranium minerals. This colloform uraninite is largely free of intergrown kaolinite, indicating a reduced activity of silica and aluminum during its formation. Similarly, the secondary uranyl minerals in contact with the colloform uraninite include the silica-free mineral compreignacite ($K_2(UO_2)_6O_4(OH)_6 \bullet 8H_2O$), consistent with a low silica activity near the colloform uraninite.

Uraninite analyses by electron microprobe show that Nopal I uraninite is oxidized significantly above the ideal reduced UO_2 stoichiometry (Table 7-1 and Figure 7-1). These analyses also recorded significant concentrations of Si (0.46 to 2.64 atom percent) and Al (0.01 to 0.77 atom percent) in all uraninite measurements. One group of uraninite crystals also had substantial Ca (1.39 to 1.77 atom percent). These elements may be incorporated in the uraninite structure or could result from additional mineral phases that are intergrown with the uraninite and are too small to be differentiated by scanning electron microscopy (SEM). For example, given the observable intergrowth of kaolinite in the granular uraninite, it would not be surprising to have a still smaller scale of kaolinite intergrowth beyond the resolution of the SEM. It is likely that portions of the measured uranium contents are also contributed by similarly small

Table 7-1. ELECTRON MICROPROBE ANALYSES OF NOPAL I URANINITE

	O	Si	Al	U	Th	Ca	K	Fe	Ti
Granular uraninite	71.15	0.79	0.11	27.95	0.00	0.01	0.00	0.00	0.00
	73.34	2.64	0.19	23.71	0.00	0.02	0.00	0.06	0.05
	70.19	0.55	0.43	27.13	0.00	1.63	0.00	0.00	0.07
	69.70	0.48	0.23	27.71	0.01	1.77	0.00	0.04	0.05
	71.61	1.74	0.77	24.48	0.00	1.39	0.00	0.00	0.00
	72.21	0.58	0.26	26.85	0.01	0.00	0.00	0.07	0.03
	73.46	1.01	0.12	25.33	0.00	0.00	0.00	0.00	0.08
Colloform uraninite	70.28	0.46	0.01	29.17	0.00	0.00	0.00	0.02	0.06

inclusions of uranyl silicates and uranyl oxy-hydroxides. Essentially no Th was found in these uraninites, whose composition has been interpreted at other deposits to indicate that the hydrothermal fluids which formed the deposit were of meteoric rather than magmatic origin (Frondel et al., 1967). Energy-dispersive X-ray analyses found no Pb in or associated with the Nopal uraninites, indicating that the deposit is relatively young.

7.3.2 Soddyite

X-ray diffractometry and electron-microprobe studies indicate that soddyite ($(UO_2)_2SiO_4 \cdot 2H_2O$) is the most abundant secondary oxidized uranium mineral in the Nopal I deposit in close association with uraninite and occurs in several forms (Figure 7-2). The original uraninite is altered to pseudomorphs of soddyite by a bulk replacement of the primary mass. These crystals are, therefore, anhedral and have maximum dimensions of about 5μm, as did the precursor crystals. The kaolinite intergrown with the original uraninite remains intergrown with the replacement soddyite. In areas with open spaces, soddyite fills the voids with relatively large (30 to 50μm) crystals, which have the form of the cavities they fill. This soddyite was precipitated along with crystals of compreignacite ($K_2(UO_2)_6O_4(OH)_6 \cdot 8H_2O$), identified by electron microprobe, which fill the remainder of the void space and have similar abundance and crystal size. In other areas, soddyite formed euhedral crystals with maximum dimensions on the order of 50 to 100 μm. These crystals occur in formerly open spaces now filled with kaolinite. In other areas, veinlets about 30μm wide are composed wholly of anhedral soddyite crystals with maximum dimensions on the order of 10 μm. These soddyite veinlets have a well-developed

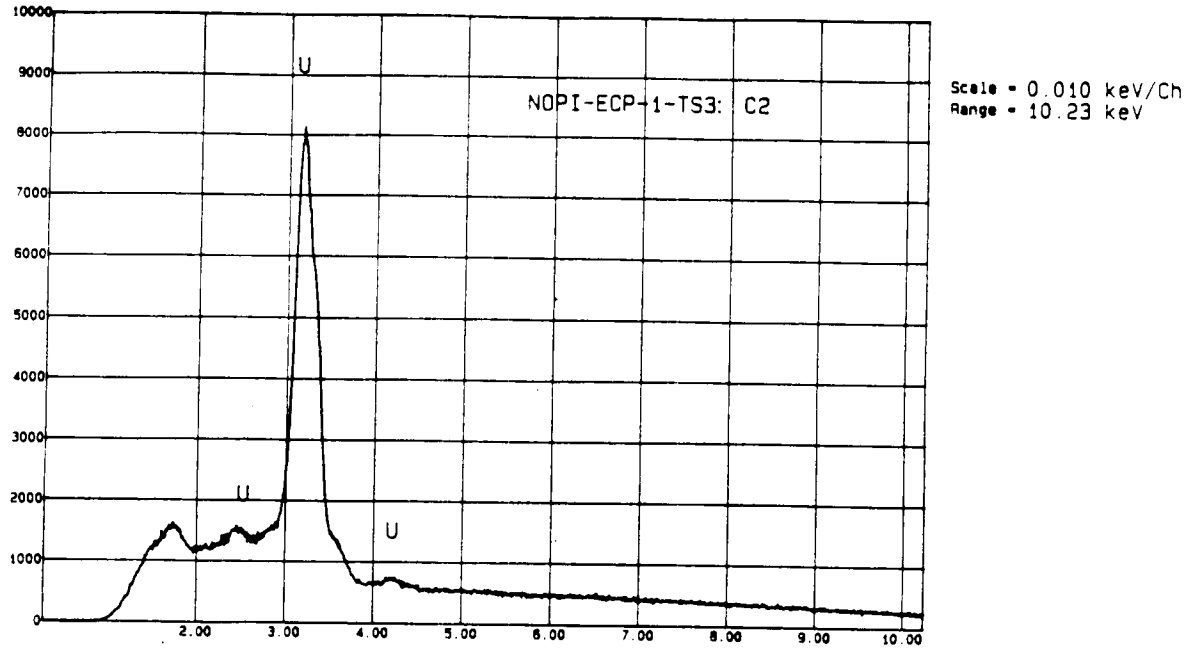

Figure 7-1. Energy-dispersive X-ray analysis of granular uraninite

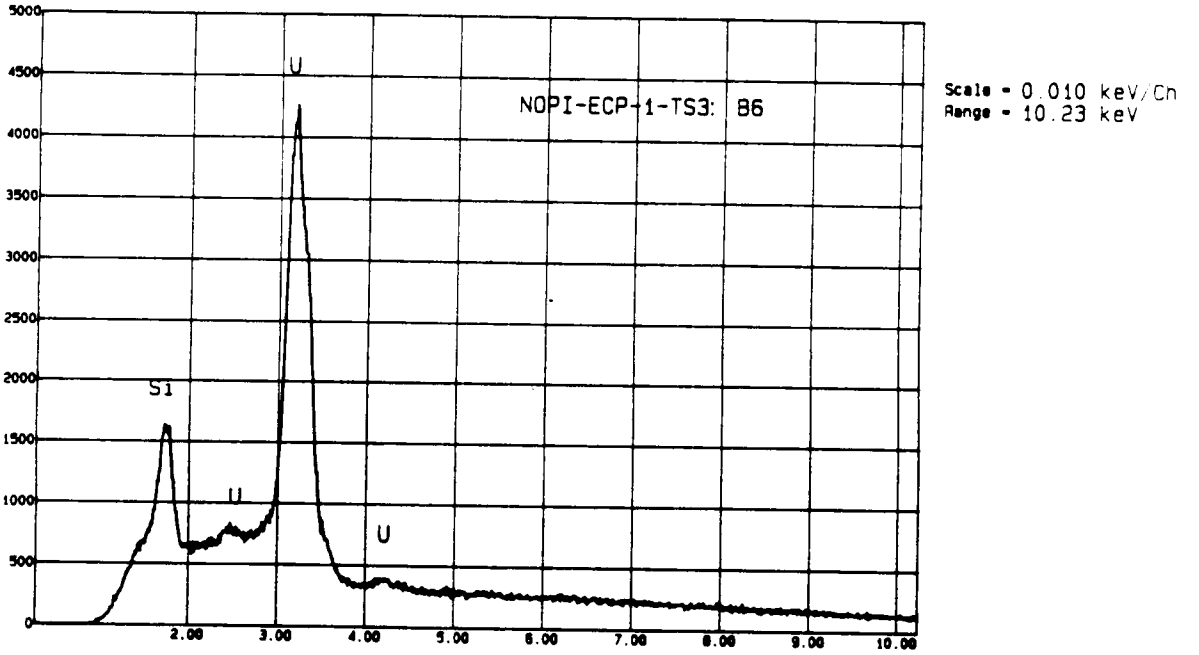

Figure 7-2. Energy-dispersive X-ray analysis of soddyite

cockscomb texture, indicating open-space filling; and these veinlets cross-cut all earlier features, suggesting relatively late formation.

7.3.3 Uranophane

Uranophane ($Ca(UO_2)_2Si_2O_7 \bullet 6H_2O$) occurs as small ($< 10\mu m$) anhedral crystals and as radiating sprays of needle-like crystals precipitated in open spaces (Figure 7-3). Uranophane tends to occur somewhat further from the uraninite than soddyite ($(UO_2)_2SiO_4 \bullet 2H_2O$) or weeksite ($K_2(UO_2)2Si_6O_{15} \bullet 4H_2O$) both on the scale of both the deposit (meters) and on the scale of individual thin sections (millimeters). In general, uranophane is more abundant where the ore has undergone late oxidation and argillic alteration.

7.3.4 Weeksite

Weeksite ($K_2(UO_2)_2Si_6O_{15} \bullet 4H_2O$) has a limited occurrence. It has not been observed in the veinlets closely related to the original uraninite mineralization. In one form of occurrence, weeksite replaces sanidine crystals in the host tuffs several kilometers from the areas of remaining uraninite. This replacement is pervasive, with no obvious relation to local fractures. The fluids appear to have migrated through the pore space of the host rock. Other weeksite fills open spaces in strongly oxidized ore with delicate sprays of radiating crystals.

7.3.5 Compreignacite

Compreignacite ($K_2(UO_2)_6O_4(OH)_6 \bullet 8H_2O$) has been identified by electron microprobe and forms a late veinlet filling juxtaposed with colloform uraninite (Figure 7-4). Compreignacite has not previously been reported at Nopal I or elsewhere in the Peña Blanca district. The irregular compreignacite crystals are anhedral, having taken the form of the original void space. Maximum dimensions of these crystals are about 30 to $50\mu m$. This compreignacite was precipitated along with crystals of soddyite ($(UO_2)_2SiO_4 \bullet 2H_2O$), which fill the remainder of the volume and have similar abundance and crystal size. Compreignacite is the only silica-free secondary uranium mineral identified in contact with uraninite at Nopal I.

7.4 DISCUSSION

7.4.1 Primary Mineralogy

The original ore mineralogy of the Nopal I uranium deposit appears to have been uraninite, pyrite, and kaolinite. These minerals precipitated from hydrothermal solutions which moved through a breccia pipe, forming anastomosing veinlets typically only a few millimeters in width. Breccia fragments vary widely in size from about 1 meter to less than 1 millimeter in maximum dimension. The margins of the breccia pipe are quite sharp, with the transition to unbrecciated host rock occurring over a distance of about 1 meter. This transition is accompanied by an equally sharp drop in the uranium content as indicated by field scintilometer

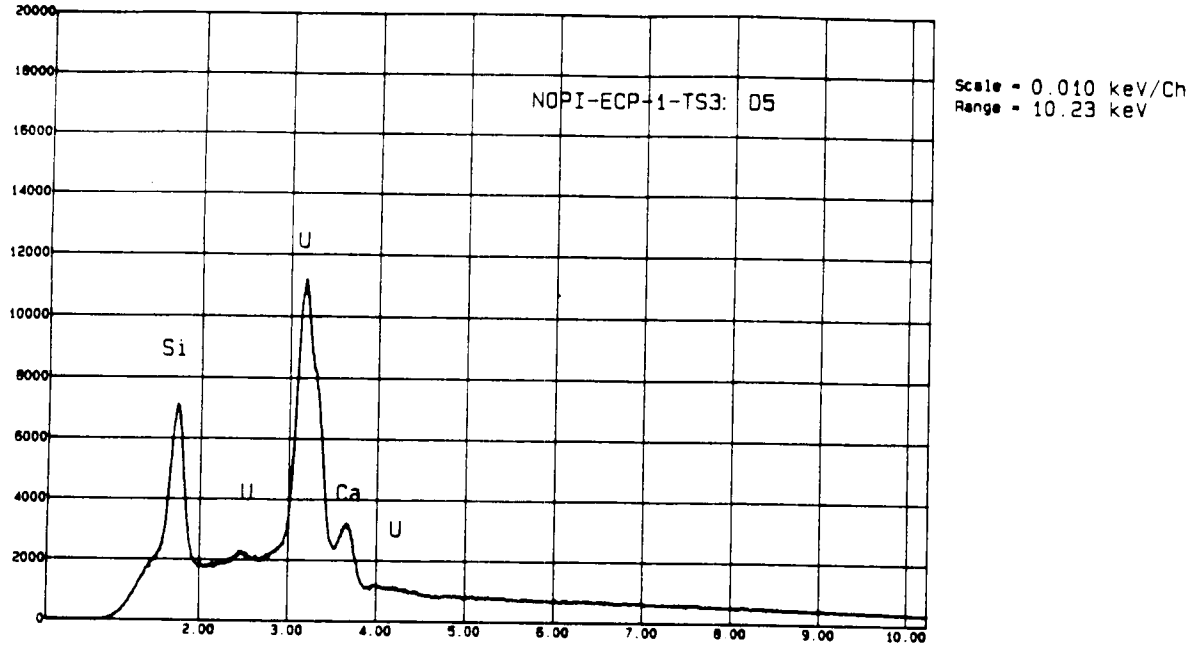

Figure 7-3. Energy-dispersive X-ray analysis of uranophane

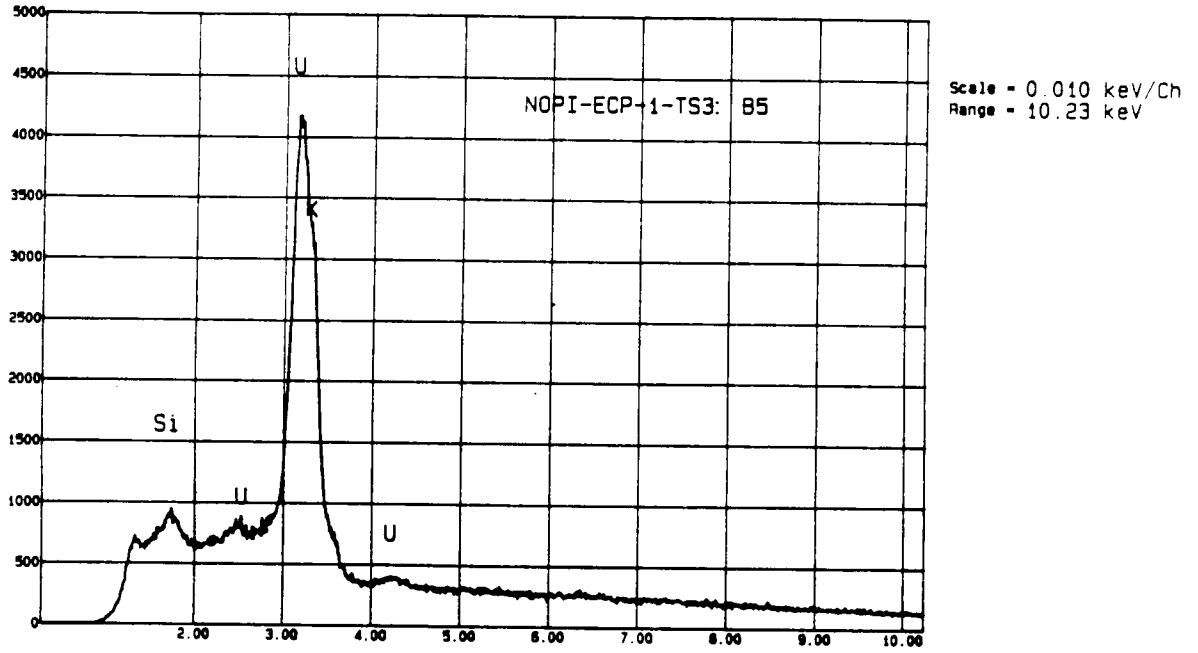

Figure 7-4. Energy-dispersive X-ray analysis of compreignacite

measurements. This abrupt change suggests that flow of the original uranium-depositing solutions was restricted to the permeable zone of the breccia pipe.

7.4.2 Oxidative Alteration and Secondary Mineralogy

The primary uraninite has been altered to a suite of secondary minerals. This alteration may have occurred in more than one event and may have spanned considerable time. It is not presently clear whether the alteration was a result of infiltrating meteoric fluids or was caused by post-depositional hydrothermal fluids passing through the ore body or some combination of these processes. The altering fluids were oxidizing and contained substantial silica, in addition to potassium and calcium. This composition probably reflects interaction of the altering fluids with the host tuffs, which have abundant silica and potassium (4.1 to 6.5 weight percent) (largely as glass shards) and modest amounts of calcium (0.4 to 4.4 weight percent) (Pearcy; and Murphy, 1991b). Calcium may also have been supplied by limestones underlying the volcanic sequence or by interaction of descending meteoric fluids with caliche near the surface (Murphy and Pearcy, 1991).

Primary uraninite is preserved only in strongly silicified areas near the center of the Nopal I orebody. In these areas, the breccia fragments are almost entirely replaced by cryptocrystalline silica and contain euhedral pyrite crystals. It is likely that the reduced permeability of these silicified zones contributed to the preservation of the uraninite by restricting flow of altering fluids to the preexisting, mineralized fractures. In some parts of the district without the silicification present at Nopal I (e.g., the Puerto I deposit), pervasive replacement of sanidine crystals by weeksite has occurred with no apparent relation to local fractures, suggesting migration of the altering fluids through the interconnected pore spaces of the host rocks rather than along fractures.

Where the reaction front between the original uraninite and the secondary uranyl silicates is observed, the oxidation of the uraninite is clearly a result of fluid flow along the uraninite-containing veinlets rather than fluids contacting the uraninite by moving through the matrix of the breccia fragments. Alteration typically produces an approximately symmetric change in the mineralization, with relatively unaltered uraninite remaining along the margins of the veinlets and the center of the veinlet filled with secondary uranyl silicates. The reaction front generally has an arcuate form, with the most advanced zone located near the center of the veinlet and recording reduced fluid flow and/or chemical reaction near the veinlet margins. Generally, the outermost edge of the veinlets has a faint iron oxide halo (about 150 μm wide) suggesting that some portion of the oxidizing fluids moving along the veinlet had migrated through mineralogically unchanged uraninite present along the veinlet margins and had oxidizing portions of the iron present in pyrite within the breccia fragments. Though the uraninite through which these fluids appear to have passed is mineralogically unchanged, it has a higher average oxidation state than unaltered uraninite, consistent with exposure to such fluids.

The fine grained ($<5\mu$m) nature of the uraninite at Nopal I presents a large reactive surface area and results in pervasive replacement of the bulk uraninite as it reacts with

the oxidizing fluids. This style of alteration produces a diffuse reaction front, with the transition from unaltered uraninite to uraninite completely replaced by uranyl silicates occurring gradually. The secondary uranyl silicates form pseudomorphs of the precursor uraninite. The altering fluids do not appear to have had any effect on the kaolinite intergrown with the original uraninite.

In addition to the pervasive replacement described above, late veinlets filled with secondary uranyl silicates (mainly soddyite) cross cut the primary uraninite, the altered uraninite, and the breccia fragments themselves. These veinlets are typically much smaller than the primary mineralized veinlets (widths are about 30 to 50 μm), and the grain size of the soddyite in these later veinlets is somewhat larger than the soddyite that forms pseudomorphs of the original uraninite (10 μm versus 5 μm maximum dimension).

Compreignacite is the only silica-free secondary uranium phase identified in contact with uraninite at Nopal I. It occurs adjacent to the colloform uraninite (the only uraninite observed without intergrown kaolinite). The colloform uraninite, occurring in vugs in small veinlets, branches off from larger veinlets containing the more typical uraninite-kaolinite assemblage. The absence of kaolinite from the colloform uraninite suggests a reduced activity of silica and aluminum during its formation. The formation of silica-free compreignacite in juxtaposition with the kaolinite-free colloform uraninite is consistent with a continued low silica activity during formation of the secondary uranium minerals. This low silica activity may have been a function of the relative inaccessibility of these vugs to reactive fluids moving preferentially along the larger veinlets.

7.5 CONCLUSIONS

The primary ore mineral assemblage of the Nopal I deposit has been tentatively established as uraninite+kaolinite+pyrite. This assemblage has undergone oxidative alteration producing a suite of secondary uranyl silicate and uranyl oxy-hydroxide minerals. Areas of the deposit in which the primary mineralization is preserved are strongly silicified, suggesting that the reduced permeability of these silicified zones contributed to the preservation of the uraninite.

The altering fluids appear to have been restricted to migration along preexisting veinlets in some areas, whereas in other areas the altering fluids appear to have migrated through the matrix of the host tuffs. Primary uranium mobility during the formation of the Nopal I deposit appears to have been essentially restricted to the breccia pipe. There is no mineralogic or radiometric indication of uranium precipitation laterally beyond the margins of the brecciated zone. Similarly, there is no evidence of migration out of the orebody during secondary oxidative alteration. Oxidation of the original uraninite appears to have occurred with only minor redistribution of the uranium within the orebody.

The alteration proceeded by pervasive replacement of the fine-grained uraninite as the altering fluids moved through the mineralized veinlets (rather than the matrix), forming diffuse, arcuate oxidative reaction fronts. Most commonly, the primary mineral assemblage (uraninite

+ pyrite + kaolinite) is replaced by a secondary suite of uranyl silicates and uranyl oxy-hydroxides dominated by soddyite ($(UO_2)_2SiO_4 \bullet 2H_2O$) near the uraninite and dominated by uranophane ($Ca(UO_2)_2Si_2O_7 \bullet 6H_2O$) further from the uraninite. Other secondary minerals have relatively minor occurrence; the composition of these less abundant phases is likely a function of local elemental activities and is not indicative of the broader state of the system during oxidative replacement of the original assemblage.

7.6 REFERENCES

Frondel, J. W., M. Fleischer and R. S. Jones. 1967. *Glossary of Uranium- and Thorium-Bearing Minerals*. 4th Edition. U.S. Geological Survey Bulletin 1250: 69.

Murphy, W. M., and E. C. Pearcy. 1991. "Source-term constraints for the proposed repository at Yucca Mountain, Nevada, derived from the natural analog at Peña Blanca, Mexico." *Scientific Basis for Nuclear Waste Management, Materials Research Society*, in press.

Pearcy, E. C., and W. M. Murphy. 1991a. *Geochemical Natural Analogs Literature Review*. CNWRA 90-008. San Antonio, Texas: CNWRA.

Pearcy, E. C., and W. M. Murphy. 1991b. *Geochemical Natural Analogs: Report on Research Activities for the Quarter April 1 through June 30, 1991*. CNWRA 91-02Q. San Antonio, Texas: CNWRA.

Pearcy, E. C., and W. M. Murphy. 1991c. *Geochemical Natural Analogs: Report on Research Activities for the Quarter January 1 through March 31, 1991*. CNWRA 91-01Q. San Antonio, Texas: CNWRA.

8 PERFORMANCE ASSESSMENT RESEARCH

by Budhi Sagar, Linda Tweedy, Tim McCartin, and A. Berge Gureghian

EVALUATION OF SNL TECHNOLOGY: TESTING OF DCM3D COMPUTER CODE

Investigators: Budhi Sagar (CNWRA), Linda Tweedy (SwRI), Tim McCartin (NRC), and A. Berge Gureghian (CNWRA)

8.1 TASK OBJECTIVE

The objective of this task is to evaluate the performance assessment technology developed by the Sandia National Laboratories (SNL) for the NRC. The SNL was the prime NRC contractor for performance assessment from the mid-seventies to 1990 when this technology was transferred to the CNWRA. Two SNL-developed computer codes DCM3D, a three-dimensional dual-porosity saturated-unsaturated flow code, and NEFTRAN-II, a discrete network transport code, are of special interest for potential application to an unsaturated site like Yucca Mountain. These two codes are being evaluated at CNWRA and at NRC to determine how well they perform as modules in assessing the performance of the total system.

8.2 INTRODUCTION

The DCM3D code was evaluated first. Work began with a review of literature on modeling of partially saturated flow [reported in CNWRA's First Annual Research Report (Gureghian and Sagar, 1991)]. A more comprehensive review on unsaturated flow has also been performed (Ababou, 1991). In Gureghian and Sagar (1991), preliminary tests consisting primarily of those problems provided by the author of the DCM3D computer code were reported. In this second and concluding part of the evaluation, problems not included in the code *User's Manual* (Updegraff et al., 1991) have been solved. The document by Updegraff et al. (1991) also discusses the dual-porosity formulation implemented in DCM3D to sufficient detail; therefore, theory of the code is not discussed here any further.

All four test problems described below were extracted from the literature. Because modeling of flow through partially saturated fractured rock is of recent origin, most of the literature considers flow in unfractured soils. In addition, the concept of dual porosity in modeling flow through fractured rock has rarely been applied to unsaturated regimes; it is even more difficult to find problems in the literature related to this concept. As outlined in Gureghian and Sagar (1991), the major difficulty in applying the dual-porosity concept is the estimation of the fluid transfer term that couples the equations describing flow in the two media (matrix and fracture). This difficulty is also encountered in other approaches. For example, when fractures are treated as networks, the practical determination of hydraulic properties of such networks is a major unsolved problem. Nevertheless, the differences need to be determined of the predicted flow fields using the dual-porosity concept and other approaches. The last problem, taken from

the International Code Intercomparison study (known as HYDROCOIN) is an effort to evaluate the differences. Data for the first three test problems have been taken from Magnuson et al. (1990).

8.3 TEST PROBLEM 1: COMPARISON WITH OUR ANALYTIC SOLUTION

Comparison with an analytic solution for one-dimensional unsaturated flow in a horizontal soil column has been discussed by Updegraff et al. (1991) in the *User's Manual* of DCM3D. Here we have added a comparison with a quasi-analytic solution representing flow in a vertical column so that the effects of gravity on flow can be simulated. For a single-porosity homogeneous medium, the quasi-analytic solution was obtained by Philip (1957). This solution is available as a FORTRAN code (INFIL - El-Kadi, 1987). The object of solving this problem was to assess the accuracy of DCM3D in determing the position of the wetting front in a soil undergoing vertical moisture infiltration.

8.3.1 Problem Description

In the test problems, the vertical soil column had a height of 15 cm. The finite difference grid was uniform with a grid spacing of 0.075 cm, thus the domain had 200 grid points. The soil was Yolo light clay, with hydraulic properties given by Haverkamp et al. (1977) - Eqn. (8-1) and Eqn. (8-2) below. The curve-fitting parameters in Eqn. (8-1) were α = 739.0 and β = 4.0, and those in Eqn. (8-2) were A = 124.6 and B = 1.77. The saturated hydraulic conductivity was taken to have a constant value of 0.04428 cm/hr. The saturated volumetric moisture content (or porosity) was 0.495, and the residual moisture content was 0.124. The pressure-head moisture-content relationship is given by

$$\theta(\psi) = \frac{\alpha(\theta_s - \theta_r)}{\alpha + [\ln|\Psi|]^{\beta}} + \theta_r \quad ; \tag{8-1}$$

and the pressure head-hydraulic conductivity relationship is given by

$$K(\Psi) = K_s \frac{A}{A + |\Psi|^B} \tag{8-2}$$

where

θ	=	volumetric moisture content,
θ_s	=	saturated volumetric moisture content (porosity),
θ_r	=	residual moisture content,
K	=	unsaturated hydraulic conductivity (cm/hr),
K_s	=	saturated hydraulic conductivity (cm/hr),

Ψ = pressure head (cm), and
α, β, A, B = curve fitting parameters.

The characteristic curves described in Eqn. (8-1) and Eqn. (8-2) are not part of the DCM3D code. These were coded for this test.

Initially the domain had a uniform pressure-head distribution of -601.8 cm, which corresponded to a moisture content of 0.238. The pressure-head boundary condition at the bottom surface corresponded to the value of the initial condition. The pressure-head boundary condition at the top surface was set to -1 cm which corresponded to full saturation.

8.3.2 Comparison of Results

DCM3D results were compared with the quasi-analytic solution of Philip generated by the INFIL code in Figure 8-1. The comparison showed reasonable agreement between the two solutions. Regarding the minor discrepancies, the INFIL code had some numerical approximations (e.g., summation of series) of its own. Overall, the DCM3D was able to simulate the problem of one-dimensional vertical infiltration reasonably well.

To solve this problem DCM3D used 1.24 cpu minutes on a VAX 8700 computer.

8.4 TEST PROBLEM 2 (BENCHMARK): TWO-DIMENSIONAL FLOW IN A SATURATED-UNSATURATED REGION

This problem deals with two-dimensional movement of moisture in a vertical cross section of an unconfined aquifer where the zone above the watertable is under unsaturated state conditions. Both the storativity and the hydraulic conductivity may be discontinuous (have a finite jump) at the watertable. For example, the storage in the unsaturated zone is due to change in moisture content caused by proximity to the watertable and drainage (or filling) of pores; in the saturated zone, storage is primarily due to compressibilities of the water and the medium. The objective of this test problem was to investigate the capability of DCM3D to deal with such changes in properties. The problem was solved in a transient mode for a long time to approximate steady-state conditions.

8.4.1 Problem Description

The physical domain was modeled as a 150-m wide by 35-m deep, vertical cross-section as shown in Figure 8-2. For the numerical solution, 30 evenly spaced nodes were placed in the x-direction. In the y-direction, a node spacing of 2 m was used from y = 0 to y = 18 m. The y-direction model spacing was reduced to 1 m after that. This led to 26 nodes in the y-direction for a total of 780 nodes. Initially the watertable gradient was assumed to be constant and equal to 2/150. This slope was represented in the simulation by imposing hydrostatic fixed-head boundary conditions in the saturated parts of the two vertical boundaries. The watertable

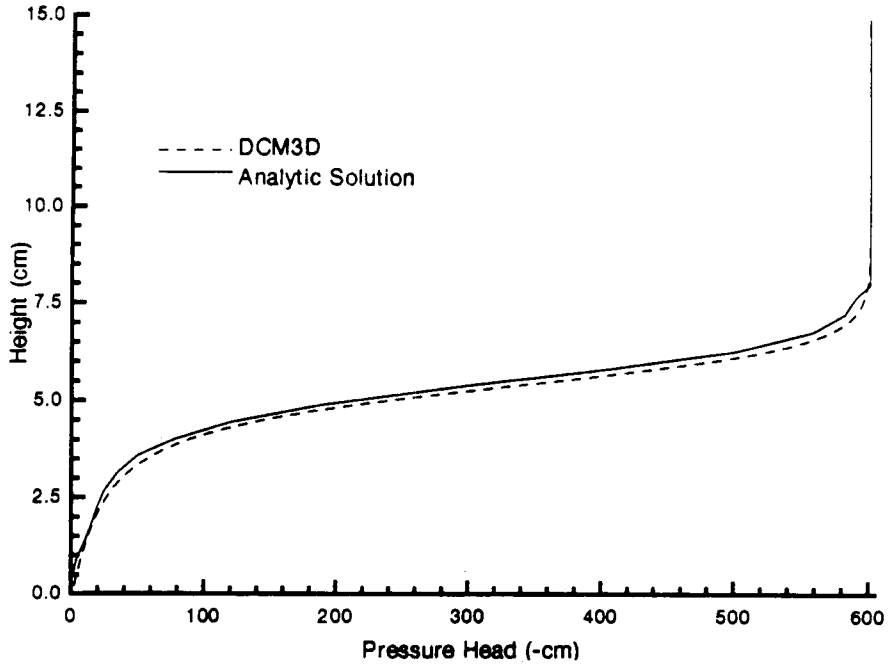

Figure 8-1. Comparison of DCM3D results with a quasi-analytic solution of a vertical infiltration problem at t = 2 hours

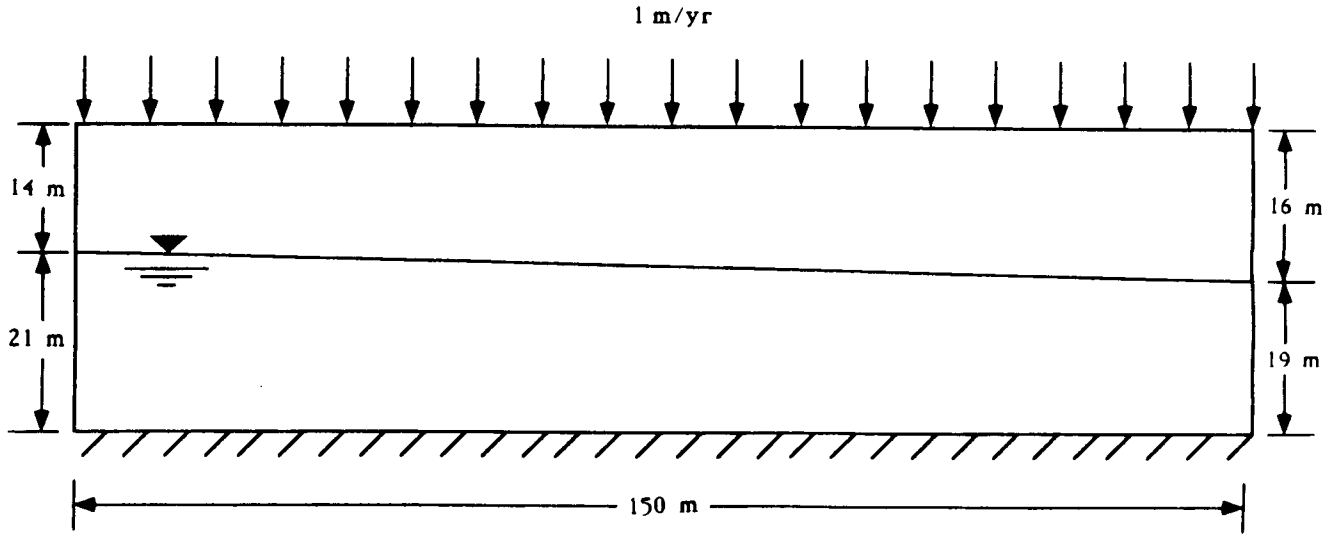

Figure 8-2. Definition sketch for Test Problem 2

itself was not an external boundary in this problem; that is, the watertable was obtained as a part of the solution except at the two external boundaries where it was fixed.

The hydraulic properties of the soil were those given by Huyakorn (1989). The saturated porosity was 0.25 and the saturated hydraulic conductivity was 750 m/yr.

The pressure-head saturation relationship is given by

$$S = 0.25 + \frac{0.75}{1+(0.2\Psi)^2} \tag{8-3}$$

and the relative hydraulic conductivity-pressure head relationship is given by:

$$K_r = [1+(0.2\Psi)^2]^{-4} \tag{8-4}$$

where

S	=	degree of saturation,
K_r	=	relative hydraulic conductivity, and
Ψ	=	pressure head.

At the top boundary, infiltration was assumed to occur at a constant rate of 1 m/yr. The bottom boundary was assigned a noflow boundary condition, as were the lateral boundaries of the model above the watertable. Pressure heads were prescribed on both upstream and downstream parts of the saturated portion of the aquifer. When using DCM3D, either the thermodynamic pressure or the pressure head can be used (but not the total hydraulic head) as the dependent variable. This means that the lateral boundaries in the saturated region have to be assigned pressure heads that vary with elevation.

The initial conditions prescribed were inconsistent with the boundary conditions. The initial conditions were assigned as though there were a watertable at a height of 18 meters. Pressure heads were assigned below 18 m according to the depth; and above 18 m, a pressure head of -10 m was assumed. However, because the problem had to be solved to a steady-state, the initial conditions were not so important.

This problem was solved by DCM3D and PORFLO-3, Version 1.0 (Runchal and Sagar, 1989; Sagar and Runchal, 1990), and results are compared below.

8.4.2 Comparison of Results

The PORFLO-3 results for this problem were taken from the report by Magnuson et al. (1990) where these results were compared with those from FEMWATER (Yeh and Ward, 1979). In Figure 8-3, steady-state pressure-head contours from DCM3D are plotted. PORFLO-3 contours are not shown, as these are exactly the same as those for DCM3D as shown in Figure 8-3. Moisture-content profiles at a section 27.5 m from the left boundary for DCM3D and 30 m

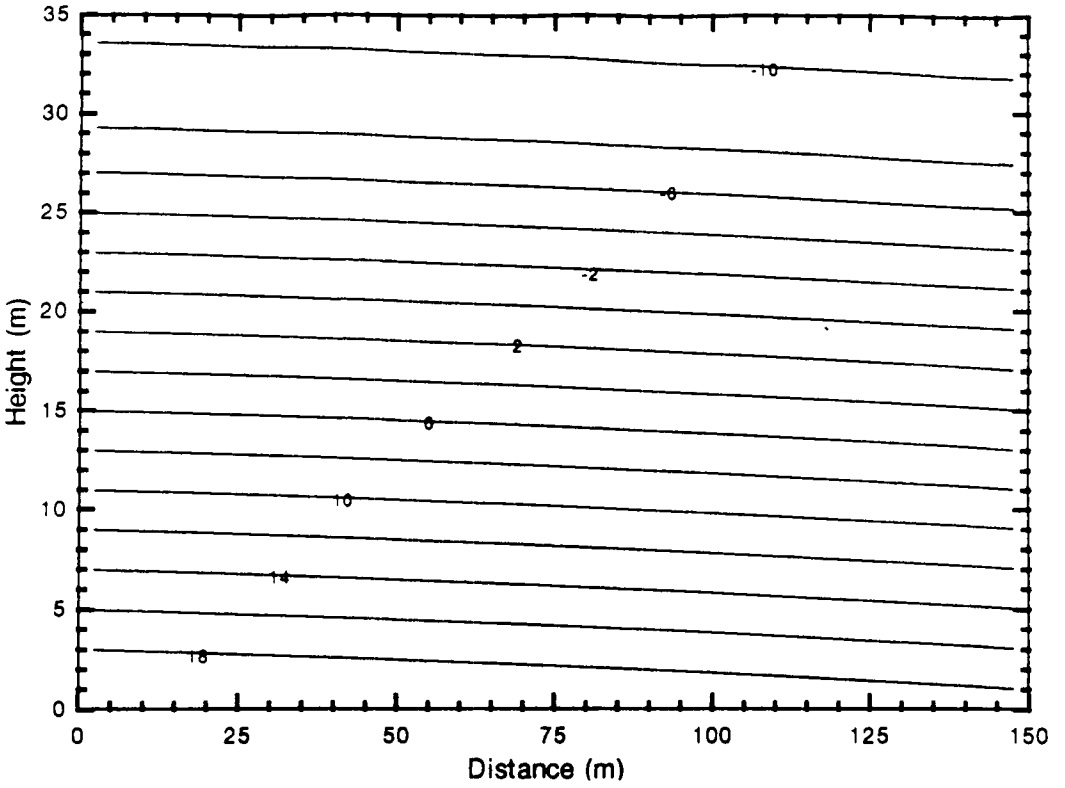

Figure 8-3. DCM3D pressure-head contour for a two-dimensional, saturated-unsaturated problem (Test Problem 2)

for PORFLO-3 are compared in Figure 8-4. The difference in locations of these sections is due to the two grid types used in the codes. DCM3D places the grid nodes in the middle of a cell, while PORFLO-3 places the cell boundary in the middle of the grid nodes. Despite this difference, the moisture contents compare favorably.

To solve this problem, DCM3D used 3.1 cpu minutes on a VAX 8700 computer.

8.5 TEST PROBLEM 3 (BENCHMARK): SIMULATION OF JORNADA TRENCH EXPERIMENT

The Jornada trench experiment is located northeast of Las Cruces, New Mexico, on the New Mexico State University College Ranch. Funded by the NRC, this experiment is expressly designed for collected data that can be used in model validation. In the following example, simulation results are not compared to the measured data but rather to simulations by another code. Hence, even though the experimental conditions are used as the input data, this test is termed a benchmark (rather than a validation) exercise. A more detailed description of this experiment was provided in the previous Quarterly Research Report (Sagar and Wittmeyer, 1991).

The Jornada test problem is conceptualized as a vertical two-dimensional, multizone, unsaturated flow problem. Soil-hydraulic properties used in this test are based on those

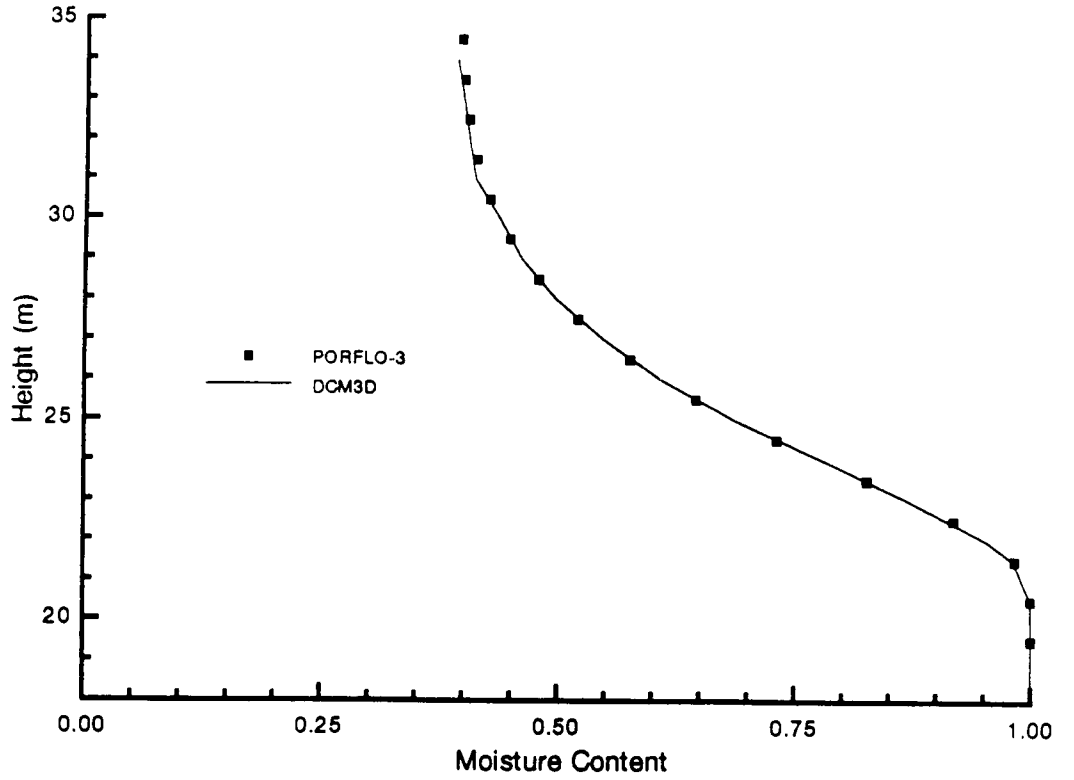

Figure 8-4. Comparison of moisture contents from DCM3D and PORFLO3 for Test Problem 2

measured at the experimental site. This particular problem involves transient infiltration of water into an extremely dry, heterogeneous soil. Because of the initial dry conditions, the problem is highly nonlinear, and therefore is a good test for DCM3D.

8.5.1 Problem Description

The computational domain of this problem was divided into four zones, as shown in Figure 8-5. A portion of the uppermost zone with a 225-cm width, measured from the top left hand corner of the domain of interest, was subjected to a water-infiltration rate of 2 cm/day (Figure 8-5). The rest of the top surface was assumed to be impervious and was modeled as a no-flow boundary. In the experiment, the lateral boundary conditions were difficult to define because the moisture content along the vertical boundaries would probably vary with time. For this test, the lateral boundaries were assumed to have zero flux crossing them. Such an assumption may cause errors (compared to the actually measured field conditions) unless the lateral boundaries are located at a great distance from the domain of interest. This problem with the lateral boundaries was not investigated further because the interest here was to compare DCM3D results to results from another code. The bottom boundary was arbitrarily assumed to have zero flux. Again, it would probably be more accurate to either extend the domain to the watertable where a zero pressure-boundary condition can be assumed or to impose a unit gradient (condition of gravity drainage). Using the first option would increase the domain size and consequently the computation time, while the second option is not available in DCM3D.

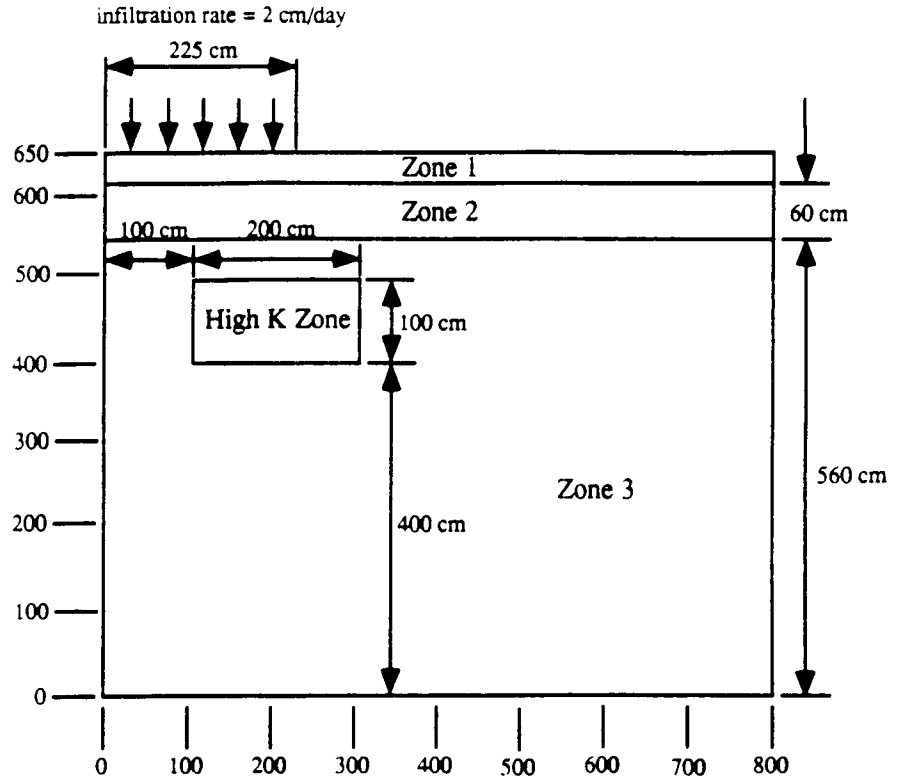

Figure 8-5. Definition sketch for the Jornada Trench experiment (Test Problem 3)

Initially, the pressure head was assumed to be uniform throughout the entire domain at -734 cm.

The physical domain modeled was 800 cm by 650 cm. There were 56 nodes in the x-direction, and 47 nodes in the y-direction (total of 2632 nodes). From x = 0 cm to x = 350 cm, and y = 350 cm to y = 650 cm, grid spacing was 10 cm. From x = 350 cm to x = 800 cm, and from y = 0 cm to y = 350 cm, grid spacing was 25 cm.

The pressure-head moisture content and relative-permeability moisture content relationships are described by the Van Genuchten (1980) equations as follows:

$$\theta = (\theta_s - \theta_r)\left(\frac{1}{1+(\alpha\Psi)^n}\right)^m + \theta_r \qquad (8\text{-}5)$$

and

$$K_r = \sqrt{\theta_e}\left\{1-\left[1-(\theta_e)^{\frac{1}{m}}\right]^m\right\}^2 . \qquad (8\text{-}6)$$

The variables are defined as follows:

θ	=	volumetric moisture content
θ_r	=	residual moisture content
θ_s	=	saturated moisture content
Ψ	=	pressure head
n	=	van Genuchten parameter
m	=	van Genuchten parameter (= 1 - 1/n)
α	=	parameter
K_r	=	relative hydraulic conductivity

The values of the input parameters for the four layers are given in Table 8-1. The solver used was the LSODES, contained in ODEPACK (Hindmarsh, 1983). A relative convergence criterion of 1.0×10^{-5} and an absolute convergence criterion of 1.0×10^{-2} was imposed.

8.5.2 Comparison of Results

Again, DCM3D results were compared to PORFLO-3 results taken from the report by Magnuson et al. (1990) in which PORFLO-3 results were compared to the results from FLASH (a code developed at INEL by Baca et al.). Earlier, Smyth et al. (1989) used the same data for a test of TRACER3D, a code developed at Los Alamos Laboratories by Travis (1984).

The simulations were run in 30-day duration. The saturations at 30 days after the start of the moisture infiltration are shown in Figure 8-6. The previous comparison of PORFLO-3, FLASH, and TRACER3D results are shown in Figure 8-7. All four codes showed a pronounced effect of the high permeability zone on moisture distribution. For this complex problem, results of all of the codes differed somewhat from each other. Figure 8-7 indicates large differences between results (e.g. in advance of the wetting front) from TRACER3D and the other codes. The DCM3D results were reasonably close to those from PORFLO-3 and FLASH.

DCM3D used 237 minutes of cpu time on a VAX 8700, while PORFLO-3 used 5.95 minutes of INEL Cray cpu time. For the same problem, the cpu times for TRACR3D and FLASH were reported to be 5.79 Hanford CRAY minutes and 16.8 INEL CRAY minutes, respectively. Unfortunately, because of different computing environments, these execution times were not directly comparable.

8.6 TEST PROBLEM 4: TWO-DIMENSIONAL FLOW THROUGH FRACTURED ROCK

The distinguishing feature of the DCM3D computer code is that it employs a dual-porosity conceptualization of the fractured porous medium instead of an equivalent porous (single

Table 8-1. VAN GENUCHTEN SOIL PARAMETERS

Zone	θ_s	θ_r	α (cm^{-1})	n	K_s
1	0.368	0.1020	0.0334	1.982	790.9
2	0.351	0.0985	0.0363	1.632	469.9
3	0.325	0.0859	0.0345	1.573	415.0
4	0.325	0.0859	0.0345	1.573	4150.0

porosity) medium or a fracture-network conceptualization. In the more common equivalent porous-medium approach, the characteristic curves for the rock matrix and the fractures are combined to form a composite characteristic curve. The composite curve assumes a rapid (with respect to the time scale of the flow being simulated) equilibration between the pressures of the fracture and matrix continua; and thus, the equilibration of pressure between the two continua is affected.

An important question is how different are the predicted flow fields for these two different conceptualizations. A convenient test case to explore this question was taken from the International Code Intercomparison study HYDROCOIN. The test case was based on a flow field associated with unsaturated-fractured tuff (Prindle, 1990). The HYDROCOIN test case was used here to examine the differences in the two conceptualizations as well as to compare the DCM3D results with the HYDROCOIN results to provide a measure of verification for DCM3D.

8.6.1 Problem Description

A complete description of the test case is provided in Prindle (1990). Only the information pertinent to the current simulations is provided here. The two-dimensional cross-section was comprised of five layers with a uniform dip of 6 degrees at unit interfaces (Figure 8-8). Additionally, a repository location and a fault zone was defined for the test case. Material properties for the various layers were reproduced from the Prindle report in Table 8-3.

The current simulations utilized modification 1 from the Prindle study. Modification 1 changed the original model description by not explicitly considering the fault zone and by modifying the rock properties according to Table 8-4. This modification was selected primarily because the beta parameter used for the van Genuchten equation was significantly lower (2.2 compared to 6.8) than the original value and was anticipated to lead to much shorter simulation times.

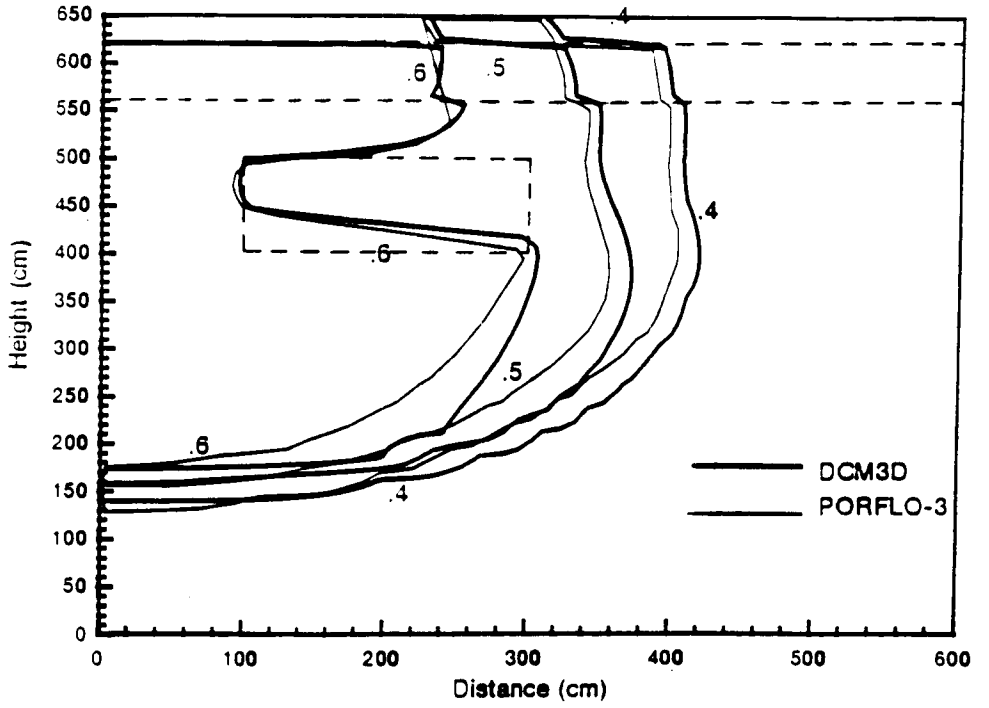

Figure 8-6. Comparison of DCM3D and PORFLO-3 results (moisture contents) for the Jornada Trench experiment (Test Problem 3)

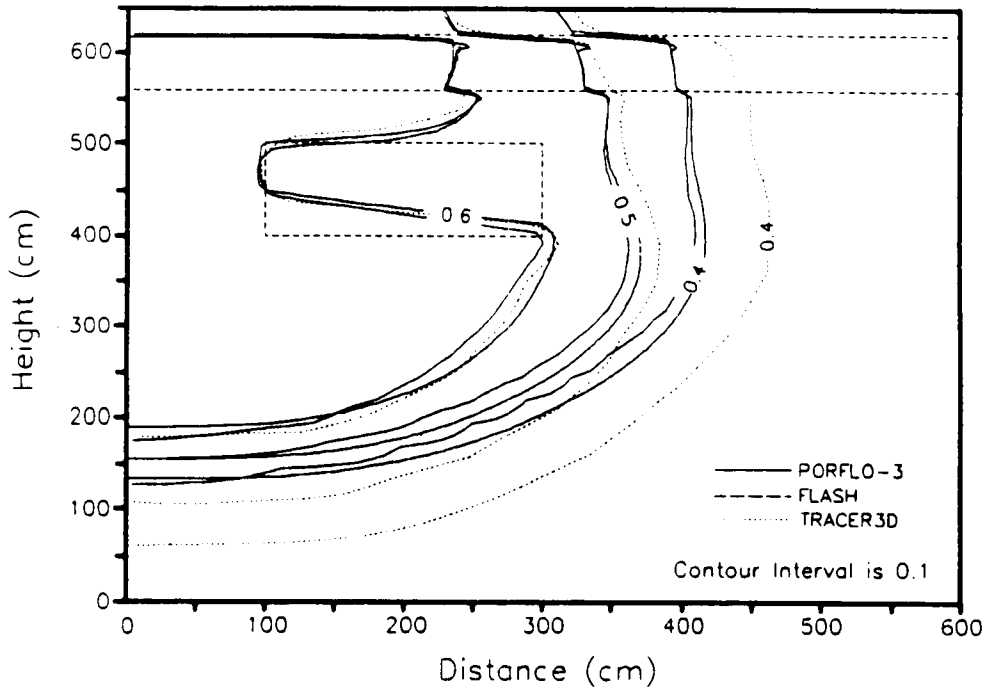

Figure 8-7. Moisture content results for Test BT-2

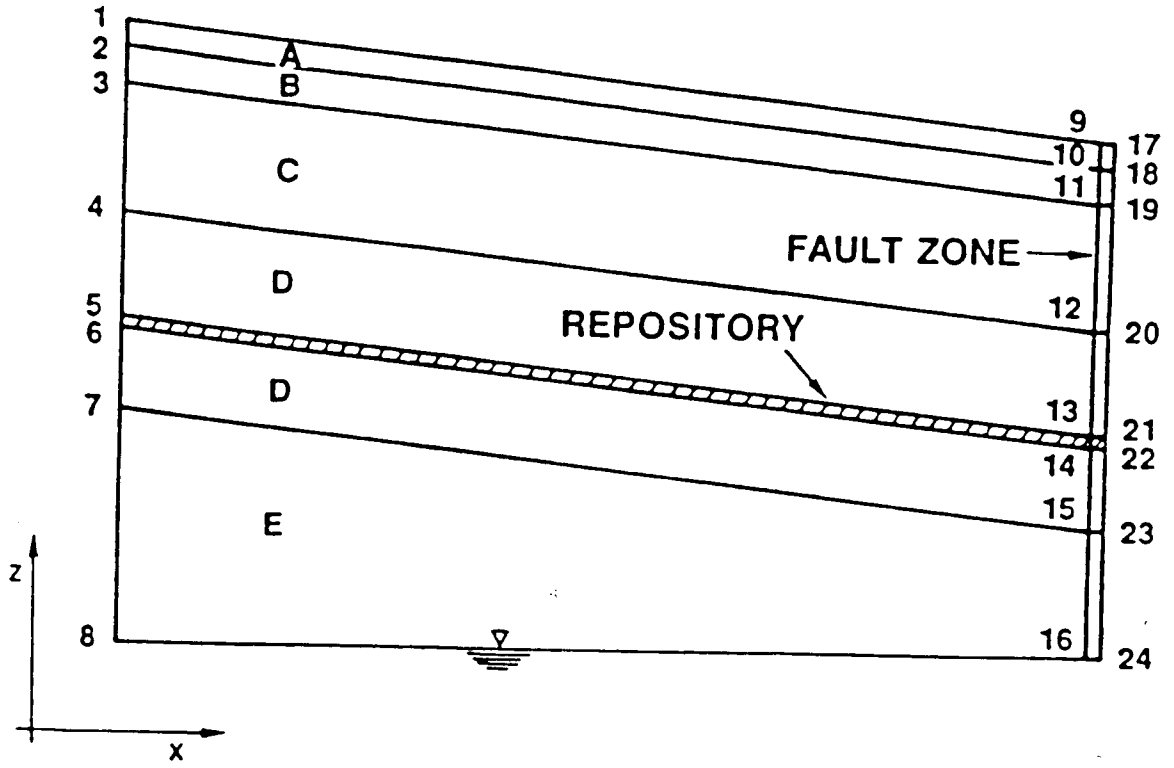

Figure 8-8. Two-dimensional base case stratigraphy (see Table 8-2 for coordinates of numbered locations) (Prindle, 1990)

The finite difference grid for DCM3D was set up to provide the finest discretization in the vertical direction for the upper units (Table 8-5) and a constant spacing in the horizontal direction. Rather than "stair-stepping" grid blocks at unit interfaces, the cross-sectional tilt was obtained by tilting gravity and increasing the depth to the watertable by 100 meters (the depth to the watertable was increased to decrease the affect of tilting the watertable boundary condition on the computational area of interest).

The tilting of gravity was considered to represent the problem description reasonably well, with the exception being near the side and bottom boundaries. Near the side boundaries, rather than a vertical boundary, the tilting of gravity causes the boundary to also appear slightly tilted. Near the bottom boundary, a significant flow is induced due to the tilting of gravity which results in a gradient of 0.1. Despite these inaccuracies, the conceptualization was considered reasonable for examining flow diversion in the upper units (top 50 meters) and the spatial distribution of flow at the repository level (400 meters below the surface).

One additional parameter (the transfer term between matrix and fracture) was needed to perform the DCM3D simulations. This parameter was based on the values in Table 8-4 and Eqn. (2-19) from the DCM3D *User's Manual* (Updegraff et al., 1991). The values thus obtained are presented in Table 8-6.

Table 8-2. COORDINATES OF THE NUMBERED POINTS IN FIGURE 8-7 (Prindle, 1990)

Point	Coordinates (m) x	z	Point	Coordinates x	z
1	0.0	635.5	13	1000.0	224.0
2	0.0	608.7	14	1000.0	219.5
3	0.0	570.6	15	1000.0	130.3
4	0.0	440.5	16	1000.0	0.0
5	0.0	329.1	17	1000.5	530.4
6	0.0	324.6	18	1000.5	503.6
7	0.0	235.4	19	1000.5	465.5
8	0.0	0.0	20	1000.5	335.4
9	1000.0	530.4	21	1000.5	224.0
10	1000.0	503.6	22	1000.5	219.5
11	1000.0	465.5	23	1000.5	130.3
12	1000.0	465.5	24	1000.5	0.0

TABLE 8-3. BASE CASE MATERIAL PROPERTIES USED FOR THE HYDROLOGIC UNITS AS DEPICTED BY LETTERS IN FIGURE 8-7 (Prindle, 1990)

Matrix Properties[b]

Unit	Grain Density (g/cm^3)	Porosity, n_m	Saturated Hydraulic Conductivity, $K_{m,b}$ m/s[c]	Residual Saturation, S_r	Alpha, α (1/m)	Beta, β
A	2.49	0.08 (0.05 – 0.15)	9.7×10^{-12} ($1.0 \times 10^{-13} - 5.0 \times 10^{-10}$)	0.002 (0.00 – 0.18)	8.21×10^{-3} (0.003 – 0.024)	1.558 (1.3 – 2.4)
B	2.35	0.40 (0.20 – 0.70)	3.9×10^{-07} ($1.0 \times 10^{-09} - 5.0 \times 10^{-05}$)	0.100 (0.00 – 0.15)	1.50×10^{-2} (0.001 – 0.031)	6.872 (1.2 – 15.0)
C	2.58	0.11 (0.05 – 0.20)	1.9×10^{-11} ($1.0 \times 10^{-13} - 5.0 \times 10^{-10}$)	0.080 (0.00 – 0.23)	5.67×10^{-3} (0.001 – 0.020)	1.798 (1.2 – 2.5)
D	2.58	0.11 (0.05 – 0.20)	1.9×10^{-11} ($1.0 \times 10^{-13} - 5.0 \times 10^{-09}$)	0.080 (0.00 – 0.32)	5.67×10^{-3} (0.001 – 0.020)	1.798 (1.2 – 2.5)
Ev	2.37	0.46 (0.30 – 0.55)	2.7×10^{-07} ($1.0 \times 10^{-13} - 5.0 \times 10^{-06}$)	0.041 (0.00 – 0.25)	1.60×10^{-2} (0.005 – 0.060)	3.872 (1.3 – 7.0)
Es	2.23	0.28 (0.20 – 0.45)	2.0×10^{-11} ($1.0 \times 10^{-14} - 5.0 \times 10^{-10}$)	0.110 (0.00 – 0.30)	3.08×10^{-3} (0.001 – 0.030)	1.602 (1.2 – 3.5)

a. Based on SNL (1987), Appendix O.

b. All base-case matrix data in this section are from Peters *et al.* (1984).

c. The matrix saturated conductivity and the bulk matrix saturated conductivity ($K_{m,b}$) are essentially the same because the factor ($1\text{-}n_f$) that converts the matrix value to the bulk matrix value is nearly equal to one.

TABLE 8-3. BASE CASE MATERIAL PROPERTIES USED FOR THE HYDROLOGIC UNITS AS DEPICTED BY LETTERS IN Figure 8-7 (Prindle, 1990) (Cont'd)

Fracture Properties[d]

Unit	Horizontal Stress[e] (bars)	Fracture Aperture (microns)	Saturated Fracture Hydraulic Conductivity (m/s)	Fracture Density[f] (no./m³)	Fracture Porosity[g], n_f
A	1.1	6.74	3.8×10^{-5} ($5.0 \times 10^{-7} - 5.0 \times 10^{-3}$)	20	1.4×10^{-4} ($1.0 \times 10^{-5} - 1.0 \times 10^{-3}$)
B	3.3	27.0	6.1×10^{-4} ($5.0 \times 10^{-6} - 5.0 \times 10^{-2}$)	1	2.7×10^{-5} ($2.0 \times 10^{-6} - 2.0 \times 10^{-4}$)
C	9.5	5.13	2.2×10^{-5} ($5.0 \times 10^{-7} - 1.0 \times 10^{-3}$)	8	4.1×10^{-5} ($2.0 \times 10^{-6} - 1.0 \times 10^{-2}$)
D	21.9	4.55	1.7×10^{-5} ($1.0 \times 10^{-7} - 1.0 \times 10^{-3}$)	40	1.8×10^{-4} ($1.0 \times 10^{-5} - 5.0 \times 10^{-3}$)
Ev	34.3	15.5	2.0×10^{-4} ($2.0 \times 10^{-6} - 2.0 \times 10^{-2}$)	3	4.6×10^{-5} ($5.0 \times 10^{-6} - 5.0 \times 10^{-4}$)
Ez	34.3	15.5	2.0×10^{-4} ($2.0 \times 10^{-6} - 2.0 \times 10^{-2}$)	3	4.6×10^{-5} ($5.0 \times 10^{-6} - 5.0 \times 10^{-4}$)

Unit	Fracture Compressibility (1/m)	Bulk Fracture Saturated Hydraulic Conductivity[h], $K_{f,b}$ (m/s)	Residual Saturation, S_r	Alpha, α (1/m)	Beta, β
A	1.3×10^{-6}	5.3×10^{-9} ($5.0 \times 10^{-13} - 5.0 \times 10^{-6}$)	0.0395 (0.0 – 0.15)	1.285 (0.2 – 6.0)	4.23 (1.2 – 7.0)
B	1.9×10^{-7}	1.6×10^{-6} ($1.0 \times 10^{-11} - 1.0 \times 10^{-5}$)	0.0395 (0.0 – 0.15)	1.285 (0.2 – 6.0)	4.23 (1.2 – 7.0)
C	5.6×10^{-6}	0.9×10^{-9} ($1.0 \times 10^{-13} - 1.0 \times 10^{-6}$)	0.0395 (0.0 – 0.15)	1.285 (0.2 – 6.0)	4.23 (1.2 – 7.0)
D	1.2×10^{-7}	3.1×10^{-9} ($1.0 \times 10^{-13} - 1.0 \times 10^{-6}$)	0.0395 (0.0 – 0.15)	1.285 (0.2 – 6.0)	4.23 (1.2 – 7.0)
Ev	2.8×10^{-6}	9.2×10^{-9} ($1.0 \times 10^{-11} - 1.0 \times 10^{-5}$)	0.0395 (0.0 – 0.15)	1.285 (0.2 – 6.0)	4.23 (1.2 – 7.0)
Ez	2.8×10^{-6}	9.2×10^{-9} ($1.0 \times 10^{-11} - 1.0 \times 10^{-5}$)	0.0395 (0.0 – 0.15)	1.285 (0.2 – 6.0)	4.23 (1.2 – 7.0)

d. Unless otherwise noted, base-case fracture information is based on Peters *et al.* (1984).
e. Horizontal stress is assumed to be one-third of the overburden weight, evaluated at the average unit depth.
f. Based on Scott *et al.* (1983).
g. Calculated as fracture volume (aperture x 1 m²) times the number of fractures per cubic meter.
h. This value of $K_{f,b}$ was obtained by multiplying the fracture conductivity by the fracture porosity.

Table 8-4. MATERIAL PROPERTIES USED IN MODIFICATION (Prindle, 1990)

Property	Unit B	Unit C	Unit D
$K_{m,b}$	1.0×10^{-7}	8.0×10^{-11}	8.0×10^{-11}
α_m	0.010	0.015	0.015
β_m	2.2	1.6	1.6
$K_{f,b}$	3.6×10^{-6}	2.0×10^{-9}	3.1×10^{-9}
n_f	9.0×10^{-6}	9.0×10^{-5}	1.8×10^{-4}

Table 8-5. DCM3D VERTICAL DISCRETIZATION INFORMATION (HORIZONTAL DISCRETIZATION IS A CONSTANT SPACING OF 50 METERS FOR 1000 METERS)

Finite Difference Row Indices	Block Thickness (meters)	Depth (meters)	Unit
1 - 35	10.0	705 - 400	Ez
36 - 55	10.0	400 - 200	D
56 - 60	10.0	200 - 150	C
61 - 63	8.0	150 - 126	C
64 - 65	6.0	126 - 114	C
66 - 67	4.0	114 - 106	C
68 - 70	2.0	106 - 100	C
71 - 100	1.0	100 - 70	C
101 - 140	1.0	70 - 30	B
141 - 170	1.0	30 - 0	A

One objective of this analysis was to compare the results assuming a composite curve with those obtained by assuming a dual-continuum approach. It was considered advantageous to implement a composite curve approach within DCM3D so as to utilize one input file for both conceptualizations. Modifications to DCM3D were made such that it would accept the composite characteristic curve as input.

8.6.2 Comparison of Results

Performance measures used for this analysis were; (1) particle paths starting along the upper boundary and (2) the spatial distribution of water flux at the repository level. The HYDROCOIN results are taken from Prindle and are presented in Figures 8-9 and 8-10. These simulation results were obtained with the computer program called NORIA (Bixler, 1985).

Although CPU times for individual runs were not provided, Prindle reported that the 94 simulations required a combined 1300 hours of CPU time on a Cray X/MP 416.

The DCM3D results utilizing the composite curve for representing the fracture/matrix continuua are presented in Figures 8-11 and 8-12. Ignoring some minor discrepancies due to boundary-condition differences, the results compare quite well with the NORIA results. This is not surprising because both programs utilizing a composite curve conceptualization.

This simulation required approximately 50 minutes of CPU time on an IBM 3090 (for comparative purposes the IBM is estimated to be 5 to 10 times slower than the Cray computer).

Table 8-6. TRANSFER FACTORS USED FOR THE UNITS IDENTIFIED IN FIGURE 8-7

Unit	Transfer Factor
A	7.92E-16
B	2.04E-14
C	1.04E-15
D	2.61E-14
Ez	3.67E-17

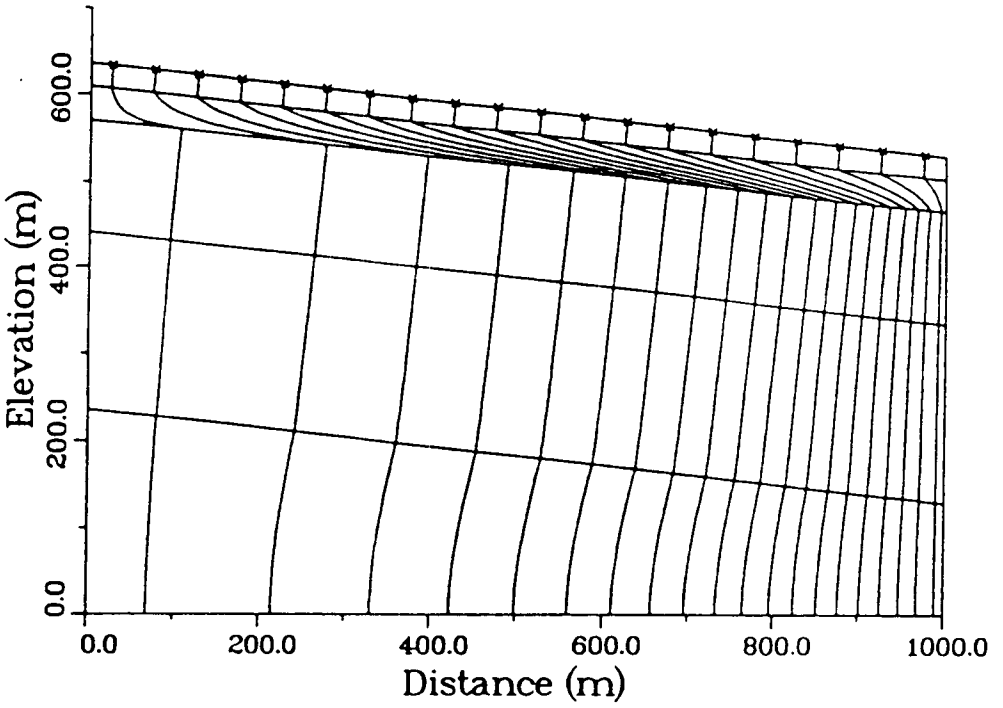

Figure 8-9. Particle paths based on the NORIA simulation (flux = 0.1 mm/yr) (Prindle, 1990)

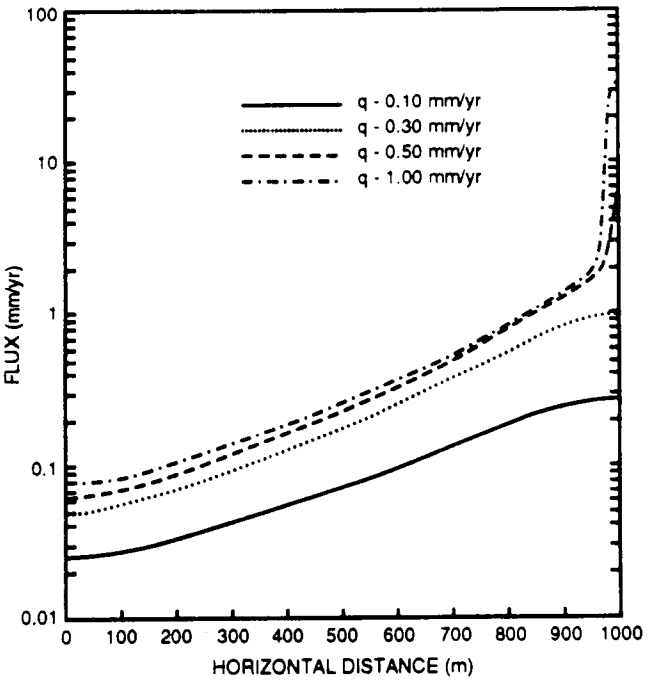

Figure 8-10. Spatial distribution of flux at the repository based on the NORIA simulation (flux = .1 mm/yr) (Prindle, 1990)

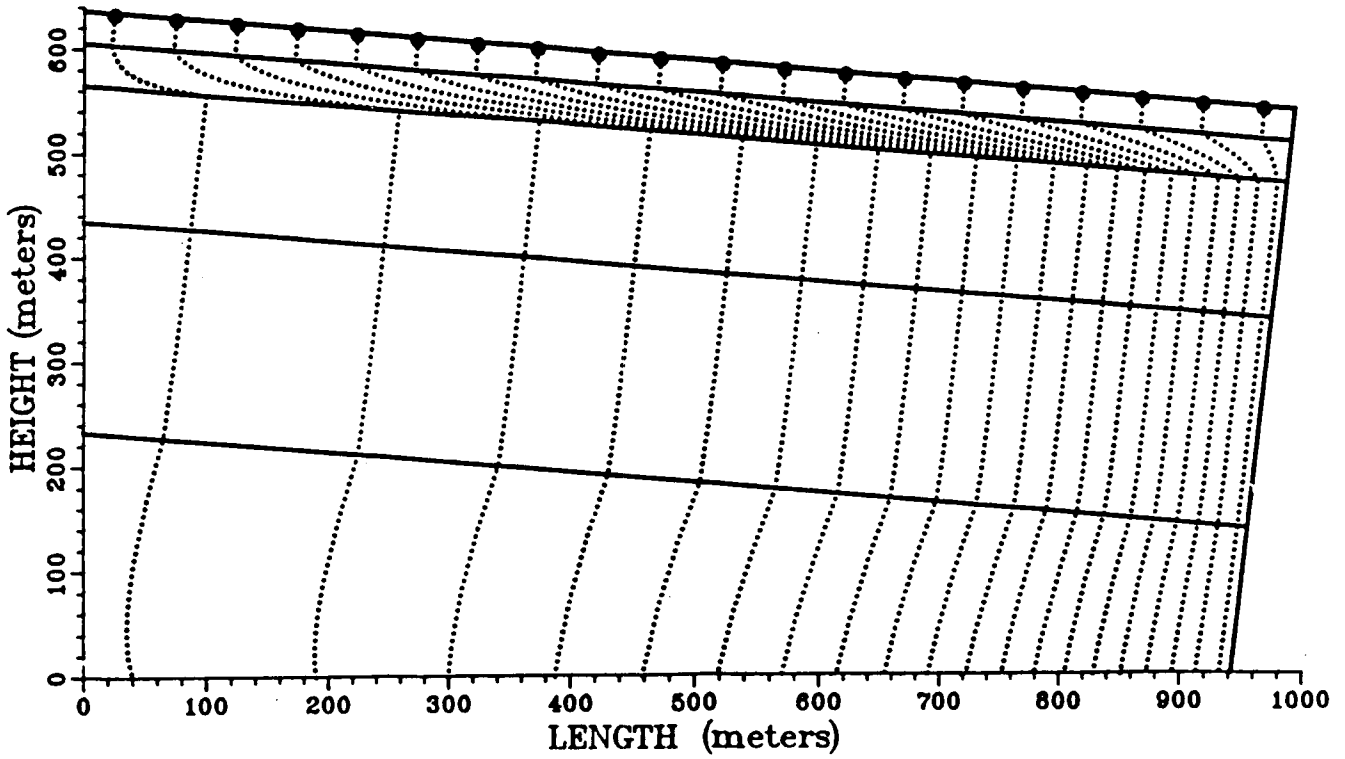

Figure 8-11. Particle paths based on the DCM3D simulation using a composite curve (flux = 0.1 mm/yr)

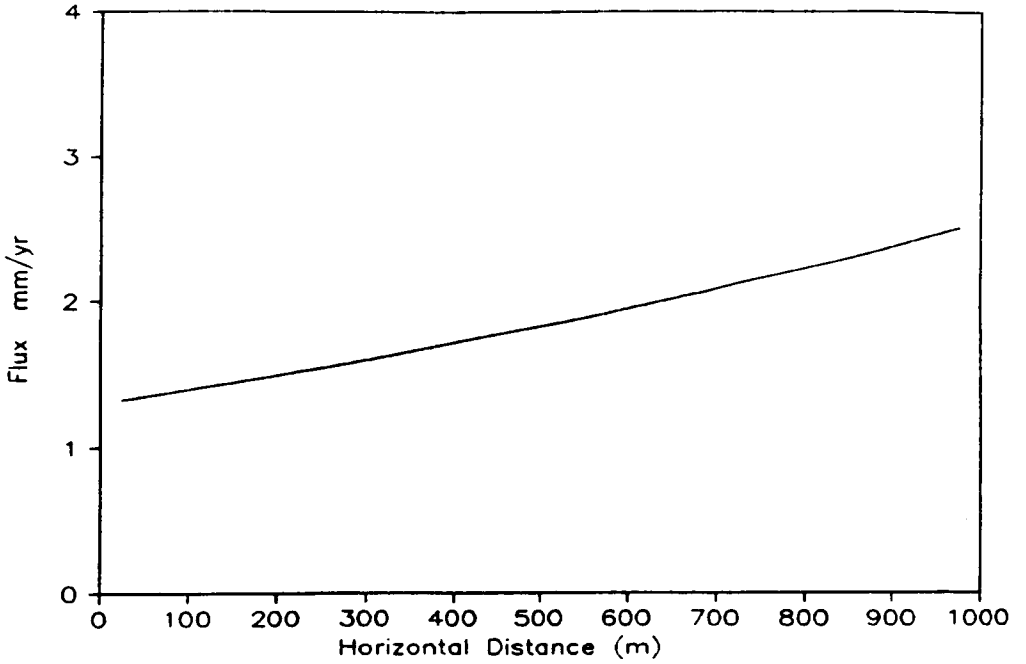

Figure 8-12. Spatial distribution of flux based on the DCM3D simulation using the composite curves (flux = 0.1 mm/yr)

The DCM3D results utilizing the dual continuum approach are presented in Figures 8-13, 8-14, and 8-15. As with the composite-curve results, the dual-continuum results compare reasonably well with the NORIA results. While a somewhat significant discrepancy does exist near the bottom boundary, it can be attributed to the tilted bottom boundary and the fact that the simulation had not reached steady-state. DCM3D does not have a steady-state option, and the user is required to select a time sufficient to reach this point. For the simulation, a point in the middle of the domain rather than at the bottom boundary was selected to reach steady-state.

The fracture particle paths did not vary significantly from the matrix paths in the dual-continuum approach due to the isotropic conditions assumed for both matrix and fractures. Future work will consider anisotropic fracture conditions and high flux rates, which could result in larger fracture flow (the current flux of 0.1 mm/year resulted in fracture flow at the repository level approximately 10 orders of magnitude lower than the matrix flow).

This simulation required approximately 8 hours of CPU time on the IBM 3090.

DCM3D results were generally in good agreement with the NORIA results. However, the dual-continuum versus the composite-curve approach needs to be examined further. To provide better insights into the differences in the models. Increased infiltration, anisotropic fracture properties, and ranges of fracture transfer terms should be utilized in future work executing the models. The current simulations however, do provide a reasonable starting point for a departure into these more difficult simulations.

8.7 SUMMARY AND CONCLUSIONS

Four test problems of increasing complexity were solved using the DCM3D computer code. In general, the code produced reasonable results for all of the four problems, indicating that the basic equations are correctly implemented in the computer code.

However, basic questions regarding the applicability of the dual-porosity approach for simulating partially saturated flow in fractured rock are not resolved by the testing discussed in this report. The main advantage of the dual-porosity approach is in its simplicity obtained by lumping the fractures as a continuum superimposed over a matrix continuum. Thus, the geometric details of the fracture network need not be considered. Presumably, such an approach is capable of considering nonequilibrium pressure distribution between the fracture and rock continua. Conceptually, such a pressure nonequilibrium will occur, for example, when the fracture surfaces are coated with minerals that alter the permeability of the fracture wall significantly. This conceptual simplicity, however, introduces a parameter that represents, in a lumped fashion, the fluid interchange between the fracture and rock continua. It is not clear how such a parameter could be measured or defined in a functional form and related to measurable media properties. It should also be clear that the dual-porosity approach does not provide information on pressure distribution at the scale, for instance, of the fracture width.

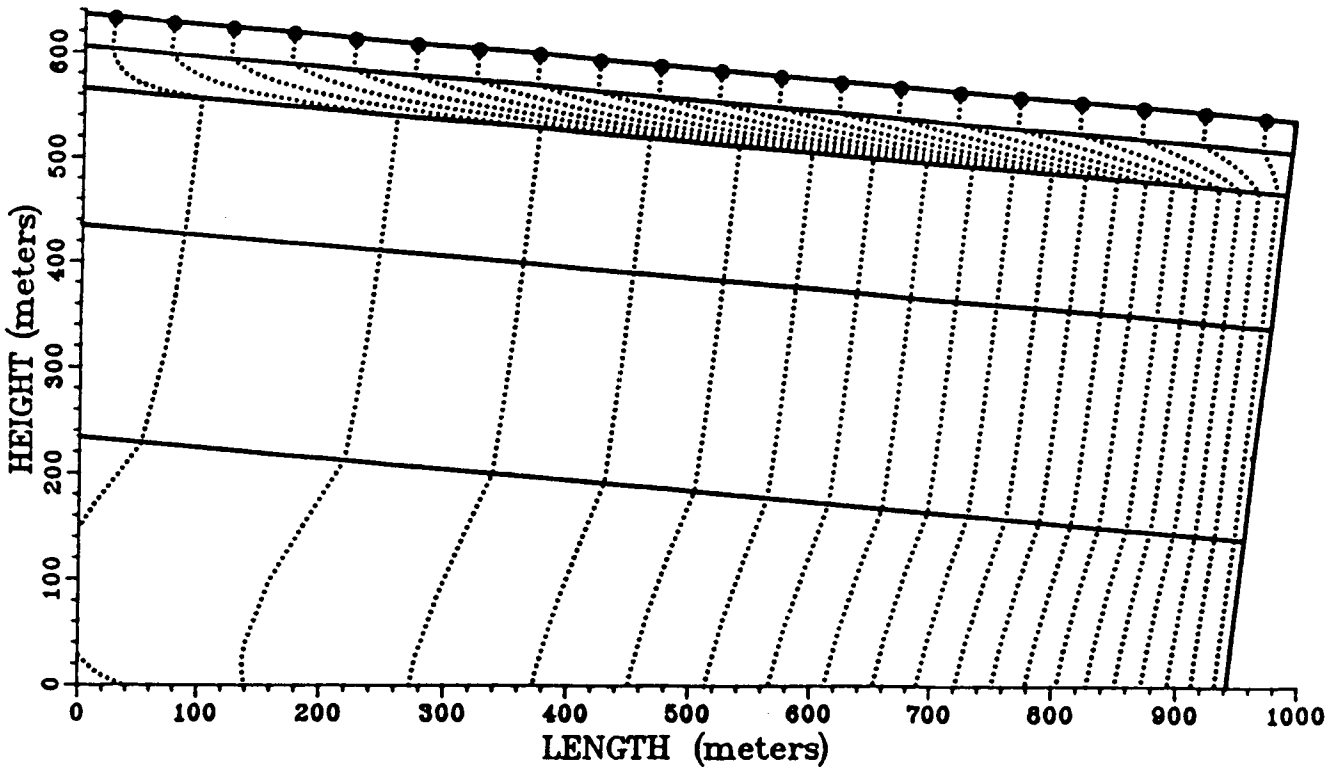

Figure 8-13. Particle paths in the matrix based on DCM3D simulations using the dual-porosity model (flux = 0.1 mm/yr)

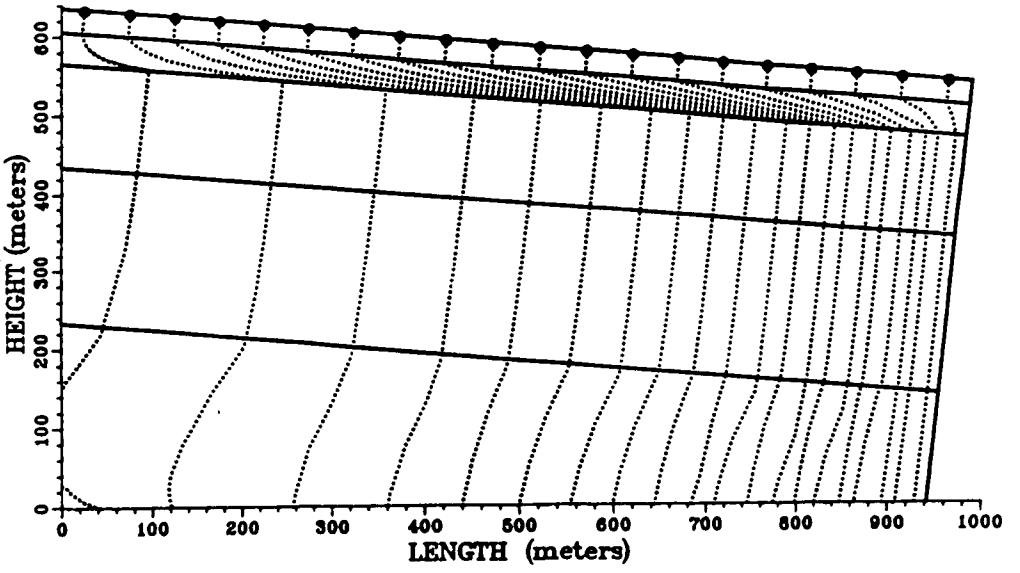

Figure 8-14. Particle paths in the fracture based on DCM3D simulations using the dual-porosity model (flux = 0.1 mm/yr)

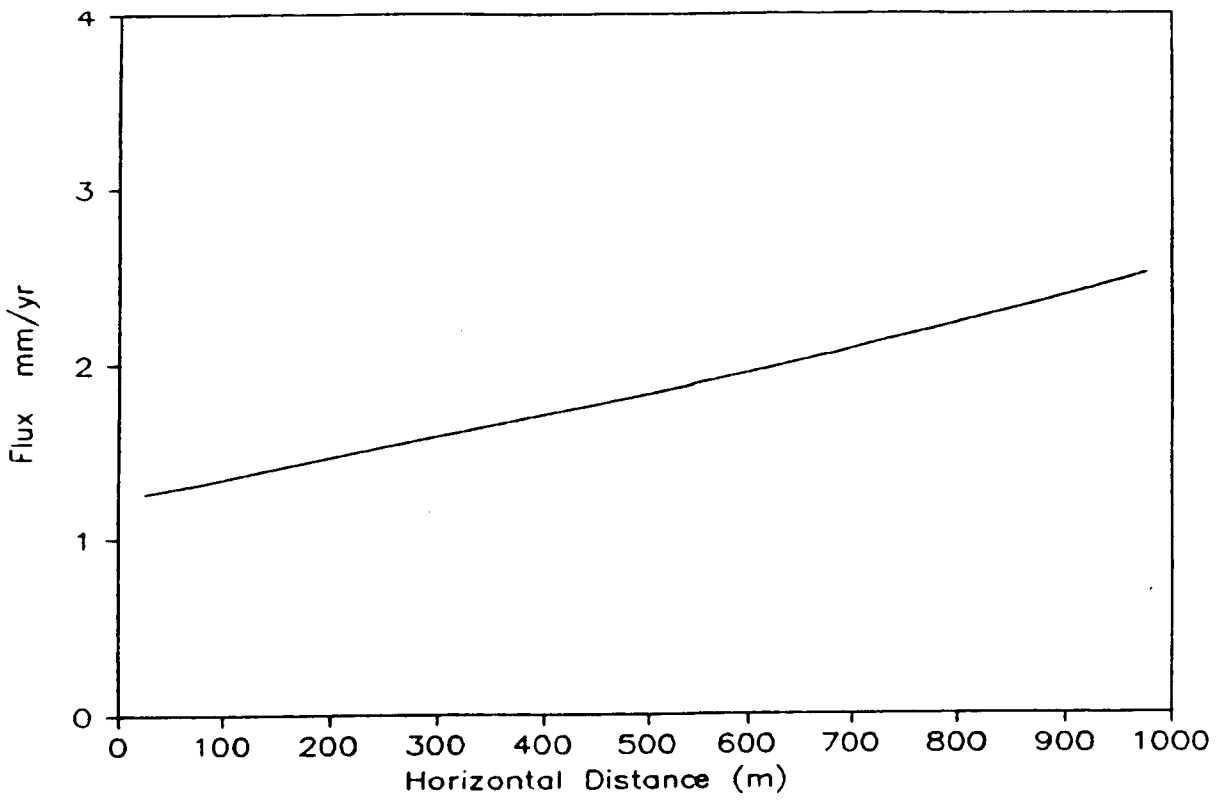

Figure 8-15. Spatial distribution of flux in the matrix based on the DCM3D

Again, this is because the fracture continuum has no definite location but is continuously superimposed over the rock continua.

Similar problems are also attendant to other approaches to modeling partially saturated flow in fractured porous media. Use of a composite characteristic curve has the same disadvantage as the dual-porosity approach in not distinguishing the distinct location and geometry of the fractures. In addition, this approach requires the assumption that locally (within a computational cell) the pressures in the fracture and the rock are instantaneously in equilibrium. However, computationally the composite-curve approach is simpler and less time consuming than the dual-porosity approach because only a single governing equation needs to be solved. The fracture-network type of modeling requires not only detailed definition of the fracture topology, but also definition of their characteristic curves. Therefore, not only are the data needs multiplied, but the computation times become large. It may be that a mixed approach is appropriate where the large faults that could control the flow system to a significant spatial scale (of the order of hundreds of meters) are represented as separate entities in the model, while the small fractures are dealt with as dual-porosity or composite curves.

As new users of the DCM3D code, we had difficulty in setting up the test problems. Some of the problems and recommendations are as follows:

- The manner in which the gravity is introduced in the model is confusing. The *User's Manual* also is not very helpful on this matter.

- The switch from thermodynamic pressure to pressure head is not straightforward; it essentially requires 'fooling' the code, and total hydraulic head can not be used as a dependent variable at all.

- The input structure in general is cumbersome; no comments are allowed, and the analyst has to input a great deal of inconsequential quantities. The input can certainly be improved to compress the input files and make these more readable.

- The options for the medium characteristic curves are too limited; at least one option allowing the input of a characteristic curve in a table format should be added.

- Only rectangular coordinates are allowed; it should be relatively a minor matter to add the cylindrical coordinates.

- Steady-state option is not available, and this probelm can not be easily fixed. If the NRC and the Center decide to use this code in a major way, then it is essential that at least some modifications be made to make it more user friendly.

We also recommend that the NRC should build into its experimental investigations examination of fracture-matrix interaction to provide insight into model applicability. This is necessary if the dual-porosity concept is to be used in preference to the composite-curve approach. Also, the idea of using an approach that combines features of the dual-porosity and fracture-network approaches should be investigated.*

---

* The authors of this report often ran into trouble while setting up the problems discussed here. When called upon, Mr. David Updegraff, developer of DCM3D, was gracious in providing advice on the phone. His help is gratefully acknowledged. The technical and programmatic reviewers at the CNWRA were also of invaluable help. They worked very hard to keep the authors in line as to format and readability of these complex problems. All errors and omissions can, of course, be attributed to the authors.

8.8 REFERENCES

Ababou, R. 1991. *Approaches to Large Scale Unsaturated Flow in Heterogeneous, Stratified, and Fractured Geologic Media.* NUREG/CR-5743. Washington, D. C.: Nuclear Regulatory Commission.

Bixler, N.E. 1985. *NORIA - A Finite Element Computer Program for Analyzing Water, Vapor, and Energy Transport in Porous Media.* SAND84-2057. Albuquerque, New Mexico: Sandia National Laboratories: 115.

El-Kadi, A. I. 1987. *INFIL.* Holcomb Research Institute, IN.: International Groundwater Modeling Center.

Gureghian, A. B. and B. Sagar. 1991. Evaluation of DCM3D - A dual continuum, 3-D groundwater flow code for unsaturated, fractured, porous media. *Report on Research Activities for Calendar Year 1990.* W. C. Patrick, ed. CNWRA 90-01A. San Antonio, Texas: CNWRA.

Haverkamp, R., M. Vanclin, J. Touma, P. J. Wierenga, and G. Vachaud. 1977. A comparison of numerical simulation models for one-dimensional infiltration. *Soil Sci. Soc. Am. J.* 41: 285-294.

Huyakorn, P. S., J. B. Kool, and J. B. Robertson. 1989. *VAM2D - Variably Saturated Analysis Model in Two Dimensions.* NUREG/CR-5352, HGL-8901. Washington, D. C.: NRC.

Magnuson, S. O., R. G. Baca, and A. Jeff Sondrup. 1990. *Independent Verification and Benchmark Testing of the PORFLO-3 Computer Code, Version 1.0.* EGG-BG-9175. Idaho Falls, Idaho: Idaho National Engineering Laboratory: 85.

Philip, J. R. 1957. Numerical Solution of Equations of the Diffusion Type with Diffusivity Concentration-Dependent II. *Australian Journal of Physics*, 10(2): 29-42.

Prindle, R. W., and P. Hopkins. 1990. *On Conditions and Parameters Important to Model Sensitivity for Unsaturated Flow Through Layered Fractured Tough; Results of Analyses for HYDROCOIN Level 3, Case 2.* SAND89-0652. Albuquerque, New Mexico: Sandia National Laboratories: 222.

Runchal, A. K., and B. Sagar. 1989. *PORFLO-3: A Mathematical Model for Fluid Flow, Heat and Mass Transport in Variably Saturated Geologic Media - User's Manual, Version 1.0.* WHC-EP-0041. Richland, Washington: Westinghouse Hanford Company.

Sagar, B., and G. Wittmeyer. 1991. Phase 2 interval project: Las Cruces Trench solute transport modeling study, plot 2, experiment A. *Report on the Research Activities for the Quarter January 1 Through March 31, 1991*. W. C. Patrick, ed. CNWRA 91-01Q. San Antonio, Texas: CNWRA.

Sagar, B., and A. K. Runchal. 1990. *PORFLO-3: A Mathematical Model for Fluid Flow, Heat and Mass Transport in Variably Saturated Geologic Media - Theory and Numerical Methods, Version 1.0.* WHC-EP-0042. Richland, Washington: Westinghouse Hanford Company.

Smyth, J. D., S. B. Yabusaki, and G. W. Gee. 1989. *Infiltration Evaluation Methodology - Letter Report 3: Selected Tests of Infiltration Using Two-Dimensional Numerical Models*. Richland, Washington: Pacific Northwest Laboratory.

Travis, B. J. 1984. *TRACER3D: A Model of Flow and Transport in Porous-Fractured Media*. LA-9667-MS. Los Alamos, New Mexico: Los Alamos National Laboratories.

Updegraff, C. D., C. E. Lee, and D. P. Gallegos. 1991. *DCM3D: A Dual-Continuum, Three-Dimensional, Ground-Water Flow Code for Unsaturated, Fractured, Porous Media*. NUREG/CR-5536 (SAND90-7015). Washington, D. C.: NRC: 140.

van Genuchten, M. Th. 1980. A closed-form equation for predicting the hydraulic conductivity of unsaturated soils. *Soil Science* 44(5): 892-898.

Yeh, G. T., and D. S. Ward. 1979. *FEMWATER: A Finite-Element Model of Water Flow Through Saturated-Unsaturated Porous Media*. Oak Ridge, Tennessee: Oak Ridge National Laboratory.

9 SORPTION MODELING FOR HLW PERFORMANCE ASSESSMENT

by Roberto T. Pabalan and David R. Turner

Investigators: Roberto T. Pabalan (CNWRA), David R. Turner (CNWRA), James D. Prikryl (CNWRA), and Paula Muller (CNWRA)

9.1 INTRODUCTION

An evaluation of the effectiveness of geologic systems as barriers to radionuclide migration requires an understanding of the chemical and physical processes by which aqueous species are sorbed on geologic materials. These processes, which may include adsorption, ion exchange, or precipitation, are commonly represented collectively by empirical parameters, such as sorption coefficient (K_d) or retardation factor (R_f), in transport calculations supporting performance assessments (PA) of geologic repositories. The accuracy, however, of these empirical parameters in quantitatively describing aqueous-solute/rock interactions for calculations of radionuclide transport often used in PA is actively debated. Transport models using these parameters, particularly those that assume constant K_d's or R_f's, do not explicitly account for many potentially important geochemical phenomena occuring during transport in natural systems (e.g., Kent et al., 1988; Siegel, 1989; Siegel et al., 1990). These include aqueous complexation, precipitation/dissolution reactions, competitive sorption, changes in groundwater chemistry, and variability in substrate composition as well as changes in temperature and pressure. Therefore, questions have been raised regarding the adequacy of transport calculations using K_d or R_f in PA (e.g., Kelmers et al., 1987).

9.2 TECHNICAL OBJECTIVES

The general objectives of this project are as follows:

- Obtain a mechanistic understanding of the important radionuclide sorption processes and the physical and chemical parameters that affect sorption behavior in the Yucca Mountain, Nevada, environment.

- Investigate the applicability of coupled-hydrogeochemical models which use simple representations of sorption phenomena to Yucca Mountain PA.

- Develop practical but scientifically defensible approaches to modeling sorption at Yucca Mountain, and the requisite databases to support such models.

The research project has been divided into three tasks, namely: Task 1 - Literature Review and Development of Approach; Task 2 - Coupled Hydrogeochemical Modeling: Application of Simplified Models to NRC Regulatory Needs; and Task 3 - Sorption Experiments. Task 1 consists of literature review of experimental, theoretical, and modeling studies on sorption processes and evaluation of available coupled reaction-transport models. A major milestone report (Turner, 1991), which represents much of the results of activities under

Task 1, was completed during this quarter and was submitted to NRC for review. Based on the review of the literature represented by this report, a workplan is being developed for Task 2 of this project. This workplan will be submitted to NRC during the early part of next quarter. Additional literature review was also conducted with an emphasis on specific sorption models, and techniques for estimating the parameters required by these models. Results of this literature review are discussed in Section 9.3. Under Task 3, experiments were initiated studying the kinetics of uranium sorption on the zeolite mineral clinoptilolite. These experiments are discussed in Section 9.4.

9.3 SURFACE COMPLEXATION MODELS by David R. Turner

9.3.1 Model Description

The sorptive behavior of many radioelements (U, Th, Pu, Np, Am) important to PA exhibits a pronounced pH-dependence (Hsi and Langmuir, 1985; Sanchez et al., 1985). For this reason alone, it has been argued that radioelement sorption cannot be modeled effectively using a K_d approach, as it cannot adequately represent the effect of changes in solution pH (Reardon, 1981; Kelmers, 1987; Kent et al., 1988).

In order to achieve a sound theoretical basis for predictive modeling, electrostatic surface complexation concepts have been advanced, largely for sorption by iron- and manganese-oxyhydroxides (Davis et al., 1978; Davis and Leckie, 1978, 1980). These concepts consider the influence of surface charge on the pH and ion activity at the surface/water interface. Discussed in more detail in Turner (1991), the three most widely used approaches include the diffuse-layer, constant capacitance, and triple-layer models. In addition, Barrow and Bowden (1987) have proposed a four-layer model to better simulate variations in adsorption maximums for different elements.

These models assume a surface comprised of amphoteric hydroxyl groups (OH_2^+, OH^0, O^-, etc.), and treat surface adsorption as a combination of equilibrium protonation/deprotonation reactions of the general form:

$$\mathbf{SOH + H^+ = SOH_2^+ \quad (Protonation,\ K_+^{INT})} \qquad \textbf{(9-1a)}$$

$$\mathbf{SOH = SO^- + H^+ \quad (Deprotonation,\ K_-^{INT})} \qquad \textbf{(9-1b)}$$

where SOH represents a neutral surface site. Intrinsic surface acidity constants $\left(K_+^{INT},\ K_-^{INT}\right)$ are defined for these reactions using mass-action considerations. In the zone disturbed by the surface charge of the adsorbent, activities of aqueous species included in the mass-action expression are assumed to be influenced by electrostatic effects according to the exponential Boltzmann expression such that:

$$a_{i,s} = a_i \left[e^{\frac{-\Psi F}{RT}} \right]^z \qquad (9\text{-}2)$$

where $a_{i,s}$ is the activity of an ion i in the aqueous phase near the charged surface, a_i is the activity in the bulk solution, $e^{-\Psi F/RT}$ is the Boltzmann factor, Ψ is electrostatic potential, z is the valence of the ion, F and R are the Faraday (J/volt equiv) and ideal gas (J/K·mole) constants, respectively, and T is absolute temperature (K).

The various complexation models differ in how the electrostatic potential (Ψ) is extended from the charged surface into the bulk solution, and how changes in solution electrolyte concentration are assumed to affect reactions at the particle surface. All models calculate total sorption by simultaneously solving equations for conservation of surface sites, charge balance, and mass-action. Perhaps the most commonly used approach (Hsi and Langmuir, 1985; Sanchez et al., 1985; Kent et al., 1988; Payne et al., 1990), the triple-layer surface complexation (TLM) model, as its name implies, assumes that the zone influenced by surface charge is divided into three layers. The outer, diffuse layer of counterions (d-plane) is separated from the charged surface by two inner layers of constant capacitance. By design, protonation/deprotonation reactions at surface sites [Eqn. (9-1)] are restricted to the inner o-plane. As a direct result of its construction, the TLM provides for the specific adsorption of ions in the middle β-plane through surface complexation reactions of the general form:

$$\mathrm{SOH + M^+ = SO^- \cdot M^+ + H^+} \quad \text{(cations, } K_{Cat}^{INT}\text{)} \qquad (9\text{-}3a)$$

$$\mathrm{SOH + A^- + H^+ = SOH_2^+ \cdot A^-} \quad \text{(anions, } K_{An}^{INT}\text{)} \qquad (9\text{-}3b)$$

where SO^-M^+ and $SOH_2^+A^-$ represent the adsorbed cation and anion, respectively. K_{Cat}^{INT} and K_{An}^{INT} are calculated using Eqn. (9-2) in a similar fashion to K_+^{INT} and K_-^{INT} such that:

$$K_{cat}^{INT} = \left[\frac{[SO \cdot M^+][H^+]\exp(-\Psi_o F/RT)}{[SOH][M^+]\exp(-\Psi_\beta F/RT)} \right] . \qquad (9\text{-}4)$$

While Eqns. (9-3) and (9-4) are written for monovalent ions (i.e., z = 1), a similar approach is valid for multivalent ions by using z > 1 in Eqn. (9-2).

9.3.2 Data Estimation Techniques

For the sorption of cations and anions on iron and manganese oxyhydroxides, Smith and Jenne (1988) have compiled TLM equilibrium constants for reactions of the form

described by Eqns. (9-1) and (9-3). Unfortunately, surface complexation models have seen limited application to a restricted number of elements, and experimentally determined values for the necessary input parameters are frequently unavailable. Faced with gaps in the database and with discrepancies between reported values (largely due to experimental uncertainty in determining site density), Smith and Jenne (1988, 1991) have developed a method for evaluating existing data and for estimating equilibrium constants for cation adsorption on iron and manganese oxyhydroxides.

Davis and Leckie (1978) suggest that the surface complexation reaction can be rewritten in terms of a surface complexation constant, log K^{SC}:

$$SO^- + M(OH)_n^{z-n} = SO^- \cdot M(OH)_n^{z-n} \qquad (\log K^{SC}) \; . \tag{9-5}$$

In turn, for cations, log K^{SC} is related to the intrinsic acidity constant K_-^{INT} such that:

$$\log K^{SC} = pK_-^{INT} - pK_n^{INT} - \log \beta_{1n} \tag{9-6}$$

where $pK_i = -\log K_i$ for a given equilibrium constant, and β_{1n} is the *n*th hydrolysis constant for the cation M^{z+}. In addition to removing uncertainty associated with the site-density determination, this approach is also desirable in that values for log K^{SC} appear to be relatively insensitive to different polymorphs of the adsorbent (Smith and Jenne, 1988, 1991). Noting the rough linear correlation between K_{Cat}^{INT} and hydrolysis constants for cations, Smith and Jenne (1988, 1991) used expressions derived to estimate first hydrolysis constants (Baes and Mesmer, 1981; Brown et al., 1985):

$$\log \beta_{11} = \text{intercept} + \text{slope} \left[g_1 \left[\frac{z}{r^2} + g_2 \right] \right] \tag{9-7}$$

to define an equation for log K^{SC} such that:

$$\log K^{SC} = a_0 + 0.10 \left[g_1 \left[\frac{z}{r^2} + g_2 \right] \right] + a_1 \log \beta_{1n} \; . \tag{9-8}$$

The constants a_0 and a_1 were determined by Smith and Jenne (1988, 1991) through least squares regression to available data for a number of transition metals. For Fe(III)-oxides, $a_0 = 2.3$ and $a_1 = -0.37$; for Mn(IV)-oxides, the values are 1.0 and -0.10 for a_0 and a_1, respectively. In Eqns. (9-7) and (9-8), r is the ionic radius (Å), and z is the charge of the ion. The parameters g_1 and g_2 are defined as:

$$\begin{aligned} g_1 &= (1 + 2S + D)(z + 2) \\ g_2 &= g(n)(z-1) + 0.1d(n-3)^2(1-S) \end{aligned} \tag{9-9}$$

where:

S = 0 if there are no s electrons in the outermost shell of the ion, otherwise, S=1;
D = 1 if d orbitals are present in the neutral metal, otherwise, D = 0;
n = the principal quantum number of the outermost shell;
g(n) = 1 when n > 1. Otherwise, g(n) = 0; and
d = the number of d electrons present in the outermost shell of the ion.

It should be noted that this approach can be used for the surface complexation of the unhydrolyzed ion by assuming that n = 0. In this case, log β_{10} = 0 by convention. Values for log β_{1n} can be determined either through experiment or calculated using a geochemical equilibrium code such as MINTEQA2 or EQ3 (Allison et al., 1990; Wolery et al., 1990).

Smith and Jenne (1991) suggest that by reorganizing Eqn. (9-6) and substituting Eqn. (9-8), values can be extracted for $pK^{INT}_{M(OH)n}$. In an effort to minimize the effects of uncertainties in site-density determination on the intrinsic acidity constants K^{INT}_{+} and K^{INT}_{-}, Smith and Jenne (1991) note that experimentally determined pK^{INT}_{+} and pK^{INT}_{-} are normally distributed about mean values of 5.0±0.5 and 10.9±0.5, respectively, for all Fe(III)-oxides. Using these values, and solving for g_1 and g_2 based on the electronic configuration of the element of interest, Eqn. (9-8) can be used to determine $K^{INT}_{M(OH)n}$ values for use in the triple-layer sorption model.

9.3.3 Data Estimation for Radionuclides

In an effort to evaluate the suitability of the approach of Smith and Jenne (1988, 1991) for estimating radioelement surface-complexation parameters, it is appropriate to derive a set of values for log K^{SC} using the estimation technique and compare the results to published results. Smith and Jenne (1991) have done this for Th^{4+}, using the data of Hunter et al. (1988). In addition, Sanchez et al. (1985) developed a set of equations of the same form as Eqn. (9-3a) to describe Pu^{4+} adsorption on goethite. Values for $K^{INT}_{Pu(OH)n}$ were determined by Sanchez et al. through a curve-fit to observed Pu-sorption data. Hydrolysis constants are available in Hunter et al. (1988) for Th^{4+}; values for Pu^{4+} are found in the thermodynamic database of the EQ3/EQ6 geochemical code (Wolery, 1990). Log β_{1n}, pK^{INT}_{-} and $pK^{INT}_{M(OH)n}$ values are listed in Table 9-1. Other necessary input parameters for Eqn. (9-9) can be determined from electronic configuration tables available in a variety of reference texts (e.g., CRC, 1982), and are included in Table 9-2.

9.3.4 Discussion and Conclusions

From comparing experimentally determined and calculated log K^{SC} values (Table 9-3), the estimation technique clearly is more appropriate for low values of n < 2. At larger values, the results diverge significantly. Smith and Jenne (1991) point out that this is perhaps to be expected, as the constants used to estimate hydrolysis constants (Brown et al., 1985) were

Table 9-1. SORPTION PARAMETERS AND HYDROLYSIS CONSTANTS FOR Th^{4+} AND Pu^{4+} SORPTION ON GOETHITE

n	$Th(OH)_n$			$Pu(OH)_n$		
	pK_{-}^{INT} a.	$\log \beta_{1n}$ b.	$\log K^{INT}_{M(OH)_n}$ b.	pK_{-}^{INT} a.	$\log \beta_{1n}$ c.	$\log K^{INT}_{M(OH)_n}$ d.
0	9.5	0	1.0	9.5	0	--
1	9.5	-3.20	-0.75	9.5	-0.5	2.5
2	9.5	-6.93	-2.4	9.5	-2.3	-2.0
3	9.5	-11.7	-9.9	9.5	-5.3	-5.9
4	9.5	-15.9	-16.8	9.5	-9.5	-12.0

a. from Balistrieri and Murray (1981).
b. from Hunter et al. (1988).
c. from Wolery et al. (1990).
d. from Sanchez et al. (1985).

developed primarily for mono- and divalent cations where n is always less than two. Smith and Jenne (1991) also propose that the tendency of Th^{4+} to form polynuclear species may lead to errors in the hydrolysis constants for $n > 1$. Plutonium, at least in the 6+ oxidation state, is especially susceptible to forming polynuclear species (Choppin and Mathur, 1991), and may be sensitive to the same limitations as Th^{4+}.

An additional possible explanation for the observed discrepancies may be the manner in which values for $K^{INT}_{M(OH)_n}$ were determined in the studies of Hunter et al. (1988) and Sanchez et al. (1985). These values were largely determined assuming that adsorption of the different hydrolyzed species is additive until the observed sorption-pH data are matched well by the triple-layer model. If more than one hydrolyzed species is necessary to fit the data, then it may be possible that the derived solution is not unique, and that the inferred values for $K^{INT}_{M(OH)_n}$ are in turn nonunique (Hunter et al., 1988). Different combinations of $M(OH)_n$ may fit the sorption-pH data equally well, and the resultant $K^{INT}_{M(OH)_n}$ provide a closer match between "measured" and calculated values. Additional studies under controlled conditions are needed to examine independently the relative contribution of the different hydrolyzed species to the observed sorption data.

Due to the lack of experimental data, estimation techniques must be used to provide the necessary parameters for the application of electrostatic models to radioelement

Table 9-2. Th^{4+} AND Pu^{4+} INPUT PARAMETERS FOR EQN. (9-8)

	z	r(Å)	g_1	g_2
Th^{4+}	4	0.99	12	3
Pu^{4+}	4	0.90	12	3

sorption. Based on the linear relationship between surface-complexation constants and hydrolysis constants, Smith and Jenne (1988, 1991) have developed a data estimation approach for the triple-layer, surface-complexation model. Application of this model to Th^{4+} and Pu^{4+} indicate that this approach may be suitable for the sorption of hydrolyzed species $M(OH)_n$ where $n < 2$. As n increases to values greater than two, however, the suitability of the technique decreases. This may be due either to the assumptions inherent in deriving the necessary constants (using mono- and divalent species only), or to the complex chemistries of Th(IV) and Pu(IV). An additional source of uncertainty is the possibility of nonuniqueness in the experimental sorption parameters considered. The estimation technique of Smith and Jenne (1988, 1991) should be used with caution pending the determination of coefficients for Eqns. (9-7) and (9-8) for multivalent species with $n > 2$.

Table 9-3. MEASURED AND CALCULATED VALUES FOR LOG K^{sc}

	$Th(OH)_n$		$Pu(OH)_n$	
n	Meas.[a]	Calc.[b]	Meas.[c]	Calc.[b]
0	10.5	10.8	--	11.8
1	12.0	12.0	12.5	12.0
2	14.1	13.3	9.8	12.7
3	11.4	15.1	8.9	13.8
4	8.7	16.7	7.0	15.3

a. From Hunter et al. (1988) and Smith and Jenne (1991). Calculated using Eqn. (9-6) and input parameters listed in Table 9-1
b. Calculated using Eqn. (9-8) and input parameters from Tables 9-1 and 9-2
c. From Sanchez et al. (1985). Calculated using Eqn. (9-6) and input parameters listed in Table 9-1

9.4 SORPTION EXPERIMENTS: KINETICS OF URANIUM SORPTION ON CLINOPTILOLITE by Roberto T. Pabalan

To develop an understanding of the important radionuclide sorption mechanisms and the physical and chemical parameters that affect sorption behavior in the Yucca Mountain environment, a literature review of experimental and modeling studies of uranium sorption on geologic media was conducted during the first calendar quarter. Results of that review were discussed in the research report for that period (Pabalan and Turner, 1991). On the basis of the literature review, a work plan for conducting experimental studies on uranium sorption on geologic media was developed. The experiments described in the workplan are designed to facilitate understanding the fundamental controls on uranium sorption; i.e., how and why sorption values change as a function of the properties of the sorbing solid and the aqueous phase. Experimental and analytical techniques and methods for data interpretation and modeling, developed in the uranium sorption experiments, will be useful in extending the studies to other actinides and radioelements. The experiments will also provide useful data for validating hydrogeochemical transport codes (Task 2 of this research project), in interpreting and modeling results derived in the CNWRA's Geochemical Analog Research Project, and in evaluating data and modeling needs for the CNWRA's Performance Assessment Research Project.

The initial focus of the experiments is uranium sorption on zeolite minerals, particularly clinoptilolite. Because the presence of laterally extensive zones of clinoptilolite-rich tuff at Yucca Mountain might provide a significant contribution to the geologic barrier for radionuclide transport, the factors that control radionuclide sorption on clinoptilolite must be understood. The major portion of the planned experiments on uranium sorption consists of equilibrium studies. However, the lack of sufficient information on the kinetics of uranium sorption on clinoptilolite precludes initiation of equilibrium experiments. Therefore, scoping experiments were initiated to determine the rate of reaction and the amount of time necessary to reach equilibrium.

9.4.1 Experimental Design

Several factors were considered in the design of the scoping experiments. The aqueous speciation of uranium(6+) and, therefore, its sorption behavior very much depend on solution pH and uranium concentration as well as pCO_2 (see discussions in Pabalan and Turner, 1991). In order to minimize complications in the interpretation of the sorption kinetics data, it was useful to conduct the experiments under pH conditions in which a single aqueous uranyl species is predominant (>90 percent ΣU). In addition, some published experimental data indicate that at pH's less than 4, where the predominant species both in the presence and absence of atmospheric $CO_2(g)$ is the uranyl ion UO_2^{2+} (Langmuir, 1978), significant sorption of uranium on clinoptilolite occurs (e.g., Katayama et al., 1974; Doi et al., 1975; Andreeva and Chernyavskaya, 1982), although it is much less than at higher pH's. By noting that the ionic size of UO_2^{2+} is smaller than the channel openings in clinoptilolite, ion exchange as a potential mechanism for the sorption of uranium on clinoptilolite under acidic pH's can be inferred. In fact, the experimental data of Andreeva and Chernyavskaya (1982) on sorption between a H^+-

form of the zeolite mineral mordenite and uranyl solutions demonstrate that a stoichiometric exchange of two H^+ ions for one UO_2^{2+} ion occurs at pH's less than 4.1.

Intuitively, one expects the rate of ion-exchange reactions between zeolites and aqueous species to be slower than surface adsorption processes, which do not involve diffusion through the intracrystalline pores of the zeolite. Thus, information on the kinetics of uranium sorption may provide clues to the probable sorption mechanism. Since the zeolite to be used in the experiments is a nearly homoionic Na-form, independent information on the role of ion exchange mechanism can also be derived by analyzing the concentration of Na^+ in solution. If ion exchange is the predominant mechanism at pH values where UO_2^{2+} is the dominant aqueous species, one would expect that the decrease in molal concentration of uranium will be one-half the increase in molal concentration of sodium.

The desire to be able to analyze the concentration of Na^+ in solution using an ion-selective electrode constrained the initial concentration of uranium and the weight of Na-clinoptilolite that were used in the experiments. Thus, 1000 ppm was chosen as the initial U concentration. A simple calculation assuming all uranium (as UO_2^{2+}) initially in solution ion exchanges with Na^+ initially in the zeolite indicates that, at equilibrium, a 1-liter solution will have a concentration of about 193 ppm Na^+. This is well within the analytic capability of a Na-selective electrode, even with a ten-fold dilution. Of course, sodium concentrations during the initial stages of reaction will be much less.

MINTEQA2 speciation calculations were done on aqueous solutions of 1000 ppm U in order to determine the equilibrium fields of predominance of uranyl species as a function of pH. The results are plotted in Figures 9-1 and 9-2 for systems in the absence or presence of atmospheric $CO_2(g)$, respectively. Figure 9-1 indicates that, where $CO_2(g)$ is not present, greater than 90 percent of total uranium occurs as the UO_2^{2+} species at pH's less than about 3.4, whereas more than 90 percent of total uranium is in the form of $(UO_2)_3(OH)_5^+$ at pH's greater than about 5.2. The same species are predominant in solutions in equilibrium with atmospheric $CO_2(g)$, except at pH's greater than about 8.2, where $UO_2(CO_3)_3^{4-}$ becomes the dominant aqueous species. $UO_2(CO_3)_3^{4-}$ constitutes 90 percent or more of total uranium at pH's of about 8.7 or greater in solutions in equilibrium with atmospheric $CO_2(g)$.

It is more convenient to conduct experiments which are open to the atmosphere; thus, the scoping experiments were constrained to be in equilibrium with atmospheric $CO_2(g)$. pH values of 3.0 and 9.0, where the predominant species are UO_2^{2+} and $UO_2(CO_3)_3^{4-}$, respectively, were chosen as the starting pH of the solutions. The experimental procedure and initial results and conclusions are given below as follows.

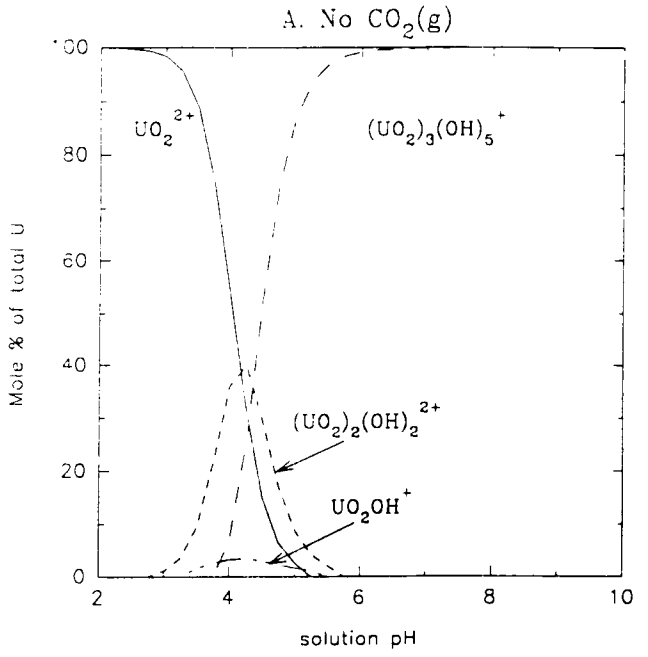

Figure 9-1. Aqueous speciation of uranium (6+) calculated using MINTEQA2 for solutions with 1000 ppm U and no CO_2 (g) present

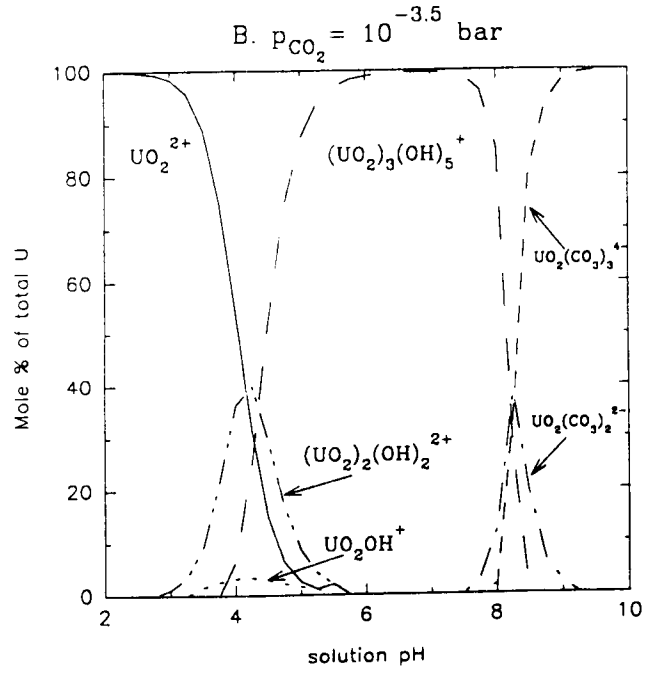

Figure 9-2. Aqueous speciation of uranium (6+) calculated using MINTEQA2 for solutions with 1000 ppm U and in equilibrium with CO_2(g) ($pCO_2 = 10^{-3.5}$ bar)

9.4.2 Experimental Procedure

9.4.2.1 Experiments at initial pH=3.0

Two experimental mixtures (in duplicate) and two control mixtures (also in duplicate) were prepared. Descriptions of each mixture follow.

Solution IA*1. Two liters of 1000 ppm U solution were prepared by weight from reagent grade $UO_2(NO_3)_2 \bullet 6H_2O$. 950 grams of the solution were transferred into each of two polypropylene bottles labeled IA*1a and IA*1b. The pH of the solutions were adjusted to 3.0 by adding dropwise 1.0 N or 0.1 N HNO_3. To each bottle, 4.5 grams of Na-clinoptilolite were added; then the mixtures were kept agitated at room temperature using a New Brunswick gyratory shaker.

If the zeolite is assumed to have a cation exchange capacity (CEC) of 2.17 mequivs./gm. based on previous work (Pabalan, 1991, 1991b), then the total CEC of 4.5 gms. of clinoptilolite is 9.77 mequivs., which is greater than the total equivalents of UO_2^{2+} (7.98 mequivs.) in 950 ml. of solution. Therefore, the zeolite can potentially sorb most, if not all, of the uranium if ion exchange is the sorption mechanism.

Solution IA*2. The solutions, which were in bottles labeled IA*2a and IA*2b, have compositions and volumes the same as those of IA*1. However, only 2 gms. of Na-clinoptilolite were added. In this case, the total CEC of 2.0 gms. of zeolite is 4.34 mequivs., which is less than the total equivalents of UO_2^{2+} in solution.

Solution IA*3. This is a control experiment to evaluate potential losses of uranium from solution to the container walls. Two liters of 1000 ppm U solution were prepared by weight from reagent grade $UO_2(NO_3)_2 \bullet 6H_2O$. Into each of two bottles labeled IA*3a and IA*3b 950 grams of the solution were transferred. The pH of the solutions were adjusted to 3.0 by adding dropwise 1.0 N or 0.1 N HNO_3. No zeolite was added to the solutions.

Solution IA*4. This is a control experiment to determine the importance of ion exchange between H^+ initially in solution and Na^+ initially in the zeolite. One liter of ultrapure (> 17 mega-ohm) water was transferred into each of two polypropylene bottles labeled IA*4a and IA*4b. Their pH's were adjusted to 3.0 by dropwise addition of 1.0 or 0.1 N HNO_3. One gram of Na-clinoptilolite was added.

Aliquots of solutions IA*1, IA*2, and IA*3 were taken periodically for analysis of uranium concentration using square-wave voltammetry in 0.1 N HCl matrix. Additional samples were taken from IA*1 and IA*2 for sodium analysis (see discussion below). During each sampling time, the pH of each solution was also measured. In addition, each bottle was weighed before and after samples were taken in order to account for changes in solution volume due to evaporation and to sample withdrawal.

After the last samples from IA*1, IA*2, and IA*3 were taken, the pH of solution IA*4 was measured, and aliquots were taken for sodium analysis. The results are given in Tables 9-1 to 9-7.

9.4.2.2 Experiments at initial pH=9.0

One experimental mixture (in duplicate) and one control mixture (also in duplicate) were prepared. Descriptions of each mixture are given below.

Solution IB*1. Two liters of 1000 ppm U solution were prepared by weight from reagent grade $UO_2(NO_3)_2 \cdot 6H_2O$. Into each of two polypropylene bottles labeled IB*1a and IB*1b, 950 grams of the solution were transferred. The pH of the solutions was adjusted to about 9.0 by the addition of reagent grade $NaHCO_3$, and solution mixing was done using a gyratory shaker. Equilibrium modeling with EQ3NR was used to determine the amount of $NaHCO_3$ necessary to raise the pH of the uranyl solutions to 9.0. This indicated that 2.594 gms. of $NaHCO_3$ are needed. Independent calculations using MINTEQA2 gave the same result.

The approach to equilibrium between the aqueous phase and atmospheric $CO_2(g)$ after addition of $NaHCO_3$, however, was slow; and the pH of the solutions was monitored periodically until it reached a constant value. Figure 9-3 shows the pH of solutions IB*1a and IB*1b as a function of time after addition of $NaHCO_3$. The arrow indicates the time at which the mixing rate was reduced and the screw caps were removed from the polypropylene bottles. The final pH of 8.93 ± 0.02 is close to that predicted by EQ3NR.

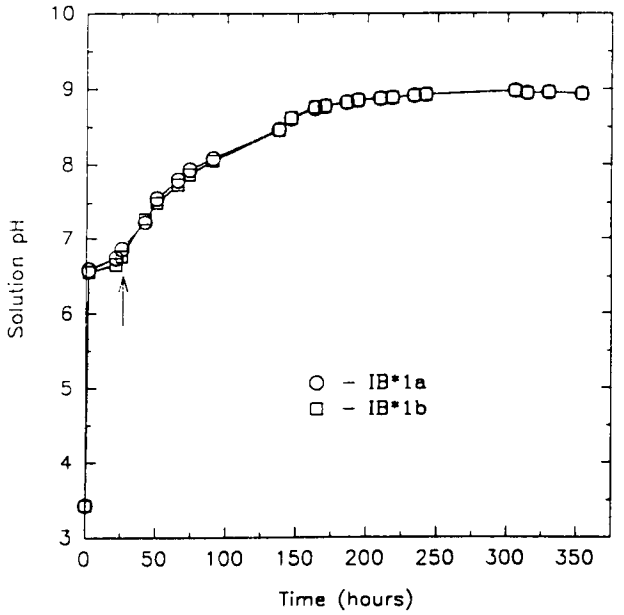

Figure 9-3. pH of 1000 ppm U solution as a function of time after addition of 2.594 gms. of $NaHCO_3$. The arrow indicates the time when the mixing rate was reduced, and the bottle caps were removed.

After equilibrium pH was achieved, 4.5 gms. of Na-clinoptilolite were added to each bottle; then the mixtures were kept agitated at room temperature using a gyratory shaker.

Solution IB*2. This is a control experiment to evaluate potential losses of uranium from solution to the container walls. The 1000 ppm U solutions with pH of about 9.0 were prepared similarly to IB*1, and were contained in bottles labeled IB*2a and IB*2b. No zeolite was added to the solutions.

Aliquots of solutions IB*1 and IB*2 were taken periodically for analysis of uranium concentration using square-wave voltammetry in 0.1 N HCl matrix. Additional samples were taken from IB*1 for sodium analysis. During each sampling time, the pH of each solution was also measured. In addition, each mixture was weighed before and after samples were taken in order to account for changes in solution volume due to evaporation and to sample withdrawal. The IB sorption kinetics experiments were initiated at the end of the third calendar quarter, and results will be given in the next quarterly research report.

9.4.2.3 Initial Results and Conclusions

The results of experiments at initial pH=3.0 are tabulated in Tables 9-4 to 9-10. Only the uranium concentrations and pH values are given, except for mixture IA*4. The initial attempt to analyze sodium in solutions containing uranium using ion-selective electrodes failed because addition of the required ionic strength adjustor, which consists of 4 M NH_4CL + 4 M NH_4OH, to the aqueous samples caused the formation of a yellow precipitate. Preliminary X-ray diffraction analysis indicates that this precipitate is $NH_3(UO_3)_3 \bullet 5H_2O$. The method to be used in the analysis of sodium in uranyl solutions will be either plasma emission spectroscopy (ICP) or atomic absorption spectroscopy (AA). The sodium samples for mixtures IA*1 and IA*2 were acidified using HNO_3 to keep the solutions stable prior to analysis. The results will be reported next quarter. For mixture IA*4, which did not have uranium present, sodium concentrations were successfully determined with Na-selective electrodes and are listed in Table 9-10.

The data in Tables 9-4 and 9-5 show that, within the analytical uncertainty of the polarographic method used in uranium analysis (± 5 percent), *no sorption* of uranium on clinoptilolite occurred for experiments with an initial pH of 3.0. In addition, results given in Table 9-8 and 9-9 indicate that there was no significant sorption of uranium on the container walls. Neither ion exchange nor surface adsorption reaction appears to have taken place between the aqueous UO_2^{2+} and the zeolite phase. However, column 5 in Tables 9-4 and 9-5 shows that significant changes in pH occurred. The initial value of 3.0 changed to a final pH of 3.64 ± 0.01 and 3.51 ± 0.01 for the mixtures IA*1 and IA*2, respectively. This suggests that ion exchange occurred between H^+ initially in solution and Na^+ initially in the zeolite phase. The smaller change in pH for IA*2 is most likely a result of the smaller mass of zeolite used in the mixture.

Table 9-4. U CONCENTRATION AND pH OF MIXTURE IA*1a versus TIME

Sample No.	Time (hours)	U concentration (ppm)		Solution pH
		Sample IA*1a*1	Sample IA*1a*2	
1	2.1	993	992	3.27
2	4.0	994	997	3.29
3	22.1	1004	1007	3.44
4	27.8	974	999	3.44
5	46.1	975	978	3.59
6	70.1	992	1008	3.64
7	93.9	1006	1011	3.64
8	166.0	1007	1025	3.64
9	214.1	1014	1005	3.63
10	261.9	1020	1008	3.63
11	284.6	1001	1001	3.64
12	334.1	1018	1012	3.65

Table 9-5. U CONCENTRATION AND pH OF MIXTURE IA*1b versus TIME

Sample No.	Time (hours)	U concentration (ppm)		Solution pH
		Sample IA*1b*1	Sample IA*1b*2	
1	2.1	997	1001	3.35
2	4.0	1015	991	3.37
3	22.1	1003	1010	3.50
4	27.8	987	991	3.50
5	46.1	994	995	3.54
6	70.1	998	1003	3.61
7	93.9	1028	1013	3.61
8	166.0	1009	1022	3.64
9	214.1	1013	1008	3.64
10	261.9	1013	989	3.63
11	284.6	997	1009	3.63
12	334.1	1019	1029	3.65

Table 9-6. U CONCENTRATION AND pH OF MIXTURE IA*2a versus TIME

Sample No.	Time (hours)	U concentration (ppm)		Solution pH
		Sample IA*2a*1	Sample IA*2a*2	
1	2.1	989	1007	3.23
2	4.0	1006	1009	3.26
3	22.3	1011	1032	3.44
4	26.9	1012	1012	3.44
5	46.0	1027	1022	3.47
6	69.9	1019	1015	3.53
7	94.0	1007	1019	3.51
8	166.0	1016	1025	3.49
9	214.1	1025	1025	3.48
10	262.5	1037	1038	3.49
11	285.9	1009	1018	3.50
12	333.9	1027	1037	3.50

Table 9-7. U CONCENTRATION AND pH OF MIXTURE IA*2b versus TIME

Sample No.	Time (hours)	U concentration (ppm)		Solution pH
		Sample IA*2b*1	Sample IA*2b*2	
1	2.1	998	996	3.21
2	4.0	1020	-	3.23
3	22.3	1017	1030	3.41
4	26.9	1011	1023	3.43
5	46.0	1020	1019	3.44
6	69.9	1005	1026	3.44
7	94.0	1021	1013	3.45
8	166.0	1015	1031	3.48
9	214.1	1029	1029	3.48
10	262.5	1007	1015	3.47
11	285.9	1009	1020	3.50
12	333.9	1028	1024	3.52

Table 9-8. U CONCENTRATION AND pH OF MIXTURE IA*3a versus TIME

Sample No.	Time (hours)	U concentration (ppm)		Solution pH
		Sample IA*3a*1	Sample IA*3a*2	
1	4.0	1012	1018	3.01
2	29.8	1023	1021	2.99
3	70.8	1028	1032	2.98
4	166.5	1007	1006	2.98
5	262.4	1029	1006	2.97
6	334.5	1024	1017	2.99

Table 9-9. U CONCENTRATION AND pH OF MIXTURE IA*3b versus TIME

Sample No.	Time (hours)	U concentration (ppm)		Solution pH
		Sample IA*3b*1	Sample IA*3b*2	
1	4.0	1015	1014	3.02
2	29.8	1015	1036	3.00
3	70.8	1026	995	2.99
4	166.5	1002	998	2.98
5	262.4	1014	1033	2.97
6	334.5	1009	1006	3.00

Table 9-10. INITIAL AND FIXED VALUE OF Na CONCENTRATION AND pH OF MIXTURES IA*4a AND IA*4b

Solution No.	Initial		Final	
	Na ppm	pH	Na ppm	pH
IA*4a	0	3.0	16.9±0.1	3.53
IA*4b	0	3.0	16.8±0.1	3.53

That ion exchange between H^+ and Na^+ took place can be inferred from the control experiment IA*4 (see Table 9-10 for results). The decrease in molality of H^+, which was calculated from the change in pH, is 7.0×10^{-4} molal. This corresponds very well with the increase in Na^+ concentration of 7.3×10^{-4} molal. Verification of ion exchange between H^+ and Na^+ in mixtures IA*1 and IA*2 needs to await analysis of sodium in those solutions. However, the above results suggest that competition with other cations in the aqueous phase reduces the importance of ion exchange as a mechanism for uranium sorption on zeolite minerals. In acidic solutions, H^+ appears to compete effectively with UO_2^{2+} for ion-exchange sites. This could be largely due to the smaller size of the hydronium ion (H_3O^+) compared to the uranyl ion (UO_2^{2+}).

9.5 REFERENCES

Allison, J. D., D. S. Brown, and K. J. Novo-Gradac. 1990. *MINTEQA2/PRODEFA2, A Geochemical Assessment Model for Environmental Systems: Version 3.0 User's Manual.* Athens, GA: Environmental Research Laboratory, Office of Research and Development, Environmental Protection Agency.

Andreeva, N. R., and N. B. Chernyavskaya. 1982. Sorption of uranyl ions by mordenite and clinoptilolite. *Radiokhimiya* 24: 9-13.

Baes, C. F., Jr., and R. E. Mesmer. 1981. The thermodynamics of cation hydrolysis. *Am. Jour. Sci. 281*: 935-962.

Balistrieri, L. S., and J. W. Murray. 1981. The surface chemistry of goethite (αFeOOH). *Am. Jour. Sci. 281*: 788-806.

Barrow, N. J., and J. W. Bowden. 1987. A comparison of models for describing the adsorption of anions on a variable charge mineral surface. *Jour. Coll. Interface Sci. 119*: 236-250.

Brown, P. L., R. N. Sylva, and J. Ellis. 1985. An equation for predicting the formation constants of hydroxo-metal complexes. *Jour. Chem. Sci. Dalton Trans.*: 723-730.

Choppin, G. R., and J. N. Mathur. 1991. Hydrolysis of actiny (VI) cations. *Radiochim. Acta 52/53*: 25-28.

Davis, J. A., R. O. James, and J. O. Leckie. 1978. Surface ionization and complexation at the oxide/water interface 1. computation of electrical double layer properties in simple electrolytes. *Jour. Coll. Interface Sci. 63*: 480-499.

Davis, J. A., and J. O. Leckie. 1978. Surface ionization and complexation at the oxide/water interface 2. Surface properties of amorphous iron oxyhydroxide and adsorption of metal ions. *Jour. Coll. Interface Sci. 67*: 90-107.

Davis, J. A., and J. O. Leckie. 1980. Surface ionization and complexation at the oxide/water interface 3. adsorption of anions. *Jour. Coll. Interface Sci. 74*: 32-43.

Doi, K., S. Hirono, and Y. Sakamaki. 1975. Uranium mineralization by ground water in sedimentary rocks. Japan *Econ. Geol.* 70: 628-646.

Hsi, C. D., and D. Langmuir. 1985. Adsorption of uranyl onto ferric oxyhydroxides: Application of the surface complexation site-binding model. *Geochim. Cosmochim. Acta 49*: 1931-1941.

Hunter, K. A., D. J. Hawke, and L. K. Choo. 1988. Equilibrium adsorption of thorium by metal oxides in marine electrolytes. *Geochim. Cosmochim. Acta. 52*: 627-636.

Katayama, N., K. Kubo, and S. Hirono. 1974. Genesis of uranium deposits of the Tono Mine. Japan. IAEA-SM-183/11. Vienena Austria: International Atomic Energy Agency.

Kelmers, A. D., R. E. Meyer, J. G. Blencoe, and G. K. Jacobs. 1987. Radionuclide sorption methodologies for performance assessment of high-level nuclear waste repositories: A perspective gained from an NRC workshop. *Nuclear Safety* 28: 515-522.

Kent, D. B., V. S. Tripathi, N. B. Ball, J. O. Leckie, and M. D. Siegel. 1988. *Surface-Complexation Modeling of Radionuclide Adsorption in Subsurface Environments*. Sandia National Laboratory, NUREG/CR-4807, SAND86-7175. Washington, D.C.: NRC.

Langmuir, D. 1978. Uranium solution-mineral equilibria at low temperatures with application to sedimentary ore deposits. *Geochim. Cosmochim. Acta* 42: 547-569.

Pabalan, R. T. 1991. Unsaturated mass transport (Geochemistry): Experimental studies. *Report on Research Activities for Calendar Year 1990.* W. C. Patrick, ed. CNWRA 90-01A. San Antonio, Texas: CNWRA.

Pabalan, R. T. 1991b. Nonideality effects on the ion exchange behavior of the zeolite mineral clinoptilolite. *Scientific Basis for Nuclear Waste Management XIV.*

T. Abrajano, Jr. and L. H. Johnson, eds. MRS Symp. Proc. 212. Pittsburgh, PA: Materials Research Society: 559-567.

Pabalan, R. T., and D. Turner. 1991. Sorption modeling for HLW performance assessment. *Report on Research Activities for the Quarter January 1 Through March 31, 1991*. W. C. Patrick, ed. CNWRA 91-01Q. San Antonio, TX: CNWRA.

Payne, T. E., J. A. Davis, and T. D. Waite. 1990. Modelling of uranium sorption to substrates from the weathered zone in the vicinity of the Koongarra ore body. *Alligator Rivers Analogue Project First Annual Report, 1988-1989*. P. Duerden ed. Menie, New South Wales, Australia: Austral. Nucl. Sci. Technol. Organization: 39-46.

Reardon, E. J. 1981. Kd's - Can they be used to describe reversible ion sorption reactions in contaminant migration? *Ground Water 19*: 279-286.

Royal Society of Chemistry. 1982. *Handbook of Chemistry and Physics, 62nd Edition, 1981-1982*. R. C. Weast and M. J. Astle eds. Boca Raton, Florida: Royal Society of Chemistry, CRC Press: B-1 and F-175.

Sanchez, A. L., J. W. Murray, and T. H. Sibley. 1985. The adsorption of plutonium IV and V on goethite. *Geochim. Cosmochim. Acta 49*: 2297-2307.

Siegel, M. D., ed. 1989. *Progress in Development of a Methodology for Geochemical Sensitivity Analysis for Performance Assessment. Speciation, Sorption, and Transport in Fractured Media*. NUREG/CR-5085, Vol.2. Washington, D.C.: NRC.

Siegel, M. D., J. O. Leckie, S. W. Park, S. L. Phillips, and T. Sewards. 1990. *Studies of Radionuclide Sorption by Clays in the Culebra Dolomite at the Waste Isolation Pilot Plant Site, Southeastern New Mexico*. SAND89-2387. Albuquerque, NM.: Sandia National Laboratories.

Smith, R. W., and E. A. Jenne. 1988. *Compilation, Evaluation, and Prediction of Triple-Layer Model Constants for Ions on Fe(III) and Mn(IV) Hydrous Oxides*. PNL-6754/UC-11. Richland, WA: Pacific Northwest Laboratory.

Smith, R. W., and E. A. Jenne. 1991. Recalculation, evaluation, and prediction of surface complexation constants for metal adsorption on iron and manganese oxides. *Environ. Sci. Technol. 25*: 525-531.

Turner, D. R. 1991. *Sorption Modeling for High-Level Waste Performance Assessment: A Literature Review*. CNWRA 91-011. San Antonio, TX: CNWRA.

Wolery, T. J., K. J. Jackson, W. L. Bourcier, B. E. Bruton, K. G. Knauss, and J. M. Delany. 1990. *Current Status of the EQ3/6 Software Package for Geochemical Modeling*. Washington, D. C.: American Chemical Society: 104-116.